Universitat Politècnica de València
I.U.I. CMT - CLEAN MOBILITY & THERMOFLUIDS
PhD program in Propulsion Systems for Transport



Doctoral Thesis

STUDY OF SPRAY-AIR INTERACTION IN A GASOLINE FUEL INJECTION SYSTEM UNDER VARIOUS FLASH BOILING CONDITIONS

Presented by:
Victor Daniel Mendoza Álvarez

Supervised by:
Dr. Raúl Payri Marín

in fulfillment of the requirements for the degree of
Doctor of Philosophy

Valencia, July 2025

Ph.D. Thesis

STUDY OF SPRAY-AIR INTERACTION IN A GASOLINE FUEL INJECTION SYSTEM UNDER VARIOUS FLASH BOILING CONDITIONS

Written by: Mr. Victor Daniel Mendoza Álvarez
Supervised by: Dr. Raúl Payri Marín

Examination committee:

Chairman: Dr. Ricardo Novella
Secretary: Dr. Christine Mounaïm-Rousselle
Member: Dr. Michele Bardi.

Reviewing board:

Dr. Christine Mounaïm-Rousselle
Dr. Michele Bardi

Valencia, July 2025

Abstract

Fuel injection in combustion systems, particularly gasoline injections, continues to play a significant role in the automotive industry and ongoing research due to its potential for high efficiency while achieving low emission. In this context, the present study aims to deepen the understanding of the key phenomena affecting spray injection and atomization, focusing on both gasoline surrogates and Ethanol.

This research analyzes two GDI injectors, both capable of operating at high injection pressures. One serves as the main reference for characterization, while the second is used for comparative purposes and validation of observed trends. Two surrogate fuels are employed to simulate different volatility properties of gasoline compounds and ultimately reproduce more extreme flashing conditions, as well as Ethanol, a representative alcohol increasingly considered in low-carbon fuel strategies.

An exhaustive methodology was conducted for employing PDPA on GDI sprays using a new instrumentation at the research center that hosted this project, the Clean Mobility and Thermofluids (CMT). Furthermore, the ambient temperature control in the vessel was improved by installing a new resistor module and isolating parts for faster and homogeneous ambient gas heating. Two custom rotated windows were also tested to optimize PDPA alignment.

For the internal flow, a characterization including the rate of momentum (ROM) and rate of injection (ROI) of both nozzles is performed. The nozzles geometry was measured using several techniques, including advanced X-ray optical techniques at the Argonne National Laboratory (ANL). Injector response was tested to typical boundary conditions such as injection and ambient pressure, fuel temperature, etc. Side-view visualization using MIE scattering technique aided in having a clear idea of the phenomena taking place at different injection conditions while performing droplet size and velocity measurements. In this sense, some of the most extreme flashing conditions produced the spray collapse phenomenon due to plumes interaction. Different collapse structures were observed, one for transitional and the other for fully collapsed sprays.

Velocity and droplet size data at various axial and radial positions confirmed expected atomization trends, particularly the positive influence of high injection pressure, ambient temperature, and flash boiling. A clear inverse relationship between R_P and droplet size across most injection conditions was seen, i.e. the higher R_P values generally corresponded to lower Sauter Mean

Diameters (SMD). However, deviations from this trend attributed to the onset of spray collapse, introduced larger droplets into the distribution.

Following this thread, a complete mapping of collapse regimes, ranging from mild to extreme, allowed to determine that droplet sizes within the collapse region were consistently higher than those in the main spray and often override the positive effects on atomization of high injection pressure or flash boiling.

The experimental methodology established here proved effective for measuring droplet velocities and sizes in the central region of the injector, even under extreme collapse scenarios. A collapse band was identified near the core of the injector under various flash boiling conditions. This region was surrounded by areas with negative velocities or reverse flow phenomena; revealing that the collapse position was strongly influenced by the most energetic jets.

Overall, these qualitative and quantitative findings are expected to contribute to ongoing research on GDI sprays involving volatile fuels, with novel application of established measurement tools, and offer a broader understanding of GDI spray behavior, and support future research on injector design, injection strategies, and combustion optimization.

Resumen

La inyección de combustible en sistemas de combustión, particularmente de gasolina, sigue desempeñando un papel importante en la industria automotriz y en la investigación actual dado su potencial para lograr una alta eficiencia con bajas emisiones. En este contexto, el presente estudio tiene como objetivo profundizar en la comprensión de los fenómenos clave que afectan la inyección y la atomización del chorro.

Esta investigación analiza dos inyectores GDI, ambos capaces de operar a altas presiones de inyección. Uno sirve como referencia principal para la caracterización, mientras que el segundo se utiliza con fines comparativos y para la validación de las tendencias observadas. Se emplean dos combustibles para simular diferentes propiedades de volatilidad de los compuestos de la gasolina y reproducir condiciones de flashing más extremas, así como Etanol, un alcohol representativo usualmente considerado en estrategias de bajas emisiones de carbono.

Se llevó a cabo una metodología exhaustiva para medidas de chorro GDI mediante PDPA usando un equipo nuevo en el centro de investigación que albergó este proyecto, el Clean Mobility and Thermofluids (CMT). Además, se mejoró el control de la temperatura en la maqueta mediante la instalación de un nuevo módulo de resistencias y aislamiento para un calentamiento más rápido y homogéneo del gas ambiente. También se probaron dos ventanas giradas para optimizar la alineación del PDPA.

Para el flujo interno, se realiza una caracterización que incluye la tasa de momento (ROM) y la tasa de inyección (ROI) de ambas toberas. La geometría de éstas se midió utilizando varias técnicas, incluidas técnicas ópticas avanzadas de rayos X en el Argonne National Laboratory (ANL).

La visualización lateral con dispersión MIE ayudó a tener una idea clara de los fenómenos que tienen lugar durante las inyecciones mientras se realizaban mediciones de tamaño y velocidad de gotas. En este sentido, algunas de las condiciones de flashing más extremas produjeron el fenómeno de colapso del chorro debido la interacción de las plumas. Se observaron diferentes estructuras de colapso, una para colapso transicional y otras para colapsos completos.

Los datos de velocidad y tamaño de las gotas en varias posiciones axiales y radiales confirmaron las tendencias esperadas de atomización, particularmente la influencia positiva de la alta presión de inyección, la temperatura ambiente y el flash boiling. Se observó una clara relación inversa entre R_P y el tamaño de las gotas en la mayoría de las condiciones de inyección, es decir, los valores

más altos de R_P generalmente correspondían a Sauter Mean Diameter (SMD) más bajos. Sin embargo, las desviaciones de esta tendencia atribuidas al inicio del colapso del chorro introdujeron gotas más grandes en la distribución.

Siguiendo esta línea, un mapeo de los regímenes de colapso, que van desde leves hasta extremos, permitió determinar que los tamaños de gota dentro de la región de colapso eran consistentemente mayores que los del chorro principal y a menudo anulaban los efectos positivos sobre la atomización de la alta presión de inyección o la ebullición instantánea.

La metodología experimental demostró ser efectiva para medidas con PDPA en la región central del inyector, incluso en escenarios de colapso extremos. Así pues, se identificó una banda de colapso cerca del centro del inyector. Esta región es rodeada por áreas con velocidades negativas o fenómenos de flujo inverso, revelando que la posición del colapso está fuertemente influenciada por los chorros más energéticos.

En general, se espera que estos resultados cualitativos y cuantitativos contribuyan a la investigación chorros GDI con combustibles volátiles, brindando una aplicación novedosa de herramientas de medición establecidas, y que ofrezcan una comprensión más amplia de estos chorros, además de apoyar futuras investigaciones sobre el diseño de inyectores, estrategias de inyección y optimización de la combustión.

Resum

La injecció de combustible en sistemes de combustió, particularment de gasolina, continua exercint un paper important en la indústria automotriu i en la investigació actual donat el seu potencial per a aconseguir una alta eficiència amb baixes emissions. En este context, el present estudi té com a objectiu aprofundir en la comprensió dels fenòmens clau que afecten la injecció i l'atomització del doll.

Esta investigació analitza dos injectors GDI, els dos capaços d'operar a altes pressions d'injecció. Un servix com a referència principal per a la caracterització, mentres que el segon s'utilitza amb finalitats comparatius i per a la validació de les tendències observades. S'empren dos combustibles per a simular diferents propietats de volatilitat dels compostos de la gasolina i reproduir condicions de flashing més extremes, així com Etanol, un alcohol representatiu usualment considerat en estratègies de baixes emissions de carboni.

Es va dur a terme una metodologia exhaustiva per a mesures de doll GDI mitjançant PDPA usant un equip nou en el centre d'investigació que va albergar este projecte, el Clean Mobility and Thermofluids (CMT). A més, es va millorar el control de la temperatura en la maqueta mitjançant la instal · lació d'un nou mòdul de resistències i aïllament per a un calfament més ràpid i homogeni del gas ambient. També es van provar dos finestres girades per a optimitzar l'alineació del PDPA.

Per al flux intern, es realitza una caracterització que inclou la taxa de moment (ROM) i la taxa d'injecció (ROI) de les dos toveres. La geometria d'estes es va mesurar utilitzant diverses tècniques, incloses tècniques òptiques avançades de rajos X en el Argonne National Laboratory (ANL).

La visualització lateral amb dispersió MIE va ajudar a tindre una idea clara dels fenòmens que tenen lloc durant les injeccions mentres es realitzaven mesuraments de grandària i velocitat de gotes. En este sentit, algunes de les condicions de flashing més extremes van produir el fenomen de col · lapse del doll degut a la interacció de les plomes. Es van observar diferents estructures de col · lapse, una per a col · lapse transicional i altres per a col · lapses complets.

Les dades de velocitat i grandària de les gotes en diverses posicions axials i radials van confirmar les tendències esperades d'atomització, particularment la influència positiva de l'alta pressió d'injecció, la temperatura ambient i el flash boiling. Es va observar una clara relació inversa entre RP i la grandària de les gotes en la majoria de les condicions d'injecció, és a dir, els valors més alts de RP generalment corresponien a Sauter Mean Diameter (SMD) més

baixos. No obstant això, les desviacions d'esta tendència atribuïdes a l'inici del col · lapse del doll van introduir gotes més grans en la distribució.

Seguint esta línia, un mapatge dels règims de col · lapse, que van des de lleus fins a extrems, va permetre determinar que les grandàries de gota dins de la regió de col · lapse eren consistentment majors que els del doll principal i sovint anul · laven els efectes positius sobre l'atomització de l'alta pressió d'injecció o l'ebullició instantània.

La metodologia experimental va demostrar ser efectiva per a mesures amb PDPA a la regió central de l'injector, fins i tot en escenaris de col · lapse extrems. Així doncs, es va identificar una banda de col · lapse prop del centre de l'injector. Esta regió és envoltada per àrees amb velocitats negatives o fenòmens de flux invers, revelant que la posició del col · lapse està fortament influenciada pels dolls més energètics.

En general, s'espera que estos resultats qualitatius i quantitatius contribuïsquen a la investigació de dolls GDI amb combustibles volàtils, brindant una aplicació nova de ferramentes de mesurament establides, i que oferisquen una comprensió més àmplia d'estos dolls, a més de secundar futures investigacions sobre el disseny d'injectors, estratègies d'injecció i optimització de la combustió.

No puedes enseñar nada a un hombre; solo puedes ayudarle a encontrarlo dentro de sí mismo
Galileo

To the wonderful family God blessed me with.

Agradecimientos

Han pasado varios años en este viaje, una etapa de la vida llena de experiencias que quedarán marcadas siempre. No puedo empezar a rememorar cada una de las vivencias sin agradecer a Dios, quien para mí es guía y destino. Sobra decir que la vida misma y la fortaleza para avanzar no se explicarían sin mi madre, quien día a día ha estado allí como un pilar fundamental y apoyo en mis pasos, para ti, mi agradecimiento y dedicatoria siempre. A mi hermano Rubén, que ha servido de faro moral y ético, como ejemplo de superación y trabajo arduo. A mi abuelo, quien ha sido a su vez un padre, recordándome siempre que hay un lado bueno que mirar. A mis sobrinas, y a los pequeños de la familia, que su sola existencia es un motivo para dar más de mí. Al resto, que ha sabido estar allí con su cariño y aprecio: las letras no podrían combinarse tal que pudieran describir mi afecto y el agradecimiento para con ellos. A mis amigos, quienes han sabido dar esa calidez familiar.

Este trabajo no se explica sin el apoyo y la presencia de mi tutor, Raúl Payri, a quien quiero agradecer por su cercanía y sus excelentes habilidades de liderazgo, que ha sabido brindar el apoyo quirúrgico para avanzar en cada paso importante, siendo esa fuente a la que acudir para consejos y orientar el proyecto hacia la mejor dirección. Asimismo, por generar un excelente ambiente de trabajo, que ha hecho amena y fluida esta experiencia.

En este orden de ideas, quiero extender mi infinita gratitud a dos profesores que han servido de consejo académico cada vez que fue necesario. Por escucharme y dar parte de su tiempo para atender mis inquietudes, y por encima de

ello, ofrecer sus conocimientos con total disposición, a Pedro y Jaime, infinitas gracias. De igual manera, al resto de profesores en el equipo: Gabi, Marcos, y demás, que cuando fue necesario otorgaron su apoyo, conocimientos y positividad. A todo el equipo de inyección, mi agradecimiento. Por otra parte, a José Vicente Pastor, quien supo compartir su experticia y conocimientos que atañen a los experimentos realizados. Además, extiendo este agradecimiento para todo el centro de investigación; no quisiera que se me escapara nadie, pero desde el equipo de secretaría, en especial a Amparo y Habi, que han sabido guiarme en cualquier proceso burocrático, hasta la dirigencia del CMT, gracias por darme la oportunidad de formar parte de este increíble grupo.

Un grupo con años de experiencia y prestigio en el campo de la investigación en motores, que durante mi estadía, la parte experimental en chorros tuvo una alta influencia por parte de los técnicos de laboratorio. A ellos, mi agradecimiento, especialmente a José Enrique, quien ha sido otra fuente de conocimientos y cuya ayuda ha sido imprescindible en el desarrollo de las actividades. También a Omar, cuya experiencia y apoyo fueron importantes para resolver problemas y para agilizar el montaje de los ensayos.

Esta tesis se llevó a cabo en el marco de la ayuda para la Formación de Personal Investigador (FPI) Subprograma 1 (PAID-01-19), financiada por la Universitat Politècnica de València. Agradezco a la Universitat Politècnica de València por abrirme las puertas de esta ciudad y financiar económicamente estos años de formación y dedicación a mi tesis doctoral, y por brindarme la oportunidad de alcanzar esta meta importante. Además, le agradezco por el financiamiento de

mi estancia internacional desarrollada en el prestigioso centro de investigación Argonne National Laboratory. En este sentido, vaya mi agradecimiento a Christopher Powell, por recibirme como un miembro más del grupo y ofrecer su apoyo. También agradecer a Brandon Sforzo, Chi y Alan como parte del grupo de fuel sprays, por los gratos momentos y enseñanzas. Una experiencia increíble.

Ha sido todo un viaje, miles de memorias adquiridas, desde las discusiones técnicas y académicas hasta las más cotidianas, que son al final las que se quedan. En ese sentido, es imposible no mencionar a los compañeros con quienes compartí estos años. A Rami y Tomás, con quienes estuve la mayor parte del tiempo en el mismo despacho, compartiendo día a día; a César y Sebastián, quienes a pesar de no compartir el mismo espacio, me brindaron su apoyo y amistad: no solo gané en todos ellos unos compañeros, sino amigos para la vida. A los amigos con quienes tuve oportunidad de cruzarme en este tiempo: Ibra, Abian, Armando, María, Juan, Javier, Alexandra, Dai, Vincenzo, Alba, Leonardo, Rodrigo, Santiago y muchos más, gracias por las bonitas vivencias. Finalmente, a los visitantes que tuve la oportunidad de dirigir, a ellos mi agradecimiento por su confianza y paciencia, así como al resto de compañeros del grupo, que se me hace imposible mencionar.

A muchos veré más o menos seguido, con alguno que compartí solamente algún saludo o una risa de pasillo en este tiempo, y otros que trascienden esta etapa para seguir compartiendo en los años por venir. A todos, gracias por aparecer en este capítulo.

Contents

Contents **i**

List of Figures **vii**

List of Tables **xi**

1 Introduction **1**
1.1 General picture 1
1.2 General scope of passenger car vehicles 4
1.2.1 Modern transportation technologies - Current framework 4
1.2.2 Specific GDI concerns 5
1.3 Objectives and methodology 7
1.4 Thesis guideline for the reader 8
References 9

2 The GDI spray formation concepts and review **11**
2.1 Introduction 11
2.2 GDI Injectors 12
2.2.1 Gasoline injection systems 12
2.2.2 Injector design considerations 13
2.2.3 Multi-hole solenoid driven type 16
2.3 Gasoline direct fuel injection Process 19
2.3.1 Fuel delivery: from tank to injector 19
2.3.2 Fuel injection: entering the combustion chamber 20
2.3.3 Combustion: fuel droplet transformation into energy . . 21
2.3.4 Emission formation and exhaust gases 22
2.3.5 Emission treatment: Cleaning the Exhaust Gases 23

2.4 Atomization and evaporation process 24
2.4.1 Atomization process in GDI Sprays 25
2.4.2 Spray Breakup Regimes and Droplet Interactions in GDI Sprays 25
2.4.3 Atomization parameters 28
2.4.4 Evaporation process 30
2.4.5 Atomization and evaporation evaluation 31
2.5 Flash boiling phenomena 31
2.5.1 Inner mechanisms leading to flash boiling 32
2.5.2 Characterizing flash boiling intensity 34
2.5.3 Spray collapse 35
2.6 Research state on GDI 36
References 40

3 Experimental tools and methodologies 53
3.1 Introduction 53
3.2 Apparatus 54
3.2.1 Injection system 54
3.2.2 Injectors 54
3.2.3 Test plan description 55
3.2.4 Fuels investigated 58
3.3 Internal flow measurement techniques 59
3.3.1 Rate of injection 59
3.3.2 Rate of momentum (ROM) 63
3.3.3 Hydraulic analysis 65
3.3.4 ROM measurement procedure 67
3.3.5 Rate of momentum correction for multi-sprays 68
3.4 GDI test rig 69
3.4.1 GDI test rig vessel 69
3.4.2 New resistor units 70
3.5 Spray visualization technique 71
3.5.1 MIE scattering 72
3.6 Spray image processing 73
3.6.1 Image masking 74
3.6.2 Image preparation 74
3.6.3 Image binarization 76
3.6.4 Contour Analysis 76
3.7 Phase Doppler Anemometry (PDA) technique 77
3.7.1 PDA measurement technique 78
3.8 PDA data processing 83

3.8.1 The Phase Doppler Particle Analysis (PDPA) equipment 83
3.8.2 Software utilization . . . 85
3.8.3 Equipment alignment . . . 86
3.9 Methodology for GDI sprays . . . 87
3.9.1 Velocity component in the sprays coordinates . . . 87
3.9.2 Data acquisition on sprays . . . 88
3.9.3 Set-up approach in GDI measurements . . . 89
References . . . 93

4 Describing the geometry and near nozzle flow 99
4.1 Introduction . . . 99
4.2 Injectors' geometry . . . 100
4.2.1 Nozzle holes distribution . . . 100
4.2.2 Internal Geometry microscopic images . . . 100
4.2.3 Tomographic images . . . 102
4.2.4 Spray core assessment . . . 103
4.3 Rate of injection . . . 103
4.3.1 Test matrix summary . . . 103
4.3.2 The ROI signal . . . 104
4.3.3 Injector comparison . . . 105
4.3.4 Fuel Effect . . . 108
4.4 Rate of Momentum results . . . 110
4.4.1 Test matrix summary . . . 110
4.4.2 Injector differences . . . 112
4.4.3 Fuel Effect . . . 114
4.4.4 Fuel temperature influence . . . 115
4.4.5 Ambient pressure impact . . . 115
4.5 Hydraulic Analysis . . . 119
4.5.1 Hydraulic coefficients . . . 119
4.6 Summary and conclusions . . . 120
References . . . 123

5 Microscopic characterization: Measurement baseline 127
5.1 Introduction . . . 127
5.2 Test Matrix . . . 128
5.3 Equipment set-up considerations . . . 130
5.3.1 The effect of optical windows . . . 130
5.3.2 Rotated windows configuration . . . 131
5.3.3 PDPA set-up values . . . 131
5.3.4 Spray axis location methodology . . . 133

5.3.5 Plume location variability with operating conditions . . 134
5.4 Visualization: spray description through MIE scattering images 137
5.4.1 Spray pattern structures 137
5.5 Penetration results 141
5.5.1 Chamber density effects 142
5.5.2 Super-heating degree by R_P effect 143
5.5.3 Penetrations differences with fuel variation 144
5.5.4 Spray width analysis 144
5.6 Summary and conclusions 147
References 149

6 Microscopic characterization: Velocity and diameter 151
6.1 Introduction 151
6.2 PDPA results: Experimental baseline 152
6.2.1 Initial droplet behavior – temporal insights 153
6.3 PDPA results: Primary velocity comparisons 159
6.3.1 Averaged velocity profiles 159
6.3.2 Radial velocities profiles 160
6.4 PDPA results: Velocity and Diameter 162
6.4.1 Droplet Size Metrics and Spatial Distribution 162
6.4.2 Operational conditions effects 169
6.5 Approaching Flash boiling conditions 171
6.5.1 Flash boiling conditions analysis 172
6.5.2 Diameter distribution under flash boiling conditions . . 173
6.5.3 SMD relation to flash boiling 174
6.6 Summary and conclusions 175
References 176

7 Exploring the spray collapse 179
7.1 Introduction 179
7.2 Test Conditions 180
7.3 Spray Collapse: Velocity behaviour in the spray jets' core . . . 183
7.4 Spray Collapse: SMD spatial distribution under extreme R_P conditions. 186
7.4.1 Diameter evolution in the center of the collapse zone . . 186
7.5 Spray Collapse: A characterization at different levels of collapse 190
7.5.1 On transitional collapse 190
7.5.2 On the vecinity of the injector centerline 192
7.5.3 Diameter particularities in the vecinity of the centerline 194
7.5.4 Towards the collapse zone 194

7.5.5 Droplet characteristics in the injector centerline 197
7.6 Discussion and conclusions 198
References 201

8 Conclusions and future works **203**
8.1 Synthesis 203
8.2 Experiemental observations 205
8.2.1 Main hydraulic characterization findings. 205
8.2.2 Main morphological observations. 205
8.2.3 Main effects of operational condition on the spray microscopic variables. 206
8.2.4 Characterization of a collapsed spray. 207
8.3 Future works 208

Global Bibliography **211**

Appendices **235**

A Appendix **235**
A.1 Conditions measured for Rate of Momentum. 235
A.2 PDA test matrix for all conditions measured 238

List of Figures

1.1 Total U.S. Greenhouse Gas Emissions by Economic Sector in 1990 and 2021. Source: Environmental Protection Agency of the United States . . . 3
1.2 Market share for different vehicles' technologies in the European Union starting 2024 [10] . . . 5

2.2 Injectors. . . . 17
2.3 Fuel pressure regulation circuit. Adapted from [41] . . . 20

3.1 Schematic of the fuel delivery system . . . 55
3.2 Injector SDI driver (a) and Continental Injector (b) . . . 56
3.4 Injection Rate Discharge Curve Indicator schematic diagram. Adapted from [14] . . . 60
3.5 Rate of Injection measurement set-up. . . . 63
3.6 Rate of momentum measurement basis [14, 16]. . . . 64
3.7 Schematic representation of the flow exiting the nozzle orifice. (a) shows how it would look in reality (b) the effective area and velocity. [16]. . . . 66
3.8 Momentum flux vessel based on Gimeno [16] work. . . . 68
3.9 Force sensor and sprays impact. . . . 68
3.10 GDI visualization test rig. [10] . . . 70
3.11 Final display of the experimental facility. . . . 71
3.12 MIE setup configuration . . . 73
3.13 Image processing steps. The frames shown are at 635 μs after SOI, for the C3539 injector with a rail pressure of 200 bar a chamber pressure of 6 bar and temperature of 60 °C and nozzle temperature of 90 °C. The fuel is Ethanol. . . . 75

3.14 Macroscopic spray parameters extracted from the contour analysis. Two structures are seen for non-collapsing (left) and collapse sprays. The conditions are depicted on the image. 77
3.15 Fringe model of crossing beams. 79
3.16 PDPA signal detection and processing. 80
3.17 PDPA angles definition. 81
3.18 The 2π ambiguity approach 83
3.19 PDPA schematics. 84
3.20 Schematics of the velocity components measured. 88
3.21 Spray evolution in the time-resolved droplets velocity acquisition. . 90
3.22 Difraction patterns seen for aligned lasers. 91

4.1 Nozzle images for both injectors with the holes distribution. The pictures are at 16x zoom. 100
4.2 Angle detection for the nozzle holes distribution with a MATLAB routine. 101
4.3 Microscopic images of the silicon molds. 101
4.4 Image of the cross section of the nozzle passages for the 6 orifice injector, C3539. 102
4.5 Shot-to-shot dispersion in the ROI and injection pressure signal. . 105
4.6 Effect of the injector pressure for both injectors using IsoOctane. . 106
4.7 Ambient pressure comparison for the C3539 injector at 200 bar of injection pressure. 107
4.8 Nozzle Temperature effect in the ROI for different fuels with the C3539 injector 108
4.9 Nozzle Temperature effect in the ROI for different fuels with the C7532 injector. 109
4.10 Effect of the fuel on the ROI. The condition shown is for 6 bar of ambient pressure, 90 °C of injection temperature, and 200 and 350 bar of injection pressure 110
4.11 Effect of the fuel on the Rate of injection. Rail pressure varied row-wise and nozzle temperature column-wise. 111
4.12 Injected mass as a function of the square root of ΔP 111
4.13 Sensor to injector separation assessment 113
4.14 Injection pressure effect for both injectors. 113
4.15 Fuel effect under several conditions. 114
4.16 Influence of the nozzle temperature on the rate of momentum at 6 bar of ambient pressure in the C3639 nozzle. 115
4.17 Influence of the nozzle temperature on the rate of momentum at several ambient pressures for the C7532 nozzle. 116

4.18 Ambient pressure effect on the C3539 nozzle for non-flashing condition. 117
4.19 Ambient pressure effect on the C3539 nozzle at flashing condition. 120
4.20 Discharge coefficients for the various conditions. 121
4.21 Velocity coefficients for the conditions measured. 121
4.22 Effective velocity for the conditions measured. 122

5.2 Optical axis rotation for PDA measurements. 132
5.3 Spray location Grid. 133
5.4 Axis location velocity map. 134
5.5 Spray's location 135
5.6 Core angle of the spray measured at different ambient pressures for 90 °C of fuel temperature. 136
5.7 MIE flashing structure for a developed spray at a frozen frame. Conditions are shown in the image. 138
5.8 MIE images for Ethanol at two extreme temperatures, showing the effects of chamber pressure variation (R_P) at each fuel temperature. 139
5.9 MIE images comparing both injector structures for a developed spray. Conditions are shown in the image. 140
5.10 Density effect on Penetration for the C3539 injector and the Hexane fuel. 143
5.11 Comparison of the effect of the superheating degree on spray penetration for Hexane and Ethanol fuels. Ambient and injection conditions are depicted in the plots. 145
5.12 Penetration changes due to the fuel properties. 146
5.13 Width variation with R_P and ambient pressure. 146

6.4 Different velocities measured both at very high injection pressure and very close to the nozzle exit. 157

7.3 Collapse velocity distribution in the center of the injector. The operating condition for the C3536 injector spray is 200 bar of injection pressure, 120°C in the chamber, the nozzle temperature is 90°C, ambient pressure 0.2 bar using Hexane as fuel, for a R_P then is 9.45. The velocities were captured at 20 mm away from the nozzle tip. 184
7.4 Comparison of 3D and upper views of velocity distributions for two injection pressures under strong collapse conditions: at T_{inj} = 110°C and P_{amb} = 0.2 bar. Fuel = Hexane and thence nd R_P = 15.81. The injector is the 6-orifice-C3539. 185

7.7 Comparison of 3D and upper views of SMD distributions for two injection pressures under strong collapse conditions. Main conditions: $T_{inj} = 110°C$ and $P_{amb} = 0.2$ bar. Fuel = Hexane, Injector is the 6 orifice C3539. Measurements captured 20 mm from the nozzle tip. 189
7.8 Characteristics of collapse under transitional flash boiling for Hexane. 191

List of Tables

3.1 Injector properties. 56
3.2 Fuel Properties. 58
3.3 Summary of the configuration parameters for the high-speed camera. 73

4.1 Measurement results for different injectors/techniques 103
4.2 Spray core assessment of the injectors' angle with the paper pinch technique. 103
4.3 Conditions to be tested: Rate of Injection 104
4.4 Fuel Properties. 109
4.5 Conditions to be tested: Rate of Momentum 112
4.6 Test conditions and corresponding R_P values for injector C3539 at $T_n = 90°C$ and $P_r = 200$ bar. 118

5.1 Conditions to be tested: PDPA measurements 128
5.2 Key Parameters and Values 131
5.3 Core angle variation per operating condition. 135

7.1 Conditions to be tested: Rate of Injection 180
7.2 Summary of spray regimes, main behaviors, and associated findings. 199

A.1 Full ROM test matrix with R_P values for each operating condition. 235
A.2 Full visualization and PDA test matrix with R_P values for each operating condition 238

Chapter 1

Introduction

1.1 General picture

Throughout history, humans have invented various methods to exploit natural resources. Energy utilization, from burning wood for fire to constructing nuclear plants, has been central to humanity's evolution and development.

In the same way, mankind's mobilization has undergone important changes. From using the wind to propel sailing ships and reaching greater distances and lands, passing through coal utilization as a primary source to create steam engines, freeing humankind from the age-long dependence upon the power of water, wind, or their own physical strength [1], reaching to our days of flying the skies on airplanes and traveling long distances in cars. This coal steam-powered machinery was reciprocating engines that converted the thermal energy of steam into mechanical work.

Reciprocating engines emerged as transformative elements in society, accelerating advancements in transportation, industry, and power generation. It became a cornerstone to building modern civilization as we know it. Its natural evolution was the internal combustion engine (ICE), which employed the chemical energy stored in fuels to extract the necessary thermal energy through combustion reactions to generate the power that moves the different parts of the mechanism and translates it to actual motion.

The ICEs have been part of human progress in the last century; they are directly or indirectly part of many elements in our daily lives, penetrating the veins of society dynamics. Their versatility and adaptability have made them

indispensable in powering various applications and industries, contributing to economic development and societal progress.

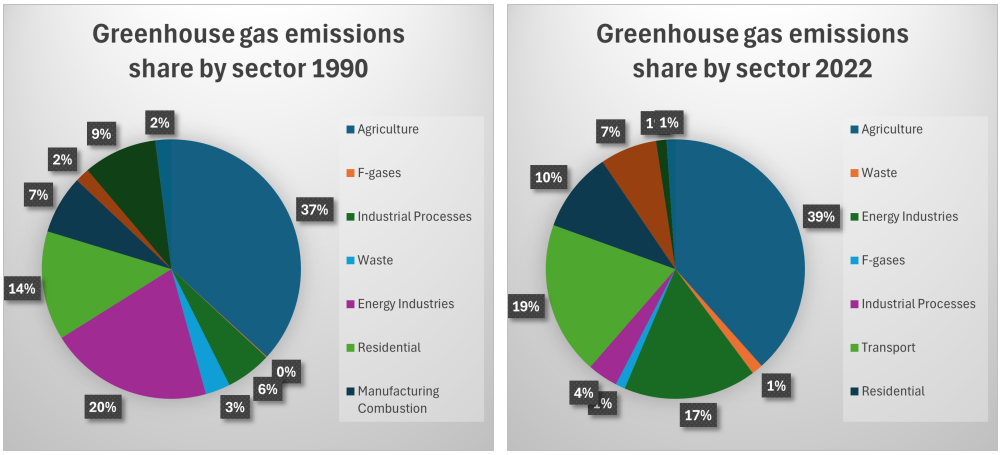
This progress has led to an ever-increasing demand for engines to exploit all of their potential; nonetheless, it has also amplified the environmental and health risks associated with hazardous byproducts of combustion. One of the products is carbon dioxide (CO_2) which is a non-condensing greenhouse gas (GHG) that traps heat from the sun and prevents it from escaping back into space, being one of the main radiative drivers for global temperature variations.

The anthropogenic influence on CO_2 release is evident, as shown by estimates from investigations conducted over the last century [2]. The human influence comes from various sources: deforestation fires, land-use changes, the use of agricultural fertilizers, and, among others, fossil fuel combustion [3]. While the available information is mostly based on models, there is a general agreement among the scientific community regarding that fossil fuel combustion is the largest single source of anthropogenic CO_2 emissions. Over the last century, the likely temperature over land increase caused by humans rounds about 1.07 °C. CO_2 emissions in the last three decades account for 42 % of the emissions over the last 150 years. In 2019, atmospheric CO_2 concentrations were the highest in the last few million years [4].

Fossil fuel combustion is used in electricity generation, transportation, industrial processes, and residential thermal control. The fossil fuel contribution on its side can be broken down into three main contributors. Coal combustion, with 43 % of CO2 emissions, natural gas (20 %), and other oil combustion such as gasoline, diesel for transportation, and other industrial processes with 33 % [5].

As per the transportation sector according to the Environmental Protection Agency of the United States, in 2021, cars, trucks, commercial aircraft, and railroads, among other sources of the transportation sector, accounted for nearly 29 % of the total U.S. GHG emissions compared to the 9 % estimated for 1990 (Figure 1.1). Also, the European Environment Agency claims that transport is responsible for about a quarter of the EU's total GHG emissions. In general, the percentage ranges from 20 to 30 % depending on the methodology used for its estimation, which highlights the transportation sector's significant impact, emphasizing the urgency for targeted mitigation strategies.

In response to these environmental and health concerns, internal combustion engines, mainly used in transportation, have undergone significant improvements over the past decades. Some technologies, such as direct injection, variable valve timing, turbocharging or supercharging, as well as lean



(a) Green House Gas 1990 *(b) Green House Gas 2022*

Figure 1.1: Total U.S. Greenhouse Gas Emissions by Economic Sector in 1990 and 2021. Source: Environmental Protection Agency of the United States

burn strategies and engine downsizing, have been incorporated into vehicles to enhance the efficiency and cleanliness of these engines.

The Paris Agreement aims to limit global warming to preferably 1.5 degrees Celsius above pre-industrial levels. By 2050, countries have committed to achieving carbon neutrality, which means that greenhouse gas (GHG) emissions must be entirely eliminated or offset by removing GHGs from the atmosphere [6]. However, the widespread adoption of new technologies that could replace ICE is still not a reality in many countries. Therefore, continuing to optimize current ICE technologies is crucial for reducing CO2 emissions in the mid-term while transitioning towards more sustainable energy solutions.

Main pollutants products from ICE

The principal concern of ICEs has been the CO2 emissions; however, some other combustion byproducts that contribute to air pollution, smog formation, and respiratory health problems are important to consider.

- Carbon Monoxide (CO) is also produced when carbon-containing fuels do not burn completely due to insufficient oxygen during combustion.
- Nitrogen Oxides (NOx) are formed when nitrogen and oxygen in the air react at high temperatures during combustion.

- Particulate Matter (PM) consists of tiny particles of solid or liquid matter suspended in the air, including soot. When inhaled, these particles vary in size and composition and have adverse health effects.
- Hydrocarbons (HC) result from the incomplete combustion of hydrocarbon fuels in ICEs, including volatile organic compounds (VOCs) contributing to smog formation, ground-level ozone, and air quality degradation.
- Sulfur Dioxide (SO2) is produced when fuels containing sulfur, such as certain grades of gasoline and diesel, are burned in ICEs. It is a precursor to acid rain and can irritate the respiratory system.
- Other hazardous air pollutants like benzene and formaldehyde

1.2 General scope of passenger car vehicles

1.2.1 Modern transportation technologies - Current framework

In response to the challenges facing the transportation industry, several alternatives have emerged in recent years. Electrification of the sector is widely considered the leading solution for achieving the cleanest and most sustainable future. However, the widespread adoption of this technology in society is still a significant challenge that this recent technology faces. Questions persist regarding electric vehicles (EVs) ability to meet the total transport energy demand. Electrification of heavy vehicles will only be possible in specific niches, and in sectors that cannot be decarbonized in the foreseeable future, other technologies show great potential to reduce the transportation carbon footprint in the short term.

The primary focus of these emerging technologies is the utilization of cleaner fuels, such as synthetic fuels, biofuels, and hydrogen. The first two are particularly promising because they can be designed to be drop-in replacements for traditional fossil fuels, meaning that they can be utilized within the existing infrastructure of internal combustion engines (ICEs), thereby reducing emissions [7, 8]. On the other side, hydrogen is employed as an energy source to generate electricity, which is then stored in fuel cells to power electric motors in hydrogen fuel cell vehicles (FCEVs). Despite the promise of hydrogen, the infrastructure required to support its widespread use is still under development. Additionally, the integration of both ICEs and electric motors in Hybrid Electric Vehicles (HEVs) has gained significant traction [9].

Time passes, and despite the advancement in electrification, the process is still slow, and ICEs are still a reality in society. According to European Automobile Manufacturers Association (ACEA) [10] new European car sales rose 10.1 % in February 2024 respect to last year. The combined market share of petrol and diesel cars was 48.4%; however, if we add the hybrid-electric vehicles, the total market share of vehicles with a direct influence of ICEs rises to 64.4% as depicted in Figure 1.2.

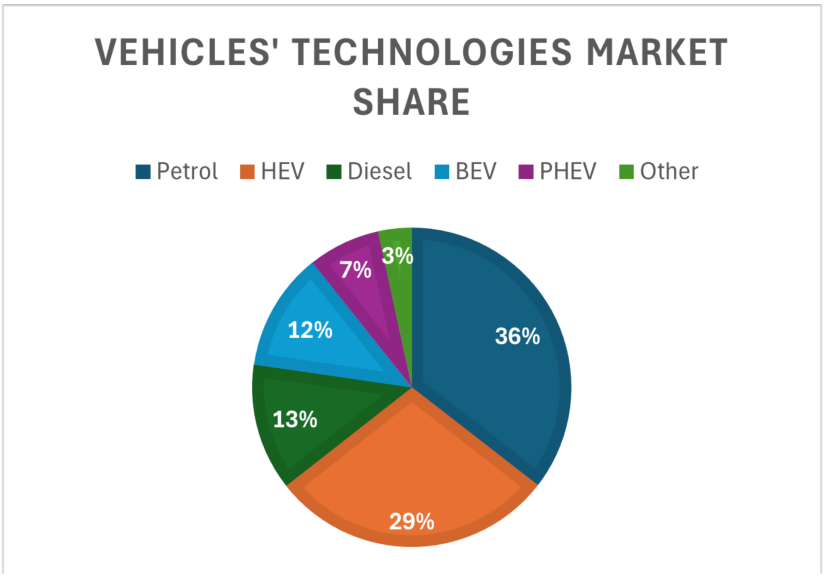


Figure 1.2: Market share for different vehicles' technologies in the European Union starting 2024 [10]

With this framework, in which the car demand is still increasing, and electrification is not keeping up with these demands, it is imperative to continue improving the current technologies and strategies to simultaneously reduce these emissions and mantain the pros given by the GDI systems [11].

1.2.2 Specific GDI concerns

The ICEs are still very influential in the transportation market. Especially Spark Ignition Direct Injection (SIDI) engines, thanks to their versatility, their high demand and the necessity for HEV engines.

GDI engines, particularly Spark Ignition Direct Injection (SIDI) engines, face challenges such as carbon oxide emissions, particulate matter, knocking, and fuel quality sensitivity [12]. In GDI engines, fuel is directly injected into

the cylinder, and when the spark is ignited, the fuel starts burning. Or at least that is the goal. The ideal ignition and combustion are mainly affected by the spray characteristic, the spark timing, and the fuel properties. In this sense, any phenomenon influencing the spray characteristic also influences the combustion and, consequently, emissions and fuel efficiency.

Recent studies on GDI engines have focused on phenomena like flash boiling and spray collapse. Flash boiling is the rapid fuel evaporation that occurs when the fuel is injected at a high temperature into an ambient with low pressure, specifically a pressure below that of the fuel vapor pressure. Spray collapse involves the merging of spray plumes into a single extended one, affecting combustion and emissions with longer spray penetration compared to a standard injection [13]. They occur in gasoline sprays because of their high volatility and the operating conditions during which the fuel is injected, with plume-to-plume interaction playing a major role [14].

Flashing sprays have shown both detrimental and beneficial effects on the combustion process. Depending on how it is used, on one hand, the flash boiling increases the potential of vapor bubbles blocking the flow and air-fuel mixture stratification; on the other hand, it depicts the benefits on enhancing fuel atomization and combustion efficiency, emphasizing its applicability for homogeneous lean combustion at high load, helping on reducing the fuel consumption and lowering the oxides of nitrogen (NOx) emissions. Some studies have explored methods to mitigate spray collapse by optimizing injector design and operating parameters.

Advancements in the study of renewable and carbon-neutral fuels aim to incorporate these fuels as additives to current fuels or employ them as drop-in replacements, thereby reducing the overall carbon footprint. However, one of the main challenges associated with them is their high volatility compared to conventional ICE fossil fuels. This heightened volatility sparks the interest on a deeper understanding of the phenomena that affect engine performance when using these newer fuels. These challenges include issues related to fuel atomization, combustion stability, and emissions, which must be thoroughly investigated to optimize the use of renewable and carbon-neutral fuels in existing ICE technologies.

In relation to flash boiling and spray collapse, they both are complex phenomena that are not fully understood and are still under numerical and experimental scrutiny. Several theories and studies have tried to explain the mechanisms that control these phenomena, however, there is still a gap in the current literature for the newer fuels and conditions to which the spray injected is subject to.

1.3 Objectives and methodology

In light of the context explained in the previous sections, this thesis aims to provide valuable data on traditional gasoline surrogates and bio-fuel candidates, focusing on the air-fuel interaction in GDI sprays under flash boiling and spray collapse conditions.

The air-fuel interaction will be examined through internal flow characterization and the atomization of droplets. The latter uses a new Phase Doppler Particle Analyzer (PDPA) equipment that measures both the droplet's velocity and diameters under different conditions. Different injection conditions will be analyzed to comprehensively understand flash boiling using state-of-the-art injectors capable of reaching higher injection pressures, including both standard and extreme engine operating scenarios.

To achieve this, the objectives include:

- Characterize GDI the injectors: it involves the geometric description, rate of injection measurements, and rate of momentum measurements.
- Integrate PDPA equipment into current facilities: a detailed analysis and description of the methodology for integrating the new PDPA equipment into current facilities, ensuring proper setup and operational readiness. Assessing the applicability of PDPA to existing facilities is essential, as it will help refine the methodology for future reproducibility and accurate measurements.
- Execute PDPA measurements in combination with spray visualization: This will allow for an in-depth analysis of how various injection parameters influence the spray atomization and overall spray structure employing several fuels.

Experimental research in the ICE's field intend to provide with analysis of factual data that can shed light on the questions alive in the field. This data is vital to validate computational models used in the design of technological advances for ICE's. The exact fuel characterization provides valuable data for model validations that allow for more precisely apply different technologies for reducing CO_2 emissions and improving the fuel economy such as variable valve timing, fuel metering, turbocharging and cylinder deactivation systems.

1.4 Thesis guideline for the reader

This thesis is structured in seven chapters through which the reader will make a journey through the concepts, methodology, and approaches employed to reach the results. It starts with an introduction (**chapter 1**) to the topic treated, the motivations behind the work realized, the current state of the engine sector, and the objectives pursued.

Following, **chapter 2** brings the basic concepts the reader must consider to understand the results achieved in this thesis. In this chapter, the basic working principles of gasoline direct injection engines are broken down. Lastly, the most recent works related to this topic are discussed to lay the foundation for this work.

chapter 3 explains the methodology followed during the thesis. The experimental facilities and equipment specifications are described together with the theory behind the techniques used to obtain the experimental data. The apparatus is also specified, in this sense, the injectors are presented. The test conditions selected for the experiments might vary for each experimental campaign, so, the specific selection is justified before the results are shown in each of the reporting chapters, nonetheless, this chapter gives a general introduction to the selected operating conditions. The main experimental campaigns found in this chapter are the internal hydraulic characterization with techniques such as rate of injection and rate of momentum, as well as side techniques employed or developed to complement the main campaign. Furthermore, the high-pressure and high-temperature visualization test rig and the adaptations carried out are illustrated. Finally, the optical technique used and the data treatment approach followed to achieve the final results are explained.

Starting with the experimental results, (**chapter 4**) shows the hydraulic characterization outcomes. This section geometrically describes the injectors used and then discusses the rate of injection and rate of momentum results. A comparison among the main variables studied is presented and the results are contrasted with previous studies. An emphasis is made in relation to the effect of the different fuels studied.

In **chapter 5** presents the general results for usual operating conditions in engines. It begins by detailing the morphological results, specifically analyzing the penetration and spray width of sprays for both injectors and different fuels. These findings are compared with existing literature data. Special emphasis is placed on the analysis of Ethanol, contrasting its behavior with other gasoline surrogates. The methodology employed for measuring the Phase Doppler

Anemometry (PDA) results is thoroughly described, highlighting the rationale behind each parameter set, which can serve as a reference for similar setups in future studies. Also, the PDA results are presented and contrasted.

Based on this framework, **chapter 6** covers the analysis of droplet velocity and size based on PDA measurements. Comparative velocity data are evaluated at the spray core under various fuels and boundary conditions. Droplet size is primarily assessed using the Sauter Mean Diameter (SMD), along with the particle size distribution. The chapter concludes with a discussion on the impact of flash boiling on both velocity and diameter measurements.

In **chapter 7**, the content focuses on the analysis of more particular phenomena, especially, the spray collapse during the injection process, integrating the results obtained from the previous chapters. This comprehensive analysis aims to understand the spray phenomena in greater detail, considering all variables collectively. As well as introducing novel spatial results on droplet characteristics in the injector axis. By combining these results, the study aims to provide a holistic view of the spray and injection dynamics, offering valuable insights that could inform the development of more efficient and effective engine technologies.

Finally, the last chapter, **chapter 8**, provides an overview of the main results attained, and a summary of the key points of every chapter; leaving some suggestions of lines of work to the future and leads that might be considered to further advance the research on this thrilling engine world.

References

[1] Dickinson, H. W. *A short history of the steam engine*. Routledge, 2022.

[2] Climate Change (IPCC), I. P. on. "Framing, Context, and Methods". In: *Climate Change 2021 – The Physical Science Basis: Working Group I Contribution to the Sixth Assessment Report of the Intergovernmental Panel on Climate Change*. Cambridge University Press, 2023, pp. 147–286.

[3] Le Quéré, C. et al. "Global carbon budget 2017". In: *Earth System Science Data* 10.1 (2018), pp. 405–448.

[4] Climate Change (IPCC), I. P. on. "Technical Summary". In: *Climate Change 2021 – The Physical Science Basis: Working Group I Contribution to the Sixth Assessment Report of the Intergovernmental Panel on Climate Change*. Cambridge University Press, 2023, pp. 35–144.

[5] (IEA), I. E. A. *World Energy Outlook 2023*. License: CC BY 4.0 (report); CC BY NC SA 4.0 (Annex A). Paris, France, 2023.

[6] Climate Change, U. N. F. C. on. *The Paris Agreement*. Accessed: 2024-06-24. 2015.

[7] Muriungi, B., Wang, L., and Shahbazi, A. "Comparison of Bimetallic Fe-Cu and Fe-Ca Oxygen Carriers for Biomass Gasification". In: *Energies* 13.8 (2020). DOI: 10.3390/en13082019.

[8] Martins, J. and Brito, F. P. "Alternative Fuels for Internal Combustion Engines". In: *Energies* 13.16 (2020). DOI: 10.3390/en13164086.

[9] Soleimani, A. et al. "Progress in hydrogen fuel cell vehicles and up-and-coming technologies for eco-friendly transportation: an international assessment". In: *Multiscale and Multidisciplinary Modeling, Experiments and Design* (2024), pp. 1–20.

[10] European Automobile Manufacturers Association (ACEA). *Press release: Car registrations February 2024*. European Automobile Manufacturers Association. 2024. URL: https://www.acea.auto/files/Press_release_car_registrations_February_2024.pdf.

[11] Duan, Y., Shi, X., Kang, Y., Liao, Y., and Duan, L. *Effect of Hydrous Ethanol Combined with EGR on Performance of GDI Engine*. Tech. rep. SAE Technical Paper, 2020.

[12] Singh, E. et al. "Particulate Matter Emissions in Gasoline Direct-Injection Spark-Ignition Engines: Sources, Fuel Dependency, and Quantities". In: *Fuel* 338 (2023), p. 127198. DOI: https://doi.org/10.1016/j.fuel.2022.127198.

[13] Li, X., Sun, Z., Yang, S., Wang, H., and Nour, M. "Flash boiling combustion of isomeric butanol and gasoline surrogate blends using constant volume spray chamber and GDI optical engine". In: *Fuel* 286.P1 (2021), p. 119328. DOI: 10.1016/j.fuel.2020.119328.

[14] Nour, M. et al. "Effect of flash boiling injection on combustion and PN emissions of DISI optical engine fueled with butanol isomers/TPRF blends". In: *Proceedings of the Combustion Institute* 38.4 (2021), pp. 5923–5931. DOI: 10.1016/j.proci.2020.10.006.

Chapter 2

The GDI spray formation concepts and review

2.1 Introduction

This chapter provides a comprehensive review of key aspects of gasoline direct injection (GDI) systems, establishing the theoretical and experimental framework for this study. GDI technology has become central to modern engine development due to its advantages in fuel efficiency, charge preparation, and emissions control, making it a critical component in hybrid powertrains and next-generation combustion strategies.

The chapter begins by tracing the evolution of gasoline injection systems, from early carburetors to contemporary direct injection technology, highlighting the advantages that have driven this transition. Following this historical perspective, the fundamental operating principles of GDI will be outlined, with particular attention to the components influencing fuel-air mixture formation, combustion efficiency, and emissions characteristics.

A key focus will be the injectors used in this study, multi-hole solenoid-driven injectors, analyzing their internal behavior and how their design influences spray formation. The discussion will then extend to the development of the fuel spray, covering key physical phenomena such as breakup, evaporation, and air-fuel interaction within the combustion chamber, involving important processes such as the atomization, as it plays a critical role in defining spray characteristics and combustion efficiency.

Provided the complexity of GDI sprays, special attention will be given to the challenges posed by flash boiling, a phenomenon arising from the rapid vaporization of highly volatile fuels under low ambient pressure conditions. The latter part of the chapter will review recent advancements in GDI technology, summarizing key trends in the field over the last years. Finally, emerging combustion strategies will be briefly discussed to provide context for future research directions.

By the end of this chapter, a solid understanding of the fundamental principles governing GDI systems will be provided, the challenges associated with their implementation, and the latest research trends shaping their continued development.

2.2 GDI Injectors

2.2.1 Gasoline injection systems

Evolution of fuel injection: from carburetors to Direct Injection

Fuel injection technology has undergone significant advancements since its inception, transitioning from mechanical systems to electronically controlled injectors that enable precise fuel metering. At first, carburetors were widely used due to their simplicity, relying on vacuum pressure from the intake, created by the engine during the intake stroke, to draw fuel into the manifold for mixing air and fuel. However, this method led to inefficient fuel-air mixing, often requiring a rich mixture to ensure proper combustion under varying operating conditions. As engine speeds increased, fuel delivery would rise correspondingly, but with limited control over mixture stratification and combustion efficiency [1, 2].

With growing concerns over fuel economy and emissions in the 1980s, regulatory pressures prompted the development of Port Fuel Injection (PFI) systems [3]. PFI technology introduced electronically controlled injectors that accurately delivered fuel into the intake manifold, improving combustion stability, throttle response, and reducing unburned hydrocarbons. However, despite these improvements, PFI still exhibited limitations, such as higher pumping losses and restricted flexibility in charge stratification [4–7].

By the late 1990s and early 2000s, stricter emission regulations and the demand for enhanced fuel efficiency led to the emergence of GDI systems. Unlike PFI, GDI injects fuel directly into the combustion chamber, offering superior control over fuel distribution, injection timing, and spray formation [8, 9]. These advancements allowed for stratified combustion strategies, leaner fuel

mixtures, and higher thermal efficiency, ultimately reducing fuel consumption and pollutant emissions [9, 10].

Modern GDI technology is further supported by electronic control systems that optimize injection parameters, ensuring precise fuel atomization and mixture formation [11, 12]. High-pressure GDI injectors, operating at up to 350 bar in actual applications, have shown to enhance spray dynamics and combustion efficiency, contributing to lower particulate matter emissions while maintaining high power output [13–15]. Among GDI injectors, solenoid-driven designs dominate due to their cost-effectiveness, durability, and reliability, making them more suitable for mass production. Although piezoelectric injectors offer faster response times and greater precision, their higher costs and complexity have limited their adoption in GDI applications [16].

With fuel being injected directly into the combustion chamber, the quality of the air-fuel mixture becomes a crucial factor influencing combustion efficiency, engine performance, and emissions. The characteristics of this mixture are largely dictated by fuel spray dynamics, making any factor affecting its formation critical to study. Existing literature highlights the importance of injector geometry, fuel properties, injection pressure, and operating conditions in shaping spray formation and combustion outcomes[17, 18].

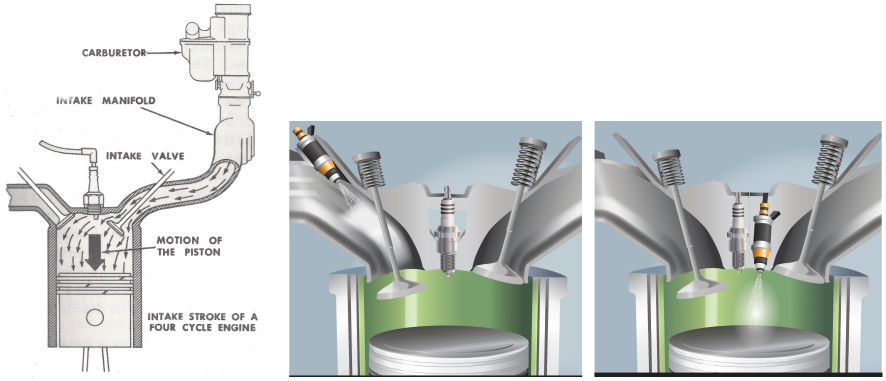


Figure 2.1: Scheme showing the evolution from carburetors to port fuel injection (PFI) and finally to gasoline direct injection (GDI) systems. Reproduced from [19, 20].

2.2.2 Injector design considerations

When designing and fabricating injection systems, several critical variables must be taken into account to optimize performance and reduce emissions. These factors directly influence spray formation, fuel atomization, and com-

bustion efficiency, playing a crucial role in engine performance and emissions control.

The spray pattern ensures uniform fuel distribution within the combustion chamber, enhancing the air-fuel mixing process. A well-optimized spray pattern improves combustion efficiency and reduces the formation of unburned hydrocarbons, lowering particulate matter (PM) and nitrogen oxide (NOx) emissions [21, 22].

Nozzle geometry

The geometry of the nozzle significantly influences fuel spray characteristics, affecting atomization, penetration, and mixture formation. Key aspects of nozzle design include hole diameter, shape, length-to-diameter ratio, and hole distribution. Smaller nozzle holes promote finer atomization by breaking the fuel into smaller droplets, enhancing evaporation and air-fuel mixing. Conversely, larger holes may increase spray penetration but can lead to incomplete mixing and higher emissions [23, 24].

The nozzle exit angle determines the spray cone angle, directly impacting fuel dispersion within the combustion chamber. A wider cone angle promotes faster vaporization and better mixture homogenization, whereas a narrower angle may result in localized fuel-rich zones, increasing soot formation.

The internal structure of the nozzle also affects fuel flow dynamics. For instance, sharp edges or abrupt transitions in the nozzle passage can induce cavitation, altering spray breakup and reducing injector durability. With a well-designed nozzle geometry, it is aimed to minimize turbulence and promote a more uniform spray distribution, ensuring stable combustion and lower pollutant emissions. Furthermore, controlling the nozzle exit angle minimizes fuel wall-impingement, which can lead to unwanted deposits and increased emissions [25].

Furthermore, the number and arrangement of nozzle holes influence spray targeting, penetration, and mixture formation. More holes generally lead to finer sprays, which enhance evaporation and improve mixture uniformity. In contrast, fewer holes may result in deeper penetration, which can benefit certain combustion modes but may also increase the risk of wall wetting and incomplete combustion [26–28].

Other key variables in injector design according to the literature [13, 18, 29–33]

- **Injection pressure and metering**: Injection pressure is a key driver of spray behavior and combustion quality. Modern GDI injectors operate at pressures up to 500 bar, significantly improving atomization, reducing droplet size, and enhancing spray penetration. High-pressure injection leads to more efficient air-fuel mixing, complete combustion, and lower emissions.

- **Needle lift and dynamics**: The motion of the injector needle determines fuel flow rate and injection timing. Faster response times enable multiple injection events, improving mixture stratification, combustion phasing, and transient response.

- **Injection timing and strategy**: The timing of fuel injection, either early, late, or in split injections, affects combustion efficiency, knocking resistance, and emissions formation. Optimized injection strategies can reduce fuel consumption and improve overall engine performance.

- **Cavitation and internal flow dynamics**: The internal flow of fuel within the injector influences turbulence, cavitation, and spray consistency. Cavitation occurs when localized pressure drops below the fuel's vapor pressure, forming vapor bubbles that collapse and cause material erosion, flow instabilities, and spray inconsistencies. Turbulence plays a critical role in maintaining spray consistency by enhancing droplet breakup and improving air-fuel mixture formation. However, excessive turbulence can create irregular spray structures, affecting penetration length and droplet size distribution. Optimizing the internal flow path of the injector, including nozzle hole shape and entry conditions, is essential to balance turbulence and minimize cavitation.

- **Fuel properties**: Different fuels, such as gasoline, ethanol blends, and alternative fuels, exhibit varying viscosity, density, and volatility, which directly impact spray behavior and atomization. For instance, ethanol's higher latent heat of vaporization influences droplet evaporation, while its lower energy density necessitates adjustments in injection strategies. Fuel volatility distribution plays a crucial role in spray atomization and evaporation dynamics. Fuels with a higher proportion of light-end components (low T10 and T50 temperatures in the distillation curve) are more prone to flash boiling, enhancing primary atomization but increasing spray collapse risk under low ambient pressures. Conversely, heavier

fractions (high T90 values) reduce flash boiling susceptibility but may compromise cold-start performance and fuel evaporation rates.

By considering these variables, injector design can be optimized to improve fuel delivery, enhance combustion efficiency, and meet stringent emissions regulations while ensuring long-term injector durability and engine performance.

2.2.3 Multi-hole solenoid driven type

These injectors utilize a solenoid mechanism to control fuel delivery, providing high precision in fuel atomization. The multi-hole design terms comes from injectors that feature multiple spray orifices through which fuel is injected into the combustion chamber, as opposed to single-hole injectors, which can result in less uniform spray distribution. Multi-hole injectors play a crucial role in improving spray characteristics such as distribution, atomization, and penetration, which directly influence combustion efficiency, emission formation, and fuel consumption [26].

Solenoid-Driven Mechanism

The solenoid-driven mechanism relies on an electromagnetic coil to control a valve that regulates the fuel flow. When current is supplied to the solenoid coil, it creates a magnetic field that moves the valve, allowing fuel to pass through the injector nozzle. This type of injector is widely used because of its relatively simple design, fast response time, and ability to operate at high frequencies. The solenoid injectors can precisely control the timing and duration of the injection event, making them highly suitable for the precise fuel delivery requirements of GDI engines.

Multi-hole injectors are widely used in modern GDI systems due to their ability to optimize fuel atomization and enhance evaporation. Their design features several orifices arranged in patterns, such as uniform circular or more complex layouts, planned to specific spray behaviors. The hole geometry and spray angle play a crucial role in defining spray characteristics, where larger angles promote better fuel dispersion, supporting homogeneous mixture formation and improved combustion efficiency. The increased number of injection points accelerates fuel-air mixing, enhancing evaporation and reducing combustion instabilities. Additionally, the size and shape of the injector holes are carefully engineered to optimize fuel atomization, control droplet size, and reduce particulate emissions by ensuring better fuel-air mixing.

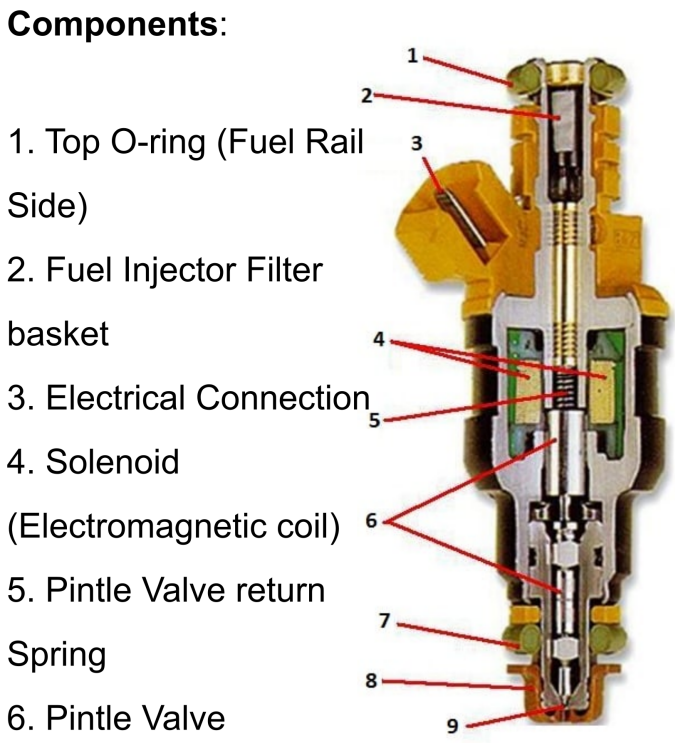


Figure 2.2: Bosch High Performance Fuel Injector Diagram. Adapted from [34].

Influence on spray characteristics

The primary influence of multi-hole solenoid-driven injectors is on the spray structure, and much of the research in GDI systems revolves around how these injectors influence the spray patterns and atomization quality. Key aspects include:

- **Atomization and spray distribution**: Multi-hole injectors are designed to atomize the fuel into smaller droplets, enhancing the fuel-air mixture and improving combustion by ensuring a more uniform distribution of the fuel in the combustion chamber. Small droplets provide a larger surface area for evaporation, allowing for better vaporization and more complete combustion. Studies such as Chang et al. [35] have shown that multi-hole injectors, compared to single-hole injectors, improve spray distribution and reduce spray penetration. This improved

distribution helps prevent fuel-rich zones, leading to more stable combustion, especially in cases where precise mixture control is required, such as during stratified charge operation, cold starts, and low-speed or part-load conditions [36]. Additionally, nozzle designs often incorporate specific spray orientation strategies, such as directing the spray toward the spark plug, to ensure reliable ignition and optimized fuel-air mixing in critical regions of the chamber.

- **Spray penetration and spray shape**: Multiple orifices help prevent the spray from overly penetrating or excessively spreading, thus reducing wall wetting and improving fuel-air interaction. This has been linked to lower particulate emissions and improved combustion efficiency. Researchers like Park and Park [37] emphasize that the injector hole geometry and arrangement play a crucial role in controlling spray cone angle, penetration depth, and droplet size distribution.

- **Spray break-up and flash boiling**: Multi-hole injectors enhance spray breakup and influence flash boiling behavior. As flash boiling occurs when fuel temperature exceeds its boiling point at ambient pressure, the fine atomization from multi-hole designs helps control vaporization dynamics. Zhao et al. [38] found that multiple spray orifices reduce the severity of spray collapse and improve spray stability under flash boiling conditions, contributing to more predictable spray behavior.

- **Combustion stability and emissions reduction**: Multi-hole injectors contribute to stabilizing the injection process, particularly under transient conditions or intermittent fuel delivery. This stabilization results in smoother combustion, lower emissions, and improved fuel efficiency. For instance, finer fuel droplets from multi-hole injectors reduce soot formation and help form a more homogeneous mixture, which leads to a more efficient combustion process [39].

According to the literature, the influence of multi-hole solenoid injectors on spray characteristics has been extensively studied, and key studies continue to explore how injector design variations affect spray dynamics, fuel vaporization, and combustion quality. Despite the benefits, multi-hole solenoid injectors are not without their challenges. One major challenge lies in the accurate control of spray distribution, especially in the presence of high pressures and temperatures typical in modern GDI systems. Furthermore, optimizing injector design to handle both steady-state and transient operating conditions remains a key area of research.

Another challenge is the impact of fuel quality on injector performance. The use of bio-fuels or alternative fuels with different viscosity and volatility characteristics can alter spray behavior and combustion efficiency. More research is needed to understand the implications of using various fuels with multi-hole solenoid injectors in GDI systems [40].

2.3 Gasoline direct fuel injection Process

Gasoline direct injection (GDI) is a fuel delivery system where fuel is injected directly into the combustion chamber at high pressure, allowing for better control over the air-fuel mixture, improved combustion efficiency, and reduced emissions. This section follows the path of a fuel droplet from the fuel tank to combustion and emission formation, including post-treatment processes.

2.3.1 Fuel delivery: from tank to injector

The journey of a fuel droplet begins in the fuel tank, where gasoline is stored at near-ambient pressure. The fuel system consists of multiple components that ensure the proper delivery of fuel to the injectors at the required pressure and flow rate.

Fuel pump system

The low-pressure fuel pump, typically located in or near the fuel tank, transfers fuel from the tank to the high-pressure fuel pump. It operates at relatively low pressures (approximately 3 to 5 bar) and supplies a steady flow of fuel to the high-pressure pump.

High-pressure fuel pump

The high-pressure pump increases the fuel pressure to values typically ranging from 50 to 350 bar to enable direct injection into the combustion chamber. The pressure is regulated based on engine load, speed, and operational requirements to optimize atomization and fuel-air mixing.

Fuel rail and pressure regulation

The pressurized fuel is delivered to the injectors through a common rail, which maintains a stable pressure and helps having a precise control over fuel delivery. A pressure sensor and regulator adjust the fuel pressure dynamically to accommodate different engine operating conditions, such as idle, part-load

cruising, high-load acceleration, and transient maneuvers. During idle and low-load conditions, fuel pressure is re duced to minimize fuel consumption and emissions. Under high-load scenarios, such as rapid acceleration or climbing steep inclines, pressure is increased to ensure proper atomization and combustion efficiency.

This fuel pressure regulation is closely interlinked with other engine control modules, including the throttle position sensor, mass airflow sensor, and knock detection system. The electronic control unit integrates these inputs to optimize combustion, maximize fuel efficiency, and minimize emissions. For instance, during cold starts, fuel pressure adjustments coordinate with ignition timing to improve vaporization and reduce hydrocarbon emissions. In turbocharged engines, fuel rail pressure is dynamically adjusted based on boost levels to prevent fuel starvation and maintain power output. These interdependencies highlight the critical role of fuel rail pressure management in achieving precise engine control and enhancing overall system performance.

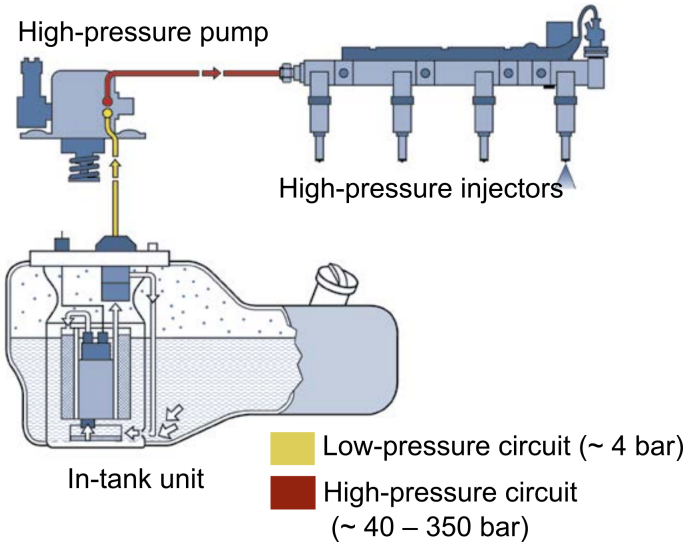


Figure 2.3: Fuel pressure regulation circuit. Adapted from [41]

2.3.2 Fuel injection: entering the combustion chamber

At the appropriate moment in the engine cycle, fuel is injected into the combustion chamber through a multi-hole solenoid-driven injector. The injection process follows several key steps: Injector opening, spray formation and air-fuel mixing.

- When the injector solenoid is energized, the injector nozzle opens, allowing high-pressure fuel to enter the combustion chamber.
- The fuel exits through multiple orifices in a finely atomized spray, with droplet sizes typically in the range of 10 to 30 μm [35, 42–45].
- The fuel spray interacts with the in-cylinder air motion, leading to further atomization and mixing.The latter process if affected by factors such as injection timing, fuel pressure, and injector design.

In general, GDI injectors can be optimized to support wall-guided, air-guided, or spray-guided mixture formation strategies, each affecting homogeneity, knock resistance, and combustion stability. Additionally, under specific conditions, the fuel may undergo flash boiling, where rapid vaporization improves atomization but may also lead to spray collapse, altering the intended fuel distribution within the combustion chamber.

2.3.3 Combustion: fuel droplet transformation into energy

After the fuel-air mixture occurs, combustion takes place when the spark plug ignites the mixture. Then, the transformation of fuel droplets into energy follows a series of key stages, significantly influencing engine performance, efficiency, and emissions. The dynamics of combustion in GDI engines are complex, involving turbulence, flame propagation speed, and in-cylinder thermodynamic conditions [46–49]. The main steps that a combustion follows inside the chamber can be summarize as:

- Ignition and flame propagation: The combustion process begins when the spark plug generates a high voltage electrical discharge, creating a localized high temperature plasma. This initiates flame kernel formation, which then expands outward as a turbulent flame front. The flame propagation speed depends on mixture homogeneity, turbulence intensity, and fuel composition. A well-mixed fuel-air charge enhances flame stability, while poor atomization or stratification can lead to incomplete combustion, knocking, or misfires.
- Pressure and temperature rise: As combustion progresses, chemical energy stored in the fuel is released, significantly increasing in-cylinder pressure and temperature. The pressure rise drives the piston downward, converting chemical energy into mechanical work. The efficiency

of this stage depends on the burn rate, ignition timing, and fuel properties. If combustion occurs too rapidly or prematurely, knocking can occur, which can damage engine components and reduce efficiency. GDI engines must carefully control spark timing, fuel injection events, and combustion chamber geometry to maximize efficiency while avoiding undesirable combustion modes.

- Heat release and expansion: The combustion heat is converted into mechanical energy as expanding burned gases push the piston downward. The efficiency of this expansion phase is critical in determining overall power output and thermal efficiency. Proper control of mixture preparation, ignition timing, and exhaust valve timing is essential to extract maximum work from the combustion event. As the piston reaches the bottom of its stroke, the exhaust valve opens, allowing burned gases to exit and preparing the cylinder for the next cycle.

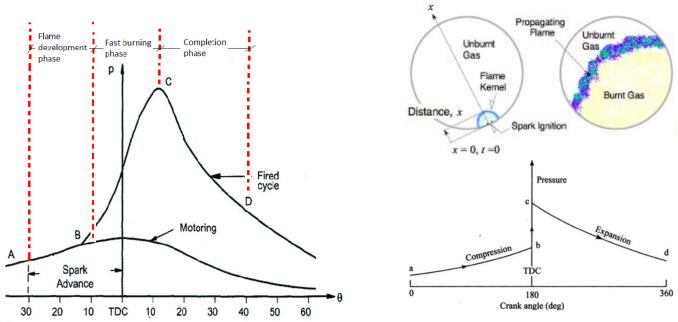


Figure 2.4: Combustion phases in Spark Ignition engines. Adapted from [50, 51]

GDI combustion is further influenced by injection strategies, such as single or multiple injection pulses, which affect mixture formation and stratification. Additionally, high injection pressures help atomize fuel more effectively, enhancing evaporation and reducing wall wetting, which minimizes unburned hydrocarbon emissions. Advancements in optical diagnostics and computational fluid dynamics (CFD) simulations continue to refine our understanding of flame propagation, turbulence effects, and ignition dynamics in GDI engines.

2.3.4 Emission formation and exhaust gases

After the combustion occurs, not all fuel is burned completely and some pollutants are generated. The primary emissions from gasoline direct injection combustion include [52–57]:

- Unburned hydrocarbons (UHC): Caused by incomplete combustion, often due to wall wetting, over-rich zones, or fuel trapping in crevices. GDI engines can have higher hydrocarbon emissions during cold start due to lower fuel evaporation rates.
- Carbon monoxide (CO): Formed under fuel-rich conditions where oxygen is insufficient for complete combustion. Carbon monoxide formation is affected by injection timing, mixture stratification, and in-cylinder air turbulence.
- Nitrogen oxides (NOx): Generated at high combustion temperatures as nitrogen from the air reacts with oxygen. High peak temperatures in GDI combustion can increase NOx emissions, necessitating exhaust gas recirculation (EGR) and catalytic aftertreatment.
- Particulate matter (PM): Fine soot particles form due to locally rich regions in the spray. Gasoline direct injection engines can have higher particulate emissions than port-fuel-injected engines, necessitating particulate control strategies such as gasoline particulate filters (GPFs) and optimized injection strategies to minimize fuel impingement on cylinder walls.
- Carbon dioxide (CO_2): A direct result of complete combustion, but must be minimized for carbon dioxide emission regulations. The efficiency of combustion, fuel type, and engine operating conditions play crucial roles in determining overall CO_2 emissions.

The exhaust gases exit the combustion chamber and travel through the exhaust manifold to undergo treatment. Modern GDI engines incorporate advanced aftertreatment systems, such as three-way catalytic converters and gasoline particulate filters (GPF), to reduce harmful emissions. Exhaust gas recirculation (EGR) strategies and variable valve timing (VVT) further contribute to emissions control by reducing in-cylinder peak temperatures and optimizing the combustion process.

2.3.5 Emission treatment: Cleaning the Exhaust Gases

To meet emission standards, the exhaust system incorporates aftertreatment devices that reduce harmful pollutants before releasing gases into the atmosphere. The most relevant components in current vehicles are [58–63]:

- **Three-way catalytic converter:** Converts carbon monoxide, hydrocarbons, and nitrogen oxides into carbon dioxide, water, and nitrogen using a platinum, palladium, and rhodium catalyst. It requires a near-stoichiometric air-fuel ratio to function efficiently.
- **Gasoline particulate filter:** Captures fine particulate matter from the exhaust and prevents gasoline direct injection-related soot emissions from reaching the environment.
- **Exhaust gas recirculation:** Recirculates a portion of exhaust gases back into the intake air, reducing combustion temperature and lowering nitrogen oxide formation.

To sum up, the fuel is pumped from the tank to the high-pressure rail. Then,high-pressure fuel is injected into the cylinder, forming an atomized spray. The air-fuel mixture is ignited by the spark plug, releasing energy. Combustion results in CO, NO_X, PM, HC, and CO_2 emissions. Finally, Catalysts, filters, and EGR clean the exhaust gases before release. This process ensures efficient energy conversion, improved fuel economy, and compliance with emission regulations while maintaining engine performance.

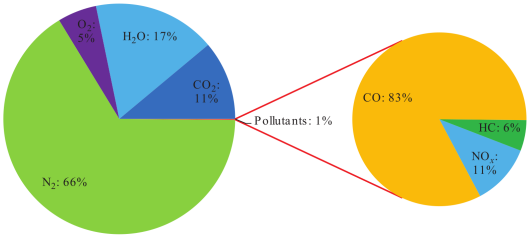


Figure 2.5: Typical exhaust composition generated in an internal combustion engine. Reprinted from [57].

2.4 Atomization and evaporation process

One of the central mechanisms of the injection process, with significant impact on combustion, is atomization. The atomization and subsequent evaporation of fuel droplets are critical processes in Gasoline Direct Injection (GDI) engines, as they govern mixture preparation, combustion efficiency, and emissions formation. Achieving a fine fuel spray with rapid evaporation enhances air-fuel mixing, improving combustion and reducing pollutant

emissions. These processes are influenced by multiple factors, including fuel pressure, injector design, ambient conditions, and fuel properties.

Compared to diesel sprays, GDI sprays operate at lower ambient densities and pressures, which reduces the aerodynamic force acting on the fuel jet. As a result, GDI relies more on fuel volatility, nozzle geometry, and pressure pulsing to enhance atomization. Furthermore, the spray plume angle in GDI is wider, with shorter penetration lengths, favoring fast evaporation over deep chamber penetration. The higher volatility of gasoline also shifts the balance between surface tension and vaporization effects, making flash boiling a central phenomenon in GDI that is absent in diesel systems.

GDI spray formation is governed by the dynamics of liquid breakup and droplet interaction mechanisms, which are critically important for achieving fast and homogeneous mixture preparation. Although the physical principles underlying spray atomization share similarities with those in diesel injection, GDI operates under distinct thermodynamic conditions, most notably lower ambient pressures and the use of more volatile fuels. These differences lead to variations in the breakup regimes, spray structure, and evaporation characteristics.

2.4.1 Atomization process in GDI Sprays

2.4.2 Spray Breakup Regimes and Droplet Interactions in GDI Sprays

The atomization process in GDI injectors is a multi-stage event influenced by several physical instabilities and aerodynamic interactions. It can be categorized into two main stages: primary breakup and secondary breakup. These are directly influenced by injector design, fuel properties, chamber conditions, and the non-dimensional parameters that characterize the relative importance of inertial, viscous, and surface tension forces as many works describe [64–66].

Primary atomization begins at the injector nozzle, where high-pressure fuel experiences a abrupt acceleration after entering the lower-pressure gas in the combustion chamber. This difference in velocity induces strong velocity gradients and shear forces at the liquid-gas interface, giving rise to Kelvin-Helmholtz instabilities [67–69]. These instabilities distort the liquid column into wave-like structures that grow in amplitude and eventually break into ligaments and coarse droplets. The primary breakup regime dominates the initial 1–2 mm of spray evolution, where these initial droplets vary in size depending on nozzle geometry, injection pressure, and ambient conditions [70–72].

As the droplets travel further into the combustion chamber, secondary atomization occurs due to increased aerodynamic interactions. At this stage, Rayleigh-Taylor instabilities are triggered, induced by local pressure gradients and acceleration differences between the fuel droplets and surrounding gas, contribute to the further fragmentation of droplets. Additionally, turbulence and in-cylinder airflow motion, such as swirl and tumble, influence droplet dispersion, promoting finer atomization and enhancing mixture preparation. This secondary breakup is critical in determining the final droplet size distribution, directly impacting evaporation rates, air-fuel mixing efficiency, and combustion quality [66, 73].

Other factors, like flash boiling, can further modify the atomization process. When the injected fuel is in a superheated state relative to the surrounding chamber pressure, rapid vaporization at the nozzle exit may lead to rapid breakup, increasing the available fuel surface area for evaporation [70, 74–76].

The breakup behavior of droplets in GDI sprays is traditionally mapped using dimensionless groups, mainly the Weber number (We), Reynolds number (Re) and Ohnesorge number (Oh or Z). Four different spray regimes can be identified depending on these numbers, as it is depicted in Figure 2.6 Rayleigh, first wind-induced, second wind-induced and atomisation regimes:

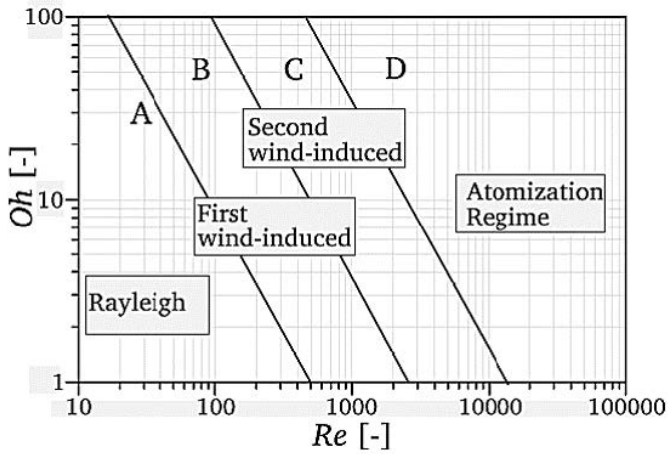


Figure 2.6: Schematic representation of the breakup regimes as function of We. Adapted from [64, 65, 77].

In GDI sprays, the typical We often exceed the threshold values for bag, bag-stamen, and shear breakup modes, resulting in a cascade of droplet disintegration into finer fragments, enhancing surface area and accelerating evapo-

ration. This regime is especially important under stratified operation or when the fuel must rapidly mix with surrounding air during limited time windows.

Spray Structure Zones:

The spray generated by a GDI injector can be divided into three zones Figure 2.7:

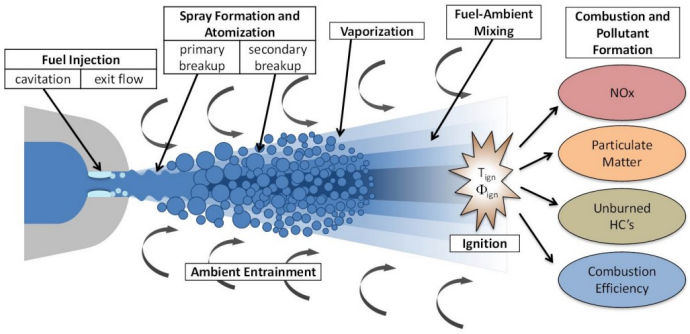


Figure 2.7: Schematic representation of the atomization process of the sprays in GDI, highlighting dense core, breakup, and dilute regions. Adapted to GDI-specific conditions from [78].

- *Dense Core Region:* Located near the nozzle exit, this zone is dominated by high liquid volume fractions and complex interactions between liquid ligaments. Optical diagnostics in this region are challenging due to the opacity of the spray.
- *Break-up and Transition Region:* This mid-spray zone is characterized by vigorous breakup of ligaments into droplets, turbulent entrainment of ambient gases, and the formation of a more spatially dispersed spray pattern. The Sauter Mean Diameter (SMD) rapidly decreases in this region.
- *Dilute Droplet Region:* Furthest from the nozzle, this zone contains dispersed droplets experiencing evaporation and transport by in-cylinder airflow (tumble, swirl). The interactions between droplets and thermal gradients become dominant, especially under stratified charge modes or near-wall zones.

After primary and secondary breakup, droplet dynamics are influenced by coalescence, collisions, and vapor shielding effects. In dense spray regions,

droplets may coalesce, affecting local SMD and vaporization rates. Vapor shielding, especially relevant in flash boiling conditions, can inhibit evaporation of trailing droplets due to the localized increase in vapor concentration. Such effects are significant in the collapse-prone operating regime of GDI injectors.

Figure 2.8 show the different drop to drop interaction that occur in the secundary break-up when the droplets are surrounded by the turbulent gas-flow, which creates aerodynamic forces on the droplet surface. Such forces may be able to overcome the superficial tension and distort the spherical shape breaking the droplet again into parcels of smaller dimensions.

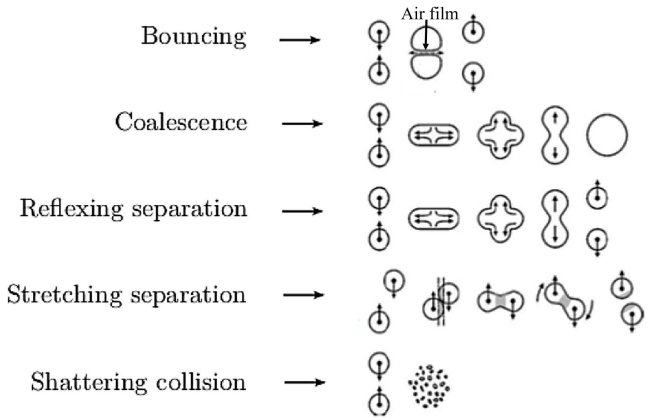


Figure 2.8: Schematic representation of the Drop-drop interaction. Adapted from [65].

2.4.3 Atomization parameters

To understand and quantify atomization, several parameters are used in both experimental and computational studies. These parameters provide insights into droplet breakup dynamics, fuel distribution, and combustion efficiency. Key parameters include [79–81]:

- *Sauter Mean Diameter (SMD)*: Represents the average droplet size based on the surface-area-to-volume ratio. Smaller SMD values indicate finer atomization and improved fuel-air mixing. In gasoline direct injection sprays, SMD values typically range between 10 to 40 µm [44, 82], depending on injection pressure and nozzle design.

- *Spray cone angle and penetration length*: The spray cone angle and penetration length together define the spatial distribution of fuel within the combustion chamber. A wider cone angle (typically 50°to 90°) promotes rapid evaporation and mixture homogeneity, while a narrower angle may lead to fuel-rich zones. Penetration lengths, ranging from 10 to 30 mm, must be controlled to prevent wall impingement, which can increase emissions and fuel consumption. Both parameters depend on injector design, injection pressure, and in-cylinder conditions.

- *Droplet velocity distribution*: Refers to the range of velocities of fuel droplets, which influences their interaction with in-cylinder airflow and evaporation rates. Droplet velocities in gasoline direct injection sprays can exceed 100 m/s at high injection pressures.

- *Spray breakup time*: The time taken for the injected fuel to fully atomize into fine droplets. Shorter breakup times improve mixture formation and combustion efficiency.

- *Weber number (We)*: A dimensionless parameter representing the ratio of aerodynamic forces to surface tension acting on fuel droplets. Higher Weber numbers promote spray breakup and finer atomization. It is defined as

$$We = \frac{\rho u^2 d}{\sigma}$$

  Where ρ is fuel density, u is droplet velocity, d is droplet diameter, and σ is surface tension.

- *Ohnesorge number (Oh)*: Describes the relationship between viscous forces, inertial forces, and surface tension. It helps characterize spray breakup regimes, particularly for understanding droplet deformation and break-up modes. Defined as:

$$Oh = \frac{\mu}{\sqrt{\rho \sigma d}}$$

  Where μ is fuel viscosity, ρ is fuel density and σ is surface tension.

- *Reynolds number (Re)*: Represents the ratio of inertial to viscous forces within the fuel jet, influencing spray turbulence and atomization behavior. It is given by

$$Re = \frac{\rho u d}{\mu}$$

.

In GDI sprays the atomization quality is mainly influenced by factors mentioned before, yet their impact is explained as follows:

- The injection pressure: Higher injection pressures (in the 100 to 350 bar range) result in finer atomization, reducing droplet size and improving vaporization rates [83, 84].
- Nozzle geometry: The number, diameter, and angle of the nozzle orifices influence spray penetration, droplet dispersion, and mixture formation [85].
- Ambient conditions: Cylinder pressure and temperature affect fuel spray behavior, with higher temperatures promoting a faster atomization [86, 87].
- Flash Boiling can either enhance atomization by increasing droplet breakup or cause spray collapse, leading to incomplete mixture preparation [86, 88].

2.4.4 Evaporation process

After the atomization, the fuel droplets evaporate, transitioning from a liquid to a vapor phase. Evaporation is driven by convective heat transfer from the surrounding gas and diffusive mass transfer of fuel molecules into the air. Several factors influence evaporation rates, including:

- Droplet Size: Smaller droplets exhibit faster evaporation due to their higher surface area-to-volume ratio.
- Ambient Temperature: Elevated in-cylinder temperatures accelerate phase transition.
- Spray Interactions: Dense spray structures can create vapor shielding effects, where accumulated evaporated fuel slows the evaporation of surrounding droplets.
- Flash Boiling: This can enhance evaporation by increasing the available surface area as the spray expands.

2.4.5 Atomization and evaporation evaluation

Experimentally, atomization and spray characteristics are analyzed using optical diagnostic techniques that provide insights into droplet breakup, velocity distributions, and evaporation behavior. Key methods include:

- High-Speed Imaging and Mie Scattering: Used to visualize spray structure and penetration.
- Phase Doppler Anemometry: Enables precise measurements of droplet size and velocity.
- Laser-Induced Exciplex Fluorescence: Helps distinguish between liquid and vapor phases, aiding in fuel evaporation studies.
- Ballistic Imaging and X-ray Radiography: Provide deeper insights into dense spray regions where traditional optical methods fail.

Computational approaches, on the other hand, complement experimental studies by modeling the complex interactions between droplets, turbulence, and in-cylinder conditions. Methods such as:

- Large Eddy Simulations (LES) and Direct Numerical Simulations (DNS) provide detailed predictions of spray dynamics and fuel evaporation behavior.
- Computational Fluid Dynamics (CFD) helps optimize injector designs and improve fuel distribution strategies.

2.5 Flash boiling phenomena

Flash boiling is a thermodynamic phase transition phenomenon that occurs in gasoline direct injection (GDI) systems when fuel is injected at a temperature above its boiling point at the operating chamber pressure, leading to spontaneous vaporization. This effect is particularly pronounced in modern GDI engines, where fuel temperatures are elevated to enhance atomization, improve combustion efficiency, and reduce particulate emissions. However, under certain conditions, excessive vapor formation can lead to spray collapse, reducing fuel dispersion and negatively impacting mixture formation [86, 89, 90].

Fuel properties play a crucial role in determining the onset and severity of flash boiling. Commercial gasoline is a complex mixture of hydrocarbons, including paraffins, olefins, and aromatics, each with distinct volatility properties. The introduction of ethanol-blended fuels has further complicated flash boiling behavior, as ethanol has a significantly lower boiling point than conventional hydrocarbons, leading to enhanced vaporization but also increasing the likelihood of spray collapse. These factors highlight the need for precise injection strategies to control flash boiling intensity and avoid combustion instabilities.

2.5.1 Inner mechanisms leading to flash boiling

Flash boiling is driven by the interplay of thermodynamics, nozzle flow dynamics, and in-chamber ambient conditions. The transition from a liquid to a vapor phase is primarily influenced by bubble nucleation and spray expansion dynamics, both of which dictate the degree of atomization and vapor formation [91, 92].

Bubble nucleation and growth

When fuel exits the injector nozzle, a sudden pressure drop occurs, triggering homogeneous and heterogeneous nucleation mechanisms. Homogeneous nucleation happens when vapor bubbles spontaneously form within the bulk liquid, while heterogeneous nucleation occurs at solid-liquid interfaces, such as nozzle walls or surface irregularities. These bubbles rapidly expand due to the pressure differential, contributing to jet fragmentation and enhancing atomization. The dynamics of this nucleation process depend on injection temperature, ambient pressure, and fuel composition [44, 93, 94].

If nucleation occurs within the injector nozzle, cavitation effects can further influence vapor formation, leading to early jet disintegration. This internal flashing alters spray morphology, affecting penetration and droplet size distribution. However, if nucleation predominantly occurs after injection into the chamber, vapor expansion effects dominate, influencing spray collapse risk [95].

The nucleation rate describes the number of vapor bubbles formed per unit time and volume in the superheated liquid. This process is primarily controlled by the local thermodynamic conditions, including fuel superheat level and pressure. According to classical nucleation theory, the nucleation rate J is given by Equation 2.1 [97, 98]:

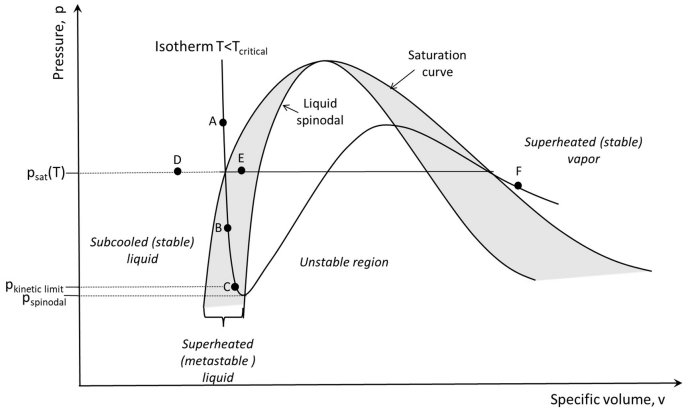


Figure 2.9: Typical pressure–volume phase diagram, indicating a subcritical isotherm. Reproduced from [96]

$$J = J_0 \exp\left(-\frac{\Delta G}{k_B T_f}\right) \tag{2.1}$$

where J_0 is a pre-exponential factor dependent on fuel properties, ΔG is the Gibbs free energy barrier for nucleation, k_B is the Boltzmann constant, and T_f is the fuel temperature. Fuels with higher volatility (e.g., Hexane) exhibit lower nucleation barriers, increasing bubble formation rates compared to less volatile fuels such as Ethanol [98].

Once nucleated, the bubble growth rate plays a critical role in determining the final spray morphology. Bubble expansion in superheated liquids is governed by the Rayleigh-Plesset equation, Equation 2.2 [97, 99]:

$$\rho\left(R_b\frac{d^2R_b}{dt^2} + \frac{3}{2}\left(\frac{dR_b}{dt}\right)^2\right) = P_v - P_a - \frac{2\sigma}{R_b} - 4\mu\frac{dR_b}{dt}\frac{1}{R_b} \tag{2.2}$$

where R_b is the bubble radius, P_v is the vapor pressure at T_f, P_a is the ambient pressure, σ is the surface tension, μ is fuel viscosity, and ρ is liquid density. The rapid expansion of vapor bubbles near the nozzle exit can lead to enhanced droplet fragmentation or cause excessive plume merging, depending on the interplay between inertia, viscous damping, and surface tension forces.

Modern studies indicate that bubble coalescence further amplifies spray collapse tendencies in multi-hole injectors, where radial plume merging is exacerbated by the volumetric expansion of vapor bubbles during early injection

under significantly superheated conditions relative to the ambient pressure. [98]. Therefore, incorporating both nucleation kinetics and bubble dynamics into spray modeling offers a more complete description of flash boiling intensity.

Spray plume expansion and breakup

The second major effect of flash boiling is spray plume expansion, where the rapid conversion of liquid to vapor increases the total spray volume. As vapor formation intensifies, droplet breakup mechanisms shift from aerodynamic-controlled fragmentation to vapor-driven disintegration. This leads to:

- Enhanced atomization: Smaller droplet sizes and increased evaporation rates, improving mixture formation.
- Plume interactions: In multi-hole injectors, excessive vapor expansion can cause adjacent plumes to merge, limiting spatial dispersion and increasing the likelihood of spray collapse.
- Penetration reduction: Vapor-driven expansion may reduce overall spray penetration, limiting charge stratification in direct injection combustion modes.

The extent to which these mechanisms impact spray morphology depends on injector geometry, hole spacing, and the pressure ratio (Rp), which governs the balance between fuel and ambient chamber pressures.

2.5.2 Characterizing flash boiling intensity

The intensity of flash boiling is often quantified using two non-dimensional parameters: Superheating degree S and/or Pressure ratio Rp.

The superheating degree defines the extent to which the injected fuel exceeds its saturation temperature at ambient pressure, Equation 2.3:

$$S = \frac{T_f - T_s}{T_s} \tag{2.3}$$

where:

- T_f = fuel injection temperature
- T_s = saturation temperature of fuel at ambient pressure

An analogous characterization of flash boiling intensity uses the superheating degree represented by the pressure ratio (Rp, Equation 2.4):

$$Rp = \frac{P_s}{P_a} \tag{2.4}$$

where:

- P_s = saturation pressure of the fuel at the fuel temperature T_f
- P_a = ambient chamber pressure

Larger Rp values indicate stronger flash boiling effects, increasing the risk of spray collapse. The typical Rp ranges associated with key phenomena are:

- $R_p > 1.0$: Flash boiling onset typically occurs when $Rp > 1.0$, as ambient pressure drops below the fuel's saturation pressure.
- $R_p \approx 1.5 - 3.0$: Moderate flash boiling effects are observed in the range $Rp \approx 1.5 - 3.0$, leading to enhanced droplet breakup and wider spray dispersion.
- $R_p > 3.0$: Strong flash boiling and spray collapse tend to occur when $Rp > 3.0$, where vapor bubbles cause plume coalescence and instability.
- $R_p \gg 3.0$: At very high Rp values (well above 3.0) under extreme superheating, explosive boiling may develop, severely disrupting spray morphology.

These threshold values are widely reported in the literature [100–102] and are strongly influenced by fuel volatility and injector geometry.

2.5.3 Spray collapse

Spray collapse results from excessive flash boiling in multi-hole injectors, where vapor expansion forces adjacent plumes to merge, reducing spray dispersion and altering air-fuel mixture distribution. However, flash boiling is not the sole contributor to spray collapse, several other factors affect spray behavior.

At high super heat levels ($S > 1.5$) or pressure ratios ($Rp > 2.5$), the excessive vapor formation forces adjacent spray plumes to merge into a single, collapsed structure. This significantly reduces the spray's spatial coverage, increasing local fuel concentrations and potentially leading to overly rich regions, affecting combustion efficiency and emissions.

High ambient density effects

Spray collapse can also occur even without strong flash boiling when the ambient density is high. Under these conditions:

- Aerodynamic drag force increases, reducing spray penetration.
- Fuel droplets experience vapor shielding, delaying atomization and increasing mixture inhomogeneity.
- Wall-wetting effects become more pronounced, leading to increased particulate formation.

Flash boiling and spray collapse occur under specific operating conditions where fuel temperature, injection timing, and chamber pressure interact to determine spray behavior. These include:

- Early injection in the intake stroke, when cylinder pressures are at their lowest, maximizing Rp and increasing the likelihood of flash boiling.
- High fuel temperatures and ethanol-blended fuels, where lower boiling points enhance vaporization, increasing the probability of plume merging.
- Low load and stratified charge combustion modes, where low ambient pressures increase flash boiling risks and cause uneven fuel distribution.
- High ambient pressure scenarios, such as turbocharged operation or high residual gas concentation, which restrict spray dispersion and increase the risk of localized fuel rich zones.

2.6 Research state on GDI

Gasoline Direct Injection (GDI) technology has gained significant attention in modern combustion research due to its potential for high thermal efficiency, fuel economy improvements, and reduced CO_2 emissions. However, GDI engines also pose challenges related to particulate emissions, mixture stratification, and injector deposits. The continued development of GDI systems is focused on fuel advancements, injection strategy optimization, and a deeper understanding of unresolved physical and chemical processes affecting combustion performance and emissions.

Alternative fuels and fuel blends for GDI engines

One of the key areas of advancement in GDI technology is the development of novel fuels and fuel blends that can improve combustion characteristics and reduce emissions. Alcohol-based fuel blends, such as ethanol, methanol, and butanol, have been widely investigated for their compatibility with GDI engines due to their high octane rating, anti-knock properties, and oxygenated nature, which improve combustion efficiency and reduce particulate emissions [103]. Ethanol blends have been found to enhance air-fuel mixture homogeneity due to their higher latent heat of vaporization, thereby reducing CO and HC emissions [104, 105].

In parallel, ammonia and hydrogen are being explored as potential low-carbon alternatives to traditional gasoline. Ammonia combustion in GDI engines presents challenges due to its low flame speed and high ignition energy requirements [106, 107]. However, research has demonstrated that blending ammonia with hydrogen or gasoline can significantly enhance combustion stability. Hydrogen-ammonia mixtures have shown promising results in improving combustion efficiency while reducing CO_2 emissions[108]. Injection strategies such as split injection and direct injection timing adjustments have been used to mitigate ammonia's slow flame speed, highlighting the importance of injection timing optimization in enabling alternative fuel use in GDI applications [109, 110]. Additionally, multi-component fuel blends, such as Isooctane, n-Heptane, Toluene mixtures, continue to be employed to study fundamental spray and combustion behaviors in GDI systems. These blends are crucial for validating numerical simulations and understanding the impact of fuel volatility on spray penetration, mixture formation, and emissions.

Unresolved phenomena affecting GDI performance

Beyond fuel advancements, unresolved physical and chemical phenomena continue to impact GDI performance. Flash boiling, a phenomenon that occurs when fuel is injected at superheated conditions, remains a significant area of study due to its impact on spray behavior and mixture formation. Flash boiling enhances atomization by increasing droplet breakup; however, excessive superheat can result in spray collapse, negatively affecting combustion stability. High-speed imaging and laser diagnostics have significantly improved the visualization of spray breakup mechanisms, while computational studies using large eddy simulations (LES) and volume of fluid (VOF) models have refined predictive capabilities for flash boiling effects. Despite these advancements, challenges remain in accurately modeling multi-component fuel effects,

as different volatility fractions evaporate at varying rates, leading to complex plume interactions.

Furthermore, injector deposits and spray degradation continue to pose issues for GDI engines. Deposits formed on injector nozzles over time can degrade spray quality, affecting fuel-air mixture preparation. Recent studies have focused on developing injector cleanliness additives, fuel conditioning techniques, and laser-induced fluorescence (LIF) imaging to analyze deposit buildup and its impact on spray penetration and combustion efficiency.

Advanced injection strategies for GDI engines

In response to these challenges, advanced injection strategies have been implemented to enhance GDI engine performance. GDI systems working at very high injection pressure of up to 35 MPa, have demonstrated significant improvements in atomization, reducing tip wetting and minimizing fuel wall films. Their employment has shown to reduce PN emissions by enhancing droplet breakup, thereby improving air-fuel mixing. However, challenges remain regarding cavitation effects inside injector nozzles, which can influence spray formation and need further investigation.

In addition, multiple injection strategies, such as split and pilot-main injection, have been explored to optimize combustion and emissions. Split injection strategies enable better mixture stratification, reducing cold-start emissions and improving fuel vaporization. Early pilot injections enhance vaporization in stratified charge operation, while late post-injections help reduce particulate emissions by improving oxidation rates [104]. Moreover, combining GDI with PFI (dual injection strategy) has been explored as a way to balance fuel economy and emissions. PFI improves fuel-air premixing, while GDI maintains high power density. Dual injection strategies have been found to be effective in reducing cold-start emissions and improving engine durability by minimizing injector deposit formation [111–114].

In this sense, GDI technology also plays a crucial role in modern hybrid powertrains which manage frequent engine restarts and variable load conditions, and where GDI contributes to achieving higher thermal efficiency. In hybrid electric vehicles (HEVs) and plug-in hybrid electric vehicles (PHEVs), engines often operate at lower loads or in start-stop cycles, which amplifies challenges such as cold-start emissions and transient spray behavior. GDI systems, with their ability to precisely control fuel delivery through high-pressure injection, are well-suited to address these challenges by improving combustion efficiency and reducing unburned hydrocarbon emissions during



Figure 2.10: Dual fuel injection system (GDI + PFI). Reproduced from Bosch Mobility Solutions Website [115]

engine restarts [116]. Moreover, hybrid engines benefit from GDI's flexibility in mixture stratification, as well as, other technologies such as dual injection strategies, which optimize combustion over a broader load and speed range while maintaining low particulate and NOx emissions [117]. Commercial hybrid engines such as Toyota's Dynamic Force and Hyundai's Smartstream have successfully integrated GDI and PFI systems to meet stringent emission standards while optimizing combustion across a wide operating range. As hybridization becomes more widespread, GDI systems are being further adapted to ensure robust performance during frequent engine shutdowns and restarts, making injection strategy optimization a key research focus in hybrid powertrain development [118].

Hybrid vehicles combine an internal combustion engine (ICE) with one or more electric motors, leveraging the strengths of both propulsion systems. The integration of GDI into these powertrains provides significant advantages, particularly in terms of thermal efficiency and fuel economy. GDI enables higher compression ratios and supports effective turbocharging, allowing for greater power output from downsized engines, an essential feature for hybrid platforms where minimizing engine size and weight is critical. This synergy enhances the overall system efficiency, optimizes packaging constraints, and contributes to reduced fuel consumption across varied driving conditions.

The adoption of GDI in hybrid engines aligns with stringent emission regulations thanks to the advances in GDI technology [117]. Furthermore, while the current outlook shows as the ultimate goal, the full vehicle electrification, current technological and infrastructural limitations make hybrids a practical interim solution. GDI technology complements this pathway by:

- *Providing Transitional Efficiency:* By enhancing the efficiency of ICEs within hybrid systems, GDI contributes to reducing the environmental impact during the gradual shift to electric vehicles.
- *Supporting Range Extenders:* In plug-in hybrid electric vehicles (PHEVs), GDI-equipped engines can serve as range extenders, offering drivers flexibility and alleviating range anxiety associated with purely electric vehicles.

Emerging combustion concepts in GDI technology

The development of emerging combustion concepts has further expanded the scope of GDI technology. Gasoline compression ignition (GCI) is an advanced combustion concept that seeks to achieve auto-ignition of gasoline-like fuels through compression, similar to diesel engines. This approach has the potential to offer high thermal efficiency and low NOx emissions but requires precise injection timing and air handling strategies. Another promising concept is reactivity controlled compression ignition (RCCI), which involves the use of dual-fuel injection (typically gasoline and diesel) to control in-cylinder fuel reactivity. By optimizing the mixing of fuels with different autoignition properties, RCCI enables highly efficient, low-emission combustion. Furthermore, hybrid combustion modes, such as spark-assisted compression ignition and homogeneous charge compression ignition (HCCI), are being investigated to improve combustion stability over a wider operating range [119].

Overall, the ongoing advancements in GDI research highlight the importance of fuel innovation, optimized injection strategies, and deeper fundamental understanding of combustion processes. Novel fuels, such as alcohol blends, ammonia, and hydrogen, present new opportunities for reducing emissions and improving efficiency. However, challenges related to flash boiling, spray collapse, and injector deposits require continued research. Advanced injection strategies, such as ultra-high pressure injection and multiple-pulse strategies, provide significant improvements in atomization and combustion control. Emerging combustion concepts, including GCI, RCCI, and hybrid modes, further push the boundaries of high-efficiency, low-emission internal combustion engines. Continued research in these areas will be critical to optimizing GDI technology for future powertrain applications [120].

References

[1] Celik, M. and Ozdalyan, B. “Gasoline Direct Injection”. In: 2010. DOI: 10.5772/9693.

[2] Zhao, H. "1 - Overview of gasoline direct injection engines". In: *Advanced Direct Injection Combustion Engine Technologies and Development*. Ed. by H. Zhao. Vol. 1. Woodhead Publishing, 2010, pp. 1–19. DOI: https://doi.org/10.1533/9781845697327.1.

[3] Burke, A., Abeles, E., and Chen, B. "The Response of the Auto Industry and Consumers to changes in the exhaust emission and fuel economy standards (1975-2003): A historical review of changes in technology, prices and sales of various classes of vehicles". In: (2004).

[4] Wang, B., Pamminger, M., Vojtech, R., and Wallner, T. "Impact of injection strategies on combustion characteristics, efficiency and emissions of gasoline compression ignition operation in a heavy-duty multicylinder engine". In: *International Journal of Engine Research* 21.8 (2020), pp. 1426–1440.

[5] Saliba, G. et al. "Comparison of gasoline direct-injection (GDI) and port fuel injection (PFI) vehicle emissions: emission certification standards, cold-start, secondary organic aerosol formation potential, and potential climate impacts". In: *Environmental science & technology* 51.11 (2017), pp. 6542–6552.

[6] Martinez, S., Irimescu, A., Merola, S., Lacava, P., and Curto-Riso, P. "Flame Front Propagation in an Optical GDI Engine under Stoichiometric and Lean Burn Conditions". In: *Energies* 10 (2017), p. 1337. DOI: 10.3390/EN10091337.

[7] Cardosa, T. J. P. L. "Port Fuel Injection Strategies for a Lean Burn Gasoline Engine". PhD thesis. University of Brighton, 2011.

[8] Tripathy, S., Sahoo, S., and Srivastava, D. "Gasoline Direct Injection—Challenges". In: (2017), pp. 367–379. DOI: 10.1007/978-981-10-3785-6_16.

[9] Zhao, F., Lai, M.-C., and Harrington, D. L. "Automotive spark-ignited direct-injection gasoline engines". In: *Progress in energy and combustion science* 25.5 (1999), pp. 437–562.

[10] Lee, Z., Kim, T., Park, S., and Park, S. "Review on spray, combustion, and emission characteristics of recent developed direct-injection spark ignition (DISI) engine system with multi-hole type injector". In: *Fuel* 259 (2020), p. 116209. DOI: 10.1016/j.fuel.2019.116209.

[11] Zhao, X. and Xiong, W. "Notice of RetractionCombustion characteristics of test and research on electronic control fuel injection system of cars GDI engine". In: *2011 Second International Conference on Mechanic Automation and Control Engineering* (2011), pp. 123–126.

[12] Xuefeng, Z. and Xiu-min, Y. "Reserch on lean burning characteristics experiment based on GDI engine". In: *2011 International Conference on Materials for Renewable Energy & Environment*. Vol. 2. IEEE. 2011, pp. 1258–1262.

[13] Yamaguchi, A., Koopmans, L., Helmantel, A., Dillner, J., and Dahlander, P. "Spray behaviors and gasoline direct injection engine performance using ultrahigh injection pressures up to 1500 bar". In: *SAE International Journal of Engines* 15.2 (2022), pp. 167–184.

[14] Takagi, Y. "A new era in spark-ignition engines featuring high-pressure direct injection". In: *Symposium (international) on combustion*. Vol. 27. 2. Elsevier. 1998, pp. 2055–2068.

[15] Lee, S. and Park, S. "Experimental study on spray break-up and atomization processes from GDI injector using high injection pressure up to 30 MPa". In: *International Journal of Heat and Fluid Flow* 45 (2014), pp. 14–22.

[16] Skiba, S. and Melbert, J. "Dosing performance of piezo injectors and sensorless closed-loop controlled solenoid injectors for gasoline direct injection". In: *SAE International Journal of Engines* 5.2 (2012), pp. 330–335.

[17] Medina, M., Bautista, A., Wooldridge, M., and Payri, R. "The effects of injector geometry and operating conditions on spray mass, momentum and development using high-pressure gasoline". In: *Fuel* 294.December 2020 (2021), p. 120468. DOI: 10.1016/j.fuel.2021.120468.

[18] Sforzo, B. A. et al. "X-ray characterization of real fuel sprays for gasoline direct injection". In: *Journal of Energy Resources Technology* 144.2 (2022), p. 022303.

[19] Lubrizol Corporation. *How It Works – PFI vs GDI Engines*. Accessed: March 20, 2025. 2023.

[20] Carburetor Blog. *How the Holley 847 Carburetor Works*. Accessed: March 23, 2025. 2023. URL: https://www.carburetor-blog.com/how-the-holley-847-carburetor-works/.

[21] Hung, D. L. et al. *A high speed flow visualization study of fuel spray pattern effect on mixture formation in a low pressure direct injection gasoline engine*. Tech. rep. SAE Technical Paper, 2007.

[22] Chigier, N., Bachalo, W. D., Reitz, R. D., Bellan, J., and Herrmann, M. "Spray control for maximizing energy efficiency and reducing emission in combustion engines". In: *Atomization and Sprays* 21.7 (2011).

[23] Hu, C. et al. “Spray dynamics characteristics in gasoline direct injection injectors at varied orifice inlet angles”. In: *Physics of Fluids* 37.1 (2025).

[24] Duke, D. J. et al. “Internal and near nozzle measurements of Engine Combustion Network “Spray G” gasoline direct injectors”. In: *Experimental Thermal and Fluid Science* 88 (2017), pp. 608–621. DOI: 10.1016/j.expthermflusci.2017.07.015.

[25] Jiang, C. et al. “Impact of gasoline direct injection fuel injector hole geometry on spray characteristics under flash boiling and ambient conditions”. In: *Fuel* 241 (2019), pp. 71–82. DOI: https://doi.org/10.1016/j.fuel.2018.11.143.

[26] Moon, S. et al. “Ultrafast X-ray study of multi-hole GDI injector sprays: Effects of nozzle hole length and number on initial spray formation”. In: *Experimental Thermal and Fluid Science* 68 (2015), pp. 68–81.

[27] Aleiferis, P. and van Romunde, Z. “An analysis of spray development with iso-octane, n-pentane, gasoline, ethanol and n-butanol from a multi-hole injector under hot fuel conditions”. In: *Fuel* 105 (2013), pp. 143–168. DOI: https://doi.org/10.1016/j.fuel.2012.07.044.

[28] Skogsberg, M., Dahlander, P., Lindgren, R., and Denbratt, I. *Effects of injector parameters on mixture formation for multi-hole nozzles in a spray-guided gasoline DI engine*. Tech. rep. SAE Technical Paper, 2005.

[29] Muhammed, H., Balaji, K., Tamilarasan, N., Sakthivel, R., et al. “A Review on Alternative Fuels: Spray Characteristics, Engine Performance and Emissions Effect”. In: *Sustainable Futures* (2025), p. 100456.

[30] Wissink, M. L. et al. “Measurement of needle and armature dynamics in a gasoline direct injector by high-speed neutron imaging”. In: *International Journal of Engine Research* 25.2 (2024), pp. 347–357.

[31] Gong, H. et al. “End-of-injection fuel dribbling dynamics of multi-hole GDI injector”. In: *Fuel* 317 (2022), p. 123406.

[32] Leng, P. et al. “Cavitation instability in real-size GDI nozzle using X-ray phase-contrast imaging”. In: *International Journal of Heat and Mass Transfer* 235 (2024), p. 126137.

[33] Martínez, M., Martí-Aldaraví, P., Salvador, F. J., and Martínez-Miracle, E. C. "In- and near-nozzle and external flow characterization in Gasoline Direct injection (GDi) engines – A review of latest technologies and trends. Part 2: Computational background". In: *International Journal of Engine Research* 0.0 (0000), p. 14680874241309959. DOI: 10.1177/14680874241309959.

[34] Injector RX. *Fuel Injector Diagram | Injector RX*. Accessed: March 23, 2025. 2023. URL: https://www.injectorrx.com/fuel-injector-cleaning-and-flow-testing-service/fuel-injectors/fuel-injector-diagram/.

[35] Chang, M., Yu, Y. S., Park, S., and Park, S. "Spray dynamics and atomization characteristics of multi-hole GDI injectors under flash boiling conditions". In: *Applied Thermal Engineering* 200 (2022), p. 117626. DOI: https://doi.org/10.1016/j.applthermaleng.2021.117626.

[36] Jin, Y. et al. "Comparison of diesel spray with small injection amount between single-hole and multi-hole injectors: results under same rail pressure and similar injection rate". In: *International Communications in Heat and Mass Transfer* 118 (2020), p. 104862.

[37] Park, J. and Park, S. "Spray Development Process Utilizing a Multi-Hole GDI Injector with Different Spray Hole Lengths and Step Hole Diameters". In: *International Journal of Automotive Technology* 23.3 (2022), pp. 641–649.

[38] Zhao, W., Yan, J., Gao, S., Lee, T. H., and Li, X. "Effects of fuel properties and aerodynamic breakup on spray under flash boiling conditions". In: *Applied Thermal Engineering* 200 (2022), p. 117646. DOI: https://doi.org/10.1016/j.applthermaleng.2021.117646.

[39] Montanaro, A., Allocca, L., Meccariello, G., and De Vita, A. "Very high-pressure sprays of gasoline from a GDI multi-hole injector". In: *Proceedings of the 29th Conference on Liquid Atomization and Spray Systems*. 2019.

[40] Wang, B. et al. "Investigation of deposit effect on multi-hole injector spray characteristics and air/fuel mixing process". In: *Fuel* 191 (2017), pp. 10–24.

[41] Robert Bosch GmbH. *Gasoline Direct Injection: Bosch Aftermarket Services*. Accessed: March 23, 2025. 2021.

[42] Abe, M., Ishii, E., and Ehara, H. "Atomized spray droplet size prediction from multi-hole nozzle for direct injection gasoline engines". In: *Journal of Fluid Science and Technology* 12 (2017).

[43] Postrioti, L., Bosi, M., Mariani, A., and Ungaro, C. *Momentum flux spatial distribution and pda analysis of a gdi spray.* Tech. rep. SAE Technical Paper, 2012.

[44] Bornschlegel, S., Conrad, C., Eichhorn, L., and Wensing, M. "Flash-boiling atomization in nozzles for GDI engines". In: 2017.

[45] Liu, Y. et al. "Spray development and droplet characteristics of high temperature single-hole gasoline spray". In: *Fuel* 191 (2017), pp. 97–105. DOI: 10.1016/j.fuel.2016.11.068.

[46] Beavis, N., Ibrahim, S., and Malalasekera, W. "Numerical evaluation of combustion regimes in a GDI engine". In: *Flow, Turbulence and Combustion* 101 (2018), pp. 1035–1057.

[47] Buschbeck, M., Bittner, N., Halfmann, T., and Arndt, S. "Dependence of combustion dynamics in a gasoline engine upon the in-cylinder flow field, determined by high-speed PIV". In: *Experiments in fluids* 53 (2012), pp. 1701–1712.

[48] Martinez, S., Irimescu, A., Merola, S. S., Lacava, P., and Curto-Riso, P. "Flame Front Propagation in an Optical GDI Engine under Stoichiometric and Lean Burn Conditions". In: *Energies* 10.9 (2017). DOI: 10.3390/en10091337.

[49] Zhou, L., Zhang, X., Zhong, L., and Yu, J. "Effects of Flame Propagation Velocity and Turbulence Intensity on End-Gas Auto-Ignition in a Spark Ignition Gasoline Engine". In: *Energies* 13.19 (2020). DOI: 10.3390/en13195039.

[50] Avila, I. I. B. "CFD modelling and analysis of the passive pre-chamber ignition concept for future generation spark-ignition engines". PhD thesis. Universitat Politècnica de València, 2023.

[51] Chala, G., Aziz, A., and Hagos, F. "Natural Gas Engine Technologies: Challenges and Energy Sustainability Issue". In: *Energies* 11 (2018), p. 2934. DOI: 10.3390/en11112934.

[52] Fayyazbakhsh, A. et al. "Engine emissions with air pollutants and greenhouse gases and their control technologies". In: *Journal of Cleaner Production* 376 (2022), p. 134260. DOI: https://doi.org/10.1016/j.jclepro.2022.134260.

[53] Du, Z. et al. "Comparison of primary aerosol emission and secondary aerosol formation from gasoline direct injection and port fuel injection vehicles". In: *Atmospheric Chemistry and Physics* 18.12 (2018), pp. 9011–9023.

[54] Uberall, A., Otte, R., Eilts, P., and Krahl, J. "A literature research about particle emissions from engines with direct gasoline injection and the potential to reduce these emissions". In: *Fuel* 147 (2015), pp. 203–207. DOI: https://doi.org/10.1016/j.fuel.2015.01.012.

[55] Wooldridge, M. S., Singh, R., Gutierrez, L. G., and Clancy, S. "Survey of strategies to reduce cold-start particulate, CO, NOx, and hydrocarbon emissions from direct-injection spark-ignition engines". In: *International Journal of Engine Research* 24.2 (2023), pp. 456–480. DOI: 10.1177/14680874211068576.

[56] Awad, O. I. et al. "Particulate emissions from gasoline direct injection engines: A review of how current emission regulations are being met by automobile manufacturers." In: *The Science of the total environment* 718 (2020), p. 137302.

[57] Grimaldi, C. N., Millo, F., et al. "Internal combustion engine (ICE) fundamentals". In: *Handbook of clean energy systems*. Vol. 2. John Wiley & Sons Limited, 2015, pp. 907–938.

[58] Ye, Z. "GDI engine exhaust aftertreatment system analysis and oxygen sensor based identification, modeling and control of lean NOx trap". In: *Internal Combustion Engine Division Spring Technical Conference*. Vol. 36789. 2003, pp. 713–719.

[59] Ma, L.-P. et al. "Kinetic study of three-way catalyst of automotive exhaust gas: Modeling and application". In: *Chemical Engineering Journal* 155.1-2 (2009), pp. 241–247.

[60] Sellnau, M. et al. "Aftertreatment System for Light-Duty Gasoline Compression Ignition (LD-GCI) for Ultra-Low Criteria Emissions". In: *Internal Combustion Engine Division Fall Technical Conference*. Vol. 88520. American Society of Mechanical Engineers. 2024, V001T05A008.

[61] Yang, J. et al. "Gasoline particulate filters as an effective tool to reduce particulate and polycyclic aromatic hydrocarbon emissions from gasoline direct injection (GDI) vehicles: a case study with two GDI vehicles". In: *Environmental Science & Technology* 52.5 (2018), pp. 3275–3284.

[62] Joshi, A. and Johnson, T. V. "Gasoline particulate filters—A review". In: *Emission Control Science and Technology* 4.4 (2018), pp. 219–239.

[63] Dong, R., Zhang, Z., Ye, Y., Huang, H., and Cao, C. "Review of Particle Filters for Internal Combustion Engines". In: *Processes* (2022).

[64] Duronio, F., De Vita, A., Allocca, L., and Anatone, M. "Gasoline direct injection engines – A review of latest technologies and trends. Part 1: Spray breakup process". In: *Fuel* 265.November 2019 (2020), p. 116948. DOI: 10.1016/j.fuel.2019.116948.

[65] Valderrama, G. and Sebastián, J. "Macroscopic and microscopic characterization of non-reacting diesel sprays at low and very high injection pressures". In: 2018.

[66] Reitz, R. D. and Diwakar, R. "Structure of high-pressure fuel sprays". In: *SAE transactions* (1987), pp. 492–509.

[67] Beale, J. C. and Reitz, R. D. "Modeling spray atomization with the Kelvin-Helmholtz/Rayleigh-Taylor hybrid model". In: *Atomization and sprays* 9.6 (1999).

[68] Reckers, W., Befrui, B., and Corbinelli, G. "Investigation of high pressure GDi conical spray atomization for spray-guided combustion systems". In: *AVL 8th International Symposium on Combustion Diagnostics*. 2008.

[69] Park, S. W. and Sik Lee, C. "Investigation of atomization and evaporation characteristics of high-pressure injection diesel spray using Kelvin—Helmholz instability/droplet deformation and break-up competition model". In: *Proceedings of the Institution of Mechanical Engineers, Part D: Journal of Automobile Engineering* 218.7 (2004), pp. 767–777.

[70] Moon, S., Li, T., Sato, K., and Yokohata, H. "Governing parameters and dynamics of turbulent spray atomization from modern GDI injectors". In: *Energy* 127 (2017), pp. 89–100.

[71] Addepalli, S. K. and Mallikarjuna, J. M. "Modelling Spray in GDI Engines: Fuel Injection Modelling". In: *Modelling Spark Ignition Combustion*. Ed. by P. A. Lakshminarayanan, A. K. Agarwal, H. Ge, and J. M. Mallikarjuna. Singapore: Springer Nature Singapore, 2024, pp. 339–389. DOI: 10.1007/978-981-97-0629-7_9.

[72] Ramirez, A. et al. "Quantitative X-ray measurements of high-pressure fuel sprays from a production heavy duty diesel injector". In: *Experiments in fluids* 47 (2009), pp. 119–134.

[73] Lee, S. and Park, S. "Spray atomization characteristics of a GDI injector equipped with a group-hole nozzle". In: *Fuel* 137 (2014), pp. 50–59.

[74] Martínez, M., Martí-Aldaraví, P., Salvador, F. J., and Martínez-Miracle, E. C. "In-and near-nozzle and external flow characterization in Gasoline Direct injection (GDi) engines–A review of latest technologies and trends. Part 2: Computational background". In: *International Journal of Engine Research* (2024), p. 14680874241309959.

[75] Wu, S., Gandhi, A., Li, H., and Meinhart, M. "Experimental and numerical study of the effects of nozzle taper angle on spray characteristics of GDI multi-hole injectors at cold condition". In: *Fuel* 275 (2020), p. 117888. DOI: https://doi.org/10.1016/j.fuel.2020.117888.

[76] Kale, R. and Banerjee, R. "Spray Collapse in a Multi-hole GDI Injector and Its Effect on In-Cylinder Combustion". In: *Two-Phase Flow for Automotive and Power Generation Sectors*. Ed. by K. Saha, A. Kumar Agarwal, K. Ghosh, and S. Som. Singapore: Springer Singapore, 2019, pp. 43–61. DOI: 10.1007/978-981-13-3256-2_3.

[77] Pilch, M. and Erdman, C. "Use of breakup time data and velocity history data to predict the maximum size of stable fragments for acceleration-induced breakup of a liquid drop". In: *International Journal of Multiphase Flow* 13.6 (1987), pp. 741–757. DOI: https://doi.org/10.1016/0301-9322(87)90063-2.

[78] Luo, K., Changxiao, S., Min, C., and Fan, J. "Level set method for atomization and evaporation simulations". In: *Progress in Energy and Combustion Science* 73 (2019), pp. 65–94. DOI: 10.1016/j.pecs.2019.03.001.

[79] Lefebvre, A. H. "Atomization and Sprays". In: 1988.

[80] Helldorff, H. von and Micklow, G. J. "Primary and Secondary Spray Breakup Modelling for Internal Combustion Engine Applications". In: 2019.

[81] Khandekar, S., Jaiswal, A. K., and Sahu, G. "Chapter Four - Spray cooling: From droplet dynamics to system level perspectives". In: ed. by J. P. Abraham, J. M. Gorman, and W. J. Minkowycz. Vol. 54. Advances in Heat Transfer. Elsevier, 2022, pp. 135–177. DOI: https://doi.org/10.1016/bs.aiht.2022.07.002.

[82] Mishra, Y. N. et al. "3D mapping of droplet Sauter mean diameter in sprays." In: *Applied optics* 58 14 (2019), pp. 3775–3783.

[83] Raza, M., Chen, L., Leach, F., and Ding, S. "A Review of Particulate Number (PN) Emissions from Gasoline Direct Injection (GDI) Engines and Their Control Techniques". In: *Energies* 11.6 (2018). DOI: 10.3390/en11061417.

[84] Lee, Z., Kim, D., and Park, S. "Effects of spray behavior and wall impingement on particulate matter emissions in a direct injection spark ignition engine equipped with a high pressure injection system". In: *Energy Conversion and Management* 213.February (2020), p. 112865. DOI: 10.1016/j.enconman.2020.112865.

[85] Bar-Kohany, T. and Levy, M. "STATE OF THE ART REVIEW OF FLASH-BOILING ATOMIZATION". In: *Atomization and Sprays* 26 (2016), pp. 1259–1305.

[86] Kapusta, Ł. J. "Understanding the collapse of flash-boiling sprays formed by multi-hole injectors operating at low injection pressures". In: *Energy* 247 (2022), p. 123388. DOI: https://doi.org/10.1016/j.energy.2022.123388.

[87] Li, X., Li, T., and Xu, M. "Effect of ambient temperature on flash-boiling spray characteristics for a multi-hole gasoline injector". In: *Experiments in Fluids* 60 (2019), pp. 1–12.

[88] Xu, Q., Pan, H., Gao, Y., Li, X., and Xu, M. "Investigation of two-hole flash-boiling plume-to-plume interaction and its impact on spray collapse". In: *International Journal of Heat and Mass Transfer* 138 (2019), pp. 608–619. DOI: https://doi.org/10.1016/j.ijheatmasstransfer.2019.04.111.

[89] Mojtabi, M., Chadwick, N., Wigley, G., and Helie, J. "The effect of flash boiling on break up and atomization in GDI sprays". In: *Proceedings of the 22nd European Conference on Liquid Atomization and Spray Systems. ILASS Europe. Como Lake, Italy.* 2008, pp. 08–10.

[90] Oh, H., Hwang, J., White, L., Pickett, L. M., and Han, D. "Spray collapse characteristics of practical GDI spray for lateral-mounted GDI engines". In: *International Journal of Heat and Mass Transfer* 190 (2022), p. 122743. DOI: https://doi.org/10.1016/j.ijheatmasstransfer.2022.122743.

[91] Guo, H., Wang, B., Li, Y., Xu, H., and Wu, Z. "Characterizing external flashing jet from single-hole GDI injector". In: *International Journal of Heat and Mass Transfer* 121 (2018), pp. 924–932. DOI: https://doi.org/10.1016/j.ijheatmasstransfer.2018.01.042.

[92] Li, X. et al. "A review on the recent advances of flash boiling atomization and combustion applications". In: *Progress in Energy and Combustion Science* 100 (2024), p. 101119. DOI: https://doi.org/10.1016/j.pecs.2023.101119.

[93] Oza, R. D. and Sinnamon, J. F. "An experimental and analytical study of flash-boiling fuel injection". In: *SAE Technical Papers* (1983). DOI: 10.4271/830590.

[94] Li, Y. et al. "An exploration on collapse mechanism of multi-jet flash-boiling sprays". In: *Applied Thermal Engineering* 134.May 2017 (2018), pp. 20–28. DOI: 10.1016/j.applthermaleng.2018.01.102.

[95] Lesnik, L., Kegl, B., Bombek, G., Hočevar, M., and Biluš, I. "The influence of in-nozzle cavitation on flow characteristics and spray break-up". In: *Fuel* 222 (2018), pp. 550–560. DOI: https://doi.org/10.1016/j.fuel.2018.02.144.

[96] Bar-Kohany, T., Arogeti, M., Malka, A., and Sher, E. "Advances in Liquid Atomization via Flash Boiling—A Global Overview". In: *Energies* 16.19 (2023), p. 6763.

[97] Brenn, G. and Valkovska, D. "Modeling of vapor bubble growth and collapse in superheated liquids". In: *International Journal of Heat and Mass Transfer* 44.14 (2001), pp. 2605–2615.

[98] Yang, W., Zhang, Z., Li, J., and Xue, Y. "Experimental investigation of nucleation rate and flash boiling spray behavior under low-pressure conditions". In: *Fuel* 267 (2020), p. 117262. DOI: 10.1016/j.fuel.2020.117262.

[99] Brennen, C. *Fundamentals of Multiphase Flow*. Cambridge University Press, 2005.

[100] Du, J., Chen, H., Li, Y., Ye, L., and Li, G. "Experimental Study on Ethanol Gasoline Flash-Boiling Spray Characteristics Using Multi-hole GDI Injector". In: *Proceedings of China SAE Congress 2019: Selected Papers*. Singapore: Springer Singapore, 2021, pp. 635–645.

[101] Li, X. et al. "Insights into Microscopic Characteristics of Gasoline and Ethanol Spray from a GDI Injector Under Injection Pressure up to 50 MPa". In: *Sustainability* 16.21 (2024). DOI: 10.3390/su16219471.

[102] Chang, M., Lee, Z., Park, S., and Park, S. "Characteristics of flash boiling and its effects on spray behavior in gasoline direct injection injectors: A review". In: *Fuel* 271.December 2019 (2020), p. 117600. DOI: 10.1016/j.fuel.2020.117600.

[103] Aleiferis, P. G. and Van Romunde, Z. R. "An analysis of spray development with iso-octane, n-pentane, gasoline, ethanol and n-butanol from a multi-hole injector under hot fuel conditions". In: *Fuel* 105 (2013), pp. 143–168. DOI: 10.1016/j.fuel.2012.07.044.

[104] Zhang, W. et al. "Effect of gasoline aromatic compositions coupled with single and double injection strategy on GDI engine combustion and emissions". In: *Fuel* 278 (2020), p. 118308. DOI: https://doi.org/10.1016/j.fuel.2020.118308.

[105] Kim, Y., Il Kim, W., Min, B., Seo, J., and Lee, K. "Experimental investigation of combustion characteristics of ethanol–gasoline blended fuel in a T-GDI engine". In: *Applied Thermal Engineering* 208 (2022), p. 118168. DOI: https://doi.org/10.1016/j.applthermaleng.2022.118168.

[106] Payri, R., García-Oliver, J. M., Bracho, G., and Cao, J. "Experimental characterization of direct injection liquid ammonia sprays under non-reacting diesel-like conditions". In: *Fuel* 362 (2024), p. 130851.

[107] He, H. et al. "An Experimental Study on the Flash Boiling Characteristics of Liquid Ammonia Spray in a Constant Volume Chamber under High Injection Pressure". In: *Processes* 12.6 (2024). DOI: 10.3390/pr12061076.

[108] Wang, D., Ji, C., Wang, S., Yang, J., and Wang, Z. "Numerical study of the premixed ammonia-hydrogen combustion under engine-relevant conditions". In: *International Journal of Hydrogen Energy* 46.2 (2021), pp. 2667–2683. DOI: https://doi.org/10.1016/j.ijhydene.2020.10.045.

[109] El-Adawy, M., Nemitallah, M. A., and Abdelhafez, A. "Towards sustainable hydrogen and ammonia internal combustion engines: Challenges and opportunities". In: *Fuel* 364 (2024), p. 131090. DOI: https://doi.org/10.1016/j.fuel.2024.131090.

[110] Chai, W. S., Bao, Y., Jin, P., Tang, G., and Zhou, L. "A review on ammonia, ammonia-hydrogen and ammonia-methane fuels". In: *Renewable and Sustainable Energy Reviews* 147 (2021), p. 111254. DOI: https://doi.org/10.1016/j.rser.2021.111254.

[111] Kalwar, A. and Agarwal, A. "Overview, Advancements and Challenges in Gasoline Direct Injection Engine Technology". In: 2020, pp. 111–147. DOI: 10.1007/978-981-15-0368-9_6.

[112] Fanick, R. E., Kroll, S., Swarts, A., and Quarderer, S. "Effects of Dual Port Injection and Direct-Injection Technology on Combustion Emissions from Light-Duty Gasoline Vehicles". In: *SAE Technical Paper Series* (2019). DOI: https://doi.org/10.4271/2019-01-0999.

[113] Bhaskara. "Advanced combustion strategies for improving ic engine efficiency and emissions". In: *World Journal of Advanced Research and Reviews* (2023). DOI: https://doi.org/10.30574/wjarr.2023.17.2.1444.

[114] Gong, C., Yu, J., and Liu, F. "Combined impact of excess air ratio and injection strategy on performances of a spark-ignition port- plus direct-injection dual-injection gasoline engine at half load". In: *Fuel* 340 (2023), p. 127605. DOI: https://doi.org/10.1016/j.fuel.2023.127605.

[115] Bosch Mobility. *Gasoline Direct Injection*. Accessed: March 30, 2025. 2024. URL: https://www.bosch-mobility.com/en/solutions/powertrain/gasoline/gasoline-direct-injection/.

[116] Jiang, Y. et al. "Impacts of cold starts and hybrid electric vehicles on on-road vehicle emissions". In: *Transportation Research Part D: Transport and Environment* 126 (2024), p. 104011. DOI: https://doi.org/10.1016/j.trd.2023.104011.

[117] Shuai, S., Ma, X., Li, Y., Qi, Y., and Xu, H. "Recent progress in automotive gasoline direct injection engine technology". In: *Automotive Innovation* 1 (2018), pp. 95–113.

[118] Agarwal, A. K., Gupta, T., and Singh, A. P. "Advanced GDI combustion strategies for hybrid engines: Challenges and opportunities". In: *Renewable and Sustainable Energy Reviews* 133 (2020), p. 110264.

[119] Agarwal, A. K., Singh, A. P., García, A., and Monsalve-Serrano, J. "Challenges and Opportunities for Application of Reactivity-Controlled Compression Ignition Combustion in Commercially Viable Transport Engines". In: *Progress in Energy and Combustion Science* 93 (2022), p. 101028. DOI: https://doi.org/10.1016/j.pecs.2022.101028.

[120] Karimi, M., Wang, X., Hamilton, J., Negnevitsky, M., and Lyden, S. "Status, challenges and opportunities of dual fuel hybrid approaches-a review". In: *International Journal of Hydrogen Energy* 46.70 (2021), pp. 34924–34957. DOI: https://doi.org/10.1016/j.ijhydene.2021.08.008.

Chapter 3

Experimental tools and methodologies

3.1 Introduction

In the following section, the reader will get into the methodology followed during this project to achieve the objectives set. First, a description of the experimental apparatus, accompanied by an explanation of the technique carried on. Later, the data processing approach is broken down into the steps taken for each technique. The methodology explained is not limited to only the theoretical part, but also, the initial steps and their results are also conveyed in this chapter. The measurements were main carried out at the CMT-Thermofluid Dynamics in the "Universitat Politècnica de València"

First, the general selection for the test conditions is presented with the motives behind them. Then, the experimental facilities and injectors are introduced with their specifications. The conditions need to be stable through a wide range of operating points, thus, the methods for regulating each condition is also explained.

The main experiments were divided into two campaigns, each complemented by additional techniques. First, the internal flow techniques are described and referenced, followed by a detailed explanation of the Phase Doppler Anemometry (PDA) technique. The internal flow techniques were employed to study the characteristics of the flow within the nozzle. These techniques provided crucial insights into the behavior of the spray. The PDA

technique was used to measure the size and velocity of droplets in the spray. This section explains the working principle of PDA and its application in the experiments. Finally, the steps followed in data processing for each technique are detailed, ensuring a comprehensive understanding of how the raw data was transformed into meaningful results.

3.2 Apparatus

3.2.1 Injection system

The fuel is supplied at a stable pressure, through the injection system formed by a low-pressure unit, a high-pressure unit, the common rail, and the injector.

The fuel is first filtered when sucked in by the low-pressure supply pump. Then, fuel pressure is elevated when it passes through a high-pressure pump powered by an electric motor. Then, it reaches a rail that is used to control the desired pressure by a valve that lets part of the fuel return to the deposit, not before going through a heat exchanger with water at ambient temperature to counter the temperature increase when the fuel is pressurized. From this rail, the fuel goes to a second rail to which the injector is connected. This last rail is used to dampen pressure surges coming from the pump, and it is here where a Kistler pressure sensor measures the target pressure.

The pressure control can be done by adjusting the electric motor rotation frequency and by regulating the closure of the valve at the first rail. The more the valve is closed, the less fuel is returned to the deposit and the pressure is increased. A diagram of this process is shown in Figure 3.1

3.2.2 Injectors

Two modern solenoid Continental fabricated multi-hole injectors were employed throughout the experimental campaign. They have similar geometry and different numbers of holes, with a top pressure of 350 bar. One injector acts as the primary reference for characterization, while the other is used for comparison and validation of identified patterns found by the phenomena of interest in this study. The main characteristics are shown in Table 3.1.

The main injector has a 6-hole nozzle labeled as **C3536** from here-forth, and the second is a 5-hole injector named as **C7532**. They possess a small deposit volume in the fuel inlet, which works as a “mini rail", helping to mitigate any remaining important changes in the injection pressure. Both were driven by a Solenoid Direct Injection Box (SDI) provided by the manufacturer with

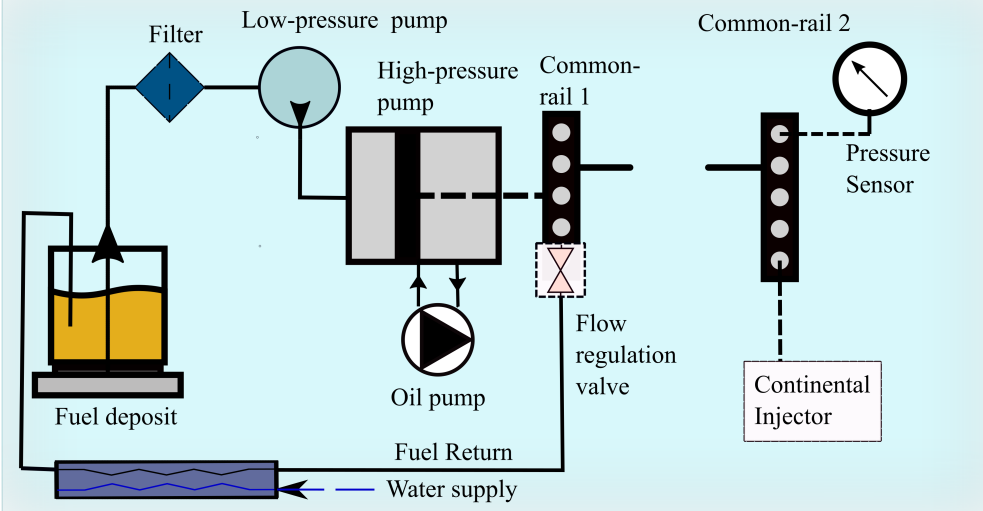


Figure 3.1: Schematic of the fuel delivery system

their preset current profile (See the bottom part of Figure 3.2), activated by a TTL signal input. The signal is comprised of a boost stage to aid needle lift and then a hold-off stage that controls injection duration. The C3639 injector exhibits a more pronounced and abrupt intensity for opening, while the C7532 injector demonstrates lower intensity. Furthermore, post the initial burst of current, the sustaining current for the C7532 injector is lower compared to the C3639 injector.

The diameters shown in the table were initially measured by an electronic microscope and later corroborated with tomographic images carried out at the Argonne National Laboratories facilities. These images will be later displayed in chapter 4

3.2.3 Test plan description

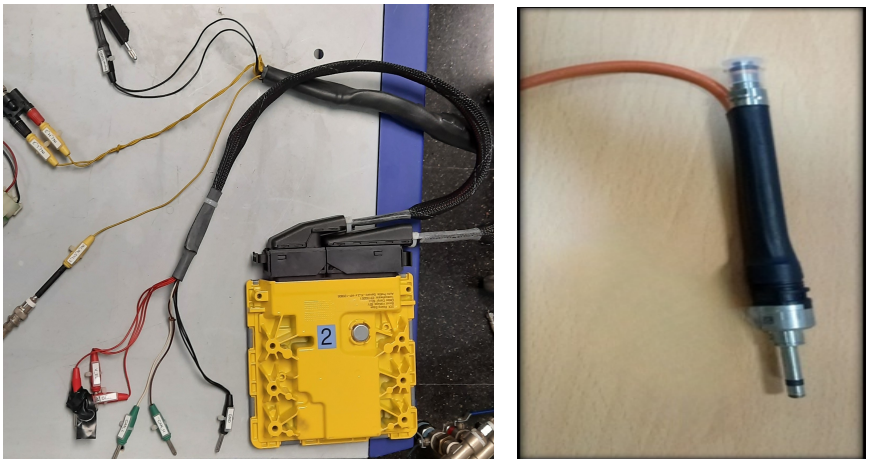
The test plan pursued was defined primarily by the operating conditions at which the injected jet is at known flash-boiling and spray-collapse conditions, the phenomena under study in this project. The selection was complemented by conditions that emulate those found in a real engine, ranging from cold start conditions, early injection, and normal functioning. They were chosen considering the Engine Combustion Network (ECN) [1] guidelines for gasoline injectors. The energizing time was chosen to set a similar hydraulic time as found in the other studies in the ECN.

The principal variables to be analyzed are:

Table 3.1: Injector properties.

Parameter	C7532	C3539	Units
Holes	5	6	-
Max. pressure	350	350	bar
Orifice diameter $\bar{Do}$	146	146	μm
Orifice length	400	400	μm
Spray angle	70	70	º
Orifice type	Cylindrical	Cylindrical	-
Spray shape	Circular	Circular	-

* Lengths of inner and outer diameters.



(a) Solenoid Direct Injection (SDI) driver. *(b) Continental injector*

Figure 3.2: Injector SDI driver (a) and Continental Injector (b)

a. (**The rail pressure $\mathbf{P}_{inj}$**), represents the pressure at which the fuel is injected. In chapter 2 the importance of this variable in the atomization process was stated; thus, analyzing to which extent this is affecting the process is of special interest. The maximum pressure that the injectors work at is 350, which was one important parameter to evaluate since it is more up to date with the current GDI engines. Besides a more commonly injection pressure value found throughout the literature was also employed [2, 3].

b. **The fuels** employed (refer to subsection 3.2.4).

c. **The ambient temperature $\mathbf{T}_{amb}$**, normally was at ambient conditions, as a dependent value to the pressure. However, when possible, it was also studied at 60 °C and 120 °C.

d. **The ambient pressure ($\mathbf{P}_{amb}$))**, which, together with T_{amb}, emulates the conditions found in an engine cylinder when the fuel is injected.

e. **The injector temperature ($\mathbf{T}_N$)**. This temperature is very similar to the fuel's, which is why it will sometimes be referenced as such in the document.

f. By combining the T_N and P_{amb}, the R_p coefficient can be calculated, which is a more convenient variable to compare in the flash boiling and spray collapse analysis.

Conducting a comprehensive parametric variation is impractical due to the exponential increase in time required. Therefore, the investigation focused on varying only the most impactful conditions across the entire test matrix. Accordingly, a reference injector and fuel were selected for analyzing the effect of classical variables such as P_{inj} and T_{amb}. The C3539 injector and IsoOctane fuel were the ones used for this aim.

The test matrix is divided into two experimental campaigns due to the limitations in the achievable conditions with each test rig. Regarding the *rate of injection measurements*, the main limitations are in the ambient temperature and back pressure variations, the latter can be only measured above ambient pressures due to the principles behind the technique, as it will be explained in section 3.3.1. For the *rate of momentum*, pressures in the vessel were set in a range of 0.2 bar up to 21 bar, which deepens the reach of the comparisons for flash boiling conditions. Injection temperatures for both techniques were ambient and 90 °C.

On the other hand, *the velocity and size measurements* were done in a specialized vessel for GDI measurements (more details in section 3.4 with the possibility to work at sub-atmospheric pressures and varying the ambient temperature as well. Here, for the PDA measurements being a point-wise measuring technique, a few extra dimensions are added to the test matrix, to include the measurement location. Two main approaches are pursued in this case: firstly, the classical approach in which the velocity is measured at different cross-sections radius of the spray. Second, measuring at the center of the injector for spray collapse conditions in order to get an insight of the droplets characteristics when this phenomenom is taking place.

The full table with the complete test matrix with the corresponding R_p for the measurements performed is presented in the Appendix A.

3.2.4 Fuels investigated

The influence of fuel properties on engine performance is a significant area of interest. Traditional gasoline, however, exhibits varying properties depending on its source and production process [4, 5]. To address this variability, standardized mixtures that emulate gasoline behavior are commonly employed in research. Typical commercial gasoline consists of a variety of hydrocarbons, predominantly alkanes, isoalkanes, and aromatics, with carbon chains ranging from C5 to C8 and some extending to C9-C10 hydrocarbon chains [5], which implies that surrogates of gasoline could have five to eight carbon atoms [6].

In this study, two representative gasoline surrogates were selected based on their distillation curves, which closely resemble those of commercial gasoline. The first surrogate, IsoOctane, is widely studied due to its octane number (crucial for knock resistance studies), which is comparable to that of commercial gasoline. This similarity is pertinent to combustion studies and simulations. However, IsoOctane does not fully replicate the volatility characteristics of gasoline. To address this limitation, Hexane was selected as it has a vapor pressure curve more akin to that of commercial gasoline.

Ethanol has garnered significant attention due to its renewable nature and potential to reduce greenhouse gas emissions compared to traditional gasoline. Previous studies have demonstrated Ethanol's favorable combustion properties, such as higher octane number and latent heat of vaporization, which contribute to improved engine efficiency and reduced knocking [7]. An additional advantage of this fuel selection is the broad range of superheating degrees covered, enabling the study of severe flash boiling conditions, as depicted in Figure 3.3. The Figure displays the liquid – vapor phase boundaries which were obtained from the NIST database Lemmon et al. [8] and represent the thermodynamic limits for each monocomponent, additionally, the diagram includes the vapor pressure curve for a commercial RON98 gasoline.

Table 3.2: Fuel Properties.

Fuel	Chelmical formula/Blend	Density [kg m^{-3}]	Viscosity [mPa s]	Boiling Point [°C]*
IsoOctane	C_8H_{18}	690.3	0.47	99.26
Hexane	C_6H_{14}	654.78	0.22775	68.71
Ethanol	C_2H_6O	789.1	1.074	78.35

* at ambient temperature.
For properties source [1, 8, 9].

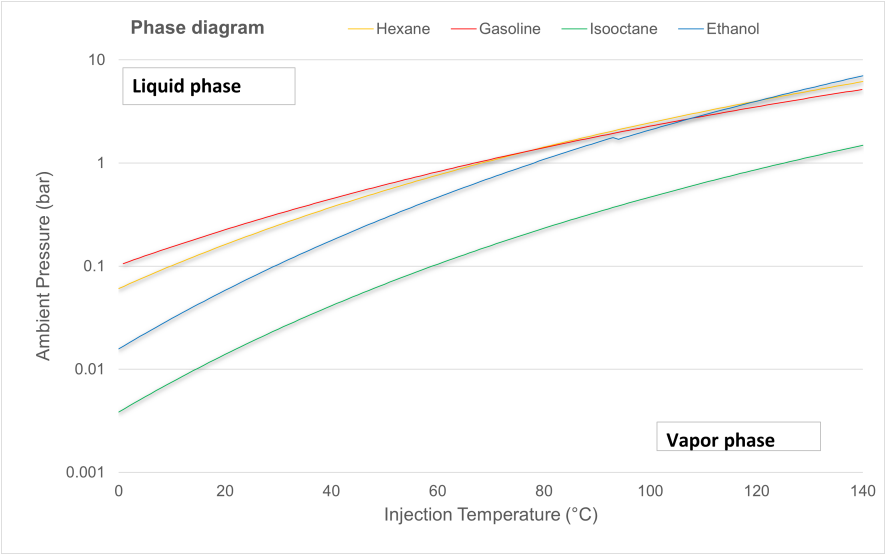


Figure 3.3: Phase diagram showing the phase curve and the most relevant measurement points across the different campaigns for each studied fuel and the typical commercial gasoline. Adapted from [10, 11] with data from the National Institute of Standards and Technology (NIST) [8].

3.3 Internal flow measurement techniques

3.3.1 Rate of injection

The rate of injection or injection rate is a measure of the variation of fuel delivery in time. It shows the mass injected in an engine per unit of time, which, in the context of precisely metering the fuel consumption in an engine, has become a vital variable to control in modern GDI technologies [**1**].

The technique is based on the pressure wave propagation in a liquid tube theory and it has been long used for Diesel injectors and adapted to GDI injectors in recent works [**3**, **4**, 12].

The instrument used in this project is an Injection Rate Discharge Curve Indicator (IRDCI) from IAV shown in Figure 3.4 [13]. The Figure shows a simplified cross-section of the instrument with two main zones divided by a piston.

Measurement principle

Starting from a pressure wave generated by an injection event in the IRDCI, the working principle of the device is explained through the wave trajectory

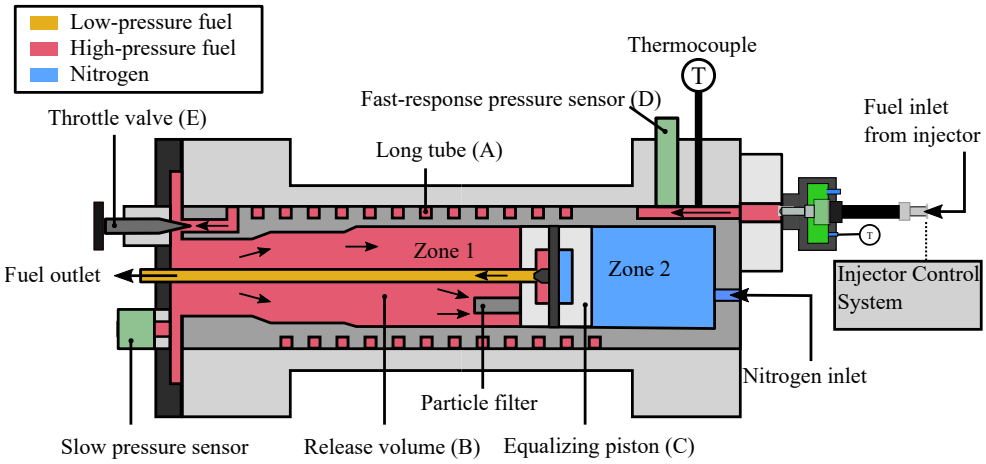


Figure 3.4: Injection Rate Discharge Curve Indicator schematic diagram. Adapted from [14]

in Figure 3.4 as follows:

The wave travels at the speed of sound, a known distance, through the long tube (A) that goes around the device up to the release volume (Zone 1), where it is damped. The pressure inside the instrument can be adjusted by using nitrogen at the desired discharge pressure, also called back-pressure (P*back*), which acts on one side (zone 2) of the equalizing piston. After the nitrogen pressure is set and it reaches an equilibrium with the fuel side, the fuel enters through the particle filter into the equalizing piston (C). The equilibrium is broken at every new injection, and the excess fuel equivalent to the fuel injected is let out through a cavity in the interstice between the two volumes. The pressure that can be set in this instrument ranges from 2 bar up to 100 bar. Setting the equipment at lower pressures is not viable since there must be a certain counter-pressure in the nitrogen (Zone 2) actuating on the equalizing piston.

For the math behind the calculations, consider a simple pressure wave traveling in a cylindrical control volume of a known cross-sectional area A_t. The momentum conservation equation, neglecting the effect of gravity, is:

$$(p_{cv} + \Delta p)\, A_t - p_{cv} \cdot A_t = \rho_f \cdot A_t \cdot a_f \cdot \Delta u_f \tag{3.1}$$

Where p_{cv} is the pressure in the control volume, Δp is the pressure difference induced by the wave, ρ_f is the density of the fuel, a_f is the speed of

sound in the fuel, and Δu_f is the variation of fuel flow velocity in the section. Solving this equation for Δp, it is simplified to:

$$\Delta p = \rho_f \cdot a_f \cdot \Delta u_f \tag{3.2}$$

The pressure variation provoked by every injection event is captured by a fast-response pressure sensor (D). The sensor must be close to the injector since the opposite would affect the signal due to it being attenuated by friction losses. In the IRDCI, the sensor is fixed, and the injector tip is inserted until a certain distance is provided by the manufacturer. The device must be tuned for the experiment in order to capture only one wave signal. The reason behind this is that when the wave exits the long tube with a relatively small diameter and enters the release volume with a bigger one, this difference induces a reflection wave that travels upstream the long tube back to the sensor. This tuning is done by the throttle valve (E) to change the cross-sectional flow area near the release volume. Besides, because of the long-tube distance, the signals are temporally divided.

Finally, the continuity equation links the pressure change induced by the wave to the mass flow rate.

$$\dot{m}(t) = \rho_f \cdot A_c \cdot \Delta u_f \tag{3.3}$$

Lastly, solving for Δu_f with the Equation 3.2 and Equation 3.3, the mass flow rate is defined as:

$$\dot{m}(t) = \frac{A_c \Delta p}{a_f} \tag{3.4}$$

Accounting for uncertainties

With the Equation 3.4 the instantaneous rate of injection signal is determined. However, the fuel added with each injection event increases as the measurement is performed, creating an artifact of continuous signal increase. This is an accumulation phenomenon that occurs when measuring with IRDCI. As other works have reported[10, 12, 14], the signal treatment published by Payri et al. [15] is implemented to correct the raw signal in the post-processing.

On the other hand, the speed of sound changes with the medium in which the wave travels. It highly depends on its composition, pressure, and temperature. Since the speed of sound is not always calculated in the same conditions as the experiment, and due to cycle-to-cycle and temperature variations in

the IRDCI, and other uncertainties, the integral of the injection rate (mass injected) might slightly differ from the mass measured by the scale. To correct this, a scaling factor can be applied to the signal [14, 16, 17]. This factor is determined by the ratio of the mass measured at the exit of the IRDCI divided by the integrated mass.

$$K_{factor} = \frac{m_{balance}}{m_{int}} \tag{3.5}$$

Summarizing this theory, some considerations must be taken into account to understand the working of the device:

- The calculation is made for a simple pressure wave in a steady flow Equation 3.2.
- The pressure variation caused by the pressure wave is related to the liquid flow velocity.
- From this signal, the instantaneous mass flow rate is determined.
- The signal must be corrected to account for uncertainties Equation 3.5, thus, each injection mass must be measured at the exit of the IRDCI.

ROI measurement setup and process

As depicted in the Figure 3.5, the injector is fixed to the IRDCI through the jacket holder designed with accesses through which a continuous coolant flow passes to maintain the nozzle at the desired temperature. Once the injector is electronically actuated, the spray goes to the vessel, generating pressure waves.

The injector temperature control was done by a thermoregulator unit that used ethylene glycol at 30 %, pumped at a rate of up to 60 L min^{-1}, heated by a 6 kW unit, and cooled down by a separate glycol supply system.

The fuel that goes out of the IRDCI is collected on a gravimetric scale to measure the mass per injection. Since every time the operating condition changes, the amount of mass injected also changes; the mass value registered is a moving average accounting for the number of injections in 100 seconds, which corresponds to a period of time in which the injected mass average stabilizes. Then, the mass flow rate measurements are recorded.

The IRDCI measures the temperature in the fuel zone with a thermocouple and pressure in the nitrogen zone. A digital oscilloscope displays these values

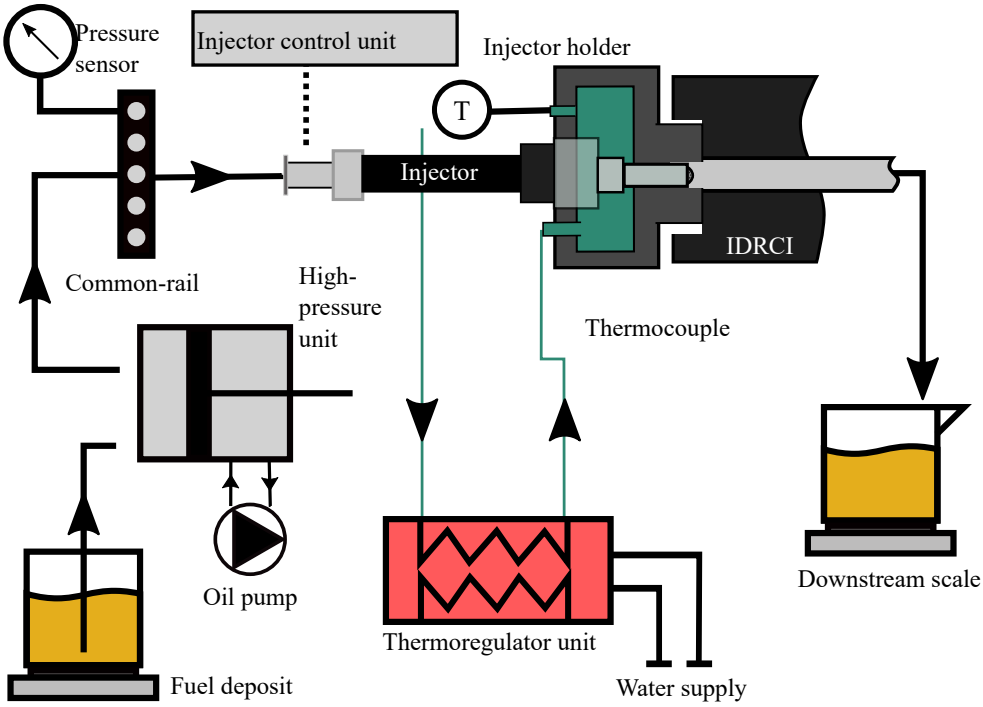


Figure 3.5: Rate of Injection measurement set-up.

and records the rate of injection, instantaneous rail pressure, and driving voltage signals for a total of 50 injections per test point at 1 Hz, and then transfers the data to the computer. The fuels' speed of sound data published in the NIST webbook [18] was used for the measurement processing. The octane data was used for iso-octane (2,2,4 - Trimethylpentane) since there was none available in the literature for the latter.

3.3.2 Rate of momentum (ROM)

Gimeno [16] presented an experimental facility to obtain a quantitative measurement of the momentum flux or rate of momentum (ROM) in a spray for a Diesel injector under realistic ambient pressure conditions. This work also introduced a new methodology for analyzing the flow right at the orifice exit, combining the ROM results with the rate of injection. This was later expanded and analyzed in detail for GDI injector by Vaquerizo [19].

The technique employed in this facility is sometimes referenced as the force method [20, 21] since it consists of placing a piezoelectric sensor in front of the spray so that when the jet hits the sensor, it outs perpendicularly to it.

According to the conservation of momentum law, the force measured will be equivalent to the total momentum of the spray.

Principle:
A simple explanation of the reasoning behind this equivalence is brought next, and more information can be found in [16, 19, 22–24]. Consider the injected spray colliding with the sensor. If a cylindrical control volume (CV) as described in Figure 3.6 between the orifice exit and the sensor surface is drawn, the momentum conservation equation can be expressed as Equation 3.6, after making the following assumptions for simplicity (Gimeno [16] explains the extended equation).

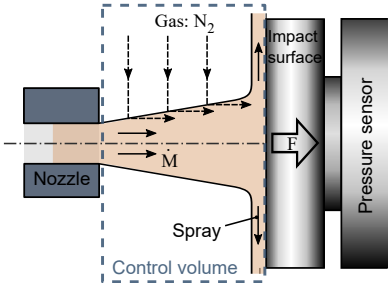


Figure 3.6: Rate of momentum measurement basis [14, 16].

- Gravity forces on the CV are negligible in comparison to other forces acting.
- The ambient pressure in the vessel is uniform. Thus, the forces acting on the CV due to pressure will be simplified to only the one with effect on the sensor.
- The spray axis is perpendicular to the sensor surface.
- The flow direction of both The nitrogen entering the CV, and the fuel exiting it after impacting the collision are perpendicular to the spray axis. Therefore, their axial component of momentum flux and the viscous stress in the axial direction are null.

$$F = \frac{\partial}{\partial t} \int_{CV} \rho \, u \, d\varpi + \dot{M} \tag{3.6}$$

Where F corresponds to the generated force by the impact with the sensor. ρ and u are the local density and velocity of the mixture moving across the

CV, ϖ is the CV surface, and finally, $\dot{M}$ represents the momentum flux at the orifice exit (perdicular to the orifice exit surface). The first term on the right side of the equation defines the momentum variations within the CV; consequently, the Equation 3.6 can be simplified for steady-state conditions as:

$$F = \dot{M} \tag{3.7}$$

Besides the assumptions made, the methodology also proves that the gas density and distance variation will not affect the momentum flux measurement: firstly, the gas density would only impact the transitory part of the injection; however, for long injections this would not represent a problem. Second, the distance between the orifice outlet and the sensor surface as long as the surface is big enough to capture all the spray and deviate it perpendicular to its axis.

3.3.3 Hydraulic analysis

The internal flow characterization plays a vital role in describing the flow and is key to precisely adjusting the time the fuel is injected. One great advantage of measuring mass flow rate and momentum rate is that when combined, they indirectly characterize the internal flow in the injector; moreover, these variables determine the amount of energy carried by the fuel jet [16]. Essentially, with these two parameters, it is possible to calculate the effective velocity (u_{ef}) at which the flow is moving through an effective area (A_{ef}). These are two parameters that describe a simplified version of the flow at the orifice outlet.

The actual jet's flow exiting the orifice is defined by the velocity profile and the density of the fluid as the scenario depicted in Figure 3.7(a). However, the profile is unknown, and several phenomena could occur simultaneously, such as hydraulic flip, cavitation, among others, which results in the flow not occupying the full geometric area. Then, the second scenario presents a flow passing through a reduced area with a uniform effective velocity.

From this point of view, the definition of the mass flow rate Equation 3.8 and momentum Equation 3.9 equations can be expressed as:

$$\dot{m} = \int_{A_0} u\rho dA = A\rho_f u \tag{3.8}$$

$$\dot{M} = \int_{A_0} u^2\rho dA = A_{ef}\rho_f u_{ef}^2 \tag{3.9}$$

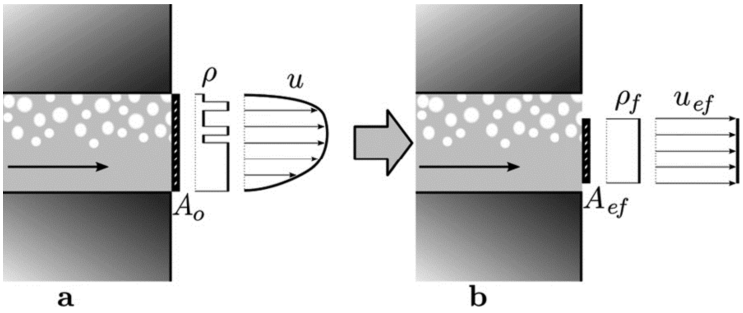


Figure 3.7: Schematic representation of the flow exiting the nozzle orifice. (a) shows how it would look in reality (b) the effective area and velocity. [16].

In these equations, $\dot{m}$ is the ROI, A_0 is the geometric exit area of the orifices, ρ_f is the density of the fuel, u represents the velocity at the exit, and $\dot{M}$ is the rate of momentum. Since the ROI and $\dot{M}$ are measured, thence, known values, the equations for velocity and area can be solved.

$$A_{\text{eff}} = \frac{\dot{m}_f^2}{\rho_f M_f} \tag{3.10}$$

$$u_{\text{eff}} = \frac{\dot{M}_f}{\dot{m}_f} \tag{3.11}$$

The comparison of these results with theoretical similes defines non-dimensional coefficients to characterize the injectors at different conditions [12, 22, 24]. Starting with the velocity coefficient (C_v), which compares the effective velocity with the maximum attainable velocity in the flow.

That velocity is calculated by applying the Bernoulli equation (Equation 3.12) to the geometry, given by a pressure drop (ΔP) between the inlet and outlet of the nozzle.

$$uth = \sqrt{2 * \Delta P / \rho_f} \tag{3.12}$$

$$C_v = \frac{u_{ef}}{u_{th}} \tag{3.13}$$

Similarly, the area coefficient defines the losses in area (probably due to the non-uniformity of the velocity profile).

$$C_a = \frac{A_{\text{eff}}}{A_0} = \frac{D_{\text{eff}}^2}{D_0^2} \tag{3.14}$$

Following, comparing the theoretical definition of the mass flow rate and momentum flux (center of Equation 3.8 and Equation 3.9) with the actual values, defines the discharge (C_d) and momentum (C_M) coefficient respectively:

$$C_d = \frac{\dot{m}}{A\rho_f u} \tag{3.15}$$

$$C_M = \frac{\dot{M}}{u_{\text{th}}^2 \rho_f A_0} = \frac{\dot{M}}{2A_0 \Delta P} \tag{3.16}$$

Lastly, by operating with the coefficients, the area coefficient (C_a) can also be calculated from the (C_d) and (C_v), Equation 3.14.

$$C_a = \frac{C_d}{C_v} \tag{3.17}$$

3.3.4 ROM measurement procedure

The fuel is delivered to the momentum flux vessel in the same way as expressed in section 3.3.1. The injector is also fixed to the vessel through a jacket holder designed for this test rig with accesses through which ethylene glycol keeps the nozzle at the desired temperature. The schematic Figure 3.8 depicts the set-up.

A digital oscilloscope captures the electrical signal generated in a piezoelectric sensor by the impact of the spray with a flat surface (the "target") placed in the sensor and orthogonal to the injector axis. The electrical signal contains the temporal variation of the force generated by the impact; thus, it is equivalent to the rate of momentum created by the injection event. The valves' operation to regulate the vessel's nitrogen flow controls the test rig's ambient pressure.

The methodology was initially developed for Diesel injectors, in which spray jets can be easily isolated; however, this task is more challenging for GDI injectors with multiple sprays. Payri et al. [22] analyzed two configurations using this method with an 8-hole injector, observing an important influence of other sprays in the measurement of an individual one; thus, they concluded that the most accurate method in this type of injector is using a frontal configuration with all the jets impacting the target. On the other hand, the plume-to-plume interaction plays a vital role in GDI sprays, something that would be ignored when trying to capture an individual jet. Accordingly, the methodology followed in the present work is a frontal configuration for the

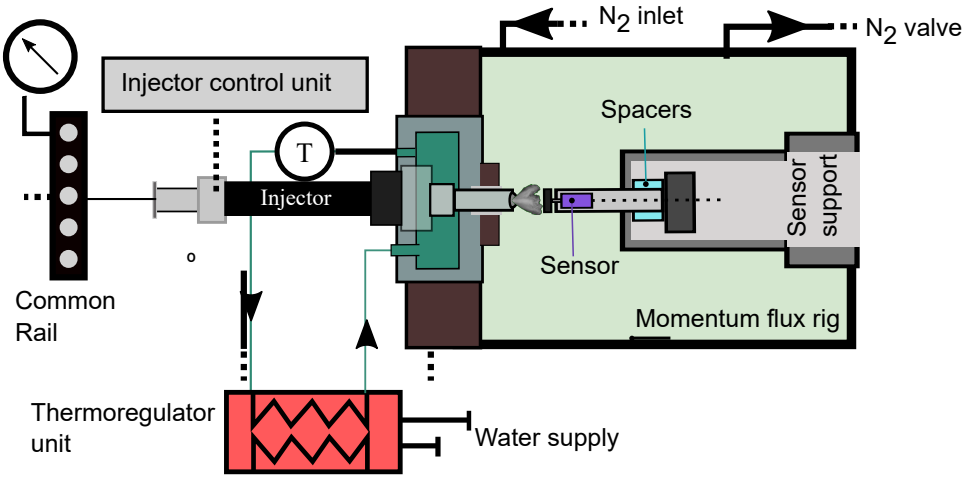


Figure 3.8: Momentum flux vessel based on Gimeno [16] work.

global momentum, with all the sprays impacting a 10 mm diameter sensor target depicted on Figure 3.9.

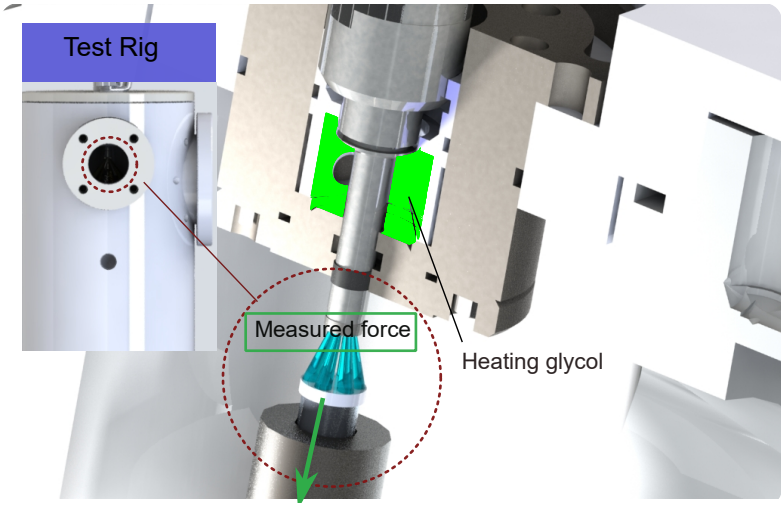


Figure 3.9: Force sensor and sprays impact.

3.3.5 Rate of momentum correction for multi-sprays

As seen, the force is measured in the sensor axis direction, which, from the sprays' point of view, only a component of the momentum is measured. To

account for this angle, the momentum signal is corrected by means of Equation 3.18 [25].

$$M_c = \sum_{i=1}^{n} \frac{M_m/n}{\cos \alpha_i} \tag{3.18}$$

M_m is the total momentum measured, n is the number of orifices impacting the sensor, and α_i is the angle of each core jet with respect to the sensor surface. Each spray is assumed to have the same contribution to the total momentum. Based on the Equation 3.18, this characterization requires knowing the spray's inclination angle in reference to the injector axis. Usually, the orifice drill angle can be inspected or reported by the manufacturer; however, it usually differs from the actual plume angle. In that sense, Shahangian et al. [25] used a plastic deformation technique to determine these angles. The basis of this technique is adapted to this aim into a paper pinch technique.

The fuel is injected onto graph paper and placed over a flat surface in front of the nozzle tip. The same parts used for the measurement setup are employed for this objective. On average, 30 injections are done until the jets penetrate the paper. With the known separation between the nozzle tip and the paper position, the approximate angle of the spray cores can be calculated using trigonometry and an internally developed code. Later, axially moving the paper's position at known steps, the coordinates of the points can be mapped along the axis to assess the variation along the axis.

3.4 GDI test rig

3.4.1 GDI test rig vessel

The facility employed to simulate the target operating conditions explained in section 3.2 consists of a heater module and a body with optical access for cameras and lasers. It has been employed in several experimental campaigns related to GDI investigations at the CMT research center. It was first used in the [19] thesis; later, it underwent several adaptations in the [10] work where more detailed specifications can be found, and finally, some parts were built for this thesis.

The components are made of AISI 1042 carbon steel. The body of the vessel (top part) has three optical accesses of 140 mm (180 mm without the optical windows mounted) and a dummy window where the control sensors and a safety valve are located. The optical windows are built in fused quartz

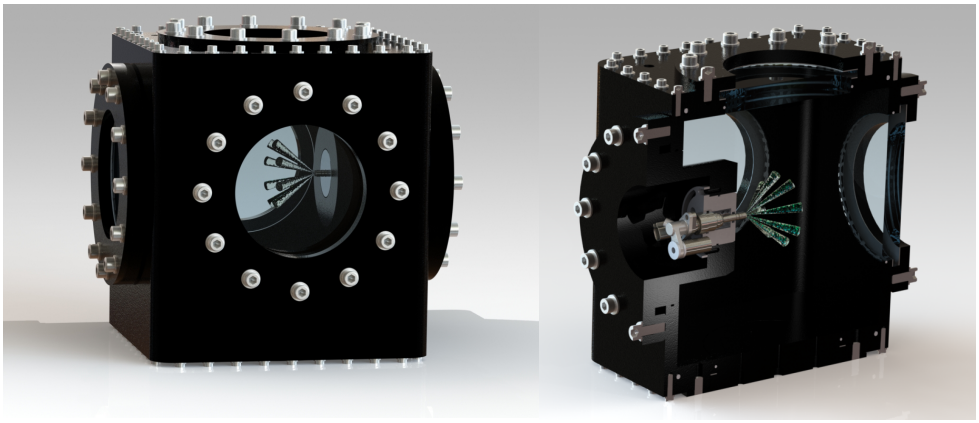


Figure 3.10: GDI visualization test rig. [10]

with a unique polish that improves transparency, which allows the employment of laser optical techniques, with a considerably wide field of view of the measurement zone.

The temperature is controlled by the continuous flow of a gas through the whole vessel. The flow starts in the heater module, which is comprised of a resistor that increases the temperature of the gas and its housing, as well as an air diffuser located at the bottom of the vessel body. The heated gas then goes to the measurement volume and is let out through a valve located at the dummy window.

3.4.2 New resistor units

Since one of the main targets is to study the flash boiling occurring during GDI engine operation, as it can occur with early injection strategies, sub-atmospheric pressures are a requirement for the fuels studied.

At low ambient pressure, the limited air mass in the vessel constrains heat transfer, making it more difficult to achieve maximum temperature. In the Bautista Rodríguez [10] configuration, temperatures only reached up to 90 degrees Celsius; besides, setting high temperatures at low pressure was time-consuming due to the required equilibrium time. To address this issue, three additional resistor units with ceramic insulation walls were installed inside the chamber (refer to Figure 3.11). This modification allowed reaching higher temperatures under both high and low-pressure conditions, reducing heat losses and decreasing the time required for measurements at high temperatures. On average, the heating time was halved for extreme conditions.

To sum up, the visualization test rig controls and monitors the ambient pressure and temperature. The values that it covers are:

- The ambient pressure ranges from 0.2 bar (200 mbar) to 15 bar (absolute pressure).
- After the inclusion of new resistor units, the ambient temperature can reach up to 200 $°C$.
- It has wide optical accesses for cameras and lasers

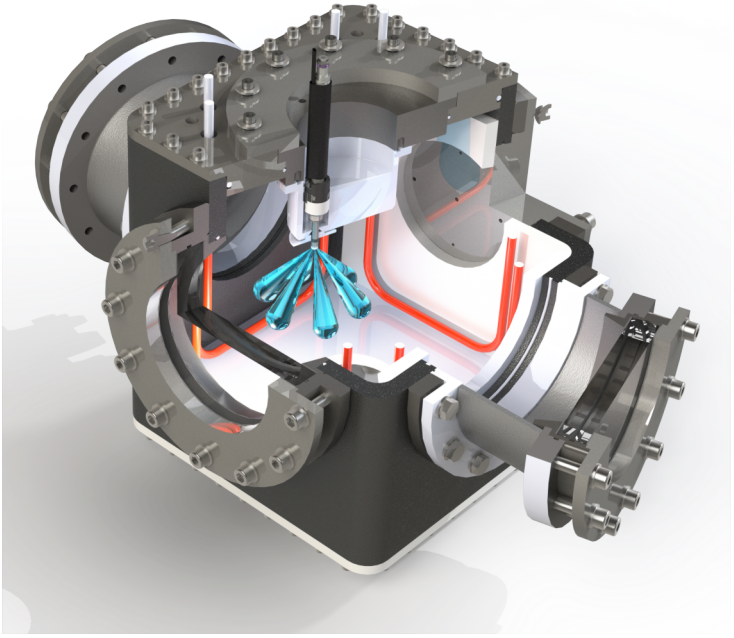


Figure 3.11: Final display of the experimental facility.

3.5 Spray visualization technique

Optical techniques are a powerful tool for non-intrusively studying high-speed flow and experimentally measuring variables of interest. They have been used to gather information with high temporal resolution on projected fuel mass, soot concentration, temperature distribution, and spray vapor and liquid morphology characteristics [10, 26–28].

In recent years, the diffused back illumination (DBI) technique has become the trend for line-of-sight liquid spray visualization, which requires having two optical aligned accesses. For this experimental campaign, only one window was available due to the simultaneous setup with the PDA equipment occupying two of the windows. Hamzah et al. [29] compared the liquid length in flashing sprays through the DBI and MIE technique, noticing that liquid penetration can be highly dependent on the setup, yet the qualitative assessments were similar for both. In this sense, although the MIE scattering technique is more difficult to set, it is a more suitable technique for this experiment for both the optical access constraint and its implementation on the spray-laser alignment for the PDA technique. Additionally, it still allows for the qualitative evaluation of the spray shape.

3.5.1 MIE scattering

The Mie-scattering (MIE) optical phenomenon refers to the elastic scattering of light from particles whose diameter is larger than the wavelength of the incident light. This phenomenon can be used in liquid spray investigation when the liquid droplets of the spray reflect the incident light [30], and a high-speed camera then captures them. The MIE setup employed in the experimental campaign is displayed in Figure 3.12 and is similar to the one used in [31].

Two white LED units equipped with a parabolic reflector to reduce the light aperture angle from 120°to 50°were used as the illumination source. The camera was aligned with the spray, with the two LEDs being symmetric to the camera axis. The vessel dummy window that acts as the background was painted with a special black paint that minimizes the reflected light, which enhances the contrast between the scattered light by the spray and the vessel wall in the background when collected by the spray for appropriate processing.

The main characteristics of the equipment employed are shown in Table 3.3. The parameters were selected as a trade-off for the maximum record velocity allowed for capturing images with a minimum of 7 px/mm of resolution in which the full evolution of the spray is seen. The exposure time is also a function of the scattering coming from the jet and the time the sensor collects this light. The more intense the scattered light is, the lower the exposure time can be. Also, the sensor quality and camera technology play a role in the set-up.

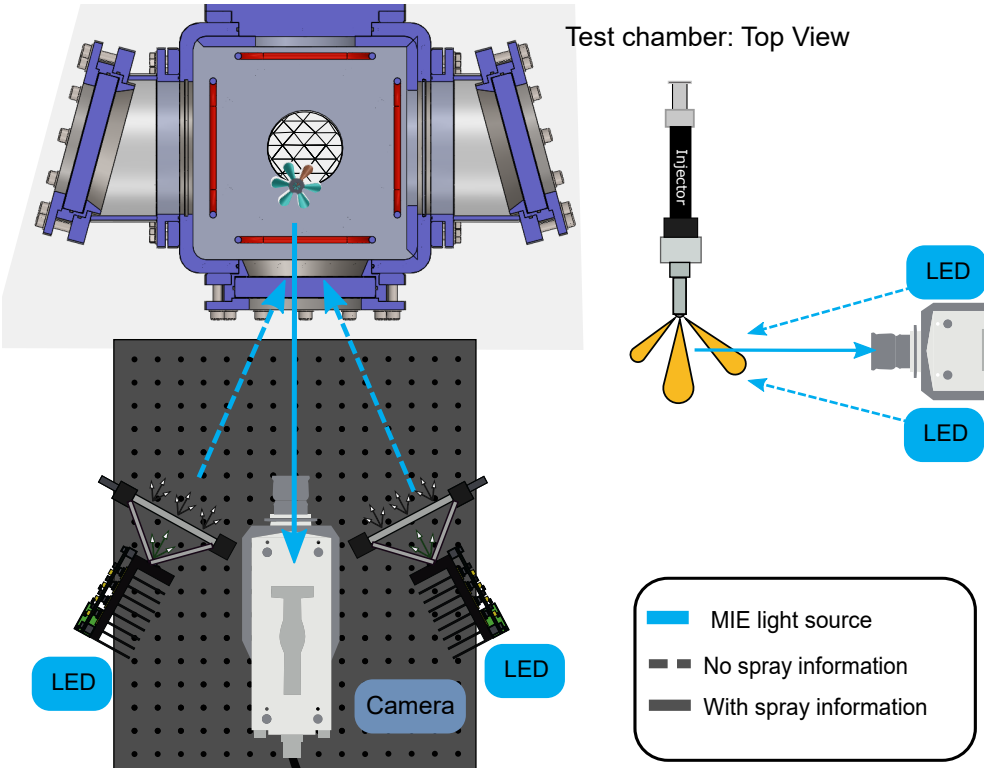


Figure 3.12: MIE setup configuration

3.6 Spray image processing

A video is composed of several images (frames), and the collection of images contains the evolution of the spray over time. Each image has information on the spray for a particular instant. The camera captures a gray-scale image,

Table 3.3: Summary of the configuration parameters for the high-speed camera.

Parameter	**Phantom V12**
Camera lens	Zeiss 70 mm f/2
Frame rate (fps)	21000
Exposure (µs)	12
Field of view (pixels)	512x512
Pixel-mm	7.1

which is read by the computer as an m-by-n array, with the pixel intensity represented as the cell value. For color images, another dimension is added to the array [32].

The image processing approach is based on image segmentation by threshold. There are four main steps to process each frame: image masking, image preparation, image binarization and filtering, and contour analysis (fully depicted in Figure 3.13). For processing the set of videos an in-house developed MATLAB routine [14, 33, 34] was implemented.

3.6.1 Image masking

One essential step in any visualization processing is the image treatment. In this stage, one aims to prepare the image for standardized processing. The gray-scale intensities from black to white displayed in the image matrix go from 0 to $2^{BitDepth}$, which, for a 12-bit image, the maximum dynamic range of a frame goes from 0 (black) to 4095 (white).

The first action taken for the image segmentation is a normalization of the pixel intensities, so the values are then in a range of 0 - 1. The normalized frame is **masked** by selecting the overall zone where the spray will be, discarding other areas such as the injector holder, windows' limits, etc. The mask is a zero-filled matrix with the same dimensions as the image, and the region of interest is represented by cells with one value. The mask matrix construction is calculated using polar coordinates with the origin of the nozzle tip and a certain angle as input. Finally, the mask is element-to-element multiplicated with the normalized frame.

3.6.2 Image preparation

Consider the video of an injection event that starts with a very dark image of the back dummy window wall of the vessel, and for the time the spray is seen, a few frames have passed. Each new image containing spray is then a composition of background and spray. To separate each frame into what is spray and what part is not, **the background is subtracted** by utilizing the Equation 3.19 where I_0 is the image of the background before the injection event, and I is the analyzed image containing the spray. The average of the first 8 frames is used for the background.

$$I = I - I_0 \tag{3.19}$$

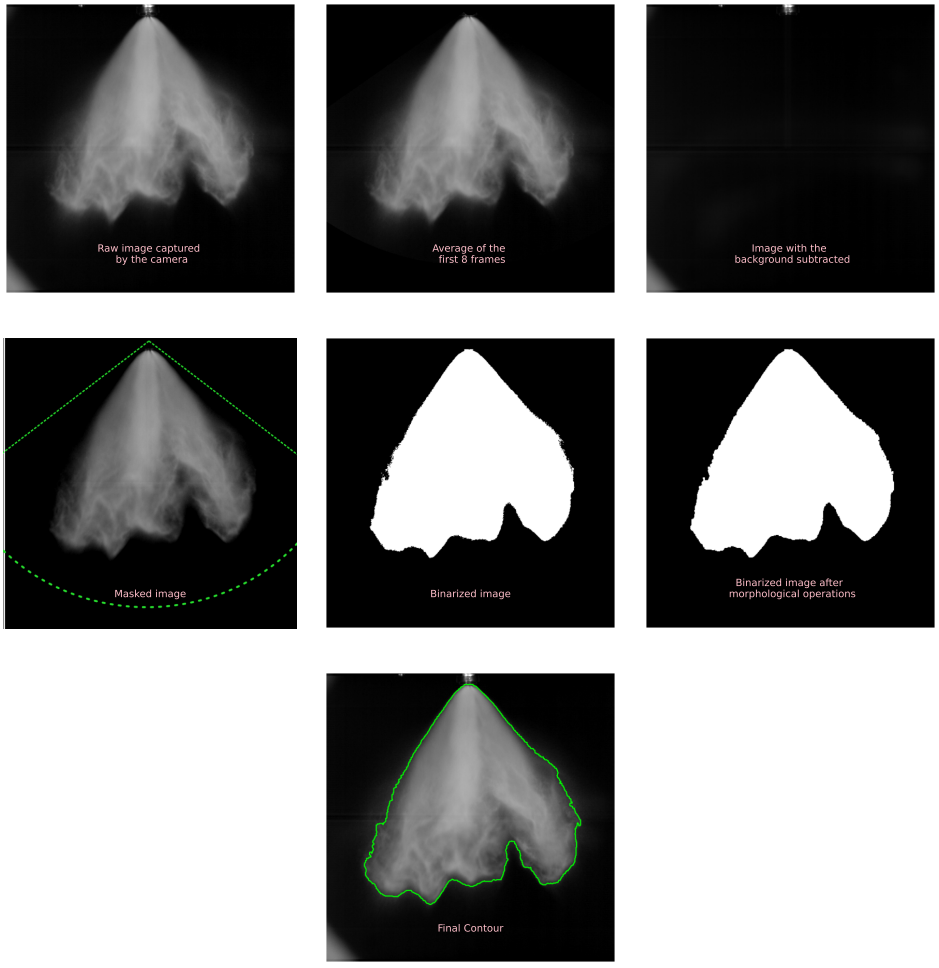


Figure 3.13: Image processing steps. The frames shown are at 635 μs after SOI, for the C3539 injector with a rail pressure of 200 bar a chamber pressure of 6 bar and temperature of 60 $^\circ C$ and nozzle temperature of 90 $^\circ C$. The fuel is Ethanol.

3.6.3 Image binarization

Later, **the spray contour is differentiated** applies an intensity level threshold for image binarization to fit better the contrast between background/spray and kept constant for the whole experimental campaign once defined. The pixels whose values are below the fixed threshold are set to zero, and the others are set to 1, which is the spray. A good initial value for the threshold is found using the OTSU method [35] , and then tuned after several iterations.

Lastly, the image is filtered through morphological image operations to account for misidentified background regions as spray [36, 37]. The operations consist of the removal of small pixel islands by performing an adapted image opening strategy. First, a connectivity criterion is used in a two-stage image erosion strategy; following, all the isolated pixel areas that are below a minimum pixel count are removed, and finally, the image is double dilated.

Now, the contour is determined as the coordinates of the pixels in the boundary between the black and white regions.

3.6.4 Contour Analysis

The metrics extraction is done over the contour detected. There are several parameters that characterize a spray. Classical variables have been the spray penetration and spreading angle. However, they have proven to fail in fully describing the spray morphology under collapse conditions [38–40]. When comparing GDI sprays under a wide range of conditions, the abrupt change in the spray shape allows for identifying different degrees of collapse.

For instance, an image depicting the contour differentiated after the aforementioned steps is shown in Figure 3.14 where two spray patterns can be distinguished. The spray on the left can be approximated to a triangle; and to the right, there is a collapse induced by the flash boiling of the spray, with a more rounded and asymmetrical shape. Due to this asymmetry, it is very difficult to compare classical parameters like the angle among conditions. The variation in the values will deeply vary with the approach taken for their calculation.

For this reason, the spray width is also calculated for each time step (frame) at a fixed distance from the nozzle tip. The value is the distance between the left and right contour limit. This parameter has been shown to be a more precise metric to characterize the spray than the spray angle.

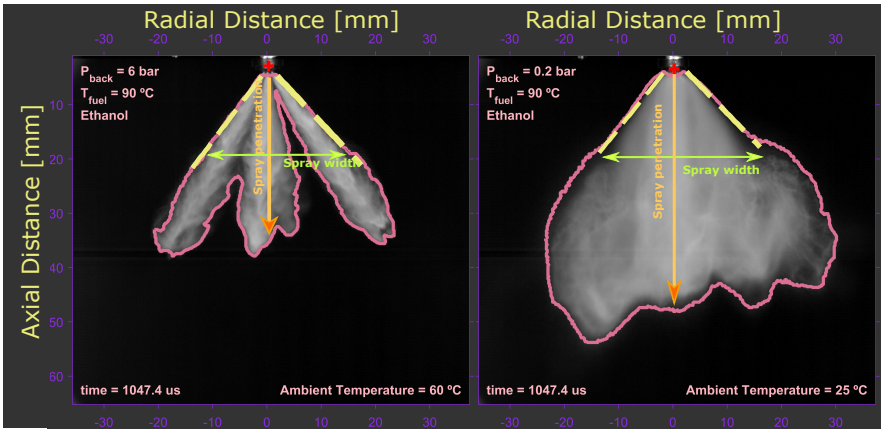


Figure 3.14: Macroscopic spray parameters extracted from the contour analysis. Two structures are seen for non-collapsing (left) and collapse sprays. The conditions are depicted on the image.

Averaging criterion

The spray width was calculated for the ten videos recorded for each operating condition. A moving average was applied to all repetitions to obtain a representative value for the calculated parameter per time step per condition[37, 41], and evaluate the shot-to-shot variability. Thus, for a time instant t_i, the correspondent value of the variable being averaged $f(t_i)$, was computed with the linear regression $f(t) = k_1 t + k_2$. The fitting constants k_1 and k_2 were calculated by solving the regression for t and $f(t)$ consisting of all the data contained in the time interval $t_i \pm \Delta t$, with Δt =150 µs. Subsequently, the average value $\bar{f}$ was estimated by evaluating t_i in the regression previously found. This process was repeated for each time-step up to the end of injection.

3.7 Phase Doppler Anemometry (PDA) technique

The following sections present a Phase Doppler Particle Analyzer (PDPA) equipment recently acquired from Dantec by the research center. The analyze the setup process and the impact of various parameters and characteristics on the measurement results are analyzed so it serves as a general guide for future measurements in the research center. The PDPA technique is highly sensitive to several variables within the test chamber and the setup itself. This analysis covers the effects of physical variables in the test chamber, the setup parameters, and the specific characteristics that influence the measurement outcomes, including scattering angle, laser focal length, and processor parameters, etc.

3.7.1 PDA measurement technique

The Phase Doppler Anemometry (PDA) technique is a widely employed optical technique in various fields [42–45] for simultaneously measuring the size and velocity of spherical particles in a fluid flow. It is a powerful tool for non-intrusive investigations of sprays. This technique is well described in the literature, and its basis is well established [46–48].

The principle derives from the Laser Doppler Anemometry (LDA) technique. It consists of analyzing the frequency shift of light scattered by a particle flowing through a volume created by at least two crossing laser beams.

Initially, the LDA technique was developed thanks to the spatial and temporal coherence that the gas laser has and employing the Doppler effect concept, which is the change in frequency of a wave in relation to an observer who is moving relative to the source of the wave.

To theoritically understand the basics of the technique, when an incoming light interacts with a particle moving at a certain velocity, the particle will scatter the light; the observer, in this case a receiver, detects the scattered light at a frequency that differs from the original due to a Doppler shift induced by the particle's motion.

In this context, the moving particle is acting as a moving transmitter; however, in practice, this frequency can be measured only with special interferometers and only for very high velocities. If, instead, two laser beams originating from the same laser impact the moving particle, light scattered from both will reach the receiver with slightly different frequencies due to the variation in the reaching angle. Additionally, when light from two sources with close frequencies overlap, their electric fields can interfere constructively and destructively depending on the relative phase difference [49]. The interference pattern leads to a periodic variation in the overall light intensity in the cross-section. The rate of this variation creates a beating effect in terms of intensity, analogous to a beat frequency.

This frequency, also called Doppler frequency, between the two light sources can be represented in the Equation 3.20.

$$f_D = f_{s,2} - f_{s,1} = \frac{2u_x \sin(\theta/2)}{\lambda} \tag{3.20}$$

The equation shown results from the difference in the frequency of both incoming source ($f_{s,1}$ and $f_{s,2}$) lights. With θ as the angle between both laser beams. u_x is the velocity in the direction of the movement (x). λ is the light

wavelength. The steps used to obtain the last equation can be found in the literature.

As seen, the Doppler frequency is directly proportional to the x-component of the particle velocity, with it finally being calculated as:

$$u_x = \frac{\lambda}{2\sin(\theta/2)} f_D \tag{3.21}$$

For a visual understanding of the phenomenon, the intersection of the laser beams, which must occur at their beam waists where the wavefronts are approximately planar and stationary due to the lasers' coherence, produces parallel planes of intermittent high-low light intensity. These are known as interference planes or fringes, oriented normal to the x-axis. Consequently, the light scattered by a moving particle varies with a frequency proportional to u_x. This fringe model depicted in Figure 3.15 helps understanding the phenomena and the further quantification of it. Beam alignment then plays an important role in order to obtain an equal separation between fringes.

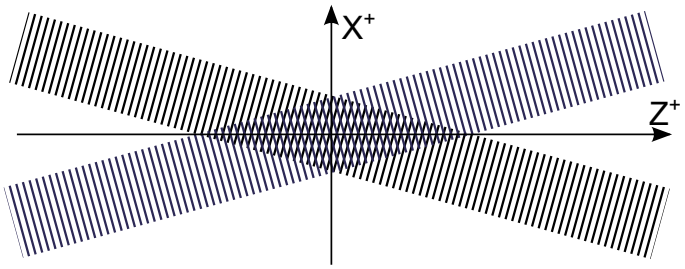


Figure 3.15: Fringe model of crossing beams.

When the particle traverses the fringes, the scattered light fluctuates in intensity with a frequency equal to the velocity of the particle divided by the fringe spacing. The scattered light is captured by the receiver which is composed by a photo-detector that transform the light intensity received into a current pulse that contains the information related to the particle velocity and noise coming primarily from the photo-detection shot noise.

Figure 3.16 shows a representation of the burst signal detected when a droplet/particle crosses the measurement volume. The shape seen in the center is owed to the normal energy distribution in the laser beams, having a higher energy in the center of the volume than that at the edges. The signal is composed by a low frequency called pedestal and the high frequency contain-

ing the Doppler signal. This low frequency is removed to get the actual Burst signal. The burst period is then used to calculate the Doppler frequency (f_D).

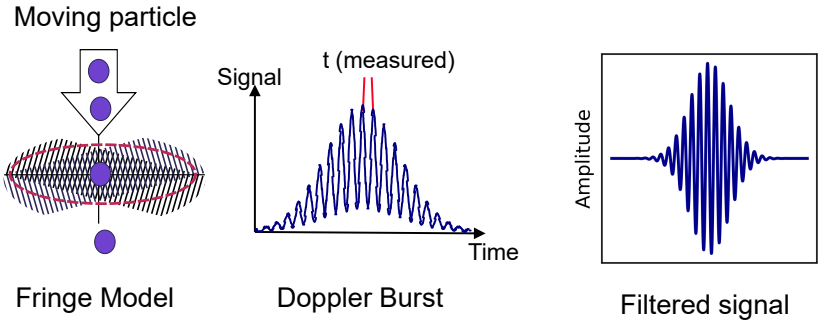


Figure 3.16: PDPA signal detection and processing.

The velocity is measured in the x-axis direction. The Doppler frequency shift occurs because the moving particle continuously changes its position relative to the fringes, effectively "seeing" the fringes move past it. Nonetheless, the frequency measured does not differentiate between a particle moving in the positive or negative direction. To account for this, an acousto-optical component (Bragg cells) adds a fixed frequency (f_0) to one of the laser beams.

By adding f_0 to one of the terms ($f_{s,2}$) in the Equation 3.20 the result of the equation derivation is:

$$f_D = f_0 + \frac{2u_x \sin(\theta/2)}{\lambda} \tag{3.22}$$

Additionally, according to this, the minimum velocity that can be measured is when f_D is f_0.

$$u_x > -\frac{\lambda f_0}{2\sin(\theta/2)} \tag{3.23}$$

So far, velocity has been defined as proportional to the temporal frequency shift of the received signal. Under this assumption, the receiver position does not influence the measured frequency, provided that the relative geometry between source, particle, and detector remains constant. Now, if a second photodetector is introduced, both detectors receive Doppler bursts at the same frequency. However, due to differences in optical path length caused primarily by their distinct angular positions relative to the measurement volume, the phases of the two signals differ accordingly. [50].

If all the geometric parameters are constant, the phase difference seen by both detectors will depend only on the size of the particle. Each burst phase can be represented mathematically as in Equation 3.24.

$$\Phi_i = \alpha\beta_i = \frac{\pi}{\lambda} D\beta_i \tag{3.24}$$

α as the size parameter contains the diameter (D) of the particle. β_i is the geometrical factor. Finally, a linear relationship between the phase difference of a detector j and i and particle size can be defined as:

$$\Phi_{ij} = \frac{\pi}{\lambda} Dx(\beta_j - \beta_i) \tag{3.25}$$

The geometrical factor β_i depends on the scattering mode, the intersection angle between the two beams (α) and the angles that define the path the scattering light follows(Φ,Ψ) toward the detector centroid. These angles are depicted in the Figure 3.17.

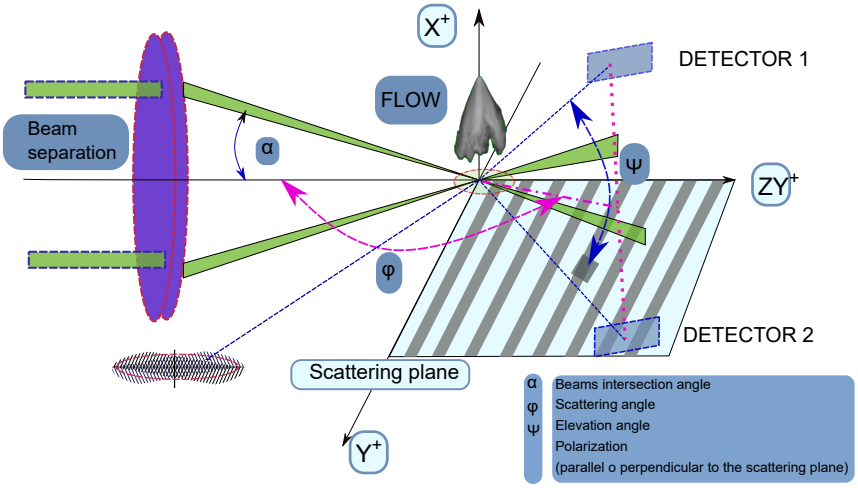


Figure 3.17: PDPA angles definition.

One of the most determinant angles here is the scattering angle, which is measured in the scattering plane from the axis of the transmitting optics (Z axis in the figure) up to the receiver optical axis.

Following a geometric optics approach, the scattering mode impact on the measurement can be assessed by ray tracing. A ray of light hitting an interface between two regions of different refractive indices (fuel droplet and air) can

be transmitted or reflected. Basically, due to the variation in the refractive index the transmitted light is bent from its incident path, hence refracted, and then outs the droplet. Hence, a geometrical factor can be expressed for each scattering mode, giving a different equation for the phase difference calculation depending on the dominant scattering mode, considering the relative refractive index (n_{rel}) calculated as the ratio of the droplet refractive index divided by the medium's one.

For the reflection case:

$$\Phi = \frac{2\pi D}{\lambda} \frac{\sin\theta \sin\psi}{\sqrt{2(1 - \cos\theta \cos\psi \cos\phi)}} \tag{3.26}$$

For the refraction case:

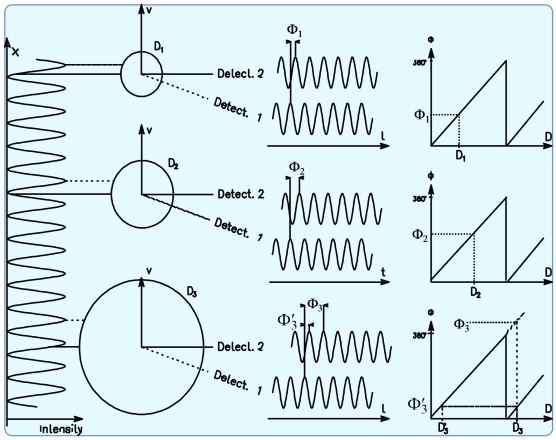
$$\Phi = \frac{-2\pi D}{\lambda} \frac{n_{rel} \sin\theta \sin\psi}{\sqrt{2(1 + \cos\theta \cos\psi \cos\phi)}(1 + n_{rel}^2 - n_{rel}\sqrt{2(1 + \cos\theta \cos\psi \cos\phi)})} \tag{3.27}$$

The light can also be reflected inside the surface of the droplet and then exit, bending again as it moves from the droplet's medium back into the air. This is the second order of refraction which equation is often solved numerically in an iterative process. Given that three scattering modes produce a different phase factor, the PDA system should be set up so that only one mode of scattering dominates the light collected by the receiving optics.

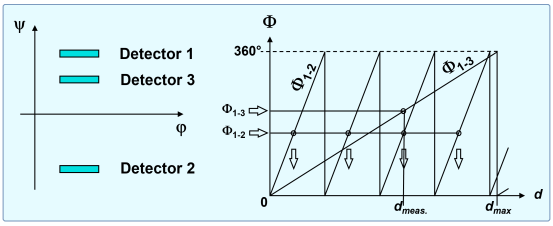
A last problem must be solved for the droplet size measurements with the addition of a third photodetector, the so called 2π ambiguity problem . Figure 3.18a depicts a classical representation of the signals for different droplet sizes. As the size increases, the phase factor also increases. However, if the particle is considerably big so that the phase difference exceeds 2π, the result given by two detectors would be the same as for a smaller particle. There is no way to tell whether the value corresponds to a droplet of diameter D_3 or D_3' (belonging to the phase -2π).

By asymmetrically positioning the three photo-detectors an additional phase difference allows identifying the correct value. The difference between a pair of detectors (U1 and U2) more widely spaced provides a greater slope in the diameter-phase relationship (Φ_{12}), resulting in higher resolution and a smaller working range. In conjunction with the first one, the other detector forms a closer pair (Φ_{13}), yielding a smaller slope, allowing for a larger measurement range but with lower resolution.

By setting properly all these parameters and finally comparing the phase differences between the two pairs of detectors, it is possible to achieve both high resolution and a broad measurement range simultaneously.



(a) The 2π ambiguity problem.



(b) The solution.

Figure 3.18: The 2π ambiguity approach

3.8 PDA data processing

3.8.1 The Phase Doppler Particle Analysis (PDPA) equipment

According to the principle explained, the schematics of the PDPA set-up is displayed in Figure 3.19.

- The light source: the laser beam is used as a source, later split into two beams that will cross and create the measurement volume after passing through a focusing lens. The source laser beam goes through a Bragg cell set that separates the beam into two beams with nearly the same intensity, and also induces an extra frequency shift to one of the beams in order to be able to measure negative velocities. This is done for two laser sources with different wavelength to measure the velocity in two directions.

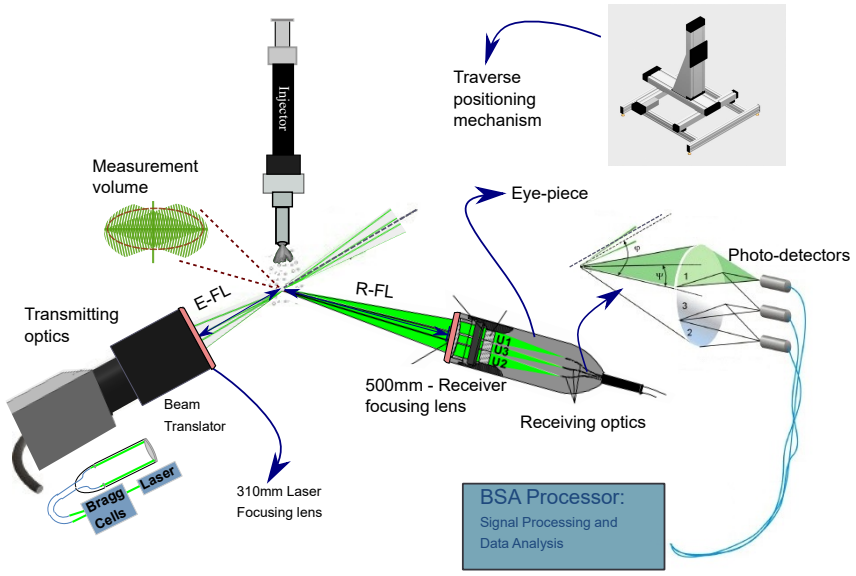


Figure 3.19: PDPA schematics.

- Beam expander set: A beam translator and a beam expander are used for fine-adjusting the crossing of the lasers. The beam translator allows to adjusting the beam separation to then go through a beam expander that increases the laser diameter. By definition, a bigger diameter permits focusing it on a smaller point.

- Optical lenses: The parallel lasers are then focused on the measurement volume. The scattered light is then collected by another focusing lens placed on the receiver. Note that the focal distance and the beam separation will define the angle θ in the Equation 3.22 as well as the fringe separation. A smaller θ angle allows to measure a higher velocity range. The receiver's focal length affects the size range of particles that can be measured.

- The receiver: A mask defines the amount of light collected by each detector and the separation between the centroid of the light transported to each detector. Three optical cables carry the light to the photo-detectors placed in the processor unit.

- The processor: The photo-detectors transform the light into an electrical signal from which the velocity is calculated. Setting the processor bandwidth to the correct one is critical to avoid noisy measurements.

Other parameters, such as the sensitivity of the photo-detectors, digital amplification, and burst validation parameters, are also set to optimize the measurement. The processor engineering also defines the limits at which the signal can be sampled and measured.

- The positioning system: The emitter and receiver are mounted on a traverse positioning system to precisely move the measuring volume across different locations in the spray.

The final values set for the actual measurements are thoroughly described in chapter 5.

3.8.2 Software utilization

The equipment, incorporates advanced technology enabling improved processing of burst signals, including the capability to capture supersonic velocities. While the processor automatically handles most of the signal processing, several key parameters must be manually configured to optimize the system's performance.

The software employed is a BSA Flow software delivered together with the PDA equipment. It works as a centralized interface to control the processor. The main validation parameters changed are:

- Velocity Range: This parameter defines the bandwidth employed by the processor for velocity measurement.
- Record length: used for limiting the length of processing peaks in the burst signal to be processed.
- Laser power: Higher laser power enhance the signal strength but also increases the noise in the measurements.
- Sensitivity: Defines how sensible the photodetectors are to the received light. Higher sensitivity can increase noise.
- Digital Multiplier for Sensitivity: An extra parameter for adjusting the sensitivity of the photodetectors. Balancing laser power and sensitivity is critical to achieving accurate and reliable data.
- Validation Parameters:

- Signal-to-Noise Ratio (SNR): Ensures the quality of the signal by distinguishing the burst signal from background noise. The higher the value, the more restrictive the validation is.
- Frequency Spectrum Validation: differentiates the burst signal from other signals based on a predefined 1st to 2nd peak ratio in the frequency spectrum.

3.8.3 Equipment alignment

With the receiver now in place and all characteristic variables defined, the next step involves focusing the receiver on the laser crossing point.

An eye-piece is utilized in the receiver that allows the visualization of the beam crossing from the receiver's perspective. The slit can be simultaneously seen as a small line in the center. With the goal of seeing the laser cross point intersecting with the slit, the pitch, and rotation angle of the receiver are tuned with a couple of adjusting screws. Essentially, this ensures that the light reaching the receiver through the slit filter is exclusively from the cross-section of the lasers.

Typically, starting with a larger slit and then gradually decreasing its size is more effective for precise adjustment. Optimal alignment is confirmed when the light reaches the photodetectors using the receiver pinhole, the smallest and most challenging filter to adjust, as its focus must be exactly on the cross-section. Additionally, the measurement cross section can be focused by changing the distance between the receiver and the cross-section. It can be fine-tuned using an adjustment screw on the receiver, allowing for forward or backward movement.

Refinement process

The alignment process was facilitated by using a constant flow generator that creates a steady stream of water particles at a constant velocity. This setup simplifies the measurement of velocities.

The alignment process commences after positioning the laser cross-section within the water flow and observing the measurement volume through the receiver eye-piece. Initially, laser power and sensitivity are adjusted to detect the current in the processor, indicating that light is successfully reaching the photodetectors. This preliminary alignment step ensures basic detection, but an improved alignment requires maximizing the current received solely through receiver adjustments.

Subsequent to achieving maximum current with fixed laser power and sensitivity settings, the validation and measuring (velocity range, etc) parameters are changed until some data rates are achieved within the system for each velocity component. Proper alignment is confirmed when the data rates for both velocity components are optimized. The receiver positioning significantly impacts the data rate measured by the system. When the measurement volume is not correctly focused, the data rate detected by the system is minimal or non-existent. The accuracy of alignment is assessed by monitoring the data rate through histograms, which record the number of droplets measured per second and provide insight into their distribution within the spray. Adjusting the pitch and rotation angles of the receiver allows real-time observation of histogram variations and data rates, enabling the determination of optimal alignment conditions. Finally, the slit filter on the receiver is gradually reduced, and the receiver positioning is adjusted to further refine the measured data rate, ensuring accurate data acquisition.

3.9 Methodology for GDI sprays

3.9.1 Velocity component in the sprays coordinates

The direction of the velocity components in relation to the spray position and angle is depicted in Figure 3.20. It illustrates two primary velocity components, with the vertical component being the most dominant, while the horizontal component, though significant, is less. It is important to note that the positive direction of the measured velocity is opposite to the movement of the droplets, which must be considered during the analysis to accurately interpret the results.

Due to the constraints in injector positioning by also aiming the measuring at the centerline of the injector axis, the chosen position was optimal for this experimental campaign for both measuring one spray of interest, accessing the axis of the injector.

(A) represents the axial distances at which the measurements were carried out. (B) shows the components of the velocity measured by the equipment. (C) illustrates the radial positions and direction at which the measurements are done across each axial position. Finally, (D) represents the path followed by the lasers in order to measure at the injector axis.

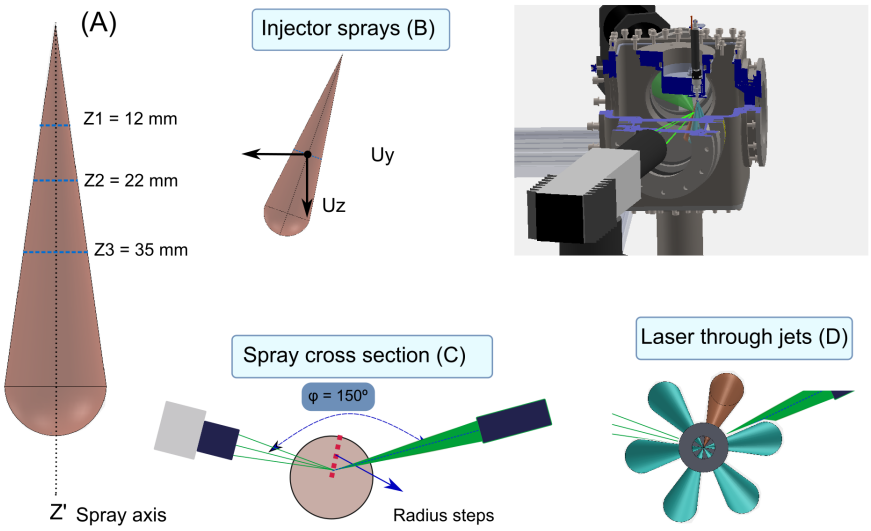


Figure 3.20: Schematics of the velocity components measured.

3.9.2 Data acquisition on sprays

During the measurements on the spray of interest, the velocity range is fine-tuned. This ensures the capture of the maximum velocity in the spray while avoiding an excessively large bandwidth. Given the significant variation in velocity observed during measurements, two specific bandwidths were employed. This limited variation simplifies the process and maintains consistency. Each droplet, recognized as a burst by the system, is validated using the signal-to-noise ratio, aiming for a validation rate exceeding 60%. Additionally, spherical validation compares the phase of the combination of the three photodetectors to further ensure accuracy.

The software is set to measure cyclic phenomena events, where each event is superposed with previous ones. The criteria for capturing data include either a minimum of 20,000 droplets or at least 50 injections in the spray axis and 25 injections for other radial positions. This approach balances measurement accuracy with efficiency, avoiding excessive data acquisition.

Using exclusively the count limit as the stop criteria is not the best option since the data rate differs along the different positions in the spray. Especially, the center of the spray often presents challenges with lower data rates compared to other radial positions, where data rates can be higher. The droplet count limit is set high to avoid bias and ensure comprehensive data collection, prioritizing accurate data capture across all injection phases.

Data structure

Figure 3.21 illustrates one of the measurements, where various injection events are superimposed to acquire a number of droplets necessary for statistical robustness. Data is analyzed by averaging the droplets over time, with the data resampled into 10μs time frame. The resampled moving average of the velocity is depicted in black.

The injection event signal can be decomposed into four distinct stages:

1. Spray injection front: This is the initial phase where the spray reaches the laser measurement volume. During this phase, the measured velocity increases until it matches the spray velocity.
2. Quasi-stationary hase of the fully open nozzle: The needle is fully open, and the spray velocity stabilizes. This stage is characterized by a consistent velocity, indicating the steady-state operation of the injector.
3. Quasi-stationary hase of the fully open nozzle with coalescence:
4. Spray tail: The needle has closed and the spray loses momentum.

The spray signal structure's velocity may change as it moves across the spray. Usually, for lower velocities, the droplet velocity dispersion is higher, and the average signal is flatter. For all cases, the start of injection (SOI) is pointed through a script based on local maximum identification. Although visualizations can capture the start of injection, the distance at which velocity is measured must also be accounted for. By calculating the start of injection, the quasi-stationary part was selected as a percentage of the spray's start and end times.

3.9.3 Set-up approach in GDI measurements

The scattering angle selection for this measurement campaign needs to consider the several variables. The dominant scattering mode is dependent on the relative refractive index. For the fuels employed, the values were very similar, and the refraction is dominant in a wide range of angles, but it is usually more optimal at values close to the Brewster angle. Two values are shown to be more common in the literature (110° and 150°) with different pros and cons. In summary, the selection is influenced by:

- Relative refractive index

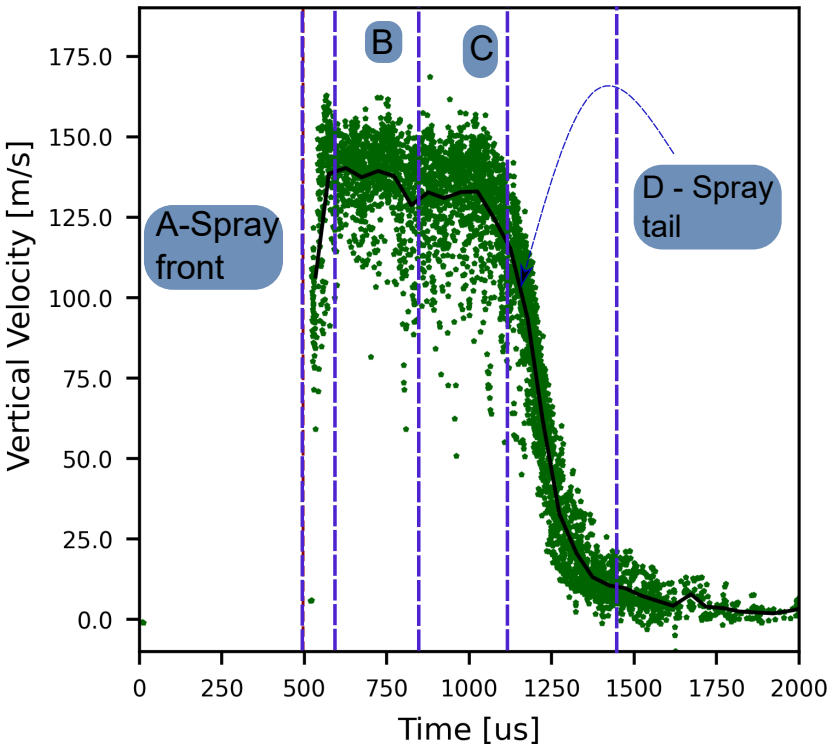


Figure 3.21: Spray evolution in the time-resolved droplets velocity acquisition.

- Polarization and laser wavelength, which are fixed by the device, also affect the choice of scattering angle.
- The scattering angle significantly impacts signal strength and signal-to-noise ratio (SNR).
- Smaller Scattering Angles (e.g., 70°/110°) enhance SNR but lower signal strength.
- Larger Scattering Angles (e.g., 30°/150°) increase signal strength but reduce SNR.

After a geometrical analysis of the vessel in which the possible injector positions and the light rays path towards the receptor, for maximizing the volume that could be covered by the measurement point without any light clipping; a 30/150°scattering angle was determined to be the most suitable for

the current PDA setup. This angle also benefits the measurement of smaller particles.

Initially, it is important to define the velocity and size range to be measured. The velocity at the nozzle exit was estimated using data from the internal flow measurements, supplemented with equations from Vlad [51], which provide velocity profiles along the spray's axial position.

To accurately set the goal velocity range, two key parameters of the Laser must be adjusted: the focal length of the emitter and the separation between the laser beams. It is essential to ensure that all laser beams intersect at the same point, which is verified using a 50μm pinhole. This alignment is critical for obtaining high-quality measurements.

To achieve this, a beam expander and beam translator were employed to fine-tune the alignment. The beam expander adjusts the size of the laser beam, while the beam translator modifies the separation of each laser relative to the emitter's optical axis. By adjusting this separation and maintaining a fixed focal length for the emitter, the intersection point of the laser beams can be accurately controlled. The final alignment is verified by passing the laser beams through the pinhole and ensuring a consistent diffraction pattern for each laser beam, as depicted in Figure 3.22.

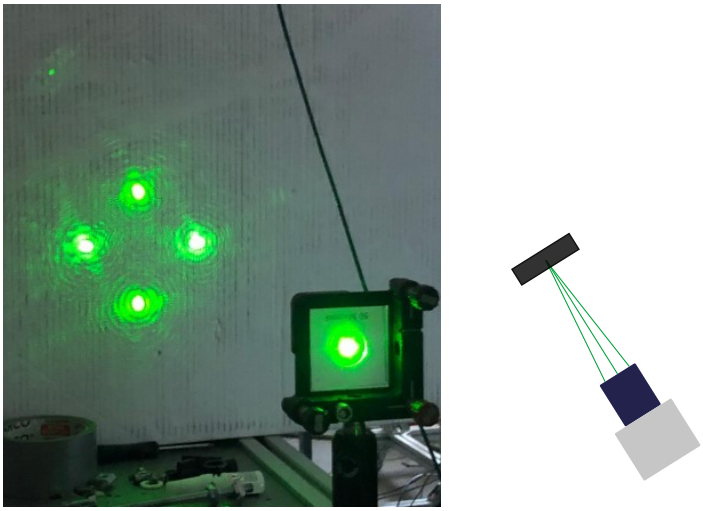


Figure 3.22: Difraction patterns seen for aligned lasers.

The emitter focal length selected was 310 mm which was sufficient to cover the full range of expected velocities. For the particle size measurements, a setup was selected to also cover a broad range of diameters. Adjustments

are made by changing the mask within the receiver, which alters the perceived separation by the photo-detectors and changing the focal length of the receiver. First, very wide range setup is tested aiming to obtaining a top limit of possible diameters, and then adjusted to a more constrained range. This ensures that larger droplets are captured while minimizing noise in the measurements.

On the receiver side, one final refinement is done through the variation in the slit size, which acts as a filter for the incoming light. Adjusting the slit size can control the amount of light reaching the photodetectors, which is particularly important for high-concentration sprays influencing the laser power and the sensitivity of the photodetectors setup. Several slit sizes were tested: 200 μm, 100 μm, 50 μm, and a 25 μm pinhole. Previous studies have shown that smaller slit sizes improve the measurement of high-concentration sprays by reducing the amount of extraneous light and improving the signal-to-noise ratio.

Before the start of the measurements, some geometrical variables must also be assessed. First, it is essential to ensure the traverse positioning system alignment relative to the measurement vessel. Although both the vessel and the traverse system were leveled, to reference their axes, the system, which moves orthogonally, was aligned with the vessel walls using the laser movement as a reference to get relative positions of the traverse system and the test rig.

Injector position and Spray of interest location.

The vessel allows to position the injector both vertically and horizontally. The typical approach in the literature for locating the injector involves aligning the spray of interest with the direction of the velocity component corresponding to the pair of lasers measuring the droplet diameter. However, the current GDI measurement approach deviates from this norm for two primary reasons.

First, extensive visualization studies on sprays under flash boiling conditions have indicated significant variability in spray angle depending on the injection conditions. Simply, aligning the spray consistently with the laser pairs is challenging because the angle variations would lead to substantial measurement inaccuracies.

A vertical injector position was selected with a slight offset from the vessel's center. This arrangement enhances the spatial coverage of the laser positioning system, avoiding the beam clipping by the windows support, allowing for the measurement of the horizontal velocity component.

For this type of injectors with multiple sprays, conducting the measurements in all jets is a very time consuming task. Thus, for this experiment only

one of the sprays was chosen for the operating conditions variation. On the other side, another objective of this experiment was to measure the velocity and droplet diameter along the center line to observe the presence and variation of droplets during injection under collapsing conditions. To achieve this, the pair of lasers measuring the diameter (vertical component) was positioned to access between two spray-jets. Additionally, it was ensured that the path of the scattered light toward the receiver corresponded to a relatively empty space between the sprays to avoid any blockage by the spray during injection. A specific angle was selected based on empirical data rather than nominal angles to avoid any blockage. This empirical method provided a more accurate representation of the spray angles.

The method consisted in scanning the velocity in a grid of positions across the sprays. This is further expanded in chapter 5.

References

[1] Engine Combustion Network. *Spray G Parametric Variation.* https://ecn.sandia.gov/gasoline-spray-combustion/target-condition/spray-g-parametric-variation/. Online; accessed 29 April 2020. 2020.

[2] Lehnert, B., Conrad, C., and Wensing, M. *GDI Sprays with up to 200 MPa fuel pressure and comparison of diesel-like and gasoline-like injector designs.* Tech. rep. SAE Technical Paper, 2020.

[3] Lee, Z., Kim, T., Park, S., and Park, S. "Review on spray, combustion, and emission characteristics of recent developed direct-injection spark ignition (DISI) engine system with multi-hole type injector". In: *Fuel* 259 (2020), p. 116209. DOI: https://doi.org/10.1016/j.fuel.2019.116209.

[4] Lacey, J. et al. "Effects of refinery stream gasoline property variation on the auto-ignition quality of a fuel and homogeneous charge compression ignition combustion". In: *International Journal of Engine Research* 18.3 (2017), pp. 226–239.

[5] Piehl, J. A., Zyada, A., Bravo, L., and Samimi-Abianeh, O. "Review of Oxidation of Gasoline Surrogates and Its Components". In: *Journal of Combustion* 2018 (2018). DOI: 10.1155/2018/8406754.

[6] Kraus, F., Martins Oliveira, A. A., Bueno Bontorin, A. C., Rouge dos Santos, A., and Cancino, L. R. "i-pentane and i-pentene as gasoline surrogates for the transport industry: a numerical analysis on ignition delay times using detailed chemical kinetics". In: *Brazilian Congress of Thermal Sciences and Engineering*. 2020. DOI: 10.26678/abcm.encit2020.cit20-0512.

[7] Anderson, J. et al. "High octane number ethanol–gasoline blends: Quantifying the potential benefits in the United States". In: *Fuel* 97 (2014), pp. 585–594. DOI: 10.1016/j.fuel.2012.03.017.

[8] Lemmon, E. W., Bell, I., Huber, M., and McLinden, M. O. "Thermophysical Properties of Fluid Systems". In: *NIST Standard Reference Database Number 69*. Ed. by P. J. Linstrom and W. G. Mallard. Gaithersburg MD, 20899, USA.: National Institute of Standards and Technology, 1998. DOI: https://doi.org/10.18434/T4D303.

[9] Pérez-Ones, O., Díaz-Rodríguez, J., Zumalacárregui, L., and Gozá-León, O. "Evaluación de propiedades físicas de mezclas etanol-agua (II)". In: *Revista Facultad de Ingeniería Universidad de Antioquia* 52 (2010), pp. 62–74.

[10] Bautista Rodríguez, A. "Study of the Gasoline Direct Injection Process under Novel Operating Conditions". PhD thesis. Universitat Politècnica de València, 2021.

[11] Payri, R., García-Oliver, J. M., Bracho, G., and Cao, J. "Experimental characterization of direct injection liquid ammonia sprays under non-reacting diesel-like conditions". In: *Fuel* 362 (2024), p. 130851.

[12] Payri, R., Gimeno, J., Martı-Aldaravi, P., and Viera, A. "Measurements of the mass allocation for multiple injection strategies using the rate of injection and momentum flux signals". In: *International Journal of Engine Research* (2020). DOI: 10.1177/1468087419894854.

[13] Bosch, W. "The Fuel Rate Indicator: A New Measuring Instrument For Display of the Characteristics of Individual Injection". In: 1966.

[14] Viera, A. "Effect of multiple injection strategies on the diesel spray formation and combustion using optical diagnostics". PhD thesis. Universitat Politècnica de València, 2019.

[15] Payri, R., Salvador, F., Gimeno, J., and Bracho, G. "A NEW METHODOLOGY FOR CORRECTING THE SIGNAL CUMULATIVE PHENOMENON ON INJECTION RATE MEASUREMENTS". In: *Experimental Techniques* 32.1 (2008), pp. 46–49. DOI: 10.1111/j.1747-1567.2007.00188.x.

[16] Gimeno, J. "Desarrollo y aplicación de la medida de flujo de cantidad de movimiento de un chorro Diesel". PhD thesis. E.T.S. Ingenieros Industriales, Universidad Politécnica de Valencia, 2008. DOI: 10.4995/Thesis/10251/8306.

[17] Salvador, F. J., Gimeno, J., Carreres, M., and Crialesi-Esposito, M. "Fuel temperature influence on the performance of a last generation common-rail diesel ballistic injector. Part I: Experimental mass flow rate measurements and discussion". In: *Energy Conversion and Management* 114 (2016), pp. 364–375. DOI: 10.1016/j.enconman.2016.02.042.

[18] Lemmon, E. W., McLinden, M. O., and Friend, D. G. "Thermophysical Properties of Fluid Systems". In: *NIST Chemistry WebBook, NIST Standard Reference Database Number 69*. Ed. by P. J. Linstrom and W. G. Mallard. 2011.

[19] Vaquerizo, D. "Study on Advanced Spray-Guided Gasoline Direct Injection Systems". PhD thesis. Universitat Politècnica de València, 2017.

[20] Cavicchi, A. et al. "Numerical and experimental analysis of the spray momentum flux measuring on a GDI injector". In: *Fuel* 206 (2017), pp. 614–627. DOI: 10.1016/j.fuel.2017.06.054.

[21] Cavicchi, A., Postrioti, L., Berni, F., Fontanesi, S., and Di Gioia, R. "Evaluation of hole-specific injection rate based on momentum flux measurement in GDI systems". In: *Fuel* 263.November 2019 (2020). DOI: 10.1016/j.fuel.2019.116657.

[22] Payri, R., Gimeno, J., Martí-Aldaraví, P., and Vaquerizo, D. "Momentum Flux Measurements on an ECN GDi Injector". In: *SAE Technical Paper 2015-01-1893*. 2015, p. 11. DOI: 10.4271/2015-01-1893.

[23] Duke, D. J. et al. "Internal and near nozzle measurements of Engine Combustion Network "Spray G" gasoline direct injectors". In: *Experimental Thermal and Fluid Science* 88 (2017), pp. 608–621. DOI: 10.1016/j.expthermflusci.2017.07.015.

[24] Payri, R., Bracho, G., Soriano, J. A., Fernández-Yáñez, P., and Armas, O. "Nozzle rate of injection estimation from hole to hole momentum flux data with different fossil and renewable fuels". In: *Fuel* 279.May (2020), p. 118404. DOI: 10.1016/j.fuel.2020.118404.

[25] Shahangian, N. et al. "Spray Orientation Assessment and Correction Method for GDI Momentum Flux Measurements". In: *"17th Conference. The Working Process of the Internal Combustion Engine"*. 2019, pp. 231–241.

[26] Du, J., Chen, H., Li, Y., Ye, L., and Li, G. "Experimental Study on Ethanol Gasoline Flash-Boiling Spray Characteristics Using Multi-hole GDI Injector". In: *Proceedings of China SAE Congress 2019: Selected Papers*. Singapore: Springer Singapore, 2021, pp. 635–645.

[27] Du, J., Mohan, B., Sim, J., Fang, T., and Roberts, W. L. "Study of spray collapse phenomenon at flash boiling conditions using simultaneous front and side view imaging". In: *International Journal of Heat and Mass Transfer* 147 (2020), p. 118824. DOI: https://doi.org/10.1016/j.ijheatmasstransfer.2019.118824.

[28] Kale, R. and Banerjee, R. "Experimental investigation on GDI spray behavior of isooctane and alcohols at elevated pressure and temperature conditions". In: *Fuel* 236 (2019), pp. 1–12. DOI: https://doi.org/10.1016/j.fuel.2018.08.153.

[29] Hamzah, A. et al. "A comparison of diffuse back-illumination (DBI) and Mie-scattering technique for measuring the liquid length of severely flashing spray". In: *20th Australasian Fluid Mechanics Conference (AFMC)*. 2016.

[30] Geschwindner, C. et al. "Analysis of the interaction of Spray G and in-cylinder flow in two optical engines for late gasoline direct injection". In: *International Journal of Engine Research* 21.1 (2020), pp. 169–184. DOI: https://doi.org/10.1177/1468087419881535.

[31] Payri, R., Martí-Aldaraví, P., Alvarez, V. M., and Bautista, A. "Evaluation of GDI spray structures under flash boiling and strong collapse conditions with diverse fuels". In: *Applied Thermal Engineering* 234 (2023), p. 121195.

[32] MathWorks. *image Function - MATLAB Documentation*. MathWorks. Accessed 2024. URL: https://es.mathworks.com/help/matlab/ref/image.html.

[33] Payri, R., García-Oliver, J. M., Mendoza, V., and Viera, A. "Analysis of the Influence of Diesel Spray Injection on the Ignition and Soot Formation in Multiple Injection Strategy". In: *Energies* 13.13 (2020). DOI: 10.3390/en13133505.

[34] Carvallo García, C. L. "Experimental study of the behavior of gasoline direct injection GDI sprays during wall impingement under realistic engine conditions." PhD thesis. Universitat Politècnica de València, 2023.

[35] Otsu, N. "A Threshold Selection Method from Gray-Level Histograms". In: *IEEE Transactions on Systems, Man, and Cybernetics* 9.1 (1979), pp. 62–66. DOI: 10.1109/TSMC.1979.4310076.

[36] Payri, R., Bracho, G., Marti-Aldaravi, P., and Viera, A. "Near field visualization of diesel spray for different nozzle inclination angles in non-vaporizing conditions". In: *Atomization and Sprays* 27.3 (2017), pp. 251–267. DOI: 10.1615/AtomizSpr.2017017949.

[37] Payri, R., Salvador, F. J., Bracho, G., and Viera, A. "Differences between single and double-pass schlieren imaging on diesel vapor spray characteristics". In: *Applied Thermal Engineering* 125 (2017), pp. 220–231. DOI: 10.1016/j.applthermaleng.2017.06.140.

[38] Yan, J., Gao, S., Zhao, W., Lee, T. H., and Lee, C.-F. "Experimental study of sprays with isooctane, hexane, ethanol and their binary mixtures under different flash boiling intensities". In: *International Journal of Heat and Mass Transfer* 179 (2021), p. 121715. DOI: https://doi.org/10.1016/j.ijheatmasstransfer.2021.121715.

[39] Kale, R. and Banerjee, R. "Spray Collapse in a Multi-hole GDI Injector and Its Effect on In-Cylinder Combustion". In: *Two-Phase Flow for Automotive and Power Generation Sectors*. Ed. by K. Saha, A. Kumar Agarwal, K. Ghosh, and S. Som. Singapore: Springer Singapore, 2019, pp. 43–61. DOI: 10.1007/978-981-13-3256-2_3.

[40] Liu, W., Lu, Y., Kang, Y., Yan, J., and Lee, C.-F. "Macroscopic characteristics of flash-boiling spray focused on plume interaction". In: *International Journal of Heat and Mass Transfer* 170 (2021), p. 120999. DOI: https://doi.org/10.1016/j.ijheatmasstransfer.2021.120999.

[41] Benajes, J., Payri, R., Bardi, M., and Martí-Aldaraví, P. "Experimental characterization of diesel ignition and lift-off length using a single-hole ECN injector". In: *Applied Thermal Engineering* 58.1-2 (2013), pp. 554–563. DOI: 10.1016/j.applthermaleng.2013.04.044.

[42] Wang, H. et al. "Promotion of particle agglomeration by different vortex generator angles based on PIV-PDPA experiment". In: *Chemical Engineering Journal* 486 (2024), p. 150308. DOI: https://doi.org/10.1016/j.cej.2024.150308.

[43] Privitera, S., Manetto, G., Pascuzzi, S., Pessina, D., and Cerruto, E. "Drop Size Measurement Techniques for Agricultural Sprays:A State-of-The-Art Review". In: *Agronomy* 13.3 (2023). DOI: 10.3390/agronomy13030678.

[44] Al-Hakim, K., Wigley, G., and Stapley, A. "Phase Doppler Anemometry Studies of Spray Freezing". In: *Chemical Engineering Research and Design* 84.12 (2006), pp. 1142–1151. DOI: https://doi.org/10.1205/cherd06014.

[45] Beleca, R., Abbod, M., Balachandran, W., and Miller, P. R. "Investigation of electrostatic properties of pharmaceutical powders using phase Doppler anemometry". In: *IEEE Transactions on Industry Applications* 46.3 (2010), pp. 1181–1187.

[46] Agrawal, Y. C. and McCullough, J. R. "Directional pedestal-free laser Doppler velocimetry without frequency biasing. Part 1". In: *Applied Optics* 20.9 (1981), pp. 1553–1556.

[47] Dodge, L. G., Rhodes, D. J., and Reitz, R. D. "Drop-size measurement techniques for sprays: comparison of Malvern laser-diffraction and Aerometrics phase/Doppler". In: *Applied optics* 26.11 (1987), pp. 2144–2154.

[48] Tropea, C. "Optical particle characterization in flows". In: *Annual Review of Fluid Mechanics* 43 (2011), pp. 399–426.

[49] Hecht, E. *Optics*. Pearson Education, Incorporated, 2017.

[50] Durst, F. and Zaré, M. "Laser Doppler measurements in two-phase flows". In: *The accuracy of flow measurements by laser Doppler methods* (1976), pp. 403–429.

[51] Vlad, T. S. "Phase doppler measurement in diesel dense sprays: optimisation of measurements and study of the orifice geometry influence over the spray at microscopic level". PhD thesis. Universitat Politècnica de València, 2007.

Chapter 4

Describing the geometry and near nozzle flow

4.1 Introduction

The spray characteristics in GDI systems plays a critical role in atomization, evaporation, and combustion processes. Fully describing it begins with the study of the internal flow inside the injector nozzle, as it governs the initial conditions of the spray formation. In this area, direct observation is challenging due to the inherent complexity and inaccessibility of the internal regions, thence, indirect experimental strategies have been developed in the sprays' research field to characterize the internal flow behavior through externally measurable parameters.

This chapter presents a comprehensive hydraulic characterization of the two injectors employed in this work, both commercially available for GDI applications. A combination of experimental techniques is used to assess their performance under a wide range of operating conditions, including ambient and injection settings that promote flash boiling. These conditions were selected to reflect realistic operating environments in gasoline engines, and were informed by guidelines established by the Engine Combustion Network (ECN) [1].

The classical characterization comprises a full description of the injector's geometries, the rate of injection (ROI), momentum flux or rate of momentum (ROM), and the hydraulic characterization based on the ROI and ROM.

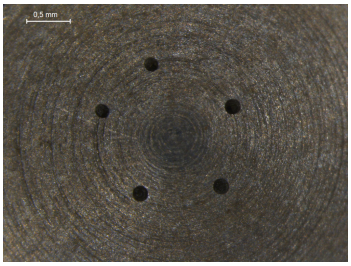
4.2 Injectors' geometry

4.2.1 Nozzle holes distribution

Frontal images depicted in Figure 4.1 of the nozzle were taken with an electronic loop. The first injector Figure 4.1a, labeled as C3539, has a six-hole configuration, while the second one (Figure 4.1b) has five holes.



*(a) Nozzle tip picture with holes distribution for the **C3539** injector.*



*(b) Nozzle tip picture with holes distribution for the **C7532** injector.*

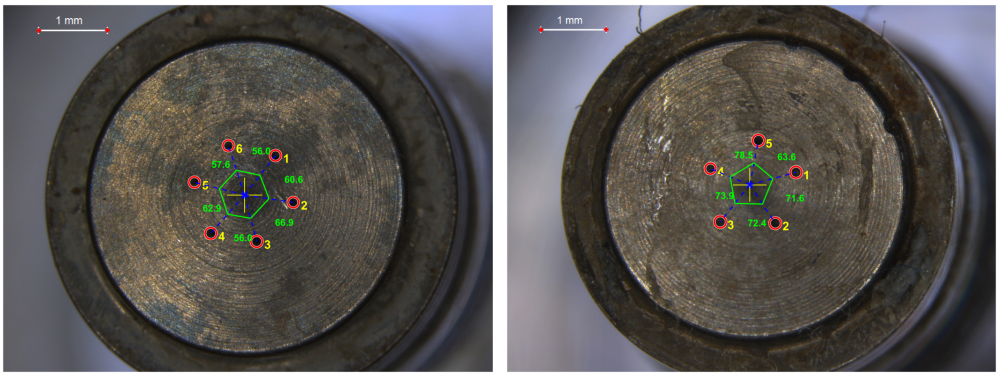
Figure 4.1: Nozzle images for both injectors with the holes distribution. The pictures are at 16x zoom.

Despite they seem to be symmetrically distributed, using a MATLAB code developed for detecting the holes and accurately measuring the angles between them, as seen in Figure 4.2, the separation angle between consecutive holes was not consistent, in fact it varies by approximately 3.6 degrees. This variation is significant and must be considered for the experiments setup and result interpretation. This analysis is crucial for aligning specific holes in the Particle Doppler Anemometry (PDA) measurements.

4.2.2 Internal Geometry microscopic images

Understanding the geometry of the holes is essential to carry out a comprehensive internal flow characterization. Detailed information about the hole shape, including nozzle conicity, hole type, and orifice diameters, is crucial. Typically, this information is provided by the manufacturer. However, it was not available in this case, necessitating further investigation.

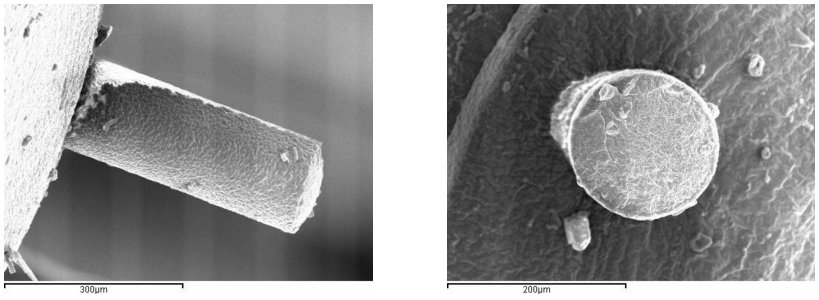
To achieve this, the characterization method described by Macian et al. [2] was used, which involves creating silicone molds of the nozzle's internal geometry. The orifices' diameter values and conicity are obtained through this technique. The nozzle used in this study was similar to the five-orifice



(a) Angles detected for the C3539 injector. *(b) Angles detected for the C7532 injector*

Figure 4.2: Angle detection for the nozzle holes distribution with a MATLAB routine.

C7532 nozzle. Figure 4.3 shows the images of the silicone molds taken by an electronic microscope of the molds after extraction from the nozzle tip.



(a) Images of the silicone mold for the C7532 injector. Lateral view. *(b) Images of the silicone mold for the C7532 injector. Frontal view.*

Figure 4.3: Microscopic images of the silicon molds.

Due to the one-piece construction of the injector, detaching the nozzle tip was not feasible; therefore, only one type of nozzle was investigated using this technique. An injector equal to the five-orifice nozzle was sacrificed for this approach.

Although the C3539 nozzle was not analyzed with these molds, a comparison can be made using the silicone diameter with the external diameter measured from the frontal images of the nozzle tip seen in Figure 4.1. An average diameter can be calculated from the detected holes. This involves

adjusting the measured diameter to account for the nozzle tip angle as we are viewing a projected image of the hole. Knowing that the injectors share the same hole shape, the uncertainty obtained when both results are compared can be applied to understand the accuracy of the external hole diameter.

4.2.3 Tomographic images

In a subsequent experimental campaign, tomographic images were obtained using X-ray imaging at the Argonne National Laboratory, Advance Photron Source (ANL - APS) with in-house techniques and methodologies [3–5], providing highly precise measurements. These tomographic images were compared with the results obtained from the electron microscope and the plastic casting technique. The comparison showed that the measurements from the simplistic casting technique were consistent with the more precise tomographic images, validating the accuracy of the initial measurements.

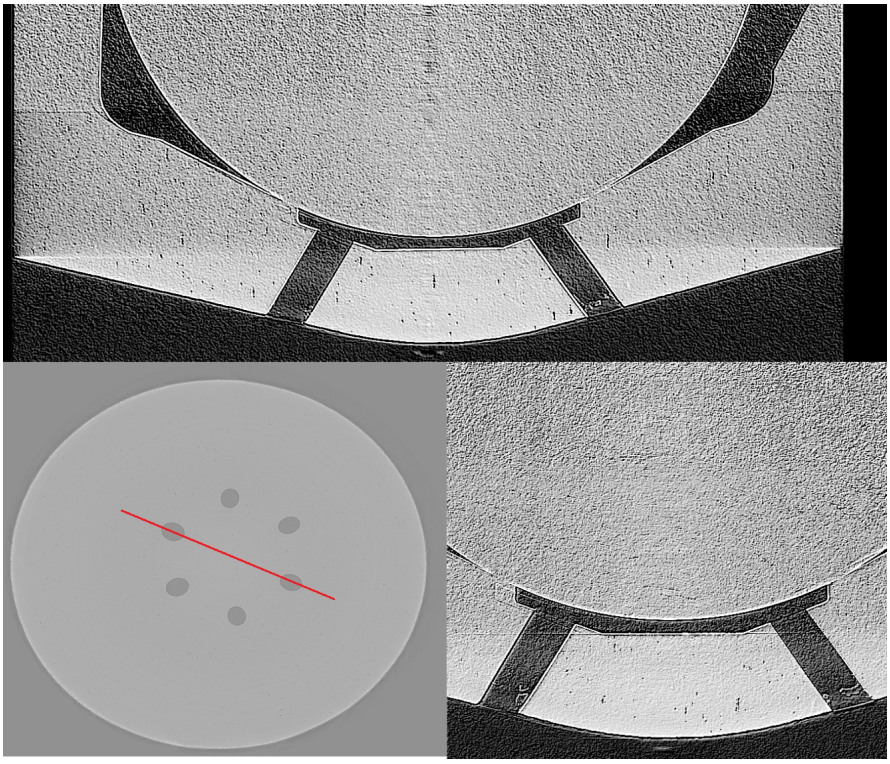


Figure 4.4: Image of the cross section of the nozzle passages for the 6 orifice injector, C3539.

The final comparison between the diameters measured with different techniques is shown in Table 4.1

Injector/Technique	Silicone	Loop image	Tomo	Units
C7532	162	171	-	μm
C3539	-	175	174	μm

Table 4.1: Measurement results for different injectors/techniques

4.2.4 Spray core assessment

The sprays' angle relative to the injector axis is determined using a spray core assessment as explained in subsection 3.3.5. Initially, the spray core measurements were conducted using the paper pinch technique, and the results showed a standard deviation of 2 degrees per repetition.

The initial measurements revealed a 5°difference between the two injectors, providing a useful baseline. The spray core angles were later refined using the PDA measurements to locate the spray core. While not highly precise, this simplistic technique offers a reliable preliminary estimate, which is sufficient to correct the rate of momentum measurements, as shown by the minimal variation when compared to more accurate methods. The results are shown in Table 4.2.

Table 4.2: Spray core assessment of the injectors' angle with the paper pinch technique.

Injector	Pr [bar]	Average angle [º]	Error [º]
C3539	200	35.0	±1
C7532	200	35.5	±1

4.3 Rate of injection

4.3.1 Test matrix summary

For the Rate of injection measurements, the conditions tested are displayed in the Table 4.3. Due to the technique limitations (section 3.3.1), the closest to ambient pressure at which the measurements could be taken at was 2 bar. For the C7532 injector only one fuel was measured for reference purposes in order to constraint the test matrix. A total of 76 operating conditions were measured.

Table 4.3: Conditions to be tested: Rate of Injection

Parameter	Operating Value	Units	Abbreviation
Fuel	IsoOctane - Hexane* - Ethanol*	-	*Fuel*
Injectors	C3539 - C7532	-	Inj
Rail pressure	50* 100* - 200 - 350	bar	P_r
Ambient pressure	2-6-15-21.5*	bar	P_b
Injector temperature	25 - 90	°C	T_n
Ambient Temperature	25	°C	T_b
Energizing time	800	µs	*ET*
Injection frequency	10	Hz	-
Injection cycles	50	-	-

** For particular conditions*

4.3.2 The ROI signal

The Figure 4.5 illustrates the shot-to-shot variability in the post-data processing rate of injection signal for each injector at an injection pressure of 200 bar and an ambient pressure of 6 bar. Along with the mass flow rate, the rail pressure drop and the activation current for each injector are depicted. The electric current profile is provided by the ECU controller.

Each operating condition was subjected to 50 repetitions, ensuring robustness in the data, and later filtered by a shot–to–shot deviation analysis through the residuals and the sigma values of a robust linear regression fit. The filtered cycles will be subsequently averaged for comparative analysis across different operating conditions. Notably, minimal variability is observed in the shot-to-shot variation of the injection rate and pressure signal within the range of up to 3%. The observed dispersion may stem from uncertainties inherent in the manufacturing process, the dynamic behavior of the injector, and potential noise (vibrations) from the IRDCI + injection system set-up used for mass flow rate measurement. This minimal variability underscores the high quality of the injector, indicating its capability to reproduce identical injections in each cycle and consistently deliver the same performance across repetitions.

The ROI signal can be deconstructed into three distinct phases: the first transient phase, which corresponds to the needle opening of the injector (the positive slope of the curve); the stable phase after the end of the positive slope, reflecting the steady state operation at each condition; and the closing phase, constituting the second signal transients. Some oscillations can be observed at the end of the injection, presumably due to the waves generated by the pressure waves traveling through the long tube. The waves generated by the

needle impacting the valve seat (when closing pushed by the spring) propagate through the pressurized fluid and create those curves. The vertical dashed lines depict the limits used for calculating the stable mass flow rate. The limits were chosen to cover 50% of the injection duration, from 20% to 70% of the total injection time. The start and end of the injection are calculated with a linear fit of the rising and falling edge of the signal. The first edge is found in the starting points between 10 % and 20 % of the maximum mass flow rate measured. The falling edge follows the same analogy between 35 % and 50 % of the maximum value got for the y-axis. The start of injection (SOI) is later adjusted with the sound speed and the distance to the sensor to account for the delays induced by this distance.

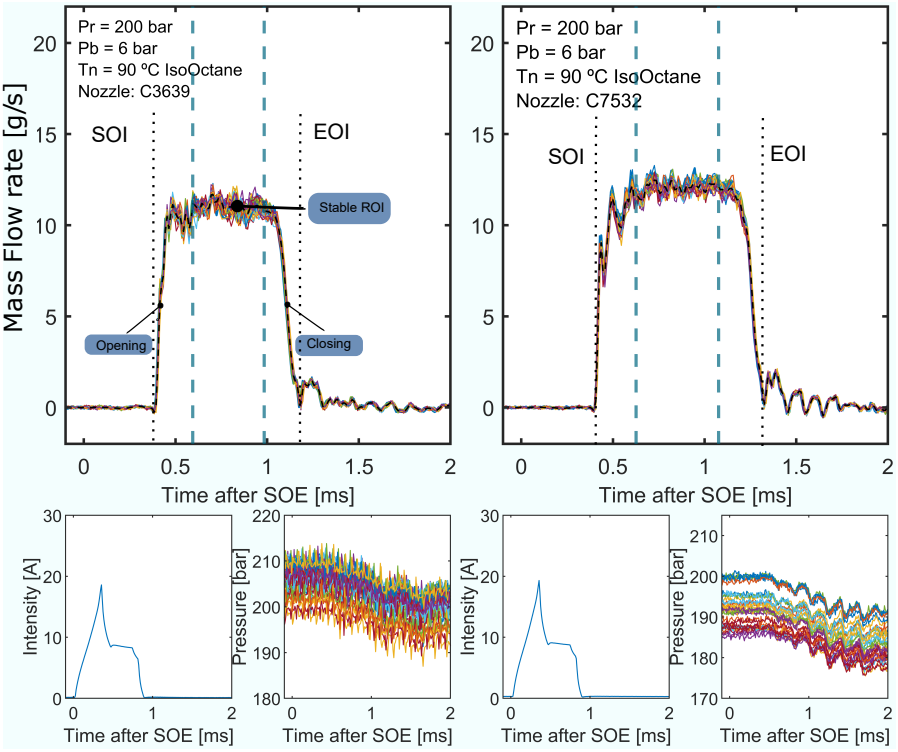


Figure 4.5: Shot-to-shot dispersion in the ROI and injection pressure signal.

4.3.3 Injector comparison

The low variability in the ROI signal points the main differences found when comparing the effect of the diverse injection parameters to the variable varied

itself. Starting with the injectors tested, Figure 4.6 displays the ROI for both injectors at different injection pressures. The injectors are differentiated by line styles and the pressures are represented by different colors. The left subplot is for the total mass flow rate injected, and the right side is the signal accounting for the number of holes, resulting from dividing the total ROI by the number of orifices of each injector, assuming an equally distributed ROI per orifice.

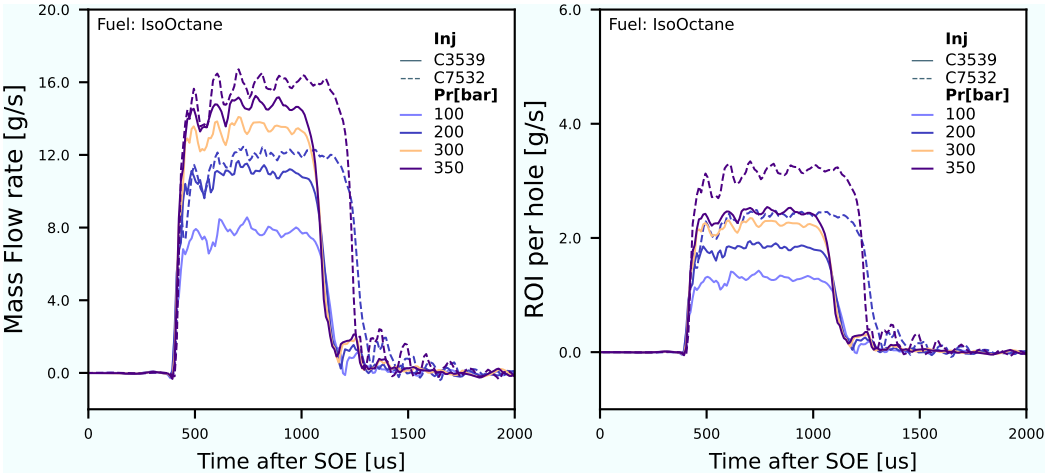


Figure 4.6: Effect of the injector pressure for both injectors using IsoOctane.

The transient parts of the injection are more important with time since it is not enough to know the stable mass flow rate to define the total injected mass, which impacts the fuel metering. The duration as a function of the injection pressure also needs to be considered nowadays.

In the figure, SOI for both injectors is the same, showing a similar performance of the needle opening for all pressures. However, the closing of the figure shows a slight difference, with a steeper close for higher pressures, which makes sense because higher pressures favor the closing of the valve [6].

On the other side, the hydraulic response is different for the injectors. For the pressures tested in both injectors (200 and 300 bar), the ROI in the C7532 injector was higher, and the hydraulic duration increased for the same energizing time.

This contrast is more evident when accounting for the number of holes, in which the dashed lines are considerably higher than the continuous ones for the same color.

Ambient pressure effect

Figure 4.7 depicts slight differences between the ROI at different ambient pressures and can be attributed to differences in measurement. The opening presents some changes in the overshot that is more pronounced for lower back pressure, and as it increases, the opening overshot is smoother.

The changes presented by the ambient pressure changes at the same injection pressure do not present an important variation on the ROI. This suggests that the pressure drop magnitude induced by this the back pressure changes usually found in GDI engines are not determinant to the ROI and the injection pressure is the leading parameter in modern technologies [7].

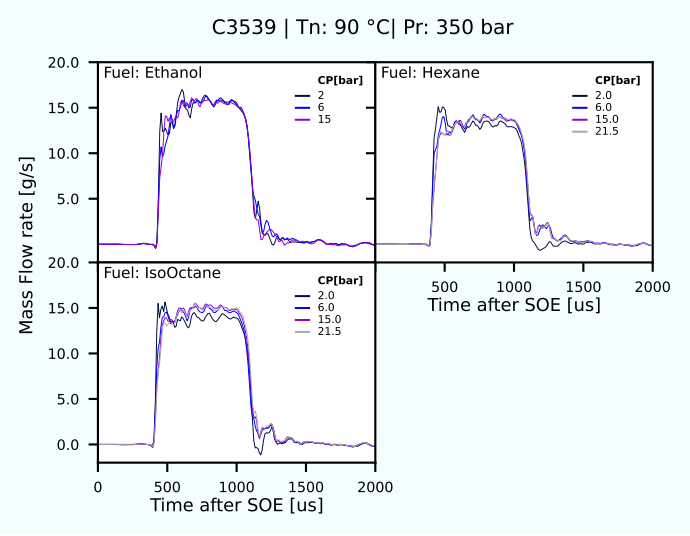


Figure 4.7: Ambient pressure comparison for the C3539 injector at 200 bar of injection pressure.

Fuel temperature

Figure 4.8 and Figure 4.9 show the temperature effect for the injectors studied at the different fuels. Here, two important changes can be visualized in two sections of the ROI curves; first, elevating the temperature results in the stable mass flow rate increasing towards the second half of the injection, and for the C3539 injector, the injection duration also increases. For the Ethanol, the SOI is advanced for the higher temperature.

The SOI is defined by the hydraulic delay, which is the difference between the moment the electric signal is sent to the injector and when the actual

injection starts. This delay is affected by several factors, the fuel viscosity, and needle lift, among others. The shorter SOI might be because of the changes in the viscosity [8, 9]; for lower viscosity, the needle movement is faster, allowing the fuel to come out quicker. The effect is more evident for the ethanol, presumably due to the magnitude of each fuel viscosity variation depending on the temperature. For Hexane, for instance, the viscosity decreases around 43 % when increasing the temperature, on the other side, for Fthanol, the diminution is 69% [10].

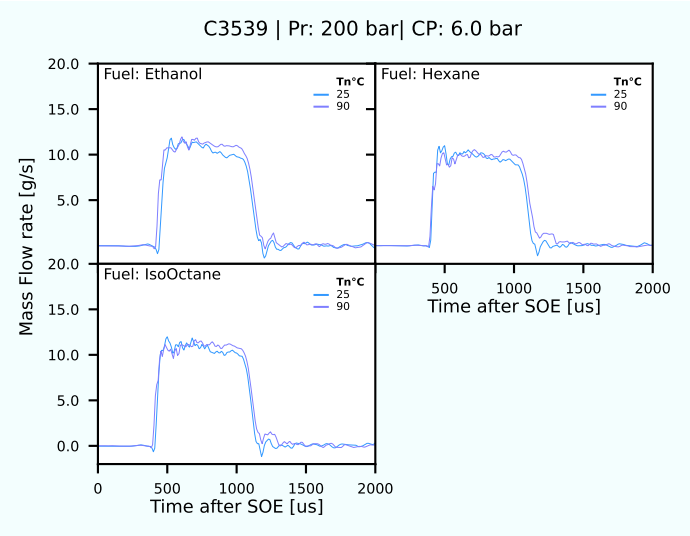


Figure 4.8: Nozzle Temperature effect in the ROI for different fuels with the C3539 injector

4.3.4 Fuel Effect

The following analysis directly explores the impact of the three fuels in Figure 4.10, where two notable distinctions emerge from this figure: disparities observed in both the transient and stabilized sections of the signal.

Regarding the transient phase, Ethanol exhibits a distinctive characteristic: the curve is displaced towards the right side of the time axis, featuring a delayed SOI. Furthermore, discernible differences in the stabilized section of the signal are observed, with Ethanol consistently registering higher values than the other fuels, which is particularly evident at higher injection pressures. Notably, Hexane consistently exhibits lower values across all operating conditions compared to both IsoOctane and Ethanol fuels.

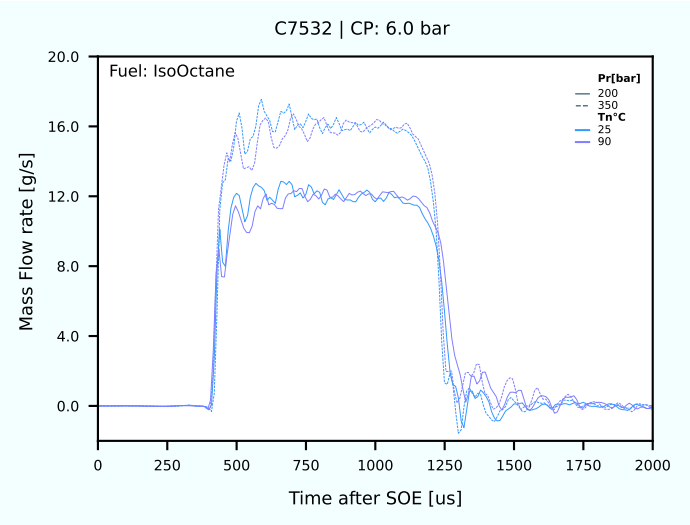


Figure 4.9: Nozzle Temperature effect in the ROI for different fuels with the C7532 injector.

This different behavior seen for Ethanol might be due to the fuel properties as previously described in chapter 3 and recalled in Table 4.4.

Table 4.4: Fuel Properties.

Fuel	Density [kg m^{-3}]	Viscosity [mPa s]	Boiling Point [°C]
IsoOctane	690.3	0.47	99.26
Hexane	654.78	0.22775	68.71
Ethanol	789.1	1.074	78.35

* at ambient temperature.
Source [10–12].

To start with, Ethanol is the most viscous and densest fuel tested, in this sense, the higher viscosity slows down the needle movement and makes it difficult to reach a complete opening [8, 13].

Considering this trend, the Figure 4.11 displays a more comparable scenario by adding another temperature in the plot. For all cases, both the retarded SOI and the smoother initial curve slope are more noticeable when operating at lower temperatures, such as ambient temperature. As seen in the previous section, the viscosity decreases at 90 °C, and the SOI is closer to the other fuels. Referring to the higher ROI encountered for the Ethanol, this might be due to its density, which can be rationalized through the fundamental equation Equation 3.4 relating the ROI and the fuel densit. This trend was also encountered by Payri et al. [14] for two fuels analyzed.

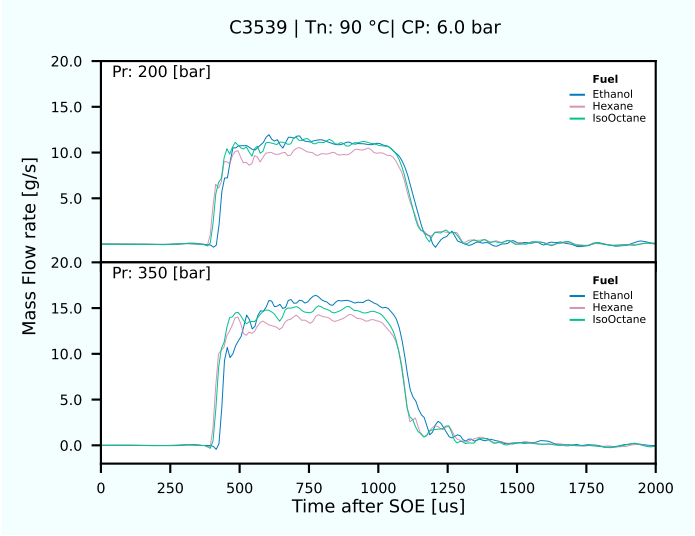


Figure 4.10: Effect of the fuel on the ROI. The condition shown is for 6 bar of ambient pressure, 90 °C of injection temperature, and 200 and 350 bar of injection pressure

To better observe the changes in the stabilized ROI, Figure 4.12 condenses the information for all fuels. The values are obtained by averaging the ROI in the 50% of the injection duration, between the vertical dashed lines depicted in Figure 4.5. The plots are divided by the injection pressure to improve the understanding of it since it is the most differential parameter. The values are plotted against the square root of the pressure drop, following the aforementioned Equation 3.4.

4.4 Rate of Momentum results

4.4.1 Test matrix summary

The values measured in this experimental campaign are similar to those made for the Rate of Injection. In comparison, two new ambient pressures are introduced, specifically sub-atmospheric pressure conditions, to expand the range of superheating degree (R_P) values under examination. This experimental campaign encompasses a total of 94 operating conditions as described in Table 4.5 and thoroughly presented in the Appendix A.

By incorporating measurements under sub-atmospheric conditions, the project aims to evaluate the impact of flash boiling on the Rate of Momentum. Besides normal injection conditions with R_P values from 0 - 1, different

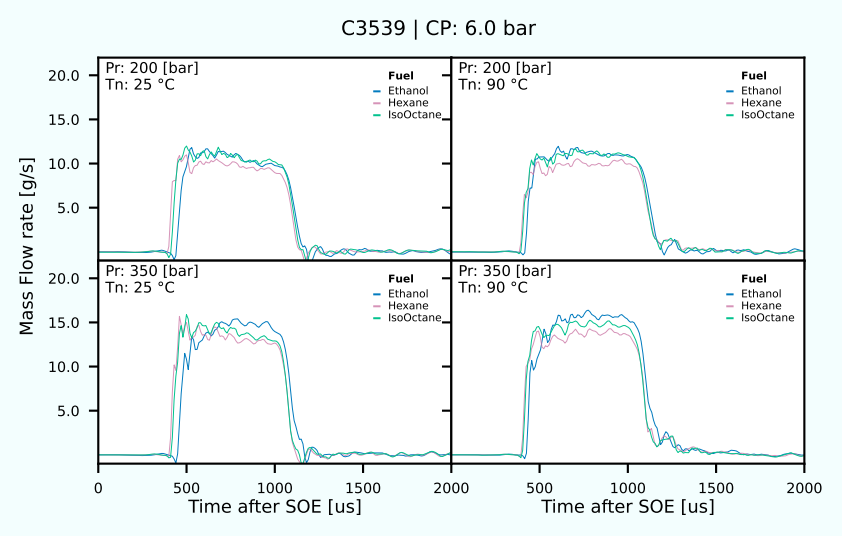


Figure 4.11: Effect of the fuel on the Rate of injection. Rail pressure varied row-wise and nozzle temperature column-wise.

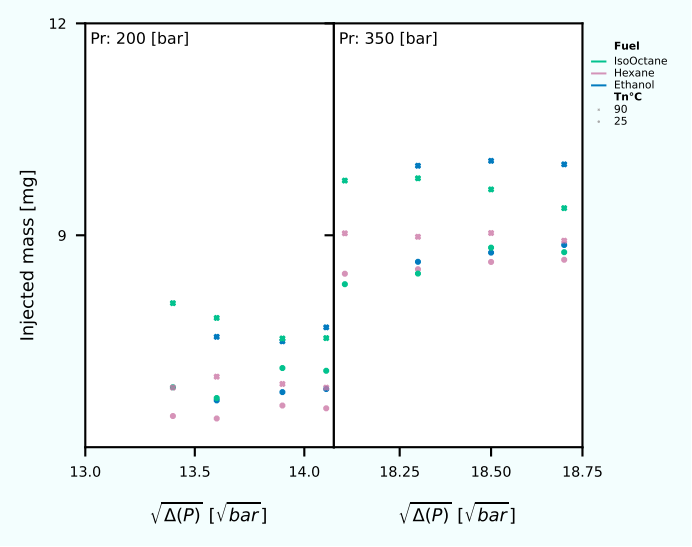


Figure 4.12: Injected mass as a function of the square root of ΔP

Table 4.5: Conditions to be tested: Rate of Momentum

Parameter	Operating Value	Units	Abbreviation
Fuel	IsoOctane - Hexane - Ethanol	-	$Fuel$
Injectors	C3539 - C7532	-	Inj
Rail pressure	50* 100* - 200 - 350	bar	P_r
Ambient pressure	0.2-0.5-1-6-15-21.5*	bar	P_b
Injector temperature	25 - 90	°C	T_n
Ambient Temperature	25	°C	T_b
Energizing time	800	µs	ET
Injection frequency	10	Hz	-
Injection cycles	50	-	-

** For a particular condition*

levels of flash boiling can also be encountered with values slightly above one, a few others near the value where the strong flash boiling starts, and other operating values at very high R_P.

Sensor target location

As outlined in section 4.2, ensuring capturing the entire spray by the sensor target is imperative. The distance was chosen so it allowed to place the sensor while being confident that the impingement area of the spray is smaller than that of its target.

This assurance of proper sensor target placement is confirmed through a separation analysis. For one set operating condition momentum measurements were conducted within a range of distances from 1 mm to 5 mm between the sensor target and the nozzle tip. The maximum distance was determined based on the maximum core angle of the spray. As depicted in Figure 4.13 consistent measured values are observed when the spray is fully captured within, conversely, when the sensor is positioned too far from the spray, a decrease in momentum is noted, indicating potential loss of parts of the sprays. The distance selected was 2.1 mm.

4.4.2 Injector differences

Figure 4.14 elucidates the injector disparities in ROM, by showing on the left side of the figure the global momentum measured and corrected for each injector, while the right side illustrates momentum plotted for each orifice, under the assumption of uniform contribution to the overall force.

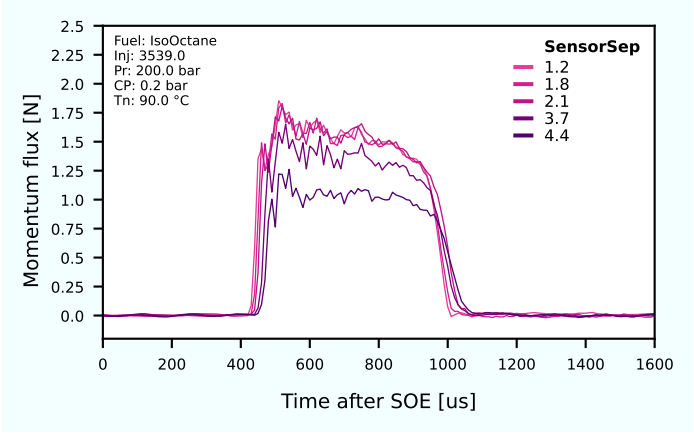


Figure 4.13: Sensor to injector separation assessment

The analysis reveals that the global rate of momentum for identical conditions is higher for the C7532 nozzle. Despite exhibiting similar design, the two injectors have different hydraulic durations for the same energizing time.

The differences in performance are evident for the ROM at each injection pressure. However, when analyzed on a per-hole basis, the differences are more remarked. These variations are likely attributable to differences in hole area.

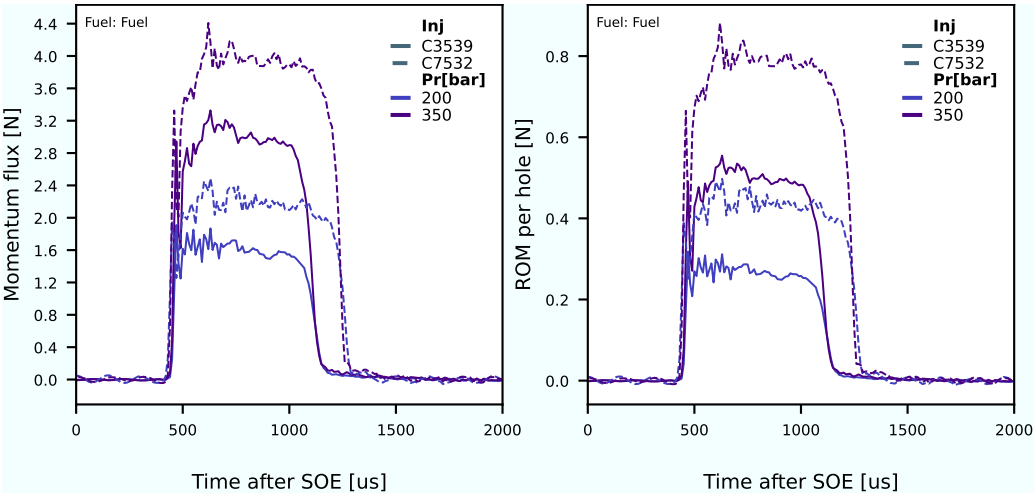


Figure 4.14: Injection pressure effect for both injectors.

4.4.3 Fuel Effect

Figure 4.15 focuses on examining the influence of different fuels, on the momentum flux, with particular emphasis on the C3539 injector. The layout of the figure has fuel temperature variations from left to right. Similarly, the upper row illustrates results obtained at a lower injection pressure of 200 bar, while the lower row depicts outcomes at higher injection pressures. The shades represent the standard deviation for the averaged repetitions.

The analysis indicates minimal variations in momentum flux among the fuels studied, particularly for Hexane and IsoOctane, serving as gasoline surrogates in this study. However, noteworthy differences are observed for Ethanol, particularly at low nozzle temperatures and high injection pressure. This behavior was observed across all the measured ambient pressures. At ambient nozzle temperature, the start of injection for Ethanol is delayed compared to other fuels, consistent with findings from the ROI analysis. Furthermore, it is observed that the overshot during the opening phase is higher at lower injection pressures. These alterations in the SOI for Ethanol are attributed to its higher viscosity, in alignment with theoretical equations where momentum is solely dependent on area and pressure drop.

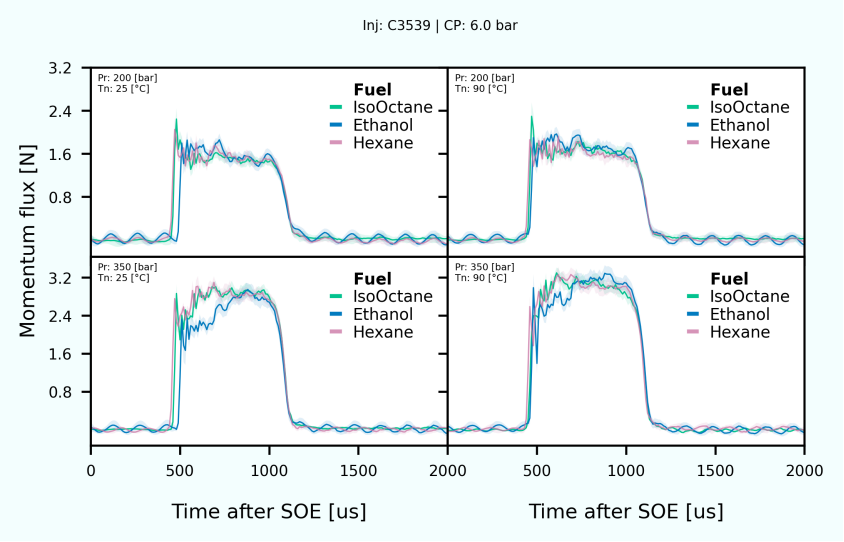


Figure 4.15: Fuel effect under several conditions.

4.4.4 Fuel temperature influence

The nozzle temperature let alone also plays an important role in GDI injectors with very volatile fuels. In this case, the analysis of Figure 4.16 the nozzle temperature variations reveals subtle discrepancies in the ROM between ambient temperature and high nozzle temperature conditions, specifically, higher ROM is observed for the latter. Additionally, slight differences are noted in the transient parts of the injection signal. Here, the closing transient is slightly longer for the higher nozzle temperature. For higher momentum results in a slower decrease during the closing phase. Notably, these trends are more pronounced for Ethanol compared to other fuels.

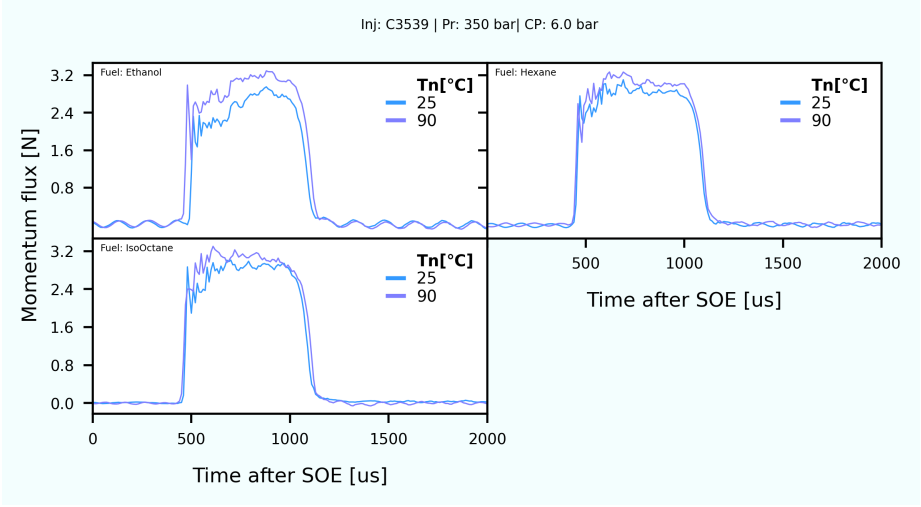


Figure 4.16: Influence of the nozzle temperature on the rate of momentum at 6 bar of ambient pressure in the C3639 nozzle.

4.4.5 Ambient pressure impact

The ambient pressure measurements analyzed in this study are presented in Figure 4.18, focusing on results obtained at an injection pressure of 200 bar using the C3539 injector.

For the discharge pressures of 6 bar, 15 bar, and 21.5 bar, the figure reveals very similar trends with only minor variations in the maximum rate of momentum and transient phases. This is consistent with results found by Shahangian et al. [15], and these minor differences are attributed to changes in ambient discharge density, as also noted by Payri et al. [7]. These studies

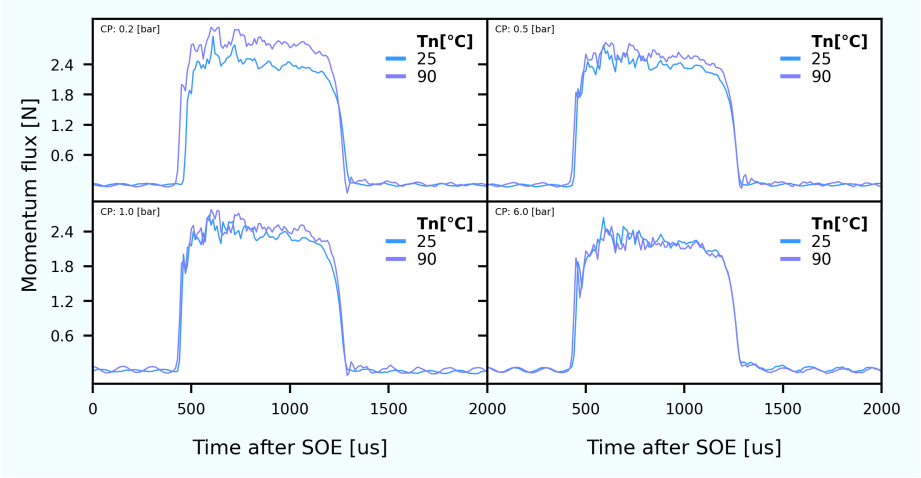


Figure 4.17: Influence of the nozzle temperature on the rate of momentum at several ambient pressures for the C7532 nozzle.

proposed that air entrainment could have a small influence on the momentum measurements.

Payri et al. [7] investigated the effect of ambient gas density by using different gases under identical conditions and observed notable differences in the momentum measurements. The assumption was that these variations were mainly due to differences in entrainment behavior. However, since the momentum flux technique captures both the liquid and gaseous contributions to the force, differences caused solely by changes in ambient density should, in principle, be less pronounced. This suggests that additional variables must be considered.

Flash boiling conditions

Variables that might be affecting the trend in the results include the influence of superheated conditions. In this sense, the ROM correction by the core angle variation must also be considered when approaching these comparisons (Equation 3.18). Considering that the variations found for the core angles at 25 °C of fuel temperature were not very notable, the differences seen in Figure 4.18 could be attributed either to the angle used in the correction or to the changes in chamber density.

Now for the conditions seen in Figure 4.18 at 25 °C of fuel temperature, which represent non-flashing conditions where the R_P values are consistently

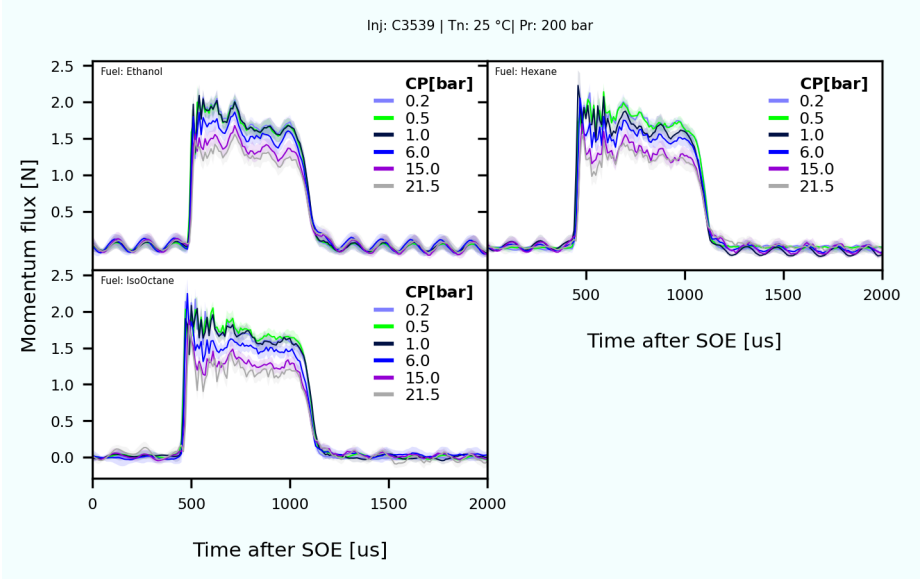


Figure 4.18: Ambient pressure effect on the C3539 nozzle for non-flashing condition.

below 1, a clear trend is observed: as back pressure increases, the ROM decreases. Conversely, in Figure 4.19, with a nozzle temperature of 90 °C, which depicts flash boiling conditions at under-pressures (0.2 and 0.5 bar). As summarized in Table 4.6, a wider range of R_P values is observed under these flash boiling conditions, including values both below and above 1 for all fuels tested, particularly Hexane and Ethanol, the full dataset, including all measured R_P values, is provided in the Appendix (section A.1).

The behavior of the momentum flux under these conditions is similar to that under non-flashing conditions but with even smaller variations. This supports the idea that flash boiling is not the primary driver of the ROM behavior seen in Figure 4.18.

Another variable known from previous studies to influence spray angle and spray width is the ambient gas density, i.e., the backpressure. In the context of this work, angle assessments have shown variations of approximately 1.5 degrees under identical ambient conditions. Furthermore, the literature typically reports angle differences in the range of 1 to 2 degrees, and in some visualizations, spray widths vary by up to 2 to 5 degrees depending on the ambient density [16]. However, when such variations are incorporated into the standard deviation of the repetitions, the shaded uncertainty bands in the ROM plots do not significantly overlap. This suggests that while ambient

Table 4.6: Test conditions and corresponding R_P values for injector C3539 at $T_n = 90°C$ and $P_r = 200$ bar.

Injector	**Fuel**	T_n [°C]	P_r [bar]	P_{CP} [bar]	R_P
C3539	Ethanol	90	200	0.2	7.903
C3539	Ethanol	90	200	0.5	3.161
C3539	Ethanol	90	200	1	1.581
C3539	Ethanol	90	200	6	0.263
C3539	Ethanol	90	200	15	0.105
C3539	Ethanol	90	200	21.5	0.074
C3539	Hexane	90	200	0.2	9.450
C3539	Hexane	90	200	0.5	3.780
C3539	Hexane	90	200	1	1.890
C3539	Hexane	90	200	6	0.315
C3539	Hexane	90	200	15	0.126
C3539	Hexane	90	200	21.5	0.088
C3539	IsoOctane	90	200	0.2	1.671
C3539	IsoOctane	90	200	0.5	0.668
C3539	IsoOctane	90	200	1	0.334
C3539	IsoOctane	90	200	6	0.056
C3539	IsoOctane	90	200	15	0.022
C3539	IsoOctane	90	200	21.5	0.016

density may slightly affect spray geometry, such small angle differences are insufficient to explain the observed ROM variations on their own.

Nevertheless, accurately identifying the location of the highest momentum zones becomes increasingly complex under varying backpressure conditions. In this chapter, the correction applied was based on spray angle assessment that considered only the geometric characteristics of the jet itself, without accounting for variations introduced by different ambient pressures. As will be shown in the following chapter, even the regions of highest velocity near the nozzle do not necessarily align with the angles measured or with the nominal drilling angle of the orifice. Moreover, no clear monotonic relationship was found between regions of high velocity and the ambient pressure, which complicates the identification of a single dominant cause for the observed ROM differences.

This leads to an important methodological reflection: the assumption that the location of maximum velocity within the spray corresponds to the direction or orientation of the overall momentum may not hold true in all cases. While it is generally expected that the central region of the spray exhibits the highest

axial velocity, this does not necessarily imply that it contains the highest momentum. Momentum is a function of both mass and velocity, and a small number of fast droplets in the core may be less significant than a larger mass of slower-moving droplets located elsewhere in the spray.

Therefore, identifying the angle of maximum velocity alone may not fully capture the real direction of momentum transfer, especially under flashing or collapsing conditions. This limitation is particularly relevant when analyzing sprays from multi-hole injectors, where collapse and interaction between adjacent jets can distort both the perceived spray angle and the actual momentum distribution.

Finally, all of this suggests that the spray angle remains one of the principal variables influencing the observed differences in ROM, as it directly determines how the force is projected and measured on the target. However, the role of ambient density cannot be ruled out, either as a direct contributor or through its indirect effect on spray angle. It is well established that density variations modify the spray structure and angle, and using a single fixed angle for ROM correction introduces uncertainty. Since no consistent correlation has been found between backpressure and angle, it is possible that other phenomena, such as air entrainment and jet interaction, also influence the momentum distribution. For this reason, future ROM measurements could benefit from the use of lighter ambient gases, such as helium, which may reduce the interplay between density-driven effects and momentum behavior, allowing for a more isolated analysis of the core spray dynamics.

4.5 Hydraulic Analysis

4.5.1 Hydraulic coefficients

Having both ROI and ROM results, the flow coefficients can be calculated (subsection 3.3.3) with the equations obtained from the literature [17–19]. These calculations were limited to conditions that were matched for both ROI and ROM.

In Figure 4.20, results of the discharge coefficients at different conditions for each fuel are depicted (note that the C7532 values are only reported for its reference fuel). A unique trend emerges when comparing small variations in the square root of the pressure drop (ΔP). Typically, an increase in the square root of ΔP results in a higher discharge coefficient; however, for this injector type, an inverse correlation was observed: the discharge coefficient decreases as the square root of the pressure drop increases. This behavior is

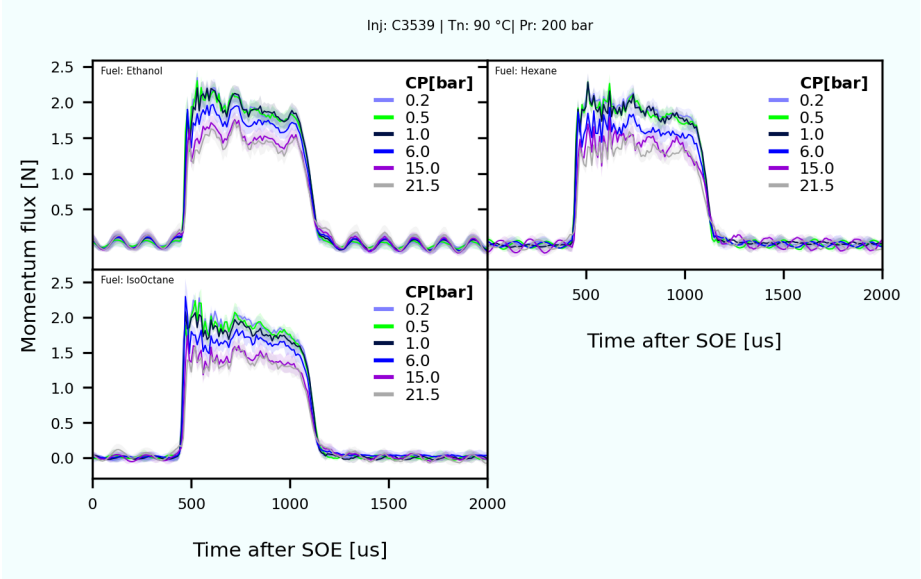


Figure 4.19: Ambient pressure effect on the C3539 nozzle at flashing condition.

consistent across all fuels, especially at higher nozzle temperatures. At lower nozzle temperatures, the values are similar among them. Consider also that the limits in the plots, ranging from 0.5 to 1, may exaggerate the observed differences, which are relatively small. Injector-wise, the C7532 shows a higher discharge coefficient.

On other end, the velocity coefficients (C_V) (Figure 4.21) show the opposite trend when comparing the two injectors: the second injector (5 orifices) has higher nozzle C_V. The velocity coefficient increases consistently with the square root of the pressure drop under all conditions, with this variation being more pronounced at lower pressure drops.

When comparing the effective velocities for different fuels in Figure 4.22, no significant differences are observed. The velocities for each injector align with the velocity coefficients, showing higher velocities at higher pressure drops, which are considerable in these cases.

4.6 Summary and conclusions

Investigations on the different parameters that have a remarkable influence on the rate of injection (ROI) and rate of momentum (ROM) have been realized. Several back pressures and injection pressures were studied for two

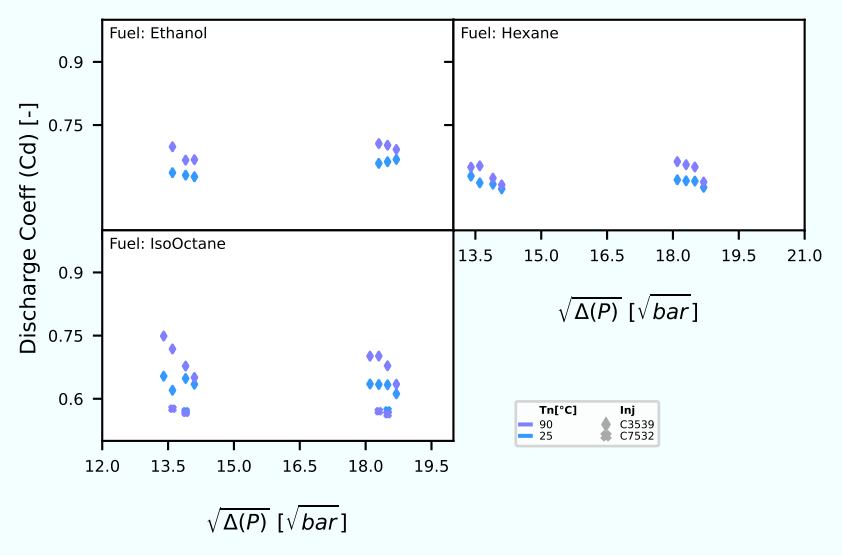


Figure 4.20: Discharge coefficients for the various conditions.

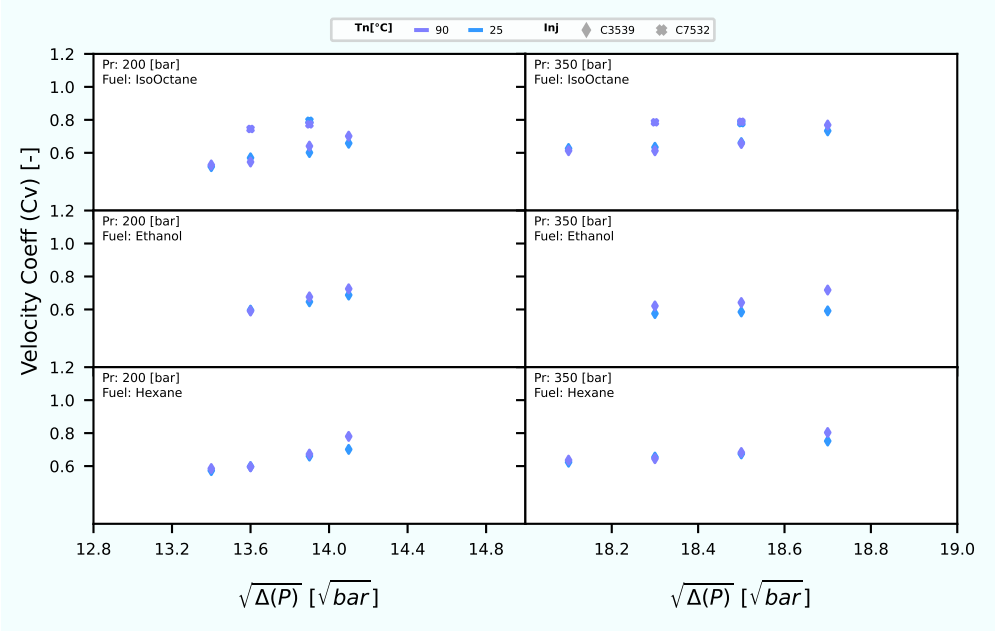


Figure 4.21: Velocity coefficients for the conditions measured.

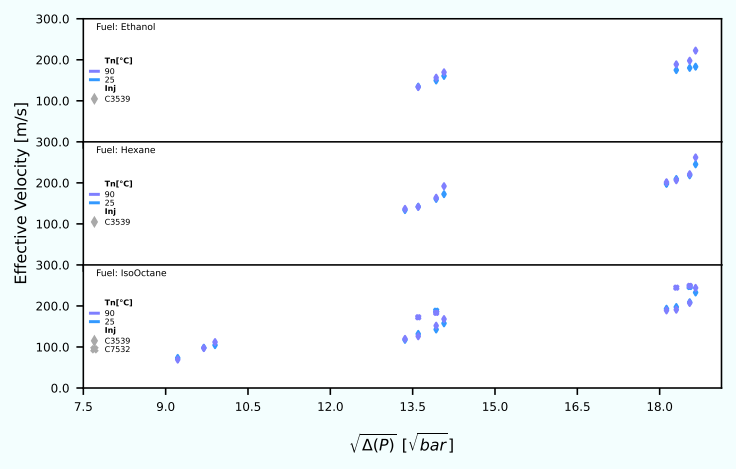


Figure 4.22: Effective velocity for the conditions measured.

nozzle temperatures, three fuels, and two GDI injectors with different number of orifices. The fuels studied are two paraffin mono components of the commercial gasoline, and one alcohol (Ethanol). The injection variables were chosen aiming at the conditions found in the normal functioning of an engine pursuing the to analyze flash boiling conditions.

- Different techniques were employed to obtain the hole shape and diameter. High-resolution microscopic images of the silicone molds provided detailed views of the internal geometry, including orifice diameters and conicity.
- The ROI did not have a significant change for the surrogates. It was only slightly different for the ethanol. The effects of this fuel are presumed to be because of its higher density and viscosity. In agreement with the literature, denser fuels are likely to increase the ROI, with the viscosity changing the transient opening and closing of the signal, not only in its needle lift velocity but also in the delay of the start of injection.
- For the injection pressure and nozzle temperature: as the injector pressure increased, the ROI and ROM rose as well. On the other side, augmenting the temperature increased the injection duration due to the reduction of the fuel viscosity.
- Slight differences seen in the global ROM which aligns with previous studies employing a similar technique in GDI multi sprays. While uncertainties in the correction angle influence the result, the ambient density

also possibly plays a role in the experiment, as previously reported in the literature.

- The ROM did not suffer significant changes for the fuels. Again, the ethanol induced a delay in the SOI for cold conditions.
- The flash boiling conditions did not influence a significant change to the ROM measurements. The pressure drop was the main driving variable.
- The discharge coefficient (C_d) for the C7532 injector depicted higher values than the C3539 injector. Even though for both injectors, the Cd did not vary much with the pressure drop, for the C3539, the Cd decreased for higher ΔP.

References

[1] Engine Combustion Network. *https://ecn.sandia.gov/diesel-spray-combustion/*. Online. 2010.

[2] Macian, V., Payri, R., Margot, X., and Salvador, F. J. "A CFD analysis of the influence of diesel nozzle geometry on the inception of cavitation". In: *Atomization and Sprays* 13 (2003), pp. 579–604.

[3] Sforzo, B. A. et al. "X-ray characterization of real fuel sprays for gasoline direct injection". In: *Journal of Energy Resources Technology* 144.2 (2022), p. 022303.

[4] Tekawade, A. et al. "Time-resolved 3D imaging of two-phase fluid flow inside a steel fuel injector using synchrotron X-ray tomography". In: *Scientific Reports* 10 (2020). DOI: 10.1038/s41598-020-65701-x.

[5] Sforzo, B., Tekawade, A., Matusik, K. E., Kastengren, A. L., and Powell, C. F. "3D Measurements of the Geometry, Internal Flow and Emerging Fuel Jet from the ECN Spray C Injector". In: *ILASS Europe 29th Conference on Liquid Atomization and Spray Systems*. 2019.

[6] Cavicchi, A. and Postrioti, L. "Simultaneous needle lift and injection rate measurement for GDI fuel injectors by laser Doppler vibrometry and Zeuch method". In: *Fuel* 285 (2021), p. 119021.

[7] Payri, R., Gimeno, J., Martí-Aldaraví, P., and Vaquerizo, D. "Momentum Flux Measurements on an ECN GDi Injector". In: *SAE Technical Paper 2015-01-1893*. 2015, p. 11. DOI: 10.4271/2015-01-1893.

[8] Salvador, F. J., Gimeno, J., Carreres, M., and Crialesi-Esposito, M. "Fuel temperature influence on the performance of a last generation common-rail diesel ballistic injector. Part I: Experimental mass flow rate measurements and discussion". In: *Energy Conversion and Management* 114 (2016), pp. 364–375. DOI: 10.1016/j.enconman.2016.02.042.

[9] Medina, M., Bautista, A., Wooldridge, M., and Payri, R. "The effects of injector geometry and operating conditions on spray mass, momentum and development using high-pressure gasoline". In: *Fuel* 294.December 2020 (2021), p. 120468. DOI: 10.1016/j.fuel.2021.120468.

[10] Pérez-Ones, O., Díaz-Rodríguez, J., Zumalacárregui, L., and Gozá-León, O. "Evaluación de propiedades físicas de mezclas etanol-agua (II)". In: *Revista Facultad de Ingeniería Universidad de Antioquia* 52 (2010), pp. 62–74.

[11] Lemmon, E. W., Bell, I., Huber, M., and McLinden, M. O. "Thermophysical Properties of Fluid Systems". In: *NIST Standard Reference Database Number 69*. Ed. by P. J. Linstrom and W. G. Mallard. Gaithersburg MD, 20899, USA.: National Institute of Standards and Technology, 1998. DOI: https://doi.org/10.18434/T4D303.

[12] Engine Combustion Network. *Spray G Parametric Variation*. https://ecn.sandia.gov/gasoline-spray-combustion/target-condition/spray-g-parametric-variation/. Online; accessed 29 April 2020. 2020.

[13] Dernotte, J., Hespel, C., Foucher, F., Houillé, S., and Mounaïm-Rousselle, C. "Influence of physical fuel properties on the injection rate in a Diesel injector". In: *Fuel* 96 (2012), pp. 153–160. DOI: 10.1016/j.fuel.2011.11.073.

[14] Payri, R., Garcia, A., Domenech, V., Durrett, R. P., and Plazas, A. H. "An experimental study of gasoline effects on injection rate, momentum flux and spray characteristics using a common rail diesel injection system". In: *Fuel* 97 (2012), pp. 390–399. DOI: 10.1016/j.fuel.2011.11.065.

[15] Shahangian, N. et al. "Spray Orientation Assessment and Correction Method for GDI Momentum Flux Measurements". In: *"17th Conference. The Working Process of the Internal Combustion Engine"*. 2019, pp. 231–241.

[16] Bautista Rodríguez, A. "Study of the Gasoline Direct Injection Process under Novel Operating Conditions". PhD thesis. Universitat Politècnica de València, 2021.

[17] Payri, R., Gimeno, J., Martı-Aldaravi, P., and Viera, A. "Measurements of the mass allocation for multiple injection strategies using the rate of injection and momentum flux signals". In: *International Journal of Engine Research* (2020). DOI: 10.1177/1468087419894854.

[18] Cavicchi, A., Postrioti, L., Berni, F., Fontanesi, S., and Di Gioia, R. "Evaluation of hole-specific injection rate based on momentum flux measurement in GDI systems". In: *Fuel* 263.November 2019 (2020). DOI: 10.1016/j.fuel.2019.116657.

[19] Gimeno, J. "Desarrollo y aplicación de la medida de flujo de cantidad de movimiento de un chorro Diesel". PhD thesis. E.T.S. Ingenieros Industriales, Universidad Politécnica de Valencia, 2008. DOI: 10.4995/Thesis/10251/8306.

Chapter 5

Microscopic characterization: Measurement baseline

5.1 Introduction

The next step to observe the spray characteristics is introducing the GDI (Gasoline Direct Injection) spray shape structure. Essentially, it is important to examine the patterns observed in the sprays and the conditions used in the process. Given the remarked changes in the spray patterns, this chapter explores those observed under different conditions. This includes results of the spray visualization campaign and analysis of key characteristics such as penetration and spray width.

The first part of this chapter establishes an overview of the standard conditions under which droplet velocities and sizes are measured, laying the groundwork. A critical part of this chapter is the evaluation of the experimental facility influence on the measurement outcomes, the impact of the vessel windows orientation on PDPA measurement set-up. Then it follows a discussion of the methodology used to precisely locate the spray of interest, which is essential for consistent data collection. Finally, the chapter includes results of the visualization campaign of the spray and analysis of key characteristics such as penetration and spray width

Overall, this chapter on one hand, introduces the type of sprays encountered and being under scrutiny, and on the other hand, it lays the groundwork

for understanding the behavior of droplets in standard conditions and subsequent more complex and critical injection scenarios.

5.2 Test Matrix

The test matrix used during both the visualization and Phase Doppler Anemometry (PDA) measurements is presentd in the Table 5.1. The table presented outlines the various conditions and parameters explored throughout the study. Specifically, it details the changes to the chamber ambient conditions, including ambient temperature and pressure, alongside variations in injection pressure and temperature.

Table 5.1: Conditions to be tested: PDPA measurements

Parameter	Operating Value	Units	Abbreviation
Fuel	IsoOctane - Hexane - Ethanol*	-	$Fuel$
Injectors	C3539 - C7532	-	Inj
Rail pressure	50* 100* - 200 - 350	bar	P_r
Injector temperature	25 - 90 - 110	°C	T_n
Ambient pressure	0.2*-0.5-1-6-12*	bar	P_b
Ambient Temperature	25 - 60 - 120	°C	T_b
Energizing time	800	µs	ET
Injection frequency	0.5	Hz	-
Injection cycles recorded by the camera	10	-	-

* For particular conditions

The operating conditions for the fuel injector were defined with particular emphasis on ensuring accurate pressure and fuel temperature during the injection process. The control of these parameters was deemed essential to obtain consistent and reliable measurements. The main measurement points corresponding to these variations are depicted in Figure 5.1, the points are marked on the plot, and allow direct comparison with the vapor pressure curves of each fuels. Several measurement points fall well above the phase boundary, indicating operation clearly within the liquid phase. In contrast, other points lie beneath the curve, within the vapor region, and are associated with strong flash boiling conditions. This graphical representation serves to contextualize the thermodynamic state of each injection scenario relative to the fuel's phase behavior.

The nominal injection temperature targeted during the experiments was 120°C. However, due to limitations in the oil heater system, it was not possible to reach this value consistently, and the injection temperature was stabilized around 110°C.

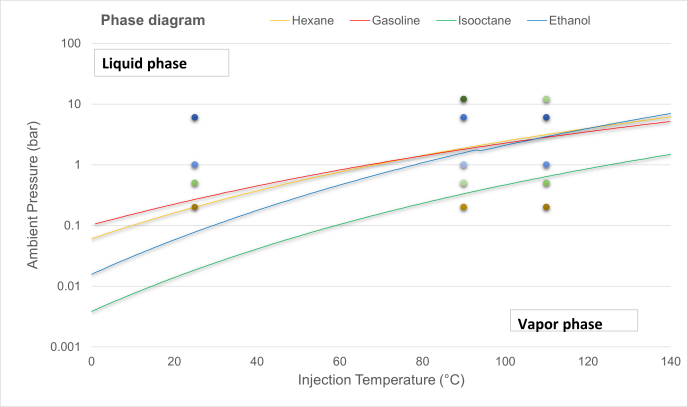


Figure 5.1: Phase diagram showing the measurement points and the phase curve for each studied fuel and the typical commercial gasoline. Adapted from [1, 2] with data from the National Institute of Standards and Technology (NIST) [3].

To capture the dynamics of the injection process, videos were recorded in accordance with the methods outlined in the methodology section, where ten repetitions were performed to ensure both repeatability and precision of the measurements. Subsequent to the video recordings, Phase Doppler Anemometry (PDA) measurements were employed to assess the atomization characteristics of the fuel spray. The central objective of this phase is to offer a detailed evaluation of the injector's performance under varying conditions, with insights drawn from both the video data and the PDA results.

The number of injections during the Phase Doppler Anemometry (PDA) measurements was deliberately defined to ensure data reliability. After an initial valoration, it was determined that performing 50 injections or counting approximately 20,000 droplets would yield the most reliable and statistically significant results (see section 3.9). Initial analyses of droplet count histograms were conducted for different positions within the spray field, with a particular focus on the central region of the spray, where the operational conditions were inherently more challenging.

These challenging conditions in the spray core revealed that, with fewer injections, it became difficult to gather sufficient droplet counts to discern clear trends in key metrics such as droplet velocity and diameter. By contrast, in regions of the spray with higher data rates, such as the periphery, fewer injections were needed to reach the desired droplet count. These regions allowed for a more efficient data collection process, given that a higher volume of data could be captured in a shorter duration.

In zones characterized by low data rates, even increasing the number of injections did not substantially improve measurement accuracy, suggesting diminishing returns from more injections in these areas. With the downside of increasing the droplet accumulation inside the chamber, complicating the fuel scavenging from the chamber. In this sense, in preliminar approaches, extended injections in low-data-rate areas failed to provide meaningful contributions to the overall measurement.

5.3 Equipment set-up considerations

5.3.1 The effect of optical windows

Upon placing the Phase Doppler Anemometry (PDA) lasers' cross-point inside the vessel, an additional consideration must be addressed. The lasers will traverse through optical glass walls, which alters the laser beams path, when varying the medium relative index.This deviation affects the crossing point of the vertical laser pairs, necessitating precise positioning of the injector nozzle tip, which serves as a reference.

Furthermore, the system's complexity increases since having another pair of lasers (second component) modifies where each pair meets. Specifically, the vertical and horizontal pairs might converge at different points due to the distinct paths traveled through the glass. This discrepancy arises because the optical window is not aligned perfectly perpendicular to the optical axis of the laser emitter and receiver. While Snell's law theoretically predicts this deviation, practical measurements are necessary to assess the impact of using a rotated window [4]; to address these challenges, velocities were measured with and without the windows.

The primary issue encountered was aligning the system. The highest data rate for one laser pair considerably differed from the other pair when the lasers passed through the normal wall. This misalignment meant that the point of maximum data rate for one component did not coincide with that of the other, requiring a decision to prioritize one component or measure them separately. Consequently, the measurement volumes of the laser pairs did not match.

To solve this, a rotated window was designed and implemented, ensuring the glass was perpendicular to the optical axis of the laser emitter and receiver. The use of rotated windows significantly enhanced the alignment process, enabling more precise focusing of the laser components and minimizing alignment errors without notably affecting velocity measurements. Comparisons between measurements taken with and without windows revealed only

minor differences, indicating the robustness of the setup. However, at high velocities, the quality of measurements declined due to reduced data collection at the spray center, likely caused by the interaction of the laser beam with the window.

5.3.2 Rotated windows configuration

Two windows were designed with an angle was selected to ensure that the laser and receptor optical axes are orthogonal to the windows Figure 5.2. The integrity and safe performance of the windows were tested with a similar approach as [1] using Finite Element Analysis(FEA) in ANSYS to minimize the windows' weight and size and maintain the ability to tolerate the same conditions as in the original setup.

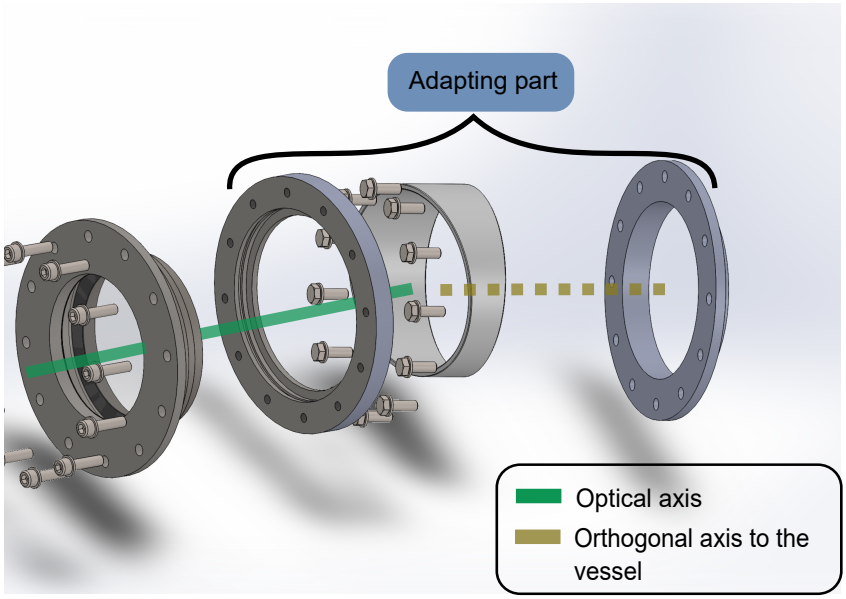
Before the measurement campaign started, leak and safety tests were carried out to guarantee that the facility could safely withstand the target conditions.

5.3.3 PDPA set-up values

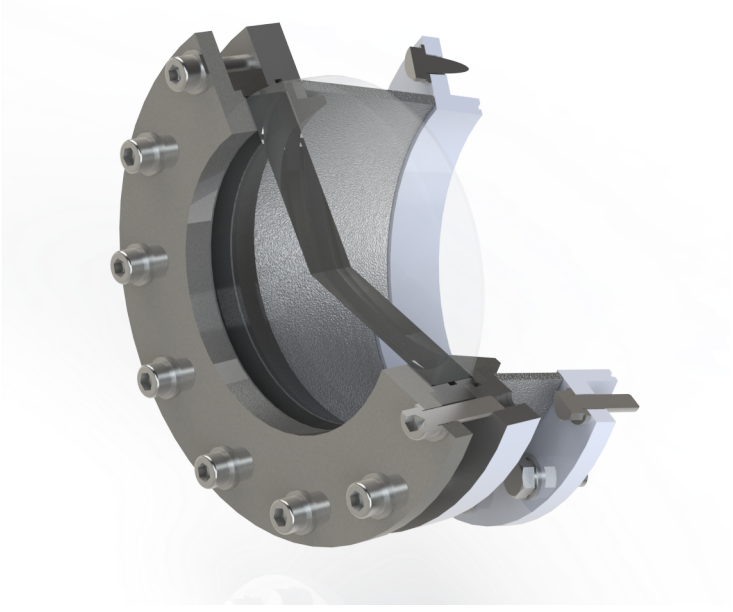
The final PDPA setup parameters employed are shown in Table 5.2:

Parameter	**Value(s)**	**Unit**
Bragg cell frequency (frequency shift)	80	MHz
Beam separation at the frontal lens	60	mm
Transmitting optic focal length	310	mm
Beam diameter ($1/e^2$) at the frontal lens, after beam expander	1.8	mm
Receiving optic focal length	500	mm
Scattering angle	30/150	°
Slit aperture	100, 50	μm
Velocity range	-36 to 300 and -36 to 244	m/s
Diameter range	up to 64	μm

Table 5.2: Key Parameters and Values



(a) Rotated window parts for rotating the optical window.



(b) Rotated window assembly.

Figure 5.2: Optical axis rotation for PDA measurements.

5.3.4 Spray axis location methodology

Velocity measurements using PDA are carried out spatially, meaning that velocities are recorded at multiple positions throughout the spray field. In the literature, this is done using various approaches. In many cases, the design angle of the nozzle orifices is used as a reference for aligning the measurements, and others, more realistic methodologies are applied in which the spray is first visualized using a high-speed camera, and through post processing, the centroid of the jet is determined relative to a fixed laser position, providing an initial reference for locating the spray core [5].

In GDI sprays such as those analyzed in this study, it has been observed that the location and direction of the jets, particularly in multi-hole injectors, can vary depending on the injection conditions. Due to this variability, more robust, comparable and reliable methods are needed to consistently identify the jet positions. In this context, the methodology adopted here defines the center of each jet as the point of maximum velocity, measured through a structured spatial mesh. For example, Figure 5.3 shows the measurement positions for locating the center of the spray at different axial positions. A fixed physical point for the PDPA laser is used as reference for the traverse positioning system in relation to the measured coordinates.

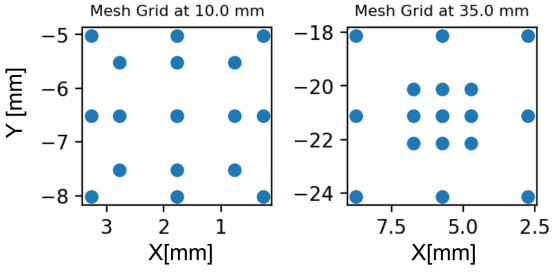


Figure 5.3: Spray location Grid.

This process involves scanning velocity values in a grid pattern across a cross-sectional plane near. Under lower injection pressures, velocities are recorded at each point with high data rate collection, and Python-based internal developed codes are then used to identify the positions of peak velocity Figure 5.4. For construction of the velocity map, the average velocity during the quasi-stationary phase of the spray is calculated. To do so, the start of injection is first identified using an internal-built methodology, which is conceptually similar to the approach used for interpreting rate of injection curves. Once the onset of the injection event is detected for the main part of the signal,

this information is used to define a quasi-stationary window centered around the core of the injection duration, comprising the central 50% of the injection event.

By repeating this process at different axial planes, the inclination angle of each spray plume can be constructed, enabling the characterization of spray orientation relative to both the laser alignment and the PDPA measurement system.

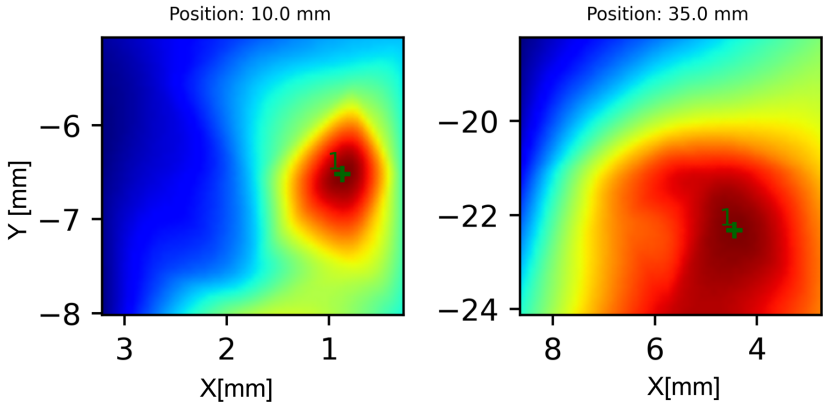


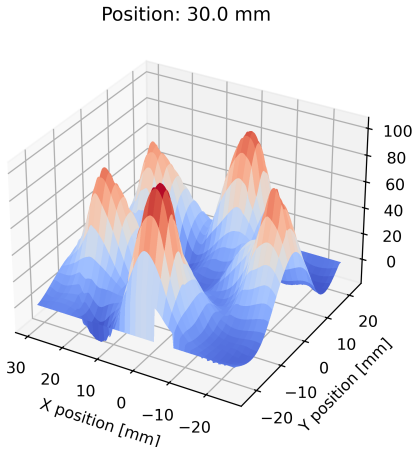
Figure 5.4: Axis location velocity map.

This tracking process can be extended to a plane below the injector and identify all the spray jets. An illustrative example is shown in Figure 5.5, where the highest velocities for each jet are identified in a single measurement plane for one of the injectors. The distribution of all spray plumes is clearly visible, helping to explain the spray structure under the given injection conditions.

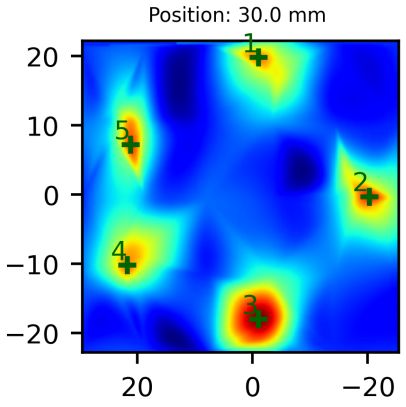
These points correspond to the number of jets expected and allow the mapping of jet centroids across multiple axial positions. Importantly, this approach not only enables the spatial distribution of velocities to be characterized, but it also offers the potential to map droplet sizes across the same measurement plane. As such, both velocity and droplet size data can be extracted in a coordinated spatial framework, enhancing the analysis of atomization behavior in complex multi-hole GDI sprays.

5.3.5 Plume location variability with operating conditions

Due to the change in the operating conditions, the spray shape also is affected. In the Figure 5.5 if the sprays location varies considerably with the operating



(a) Sprays' location in 3D view at 30 mm for the C7532 injector



(b) Sprays' location footprint at 30 mm for the C7532 injector

Figure 5.5: Spray's location

condition, the measurements of velocity and droplet size. will result affected. The main changes are seen with changes in the superheating degree. The results encountered can be summarized in Table 5.3.

Table 5.3: Core angle variation per operating condition.

Injector	T_n [°C]	P_b [bar]	Average [°]
C3539	90	0.2	37.0
C3539	90	0.5	37.0
C3539	90	1	39.9
C3539	90	6	39.7
C3539	90	12	36.6
C7532	90	0.2	28.6
C7532	90	0.5	30.4
C7532	90	1	32.2
C7532	90	6	34.1
C7532	90	12	34.1

The changes found are in a range of 5 degrees among conditions. The results are extended in Figure 5.6, for most of the conditions, the angle values varied in positions closer to the nozzle tip in relation to farther positions by around one degree.

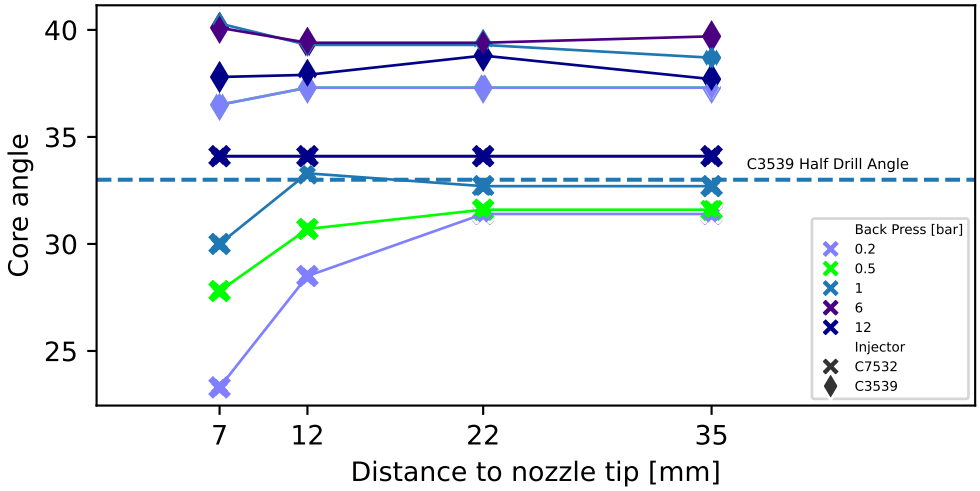


Figure 5.6: Core angle of the spray measured at different ambient pressures for 90 °C of fuel temperature.

On another side, the results show a non-monotonic trend between ambient pressure and spray angle. At low pressures (0.2 and 0.5 bar), the angles are smaller (around 36.5°). At medium pressures (1 to 6 bar), the angles increase to about 40–42°. However, at the highest pressure (12 bar), the angle decreases again to around 37–38°. This behavior suggests that, although higher ambient pressure could increase spray angle due to stronger jet compression, other effects such as partial collapse and flash boiling inside the injector influence the spray direction; which effects are more pronounced in the six hole injector because the holes are closely spaced.

Therefore, the spray angle at the point of maximum velocity does not have a simple relationship with ambient pressure. This indicates that spray orientation is a complex and spatially distributed phenomenon, influenced by multiple interacting factors; and also suggests that these core angle values must be interpreted carefully, since these represent single-point measurements of maximum velocity angle to define spray direction, as it may oversimplify the real spray behavior. Consequently, they may not be the most appropriate in other measurements such as rate of momentum measurements corrections, as discussed in the previous chapter.

In the present work, the location of maximum velocity is used as a reproducible reference for comparative analysis across conditions. This helps identify the presence and displacement of high-velocity regions without relying solely on the nominal drilling axis, which may differ significantly from

the actual spray core, especially under diverse collapse regimes. In such cases, relying on this core angle reference avoids misalignment and ensures that measurements are not taken outside the effective spray region, which may not be distinguishable or centered under certain operating conditions.

5.4 Visualization: spray description through MIE scattering images

This section addresses the influence of fuel type, ambient conditions and superheating degree by means of the ratio of saturation pressure to ambient pressure (R_P) variations on spray morphology, focusing on the behavior of the different fuels. Each fuel exhibits unique features, leading to varied spray patterns, especially as R_P values change which is key to later understanding the dynamics of fuel atomization and spray formation. Previous studies have already explored this topic with different injector hardware, highlighting the key differences that occur with variating injection and ambient conditions [1, 6–9].

In certain conditions, a white shading mark is visible in the recorded images, primarily due to the chamber windows being closed and some droplets not being able to be renovated, causing them to stick to the glass. It is important to consider that this liquid film can affect the PDA measurement quality by inducing irregularities in the passage of the lasers. On the other hand, different spray structures are observed, which may have various effects on the measurements and will be addressed in the following subsections.

5.4.1 Spray pattern structures

The main changes observed when comparing fuels at the main operating conditions occur for Hexane, which, at very high R_P values, exhibited an extremely collapsed fuel spray structure, as shown in Figure 5.7. The Figure compares column-wise the different fuels studied, and row-wise the effect of R_P by means of ambient pressure changes. For the rows at high ambient pressure, although variations in the spray characteristics are observed, the overall spray morphology remains consistent across all fuels and similar operating conditions.

When comparing Ethanol and Hexane in the same Figure to further explore the role of R_P in spray shape behavior, Hexane, being a more volatile fuel, demonstrated greater sensitivity to changes in R_P, while Ethanol exhibited more stable spray characteristics. Due to its high volatility, Hexane showed irregular shapes at extreme conditions, with a marked change at very

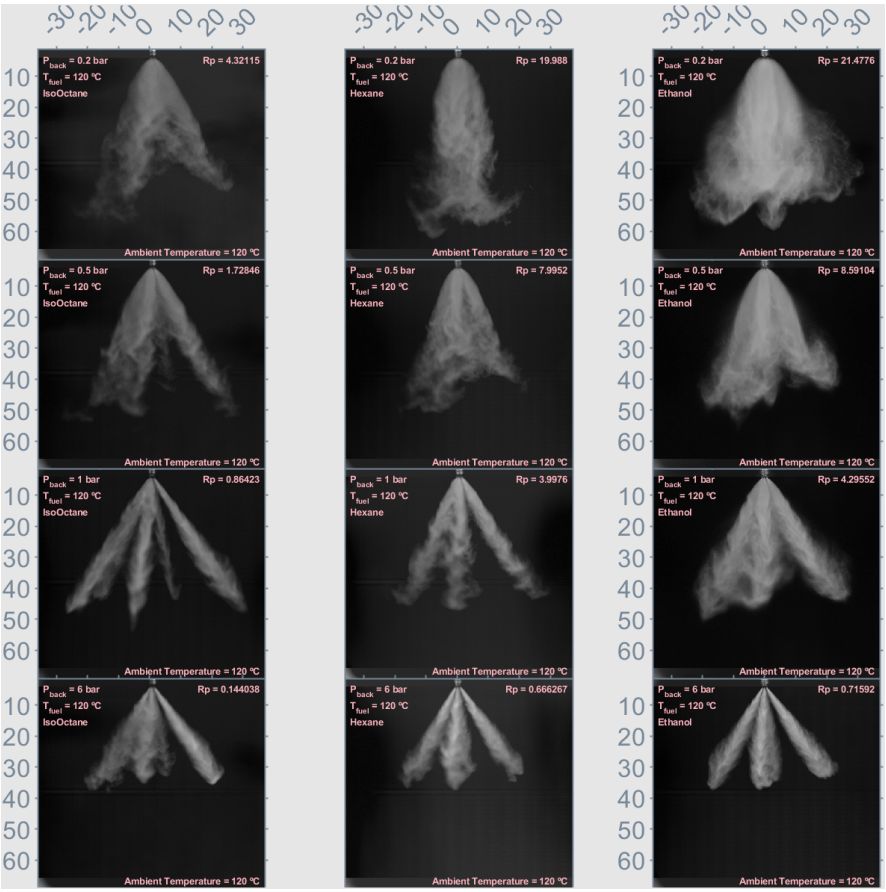


Figure 5.7: MIE flashing structure for a developed spray at a frozen frame. Conditions are shown in the image.

high temperatures, probably attributed to faster evaporation and stronger collapse. As per the expansive effect of flash boiling, for Ethanol at ambient pressure it is clear how the individual jets display a more expansive spray formation.

Stepping into the variations at elevated fuel temperatures for Ethanol, Figure 5.8, specifically at 90°C and 110°C, significant differences emerged in the spray behavior, primarily driven by R_P variations. Flashing structures are seen at 90°C, which then transition to more collapsed shapes at 110°C, this is seen at all ambient pressure, denoting the fuel temperature effect on rapid vaporization and expansive shape formation

The analysis of the 5-hole injector (C7532) at an ambient temperature of

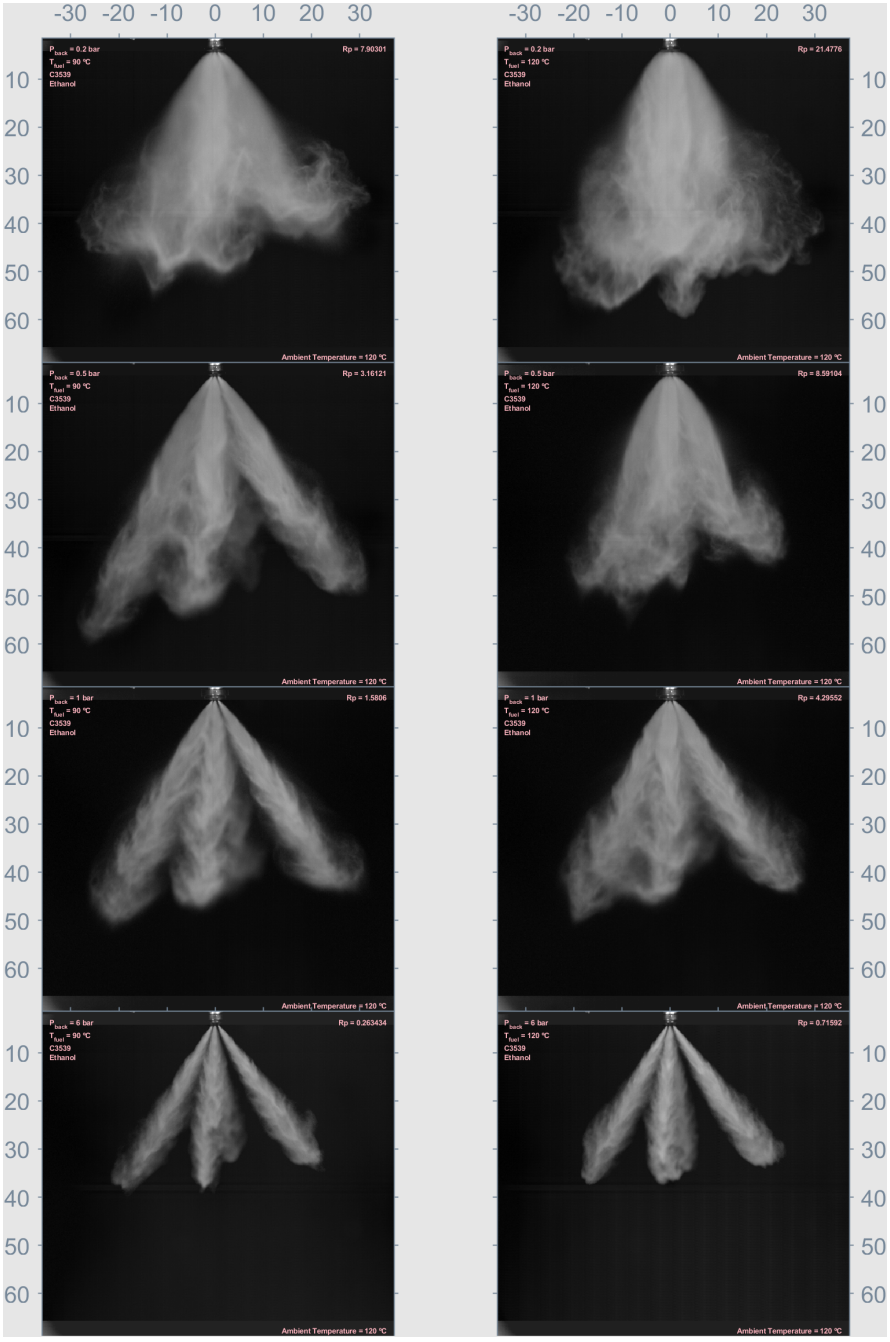


Figure 5.8: MIE images for Ethanol at two extreme temperatures, showing the effects of chamber pressure variation (R_P) at each fuel temperature.

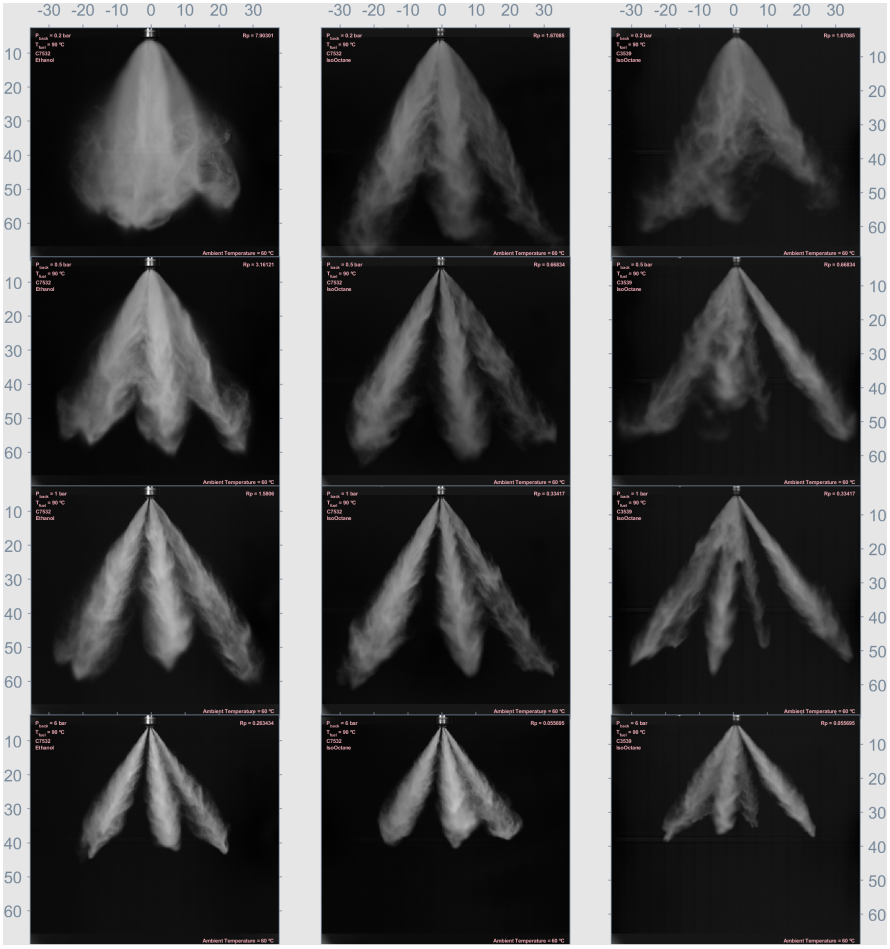


Figure 5.9: MIE images comparing both injector structures for a developed spray. Conditions are shown in the image.

60°C provides further insight into how other parameters, such as jet separation, affect the spray shape.

Figure 5.9 shows the spray shapes of Ethanol and IsoOctane for the 5-hole injector, while keeping the 6-orifice injector in the last column for comparative purposes. The same behavior observed for the C3539 injector appears again, with Ethanol showing significant changes in atomization as more expanded structures are observed in comparison to IsoOctane. As the ambient pressure decreases, Ethanol's rapid vaporization leads to a more expansive and better atomized spray. In contrast, IsoOctane, having lower volatility, demonstrates relatively stable behavior across the ambient pressure range, with less variation in its atomization characteristics.

If this IsoOctane/C7532 column spray pattern is compared to that at the right for the 6-orifice injector, it becomes apparent how at very low ambient pressure, IsoOctane presents clearer signs of collapse in the injector with more orifices. This is confirmed by visually comparing the same conditions for Ethanol between Figure 5.9 and Figure 5.8. It is evident that the injector with more holes displays more collapsed structures across the condition grid. This supports the literature which states that collapse is very dependent on the proximity of the spray jets [10, 11], and that for injectors with fewer jets, a higher degree of flash boiling is required to initiate collapse [12, 13].

The differences in volatility between Ethanol and IsoOctane play a crucial role in their spray dynamics when injected under the same conditions. Ethanol's higher volatility and temperature sensitivity result in more dynamic spray behavior, leading to significant variations in spray morphology. Meanwhile, IsoOctane's lower volatility allows for more stable and predictable spray characteristics.

5.5 Penetration results

The analysis of spray penetration, a fundamental parameter in spray dynamics, provides critical insights into how far and how fast the spray plume extends into the combustion chamber. This parameter is essential, as it directly impacts several key aspects of combustion and injection processes. Specifically, penetration length influences spray impingement on the piston surface, significantly affecting engine performance, emissions, and overall efficiency. Additionally, penetration length is closely related to the formation of the air-fuel mixture, a factor integral to achieving efficient combustion and optimizing fuel economy.

In this section, the primary focus is on assessing spray penetration in relation to chamber density, which encompasses ambient conditions such as temperature and pressure variations present during fuel injection. These conditions exert a direct influence on fuel behavior as it enters the chamber, affecting the spray's morphology, structure, and distribution. Furthermore, the analysis considers the impact of superheating degree, a parameter that combines fuel temperature with ambient pressure for each fuel, to examine its influence on spray penetration [14].

Additionally, this part also approaches an analysis of radial spray expansion. This parameter reflects the lateral spread of the spray upon injection, providing insights into the interaction between chamber conditions and fuel properties, helping to determine whether the spray exhibits a narrow or wide structure under varying conditions.

5.5.1 Chamber density effects

In examining the impact of density on spray penetration, the findings align closely with established trends in the literature, showing that ambient density, particularly when influenced by changes in ambient pressure, is the dominant factor in determining spray behavior. Figure 5.10 depicts higher ambient densities leading to slower spray velocities and reduced penetration distances, consistent with well-documented trends. When ambient pressure is high, the denser air in the chamber creates greater resistance to the spray, reducing its penetration.

At higher ambient pressures, increased temperatures tend to decrease spray penetration, as they contribute to the deceleration of the fuel spray within the chamber, indicating a multifactorial effect where density and temperature interact to influence spray development. For example, at ambient pressure, the spray penetration increases as chamber temperature decreases. This may be partly due to a portion of the spray's penetration being lost to vaporization, as suggested by an increase in vapor pressure, although this vapor phase is not captured directly in the current measurements.

Lower temperatures slow the rate at which fuel vaporizes, resulting in less energy lost to phase change and thus allowing the spray to penetrate further before dissipating, and the spray tends to fully as the chamber temperature increases [15].

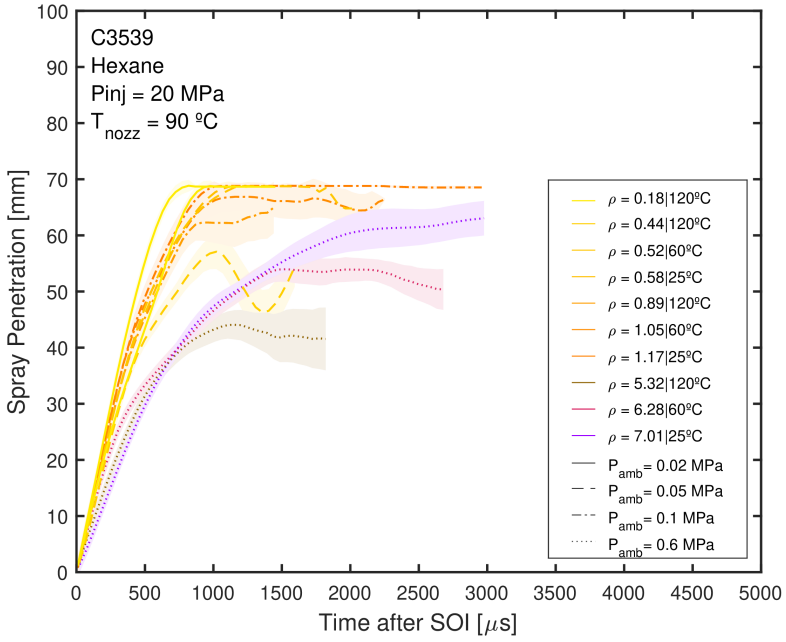


Figure 5.10: Density effect on Penetration for the C3539 injector and the Hexane fuel.

5.5.2 Super-heating degree by R_P effect

Based on the specific density variations introduced in the vessel setup, it is generally expected that higher density conditions would induce higher resistance in the way of the spray. This behavior is reflected in the results in Figure 5.11, where penetration decreases significantly under higher ambient pressure conditions, understanding that increased back-pressure intensifies resistance, particularly for denser fuels.

Interestingly, the penetration behavior was more linear for fuels with lower density. Under reduced aerodynamic resistance, these fuels tend to exhibit more predictable and stable penetration patterns, as their lower inertia allows for faster response to changes in ambient conditions. On the other side, reduced ambient resistance leads to greater spray velocity and deeper penetration, especially for lower-density fuels.

However, a clear non-linear effect was observed at certain density-temperature combinations, particularly at elevated temperatures. In all cases, pressure remained the dominant variable: higher ambient pressure conditions

generated the lowest penetration profiles, represented in the plots as the three lower dotted lines. These lines are differentiated by the vessel temperature in which the fuel was injected.

5.5.3 Penetrations differences with fuel variation

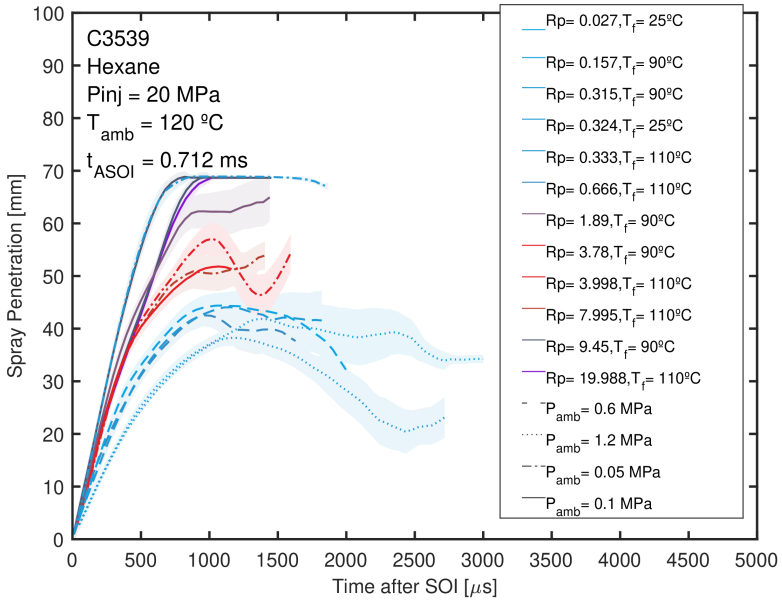
On one of the side of the flashing conditions is the fuel impact on the spray development. Figure 5.12 shows the penetration behavior as a function of fuel type, the results show a clear trend associated with fuel density. Ethanol, the densest of the tested fuels, consistently exhibits the highest spray penetration across all tested conditions, this is followed by IsoOctane, with Hexane showing the lowest penetration. These findings are consistent across the different measurement points and align well with trends reported by authors like Bautista Rodríguez [1], Nayak et al. [16], and Yan et al. [17]. Although the higher fuel density might create higher drag in its interaction with the gas density, the higher momentum displayed by denser fuels is the leading variable.

In summary, lower ambient backpressure conditions, which correspond to higher R_P values, tend to reduce air resistance and favor longer spray penetration. Nevertheless, even under these enhanced flash boiling scenarios, the density of the chamber remains a dominant factor. Ethanol maintains greater momentum and thus reaches further axial distances, while the lower-density fuels decelerate more rapidly due to their reduced inertia and enhanced vaporization. This fuel dependent behavior reinforces the importance of physical fuel properties in determining macroscopic spray characteristics under varying thermodynamic conditions.

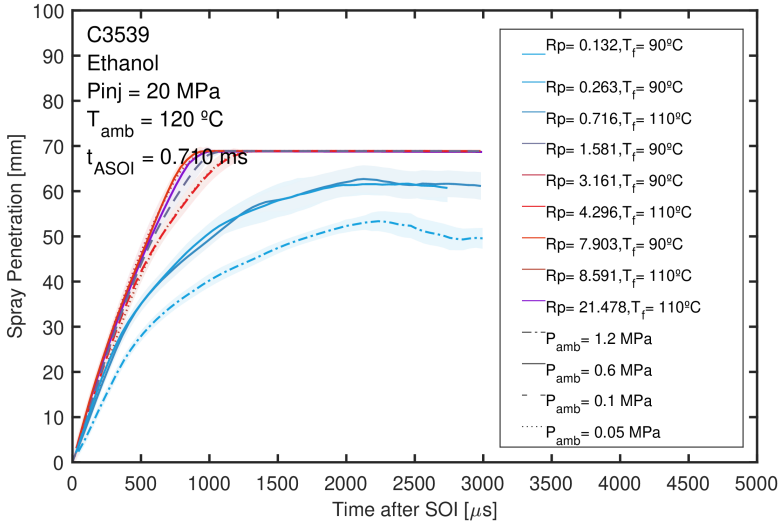
5.5.4 Spray width analysis

Previous studies have identified the spray width as a more informative parameter for spray characterization compared to a single characteristic angle, primarily due to its variations along the spray axis. The irregular structure of the spray makes it difficult to define a fixed plume angle, as spatial variations occur both along the spray length and at the spray end. However, such variations are less pronounced in the present data set.

Figure 5.13 shows the variations in spray width, measured from both edges at a fixed axial position. The primary observable differences relate to a spray angle that remains consistent up to 15 mm. The rate of variation between axial penetration and radial expansion is largely uniform across all test conditions, including those exhibiting high R_P values. However, spray shape variations,

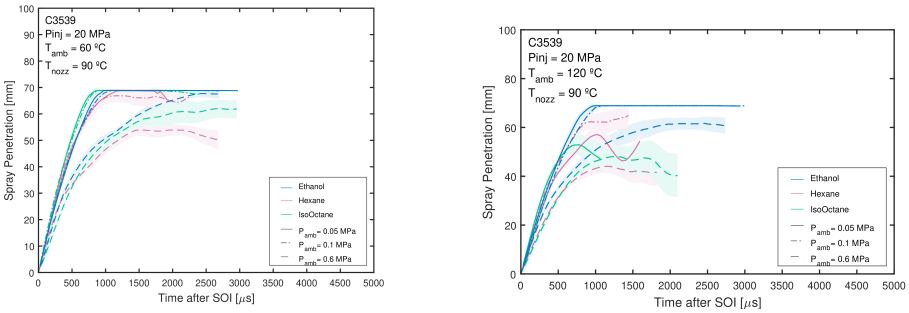


(a) Effect of the superheating degree for the Hexane fuel.



(b) Effect of the superheating degree for the Ethanol fuel.

Figure 5.11: Comparison of the effect of the superheating degree on spray penetration for Hexane and Ethanol fuels. Ambient and injection conditions are depicted in the plots.



(a) Penetration changes due to the fuel properties at normal ambient temperature. *(b) Penetration changes due to the fuel properties at high ambient temperature.*

Figure 5.12: Penetration changes due to the fuel properties.

as depicted in Figure Figure 5.8, become evident when comparing 25°C and 110°C at very low ambient pressures. Notably, the most significant changes occur at the leading edge of the spray rather than at its origin. While spray width variations remain minimal up to 15 mm, they become more pronounced beyond this range. Under collapse conditions, these variations appear earlier, but not distinctly enough to establish a clear correlation.

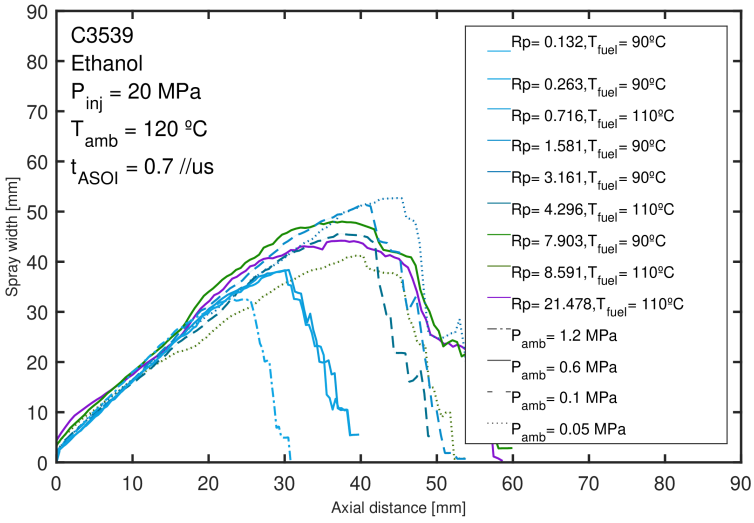


Figure 5.13: Width variation with R_P and ambient pressure.

A key distinction between this study and prior research is the injector hole configuration. Whereas previous investigations primarily analyzed eight-hole

injectors such as the ECN Spray G [6], the injectors tested here feature six and five holes, significantly influencing spray plume collapse dynamics. Additionally, the methodology employed in this work relies on a MIE scattering diagnostic, which, while effective for qualitative analysis, lacks the precision of more direct techniques, such as DBI, in delimiting the spray boundary, where variations in the selected limit introduce an uncertainty of up to 20%.

Although qualitative images of plume collapse clearly highlight differences between conditions, precise quantification was not pursued in this study.Further analysis of the strong collapse case (0.2 bar ambient pressure, 110 °C fuel temperature) revealed a high fuel concentration in the spray core, as indicated by light intensity distributions along the axis. However, the exact spray boundary remains indistinct, complicating direct comparisons. In this way, spray width variation between collapsing and non-collapsing conditions at the same axial position is approximately 1.5 mm, accounting for $\sim$ 5% of the total detected width. While this difference is measurable, it remains relatively small compared to the 20% methodological uncertainty.

To sum up, the results presented in this section are significant. They reveal clear differences across the various injection types and operating conditions studied. These findings underscore the importance of characterizing sprays under a wide range of thermodynamic conditions, given the strong influence such parameters exert on injection behavior. However, as also noted in previous research, experimental visualization techniques have inherent limitations when it comes to fully characterizing high-intensity flash boiling or plume collapse phenomena, as Oh et al. [18] also emphazises in their work. .

While qualitative visualization remains valuable for identifying general spray structure and early collapse indicators, it often falls short in resolving the finer-scale events associated with severe flash boiling regimes. These limitations have been motivate the need to complement optical diagnostics with more precise quantitative measurements. For this reason, the next section explores additional metrics, specifically droplet size and velocity measurements, which offer a more robust and quantifiable means to understand spray behavior under challenging injection conditions.

5.6 Summary and conclusions

This chapter represents the first interaction with PDPA measurements, highlighting the key considerations required for setting up the experiments. It also shows how these measurements integrate with visualization techniques to provide a baseline understanding of spray behavior, which is then linked to

a methodology capable of accurately capturing velocity fields in this type of spray.

It analyzed the sprays' behavior under various injection conditions, with particular emphasis on flash boiling scenarios. The objective was to understand how these conditions influence the macroscopic morphology, setting the groundwork on how this could extrapolate to PDPA measurements and result.

The analysis began with the general morphological characterization of spray structure under different injection modes, providing an overview of how spray shape and distribution vary with operating conditions. This was followed by an optical assessment of the spray behavior for different fuels, using morphological penetration and spray width comparisons. The main findings of the chapter are presented below:

- The experimental window configuration affected the accessibility and quality of PDA measurements during the measurement set-up.
- It was observed that different test conditions, such as flash boiling or boundary operating conditions, strongly influenced the position of the spray jets. Therefore, establishing a consistent and comparable positional reference across conditions was essential to ensure reliable analysis.
- A velocity scanning approach across different regions of the spray proved useful for identifying high-velocity regions, which were then used to define the spray core and reduce potential information loss caused by spray displacement under varying conditions.
- The MIE scattering images revealed distinct types of collapse induced by flash boiling, as well as varying degrees of spray expansion depending on the flash boiling conditions of each fuel.
- When comparing the spray images obtained from the 5-hole and 6-hole injectors under identical injection conditions, it was observed that the 6-hole injector consistently exhibited higher levels of collapse. This observation aligns with findings in the literature, which claim that the distance between spray jets and the plume interaction are critical factors in defining the collapse phenomena. Given that the orifices are quasi-symmetrically distributed in both injectors, the increased proximity between the orifices in the 6-hole configuration appears to enhance plume interaction and promote collapse formation.

- Among the tested fuels, Ethanol, which had the highest density, showed the faster penetration. In contrast, Hexane displayed the most consistent and linear penetration behavior across a wide range of conditions.

References

[1] Bautista Rodríguez, A. "Study of the Gasoline Direct Injection Process under Novel Operating Conditions". PhD thesis. Universitat Politècnica de València, 2021.

[2] Payri, R., García-Oliver, J. M., Bracho, G., and Cao, J. "Experimental characterization of direct injection liquid ammonia sprays under non-reacting diesel-like conditions". In: *Fuel* 362 (2024), p. 130851.

[3] Lemmon, E. W., Bell, I., Huber, M., and McLinden, M. O. "Thermophysical Properties of Fluid Systems". In: *NIST Standard Reference Database Number 69*. Ed. by P. J. Linstrom and W. G. Mallard. Gaithersburg MD, 20899, USA.: National Institute of Standards and Technology, 1998. DOI: https://doi.org/10.18434/T4D303.

[4] Rashed, R. "Geometrical optics". In: *Encyclopedia of the history of Arabic science*. Routledge, 2019, pp. 618–646.

[5] Valderrama, G. and Sebastián, J. "Macroscopic and microscopic characterization of non-reacting diesel sprays at low and very high injection pressures". In: 2018.

[6] Payri, R., Martí-Aldaraví, P., Alvarez, V. M., and Bautista, A. "Evaluation of GDI spray structures under flash boiling and strong collapse conditions with diverse fuels". In: *Applied Thermal Engineering* 234 (2023), p. 121195.

[7] Sharma, N. and Agarwal, A. K. "Macroscopic spray characteristics of a gasohol fueled GDI injector and impact on engine combustion and particulate morphology". In: *Fuel* 295 (2021), p. 120461.

[8] Duronio, F., De Vita, A., Montanaro, A., and Allocca, L. "Experimental investigation and numerical cfd assessment of a thermodynamic breakup model for superheated sprays with injection pressure up to 700 bar". In: *Fluids* 8.5 (2023), p. 155.

[9] Li, X. et al. "Investigations on the impact of phase change on single plume flash boiling radial expansion and drop-sizing characteristics". In: *Applied Thermal Engineering* 202 (2022), p. 117911. DOI: https://doi.org/10.1016/j.applthermaleng.2021.117911.

[10] Wu, S., Yang, S., Wooldridge, M., and Xu, M. "Experimental study of the spray collapse process of multi-hole gasoline fuel injection at flash boiling conditions". In: *Fuel* 242 (2019), pp. 109–123. DOI: https://doi.org/10.1016/j.fuel.2019.01.027.

[11] Guo, H. et al. "Comparison of spray collapses at elevated ambient pressure and flash boiling conditions using multi-hole gasoline direct injector". In: *Fuel* 199 (2017), pp. 125–134. DOI: 10.1016/j.fuel.2017.02.071.

[12] Rachakonda, S. K., Paydarfar, A., and Schmidt, D. P. "Prediction of spray collapse in multi-hole gasoline direct-injection fuel injectors". In: *International Journal of Engine Research* 20.1 (2019), pp. 18–33. DOI: 10.1177/1468087418819527.

[13] Li, Y. et al. "An exploration on collapse mechanism of multi-jet flash-boiling sprays". In: *Applied Thermal Engineering* 134.May 2017 (2018), pp. 20–28. DOI: 10.1016/j.applthermaleng.2018.01.102.

[14] Du, J., Mohan, B., Sim, J., Fang, T., and Roberts, W. L. "Experimental and analytical study on liquid and vapor penetration of high-reactivity gasoline using a high-pressure gasoline multi-hole injector". In: *Applied Thermal Engineering* 163 (2019), p. 114187. DOI: https://doi.org/10.1016/j.applthermaleng.2019.114187.

[15] Duy, N. H. X. and Lim, O. "An investigation of the effect of chamber temperature on macroscopic spray characteristic under GCI engine conditions". In: *Fuel* 346 (2023), p. 128239. DOI: https://doi.org/10.1016/j.fuel.2023.128239.

[16] Nayak, G. et al. "An Experimental Investigation into the GDI Spray Characteristics of Ethanol and Lemon Peel Oil". In: *Conference on Fluid Mechanics and Fluid Power*. Springer. 2022, pp. 67–79.

[17] Yan, J., Gao, S., Zhao, W., Lee, T. H., and Lee, C.-F. "Experimental study of sprays with isooctane, hexane, ethanol and their binary mixtures under different flash boiling intensities". In: *International Journal of Heat and Mass Transfer* 179 (2021), p. 121715. DOI: https://doi.org/10.1016/j.ijheatmasstransfer.2021.121715.

[18] Oh, H., Hwang, J., White, L., Pickett, L. M., and Han, D. "Spray collapse characteristics of practical GDI spray for lateral-mounted GDI engines". In: *International Journal of Heat and Mass Transfer* 190 (2022), p. 122743. DOI: https://doi.org/10.1016/j.ijheatmasstransfer.2022.122743.

Chapter 6

Microscopic characterization: Velocity and diameter

6.1 Introduction

With the context of GDI spray morphology and its potential influence on PDPA measurements established, this chapter evaluates the impact of the operating conditions on velocity and diameter measurement results.

It begins by introducing the main velocity and diameter outcomes reported by the PDA measurements. First, the positional and geometric framework where the velocities are measured is revisited, explaining how this setup might affect the reported results. Then, the transient velocity data are presented, highlighting the most critical and challenging conditions; discussing their influence on the final results. Next, the velocities are compared across the key variables studied in this project, starting with fuel and chamber conditions, followed by characterization of the radial velocity profiles.

The chapter then shifts focus to diameter results, beginning with particle size variations that define the spray region; then performing an analysis of droplet size distribution characteristics. Comparisons across different conditions are made primarily in terms of droplet size distributions and the Sauter Mean Diameter (SMD) values.

Finally, the chapter explores flash boiling conditions and their potential benefits for the measurement outcomes.

6.2 PDPA results: Experimental baseline

Velocity components and coordinate system

Droplet velocity represents the kinetic energy imparted by the injector and is vital to evaluating the interaction between the spray and surrounding gas. Velocity gradients downstream reflects the variation between initial momentum and resistance forces such as drag and turbulent dissipation.

Before getting to the velocity results in detail, it is important to restate the reference frame and coordinate components used throughout the study. The measured velocity corresponds to a combination of the velocity components registered by the PDPA system. Initially, the vertical velocity component was selected as the primary measurement direction due to its alignment with the dominant spray axis in most test cases. In the experimental setup, the injector was mounted in a near to the vertical position, and the spray cone angle, defined relative to the injector axis, remained below 43° in the majority of studied conditions.

Despite the fact that complete droplet velocity tracking in three-dimensional space would require the measurement of three components, only two components, vertical (u_z) and horizontal (u_x), were measured in this study. This limitation is inherent to the two-component PDPA system, which restricts the measurable velocity vector to a two-dimensional plane. Therefore, for transient plots and radial profiles, only the vertical component was used to represent the spray motion. However, for global or averaged quantities, a correction was made to estimate the true axial component of velocity (u_{axial}), by using a transformation matrix that accounts for the angular orientation of the spray axis.

The spray axis the measurement plane, forms an angle θ with the vertical direction, and the axial and radial velocity can be determined from the measured components via:

$$\begin{bmatrix} u_{\text{axial}} \\ u_{\text{radial}} \end{bmatrix} = \begin{bmatrix} \cos(\theta) & \sin(\theta) \\ -\sin(\theta) & \cos(\theta) \end{bmatrix} \cdot \begin{bmatrix} u_z \\ u_x \end{bmatrix} \tag{6.1}$$

This transformation enables the recovery of spray-relevant components for qualitative and quantitative analysis. The vertical velocity component aligns with the droplet sizing measurement direction, which is another instrumental constraint that influenced the optical configuration selection.

Optical degradation due to chamber window contamination, as well as, optical path being blocked by very concentrated fuels under dense spray con-

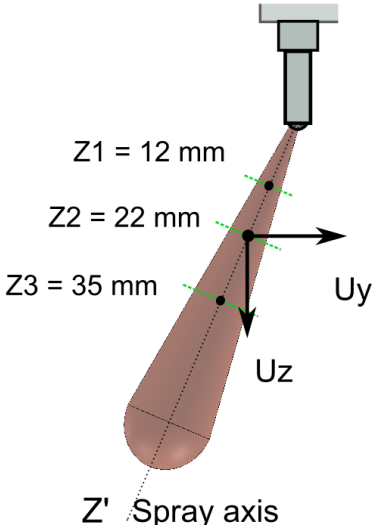


Figure 6.1: Relation between spray coordinates and measured coordinates.

ditions, led to partial data loss. These cases were identified and excluded based on the filtering criteria developed internally, which flags insufficient droplet counts for statistical validity. Only datasets meeting droplet count thresholds criteria during the quasi-stationary phase of injection are considered valid. This filtering approach was necessary to maintain a good integrity of the comparisons, since some measurements were affected by limitations in optical access or measurement reliability.

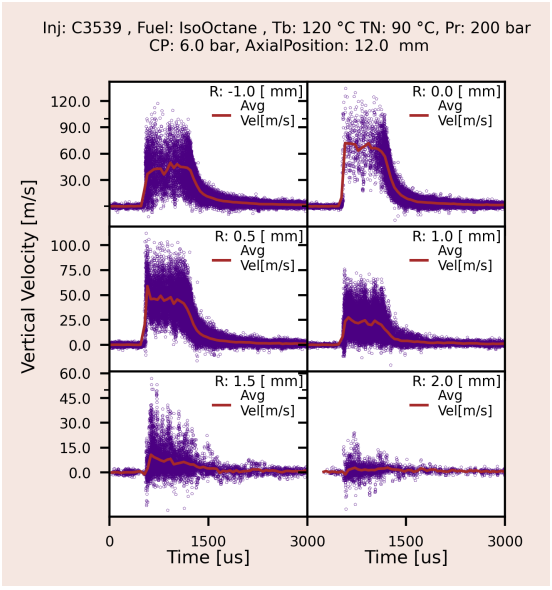
Although this approach led to the exclusion of certain conditions, especially those under high ambient pressure regimes or very close to the nozzle exit, the retained dataset reflects consistent and robust measurement quality. Consequently, some discontinuities may appear in condition-dependent plots, however, this filtering allows comparisons made on unbiased foundation.Given the large number of test scenarios, only the most representative and frequently encountered cases are discussed.

6.2.1 Initial droplet behavior – temporal insights

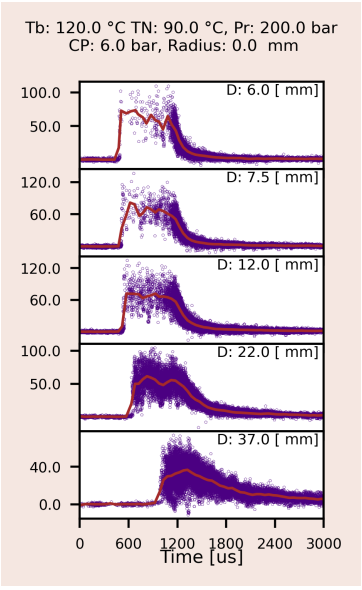
The temporal evolution of the velocity is presented as a first-layer observation. Although both droplet velocities and diameters were measured simultaneously, this analysis initially focuses on velocity data, as it provides clearer insight into flow behaviors and measurement constraints. Furthermore, given the constraints of the setup and the emphasis on qualitative comparison, most

transient velocity plots presented in the following sections focus on the vertical velocity component (u_z), which retains a dominant role in characterizing spray structure under the observed conditions. It examines the various spray patterns and structures observed in the PDA velocity measurements.

The first type of pattern seen in Figure 6.2a corresponds to a GDI representative condition under moderate ambient temperature and pressure in the facility. The chamber condition depicted is set at 120 °C and 6 bar, while the injection pressure was relatively high. The fuel was preheated to 90 °C, replicating warm engine conditions.



(a) Time-resolved velocity at different radius steps at a fixed axial distance.



(b) Velocity evolution along the spray core.

Figure 6.2: Time-resolved velocity transients for a fuel under high ambient chamber pressure displaying the variation in velocity.

The figure can be interpreted from left to right and up-down by considering the radial position across the spray, effectively representing a transverse section through the spray plane at certain axial position. As the measurement approaches the centerline, R0, the dispersion of velocity during the quasi-stationary phase becomes less pronounced. However, moving outward from 0 mm to 2 mm in radial position, a sharp decrease in mean velocity is observed. The read line represents the moving average of the velocities in a time window of $50/us$.

Additionally, Figure 6.2b illustrates the axial development along the spray axis. In this case, all measurements are concentrated at radius zero, tracking the spray evolution from the nearest axial position to the farthest one downstream. As expected, measurements taken closer to the injector become increasingly challenging, and fewer valid droplets can be captured. While in many cases the tail of the injection is well measured, depending on the operating condition, some of the measurements were either successfully used or discarded post-analysis due to insufficient droplet counts in the quasi-stationary phase.

The variability in measurement counts in this phase introduces uncertainty and potential bias. Therefore, in the forthcoming analyses, any measurement within the quasi-stationary window that did not meet a minimum droplet count threshold is excluded.

As per the velocity trends observed, as expected from momentum conservation, the overall velocity magnitudes were governed by the pressure difference between injection and chamber. On the other side, in Figure 6.3, low ambient pressure conditions exhibited a sharply defined and stable velocity profile, during the early and central injection phases. Small velocity deviation was observed near the core, suggesting a more coherent and laminar flow. However, moving radially outward from the core, velocity decreased rapidly over short distances, indicating steep spatial gradients.

This had implications for spatial resolution measurements consideration; this structure required finer radial steps of 0.5 mm to 1 mm to track the radial evolution to the necessary cases. Unlike the 6 bar structure, which showed broad radial dispersion, this case was characterized by a concentrated core and abrupt velocity transitions in the outer region.

Another key difference was the magnitude of measured velocity near the nozzle. While theoretical velocity based on Bernoulli's principle depends on the pressure drop, measured velocities showed substantial reduction even 12 mm downstream from the nozzle exit. This discrepancy reflects both energy losses and measurement challenges under high-density conditions.

In section 4.4, the rate of momentum measurements analyzed for the effect of back pressure very close to the nozzle, showed differences relatively minor compared to the current observations. When comparing velocities measured under ambient pressures of 6 bar and 0.5 bar, the reduction in velocity downstream becomes far more pronounced. This highlights the significance of ambient pressure in shaping velocity decay.

In the first case presented, elevated ambient pressure and density likely

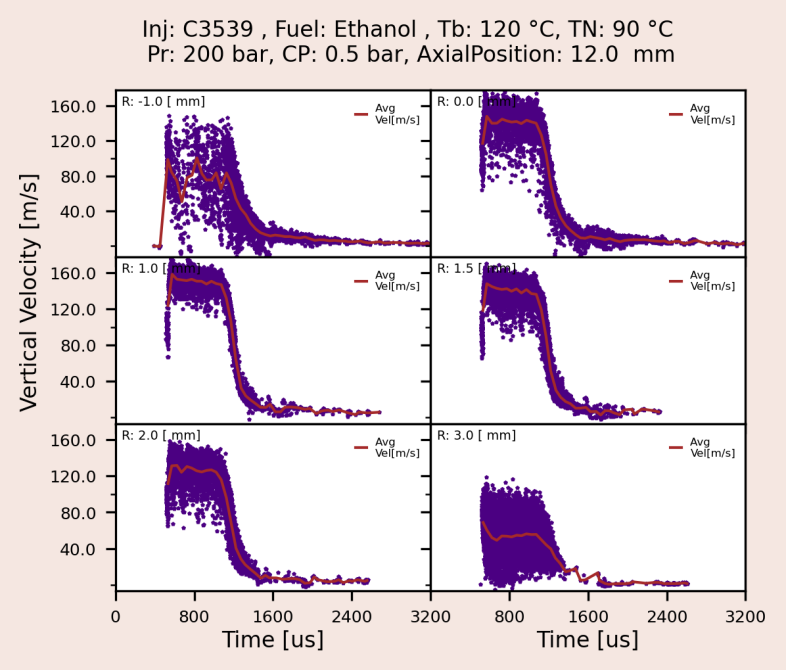
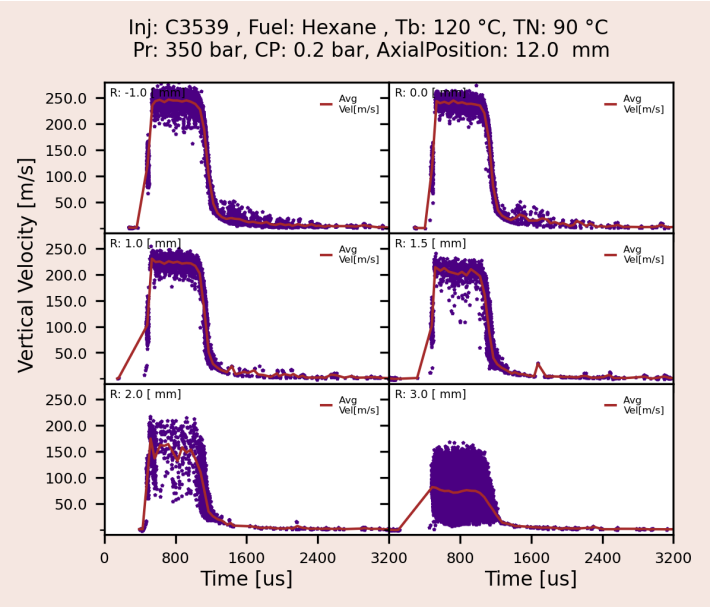


Figure 6.3: Time-resolved velocity transients under low ambient pressure fuel displaying the variation in velocity at different radius steps at a fixed axial distance.

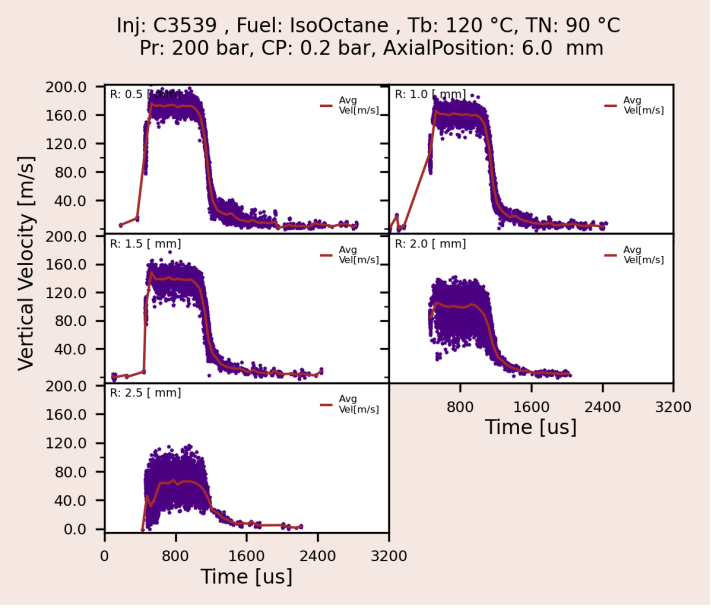
led to rapid energy dissipation within the first millimeters, possibly due to immature atomization and incomplete breakup, resulting in velocities over 60 m/s at 12 mm. On the contrary, the second case, yielded velocities approaching 170 m/s, indicating less energy loss. This contrast highlights the role of gas-liquid interactions in the early-phase of the spray development in defining near-nozzle momentum.

As the sprays can expand and reduce opacity, with near flash boiling conditions, permitted a higher resolution velocity measurements near the spray core, Figure 6.3. Both by improving optical access to the lasers cross points, and expected enhanced atomization. This effect allows to measure even more pronounced structures as in Figure 6.4a, where extremely high velocities under 350 bar injection pressure were recorded at around 12 mm downstream with velocities higher than 250 m/s. Or even allowed to measure high velocities closer to the nozzle exit in Figure 6.4b.

These measurements, made possible by the clearer spray core, allowed for detailed tracking of spatial velocity peaks across varying conditions. Flash boiling intensity by ambient pressure changes were identified as the dominant



(a) Velocity patterns seen at high R_P conditions for Hexane at very high injection pressure.



(b) Velocity patterns seen at high R_P conditions for IsoOctane very close to the nozzle.

Figure 6.4: Different velocities measured both at very high injection pressure and very close to the nozzle exit.

variables governing the accessibility and stability of high-velocity regions. In conditions where the spray was too dense, velocity could not be reliably measured due to beam scattering or cloud interference.

If we compare now this information for a representative condition in the different spray positions, it is possible to evaluate the spatial velocity development both radially (left to right) and axially (top to bottom) Figure 6.5. This analysis enables a detailed understanding on how the vertical component of the spray velocity evolves from the injector centerline outward and downstream from the nozzle. The velocity profiles confirm the validity of the measurements across all positions, as they exhibit a consistent decay with increasing radial distance and axial displacement. As expected in spray behavior, moving further from the spray core results in progressive energy loss of the droplets due to both radial expansion and interaction forces within the chamber.

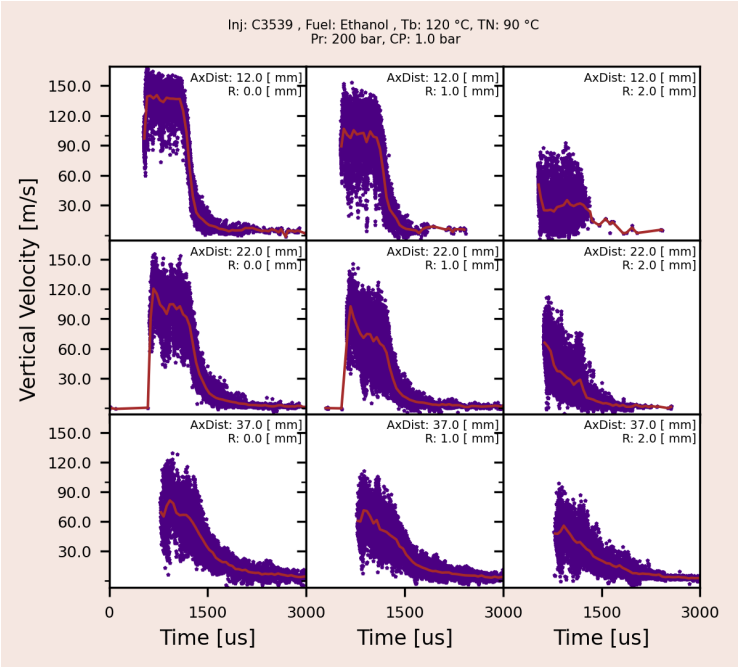


Figure 6.5: Spray spatial expansion, radial vs. axial evolution. Injection conditions specified in the plot.

In the same sense, a comparison is made across three different injection pressures, ranging from 50 bar to 200 bar. Here, the velocity evolution is assessed along the axial direction at a fixed radial position, $R = 0$, to study how spray velocity varies under otherwise a similar boundary condition Figure 6.6.

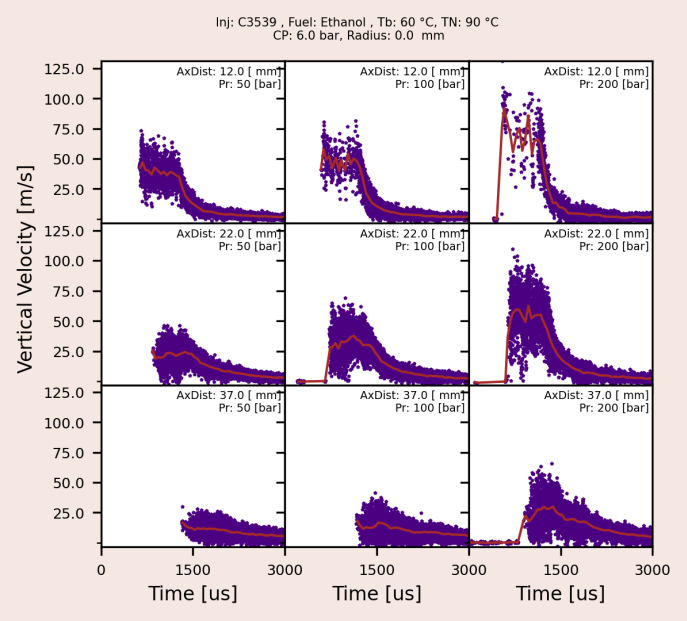


Figure 6.6: Velocity transient comparison under varying injection pressures for a fixed condition and different axial positions.

This initial approach to characterizing the influence of injection pressure within fixed boundary conditions reveals not only the expected impact of pressure on spray dynamics but also its effect on the quality of velocity measurements. At axial positions located very close to the nozzle, the combination of high injection pressure and elevated ambient pressure complicates laser access and increases measurement uncertainty. As observed when increasing the injection pressure from 50 bar to 200 bar, data capture quality decreases. This is likely due to both a denser spray core resulting in more concentrated scattering fields, and poor atomization quality, which limits the penetration of the laser into the spray at $R = 0$.

6.3 PDPA results: Primary velocity comparisons

6.3.1 Averaged velocity profiles

The average velocity calculated can be used to confirm trends observed across different operating conditions and varying physical properties. To compare the two main fuels used under a fixed operating condition, Figure 6.7 is presented, where several trends identified in the rate of momentum campaign are

corroborated. Ethanol continues to show slightly higher velocity values compared to the other fuels, a result attributed to its higher density among the tested candidates. However, this trend reverses farther downstream from the nozzle, suggesting that atomization effects may play a more dominant role at greater distances, as larger droplets tend to retain their velocity longer.

Velocity measurements are validated for both injectors and across the different spatial positions, consistently aligning with expectations. These results closely correspond to the previously discussed momentum data, as outlet velocity is inherently linked to the momentum flux at the orifice. The five-hole injector exhibited a higher mass flow rate due to its greater injection rate at equivalent injection duration, along with its larger orifice diameter and momentum flux. Consequently, under the same operating conditions, higher velocities were recorded for the five-hole injector compared to the six-hole one. Additionally, as expected, velocity values declined with increasing radial and axial distance from the injector, reflecting the natural decay in spray momentum. Moon et al. [3] also found a diminishing of the axial flow by increasing the number of holes in the nozzle, attributing this trend to a decrease in the sac pressure and following attenuation of the vena contracta effect.

As shown in the momentum measurements from chapter 4, Ethanol and IsoOctane generally produced higher velocities than Hexane; while Ethanol displayed slightly higher momentum, its velocity values in the PDA measurements were comparable to those of IsoOctane. Hexane, by contrast, tended to exhibit lower velocities at farther axial positions, however, near the nozzle and under flash boiling conditions, Hexane showed increased velocity, likely due to enhanced internal expansion and droplet acceleration driven by its high volatility.

6.3.2 Radial velocities profiles

Velocity ratio profiles of the velocity over the velocity in the spray centerline, provide normalized insights into how is distributed the velocity along the spray section, as depicted in Figure 6.8. More volatile or less dense fuels tend to expand faster and decelerate more quickly due to lower inertia and enhanced evaporation.

Velocity ratio profiles represented by the mean velocity, provide insights into how is distributed the velocity along the spray section, as depicted in Figure 6.8. More volatile or less dense fuels tend to expand faster and decelerate more quickly due to lower inertia and enhanced evaporation.

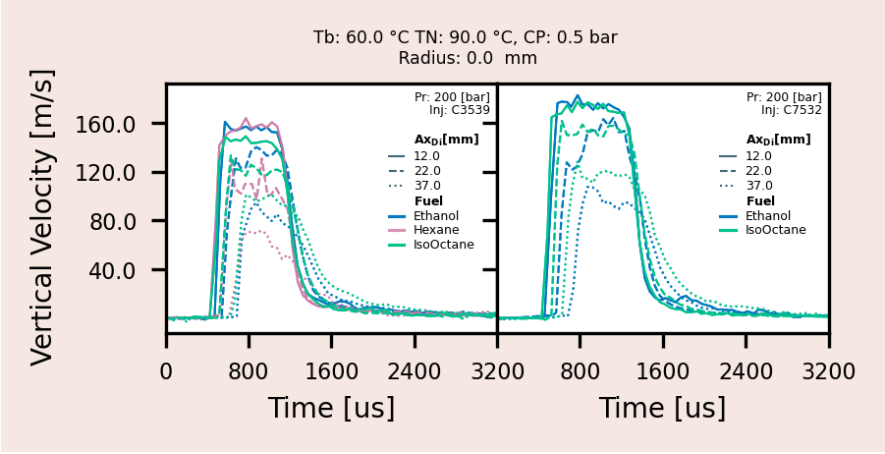


Figure 6.7: Averaged velocity comparison for different fuels in a spray for each injector. Two levels of axial positions are represented by the line style employed.

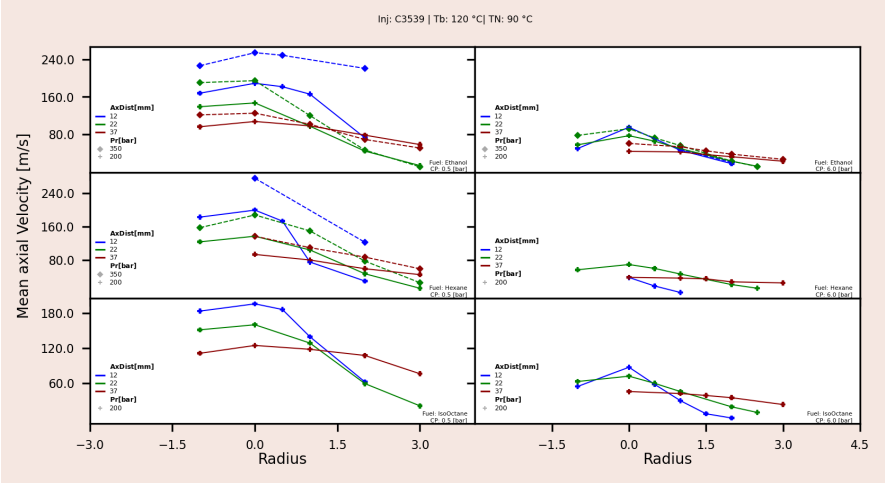


Figure 6.8: Normalized velocities profiles along the radius of the spray at different Axial positions and fuels. Conditions displayed in the figure.

It is important to mention that, although the positioning methodology was able to locate the maximum at R0 in most conditions, this was not always the case, for a highly volatile fuel like Hexane. At low ambient pressure, the actual peak velocity frequently shifted, with the offset being more pronounced under strong flash boiling. In fact, for most conditions with Hexane, the velocity peak did not align precisely with the calculated center, although it often remained within a close range, implying its sensitivity to small changes in injection ambient pressure and injection temperature. Preempting that scenario, measurements were performed across the radial calculated center, extending from negative to positive positions, to capture this shift. For this plot, when necessary, a phase adjustment was applied to realign the velocity profile with the actual peak position in order to assess the velocity decay from the peak velocity to the periphery.

The velocity points are shown only for conditions with sufficient droplet counts in the quasi-stationary phase, ensuring statistical robustness, which explains some missing radius points in the plot. The rate of velocity decay varied significantly with ambient pressure. Under low back pressure conditions, the velocity decreased sharply with radial distance, indicating a narrower and more focused spray. This steep decay was especially evident at high R_P values, where small displacements from the centerline led to rapid velocity loss. This behavior is consistent with previously reported effects of high R_P in narrowing the spray width and contracting the initial jet angle.

6.4 PDPA results: Velocity and Diameter

6.4.1 Droplet Size Metrics and Spatial Distribution

Droplet sizing is central to understanding spray breakup, fuel-air mixing, and evaporation efficiency in GDI sprays. The following figures employ three statistical size descriptors: the arithmetic mean (D10), the median diameter (D50), and the Sauter Mean Diameter (SMD or D32) which are defined as follows.

$$\mathrm{SMD} = D_{32} = \frac{\sum n_i d_i^3}{\sum n_i d_i^2} \tag{6.2}$$

$$D_{10} = \frac{\sum n_i d_i}{\sum n_i} \tag{6.3}$$

$$D_{50} = d \quad \text{such that} \quad \sum_{d_i<d} n_i = \frac{1}{2}\sum n_i \tag{6.4}$$

D10 is sensitive to shifts in the early atomization stage and represents the frequency of tiny droplets. D50 offers a central measure of the distribution, and finally the most commonly used descriptor for droplets size analysis, the SMD, the most representative for modeling spray evaporation and combustion since it is directly related to the surface-area-to-volume ratio. In this sense, SMD is used as the principal metric in all comparisons between operating conditions or physical factors, such as fuels and injectors, because of its greater physical relevance, as the spray literature suggest.

Figure 6.9 shows a measurement of particle sizes by the PDPA system accompanied by the mean diameters calculated. The time window used for measuring each SMD point is based in a 50 *um* time window. The velocity average is depicted so the reader can observe the changes seen once the injection starts, then during the injection and once it has finished. Further in the text, the quasi-stationary portion of the injection will be the one employed for averaging values representing one condition.

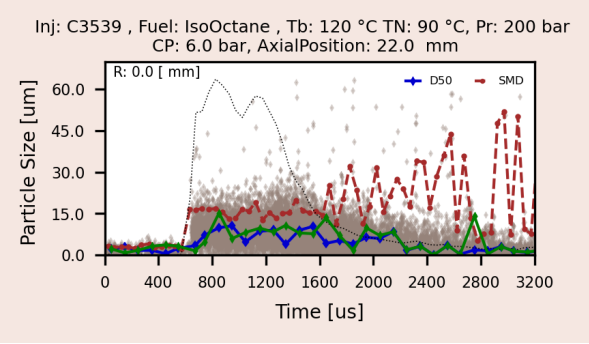


Figure 6.9: Diameter statistics considering the velocity. Velocity is scaled to fit the droplet measurements range for this case. operating condition is shown in the Plot.

The trends depicted in the plot clearly show that the SMD is consistently larger during the quasi-stationary phase of the injection event. This highlights the influence of larger droplets on the overall spray measurement, particularly in terms of how the PDA system captures the spray structure. In contrast, the D_{50} and D_{10} diameters exhibit minimal variation across the same measurements, indicating that smaller droplets contribute less significantly to the dynamic changes observed in this phase.

It is worth noting that once the injection event concludes, the SMD begins to fluctuate more noticeably. These oscillations, both upward and downward, are likely to bias the result due to the presence of residual droplets remaining in the chamber. These include droplets from previous injections, as well as, slower or lagging droplets still traveling through the measurement point after the spray tail has passed. Such contributions will not be considered part of the primary analysis, as they do not represent the active injection process.

To ensure consistent characterization of the spray during the quasi-stationary phase characerization, a time window was defined. The injection duration was previously analyzed in chapter 4, which confirmed that although variations exist with changing injection conditions, the overall duration remains stable enough for consistent time-based sampling. Additionally, the injection start time was accurately determined using an internally developed detection algorithm, ensuring the time window always falls within the quasi-stationary phase for all tested cases.

Particle size transient profiles in different spatial locations

Figure 6.10 and Figure 6.11 are constructed to represent the evolution of the droplet diameter per injection along the main axial and radial positions. Across these spatial dimensions, the dominant trends observed remain consistent under both high and very high injection pressures, even when accounting for variations in ambient back pressure. In particular, the relationship between the SMD and D_{50} remains stable. For clarity in visual representation, D_{10} has been excluded from these figures to reduce noise and enhance readability.

In most cases, the overall trend persists across all tested conditions; however, as the measurement point moves further from the nozzle, both axially and radially, the gap between the SMD and D_{50} narrows. This suggests a more uniform droplet distribution at positions farther from the injector, likely due to ongoing atomization and spatial dispersion of the spray.

The same trend is also preserved at higher injection pressures, such as 200 bar and 350 bar. Similar behavior is observed at back pressures of 6 bar when sufficient data was captured during the injection. Nonetheless, at lower ambient pressures, particularly at or below 0.5 bar, variations in the SMD within the quasi-stationary phase become more pronounced. These fluctuations suggest a higher degree of instability in droplet breakup and distribution under low-resistance ambient conditions. In general, while most droplets are concentrated in a narrow range of diameters for these conditions, as also seen in the low variability of D_{10} and D_{50}, the higher SMD values suggest that a

smaller fraction of large droplets is skewing the mean. under those conditions, particle size are usually smaller, however, bigger droplets encountered shift the SMD (more sensitive to bigger sizes) to higher values.

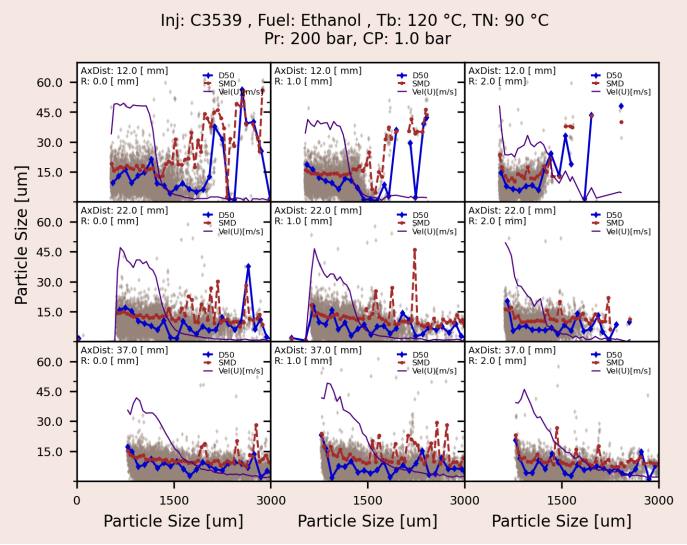


Figure 6.10: Spatial map of different diameters showing radial and axial evolution under reference conditions. At high injection pressure and room ambient pressure.

To further analyze the droplet size distribution within the spray, a probability density function (PDF) plot is used to statistically describe the likelihood of encountering droplets of specific diameters under different injection conditions. This representation condense the previously shown time-resolved frame analysis by shifting the focus from transient spray development to the distribution of droplet sizes observed throughout the quasi-stationary phase Figure 6.12.

The analysis confirms that during the quasi-stationary phase, variations in droplet size are generally limited. However, a notable exception occurs under high-volatility conditions, where a broader range of droplet sizes is observed. These cases show increased variability in the droplet population, suggesting a stronger influence of volatile fuel behavior on atomization dynamics. While further discussion is reserved for subsequent sections, this preliminary observation highlights the relevance of volatility in shaping the size distribution of droplets even within stabilized spray phases.

It is important to note that this analysis deliberately excludes droplets detected after the end of injection, as they are not representative of the pri-

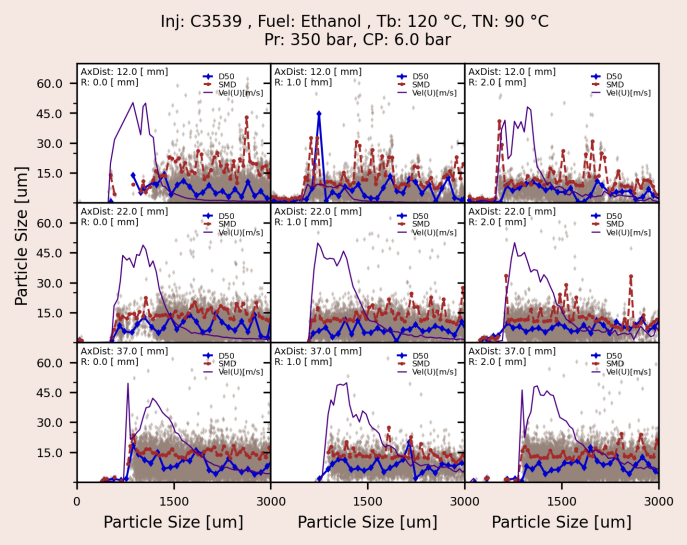


Figure 6.11: Spatial map of different diameters showing radial and axial evolution under reference conditions. At very high injection pressure and high ambient pressure.

mary spray structure. Although such droplets may still impact combustion or mixture formation.

The droplet size distribution is shown to concentrate around smaller droplet sizes near the spray axis, while moving radially outward leads to a gradual shift toward even smaller diameters. This spatial trend is also reflected in the SMD, which decreases both with increasing axial distance from the nozzle and with radial displacement from the spray centerline. A trend broadly seen in the literature [4, 5].

At the most outer radial position, R2, the PDF broadens, indicating greater variability in droplet sizes. Although the mean droplet sizes are smaller at these peripheral locations, the increased wideness suggests enhanced heterogeneity in the atomization process. This behavior is reported here for a standard injection condition with a backpressure of 1 bar, though this trend may vary under flash boiling conditions, which will be discussed in later sections.

The KDE line constructed from the PDF distribution provides a continuous representation of the droplet size distribution, offering a smoother profile that can be used for comparison across different test cases. These KDE curves allow for a direct and intuitive visual comparison of how droplet distributions vary with changes in fuel type, injection conditions, or injector design.

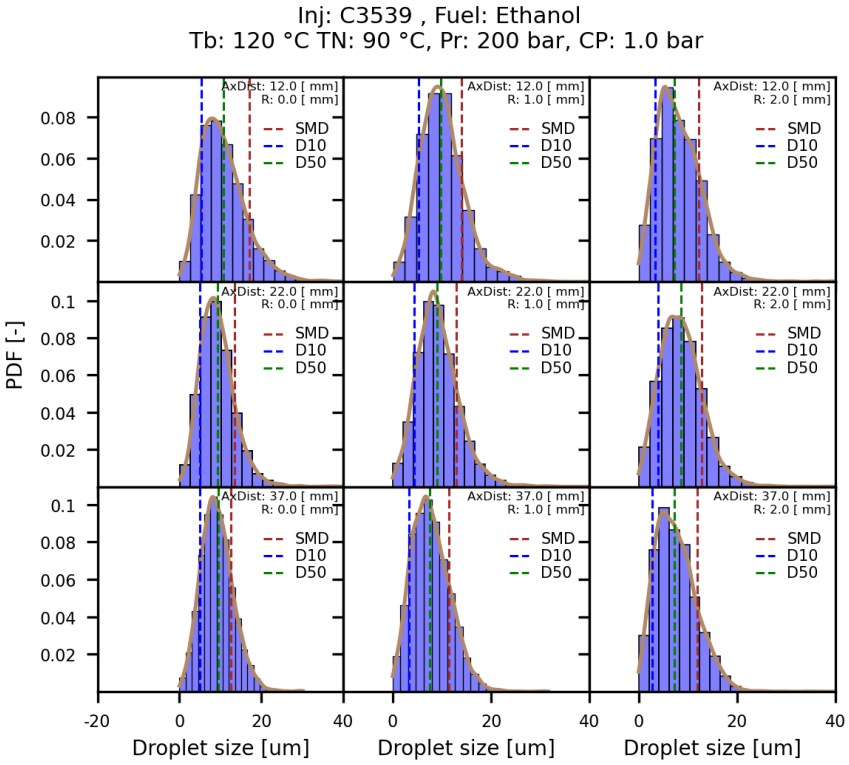


Figure 6.12: PDF for droplet size at different axial positions.

Droplet size distribution by injection pressure

If we now take the same droplet size distributions and their corresponding KDE lines and compare them across key injection parameters, such as injection pressure and measurement position within the spray frame, a general pattern emerges, as seen in Figure 6.13. At higher injection pressures, the distributions are consistently skewed toward smaller diameters, with most of the data concentrated on the left side of the histogram. This trend holds across all conditions analyzed, indicating that higher pressure enhances atomization and leads to a narrower droplet size range.

As the injection pressure decreases, the distributions shift slightly to the right, suggesting the presence of larger droplets. However, this shift becomes more pronounced only at greater axial distances from the nozzle, particularly at 37 mm. At this location, the effect of pressure reduction is more evident, with the distributions becoming more dispersed and further deviating from

a sharply peaked center. These findings suggest that droplet size variability increases with both lower injection pressures and greater spray penetration, reflecting a decline in atomization efficiency as the spray develops downstream.

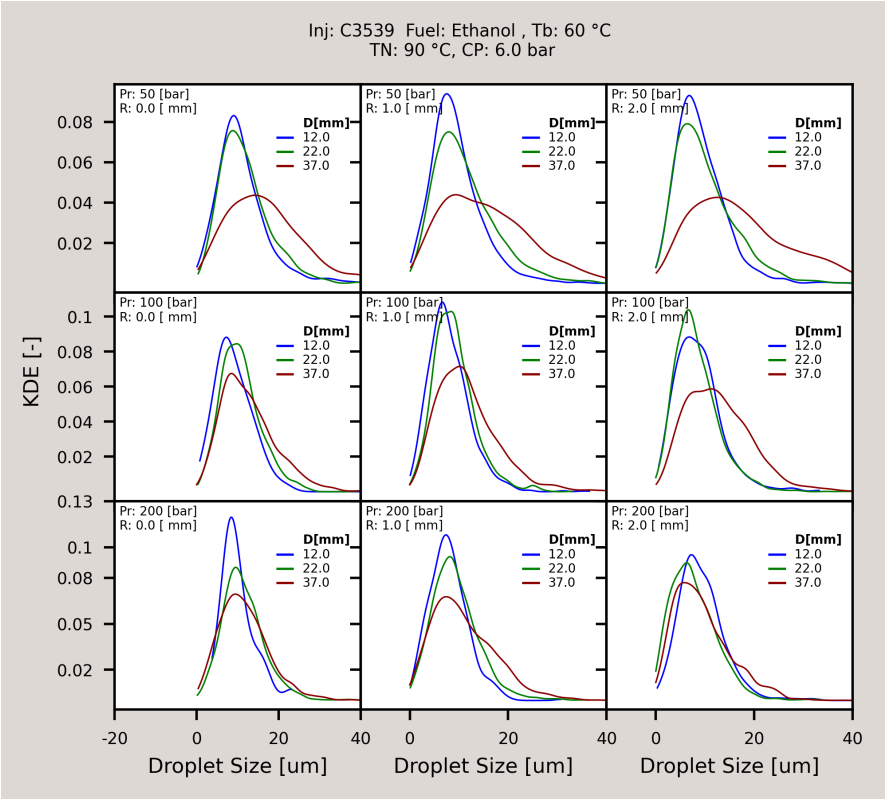


Figure 6.13: KDE comparison for various positions along a spray at a given operating condition.

The KDE curves also reveal clear differences in droplet size distribution influenced by fuel properties, Figure 6.14. Highly volatile fuels such as Hexane and IsoOctane consistently exhibit distributions shifted toward smaller diameters with narrower, more concentrated profiles. This behavior reflects enhanced atomization performance, particularly under standard injection conditions. In contrast, Ethanol presents broader distributions and consistently larger droplet diameters, which are attributed to its lower volatility and higher viscosity and density. This trend is observed across both injectors tested and remains consistent at various axial and radial measurement locations, confirming that alcohols sprays have larger droplets provoked by their higher surface tension, viscosity, and latent heat of evaporation [6].

When comparing the two injectors, one with five holes and slightly larger orifice diameters, and the other with six smaller holes; the first generally produced larger droplets across all fuels, Ethanol continued to show the widest and most dispersed distributions. Although IsoOctane typically showed finer atomization than Ethanol, its distribution remained broader than that of Hexane. Additionally, time-resolved droplet diameter plots revealed the presence of large droplets, especially under flash boiling conditions, characterized by high fuel temperature and reduced ambient pressure.

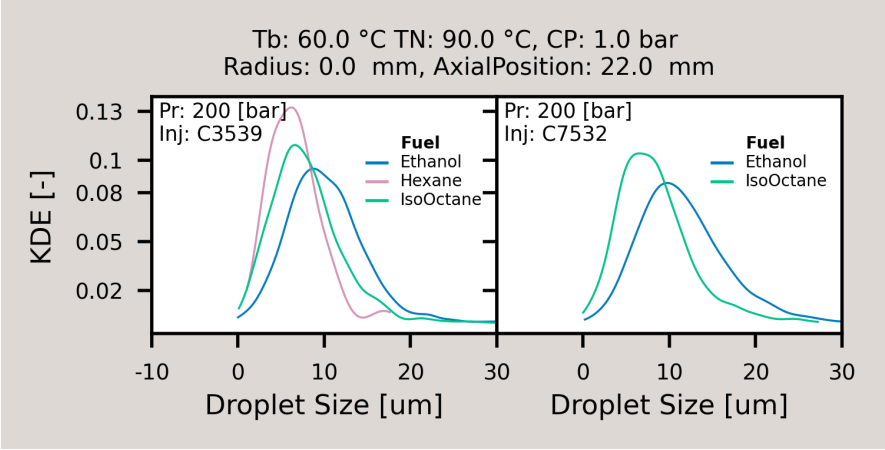


Figure 6.14: KDE comparison for various fuels and injector variation for a fixed condition.

6.4.2 Operational conditions effects

Figure 6.15 depicts a comparison between two fuels under identical operating conditions reveals that SMD values during the transient phase remained generally stable and similar across cases. However, the trend where the five-hole injector produced slightly larger droplets compared to the six-hole injector is confirmed, as well. This effect was particularly evident at low ambient backpressure, suggesting that counterpressure is a key factor influencing droplet size distribution during injection.

At higher backpressure levels, toward the right side of the plots, this difference persisted, with the five-hole injector continuing to show higher SMD values. This is attributed to its larger orifices and lower total hole count, which result in reduced atomization efficiency under certain conditions.

The figures compare Ethanol and IsoOctane across two axial positions, with fuel type changing from left to right and axial position varying from top

to bottom. The most pronounced injector-related differences were found in the IsoOctane case, while Ethanol showed less sensitivity to injector configuration. Across conditions, the five-hole injector generally produced slightly larger droplet sizes.

It is important to clarify that the very small diameters observed at the beginning of the injection plots represent residual droplets left in the chamber from previous injection events. These precede the actual start of injection, which is indicated by the appearance of sharp peaks or dotted vertical lines in the plot, representing the scaled velocity signal. As also reported in previous studies, increased variability in droplet size tends to occur near the end of injection, particularly at peripheral spray regions [7].

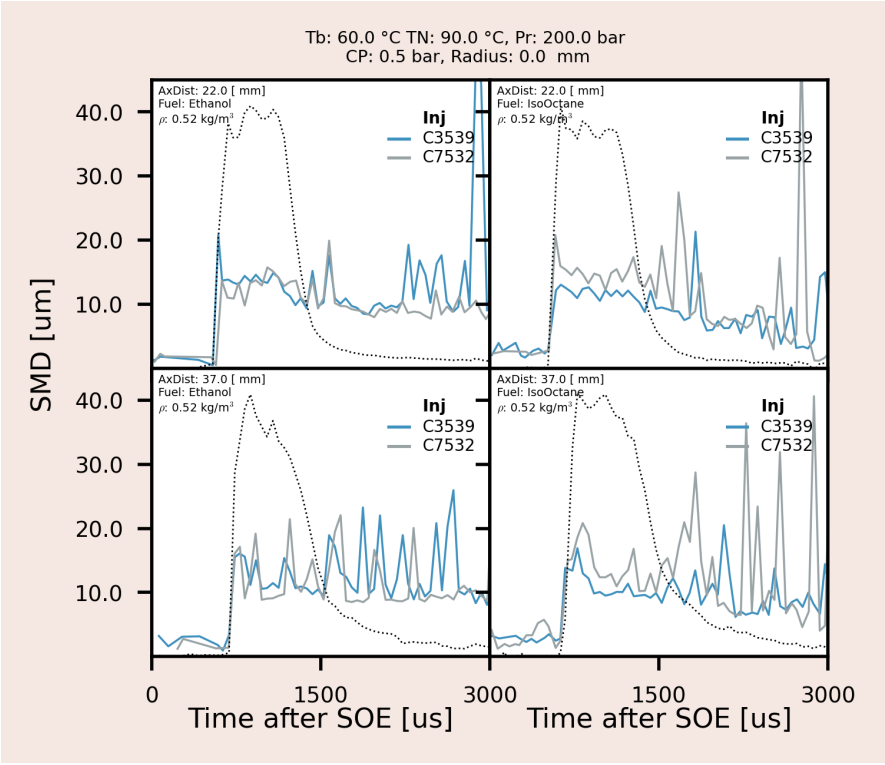


Figure 6.15: SMD transient comparisons for two nozzles.

Considering now the evaporative effects of the ambient temperature, the trends depicted in Figure 6.16 show a general decrease in SMD with increasing chamber temperature. The multiplot figure is structured such that each subplot varies horizontally by ambient backpressure, increasing from left to right, and vertically by axial distance, with two axial positions represented.

Within each subplot, boxplots display the SMD variation at different ambient temperatures.

Each box in the plot aggregates data from several fuels, all evaluated at the spray center, defined here as the closest available radial positions to the injector axis. These boxplots statistically represent the droplet diameter distribution at each ambient temperature, combining all fuels under fixed pressure and axial position. This arrangement enables the evaluation of the temperature-driven evaporative effects while minimizing interference from spatial and pressure-related variables.

In general, the median droplet diameter decreases as temperature rises, consistent with enhanced evaporation and finer atomization. However, one of the main contributors to the variability observed within each boxplot is Hexane, which due to its high volatility, tends to introduce wider droplet size distributions, especially under strong flash boiling conditions and when measurements are taken close to the nozzle. Under these specific circumstances, Hexane can lead to unexpectedly high SMD values, as early plume expansion, coalescence, or incomplete atomization near the nozzle may counteract the expected reduction in droplet size.

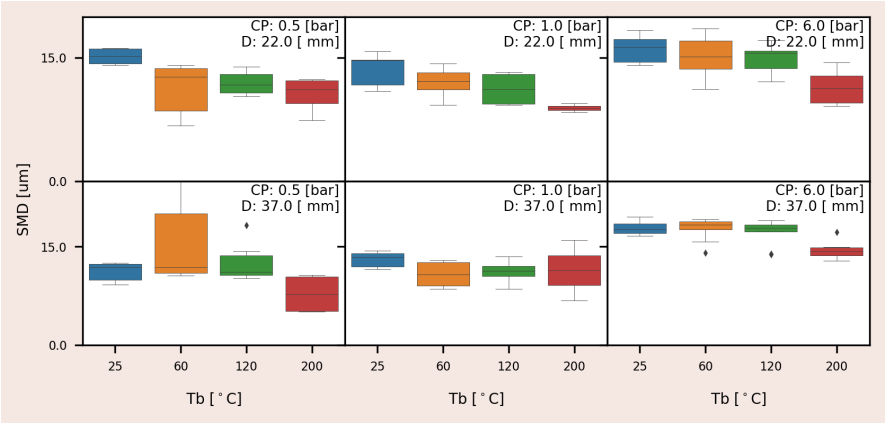


Figure 6.16: Ambient temperature trends for SMD at different ambient densities. Each box contains variations in fuel and radius very close to the center. The top row shows the results at closer distance to the nozzle, and the second row is at a farther axial position (D).

6.5 Approaching Flash boiling conditions

Now concentrating in the main variables that create a change in the flash boiling regime, besides the fuels, the variations to be considered are the fuel

temperature and ambient pressure.

6.5.1 Flash boiling conditions analysis

Having compared the effects of ambient temperature and droplet size and velocity in different positions in the spray, this section focuses specifically on the variables governing flash boiling regimes. The analysis is limited to those test cases with high R_p (used as an indicator of flash boiling).

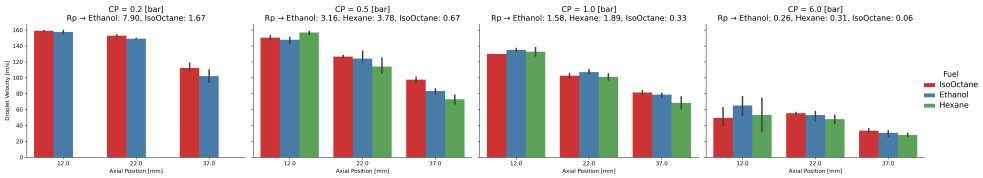


Figure 6.17: Droplet velocity at three axial positions for different fuels under varying ambient pressure. R_P values indicated per fuel at each CP level. Measurements at 90°C and 200 bar of injection pressure at the core of the spray.

The bar plots in Figure 6.17 present droplet velocities measured at the three main axial positions for four levels of ambient counter-pressure, ranging from 0.2 to 6.0 bar. The observed trends suggest that under low backpressure conditions, the primary variable influencing the initial velocity of the spray is fuel density. Despite differing degrees of R_P, which strongly influence flash boiling intensity, IsoOctane consistently exhibits slightly higher velocities than Ethanol at the nozzle exit. Hexane, owing to its high volatility and lower density, also maintains high initial velocities near the nozzle, but shows a sharper decline in velocity with axial distance. The velocity measurements for the latter fuel at 0.2 bar are excluded from this comparative analysis, as MIE images revealed before in this chapter, Hexane, under very low back-pressure and high injection temperatures, undergoes plume collapse at 90°C, in which plumes are not clearly identifiable.

As backpressure increases, other aerodynamic effects, particularly fuel–air interactions, begin to dominate. Under ambient conditions (1.0 bar), the fuel with the highest density, Ethanol, tends to retain the highest velocity throughout the spray. In contrast, fuels like Hexane, which exhibit high initial velocities at low pressures, lose momentum more rapidly along the axial direction. This trend is attributed to spray expansion due to flash boiling, which reduce axial momentum farther downstream.

As shown in earlier velocity profile analyses, higher ambient counterpressure generally results in lower overall velocities. Notably, near the nozzle

(12 mm), Ethanol retains the highest velocity among the fuels tested, likely due to its density and ability to sustain momentum. These trends are consistent with the momentum measurements discussed in chapter 4, where the measured momentum at the nozzle exit was found to be very influenced by the fuel's injection temperature and density, with relatively minor variations across fuels at the point of injection. However, as the spray travels downstream, these small differences amplify, especially under evaporative or flash boiling conditions.

6.5.2 Diameter distribution under flash boiling conditions

Figure 6.18 targets the droplet size distribution in relation to the different flash boiling regimes described in the literature and categorized in chapter 4. Based on the R_P, these regimes are generally classified into: non-flashing, transitional or incipient flashing at low R_P values, and extreme flash boiling, which occurs at elevated R_P values and may or may not lead to plume collapse depending on other influencing parameters.

The droplet size distributions for Ethanol, display consistent trends in SMD values, with larger average droplet sizes expected due to its physical properties. However, within each flash boiling regime, slight variations in the shape of the distribution can be observed for Ethanol, indicating that even for the same fuel, the extent and mode of flashing affect spray structure.

When comparing across fuels, the influence of the flash boiling regime on droplet size becomes more evident. For the same level of flashing, Ethanol generally produces higher SMD values than Hexane and IsoOctane. Both of the latter fuels exhibit similar and lower SMDs, suggesting that fuel volatility and physical properties have a strong influence on atomization, even under equivalent thermodynamic conditions.

As flash boiling intensity increases, atomization improves up to a transitional regime, where droplet distributions become more compact. In this stage, the number of distinct droplet size classes decreases, and the SMD also declines, indicating enhanced breakup and finer spray structure. However, under strong flash boiling conditions, this trend reverses. Distributions broaden again, and larger droplets begin to appear, possibly due to plume collapse and secondary coalescence. This reversal suggests that excessive flashing may lead to less efficient atomization in some cases, resulting in a shift in the overall distribution and a modest increase in SMD.

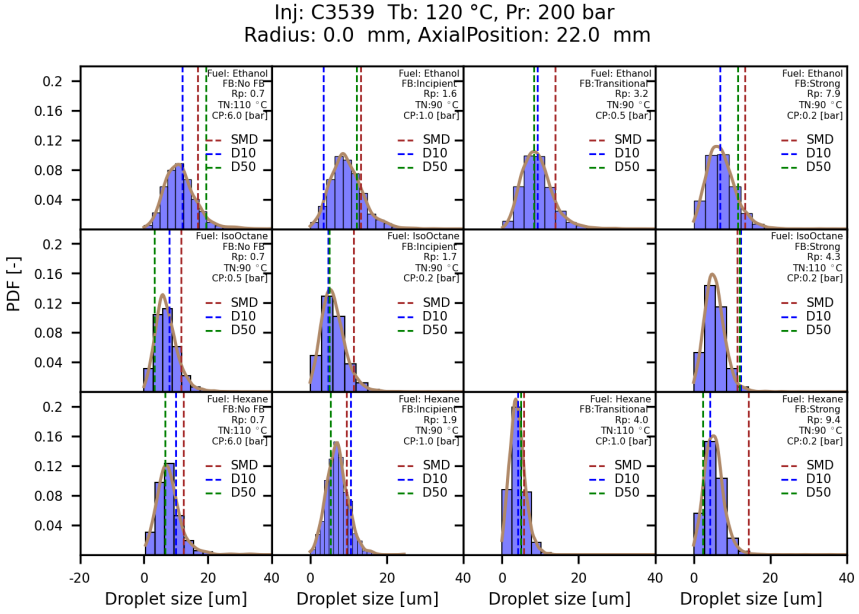


Figure 6.18: Droplet distribution separated by Fuel and flash boiling regime.

6.5.3 SMD relation to flash boiling

To further explore the role of flashing levels, the measured SMD values were plotted against R_P on a semi-logarithmic scale, with R_P on the logarithmic x-axis and SMD on the linear y-axis. The results reveal a generally linear inverse relationship between $\log(R_P)$ and SMD: as R_P increases, droplet sizes tend to decrease, confirming the progressive enhancement of atomization under stronger flash boiling conditions.

However, within specific R_P intervals, particularly those corresponding to transitional and strong flash boiling, there is significant variability in droplet size. For example, in the case of Hexane at 110°C, especially at lower R_P values, the onset of collapse introduces considerable scatter in the SMD values.

While SMD generally decreases with increasing R_P, at very high R_P values, where collapse becomes dominant, a reversal occurs. In these regimes, SMD values increase again, suggesting that excessive flash boiling can lead to plume merging or droplet re-agglomeration, reducing atomization quality. This behavior is most evident in the Hexane results, where SMD reaches a minimum and then rises as R_P increases. Ethanol also follows this general trend, though its higher density appears to buffer some of the extremes observed in lighter fuels.

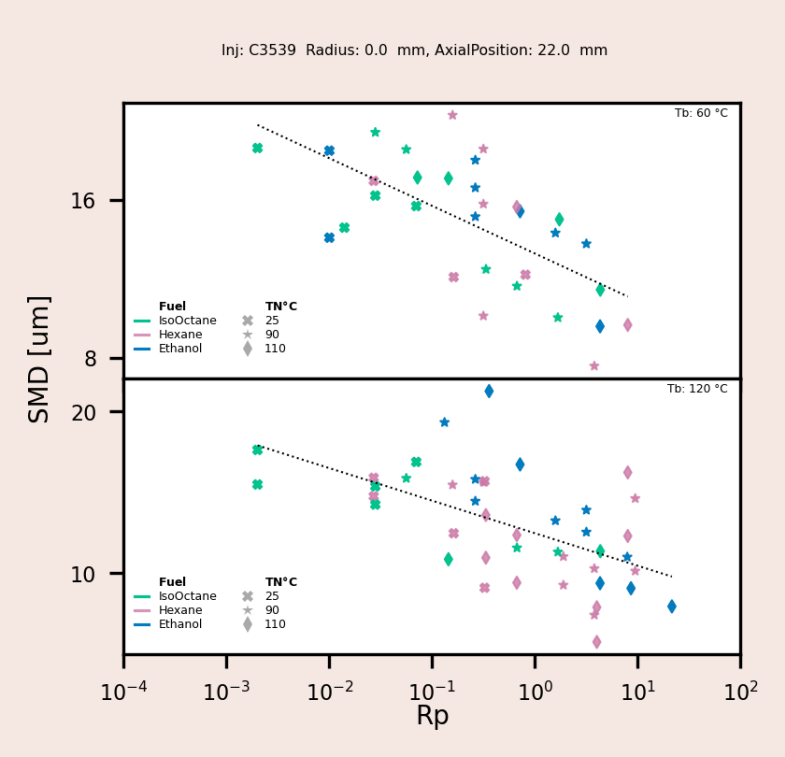


Figure 6.19: SMD trends compared vs R_P (based on CP).

6.6 Summary and conclusions

This chapter focused on droplet-level analysis, examining the velocity and size of droplets during injection using Phase Doppler Particle Anemometry (PDPA). The methodology section included a detailed explanation of the alignment, calibration, and validation of the PDPA system, applied to two different injectors and three fuels across a range of operating conditions.

- Characterizing the influence of injection pressure within fixed boundary conditions revealed not only the expected impact of pressure on spray dynamics but also its effect on the quality of velocity measurements. At axial positions located very close to the nozzle, the combination of high injection pressure and elevated ambient pressure complicates laser access and increases measurement uncertainty. As observed when increasing the injection pressure from 50 bar to 200 bar, data capture quality decreases. This is likely due to a denser spray core, resulting in more

concentrated fuel, which limits the penetration of the laser into the spray at $R = 0$.

- Flash boiling intensity by ambient pressure changes was identified as the dominant variable governing the laser accessibility and stability of high-velocity regions.
- Hexane, under conditions where $R_P > 3$, consistently exhibits plume collapse leading to a central redistribution of large droplets within the spray core.
- Kernel Density Estimation (KDE) analysis reveals that flash boiling does not always result in finer atomization; instead, droplet distributions become more dispersed.
- An increase in injection pressure does not necessarily improve atomization when spray collapse is present, highlighting the complex interaction between pressure and vaporization dynamics.
- Under standard flash boiling conditions with low values superheating degree, the influence of flash boiling and the role of fuel properties in determining droplet size compete against each other to define the dominant variable. As the degree of flash boiling increases, the effect of flash boiling becomes more pronounced and progressively takes over the fuel characteristics influence.
- A logarithmic inverse relationship between R_P and Sauter Mean Diameter (SMD) is established, with a trend reversal at extreme R_P values, in agreement with observations in the literature.

References

[1] Bautista Rodríguez, A. "Study of the Gasoline Direct Injection Process under Novel Operating Conditions". PhD thesis. Universitat Politècnica de València, 2021.

[2] Payri, R., Martí-Aldaraví, P., Alvarez, V. M., and Bautista, A. "Evaluation of GDI spray structures under flash boiling and strong collapse conditions with diverse fuels". In: *Applied Thermal Engineering* 234 (2023), p. 121195.

[3] Moon, S. et al. “Ultrafast X-ray study of multi-hole GDI injector sprays: Effects of nozzle hole length and number on initial spray formation”. In: *Experimental Thermal and Fluid Science* 68 (2015), pp. 68–81.

[4] Wang, B. et al. “Investigation of deposit effect on multi-hole injector spray characteristics and air/fuel mixing process”. In: *Fuel* 191 (2017), pp. 10–24.

[5] Liu, Y. et al. “Spray development and droplet characteristics of high temperature single-hole gasoline spray”. In: *Fuel* 191 (2017), pp. 97–105. DOI: 10.1016/j.fuel.2016.11.068.

[6] Kale, R. and Banerjee, R. “Experimental investigation on GDI spray behavior of isooctane and alcohols at elevated pressure and temperature conditions”. In: *Fuel* 236 (2019), pp. 1–12. DOI: https://doi.org/10.1016/j.fuel.2018.08.153.

[7] Valderrama, G. and Sebastián, J. “Macroscopic and microscopic characterization of non-reacting diesel sprays at low and very high injection pressures”. In: 2018.

Chapter 7

Exploring the spray collapse

7.1 Introduction

Gasoline direct injection (GDI) systems operate under a wide range of thermal and pressure conditions that can lead to non-standard spray behaviors such as flash boiling and spray collapse. Since the air-mixture formation and subsequent processes in engines are mostly governed by the fuel injection, these phenomena significantly influence the atomization process and affect combustion, evaporation, and emissions [1]. This chapter aims to explore these advanced behaviors through detailed analysis using spatially and temporally resolved droplet measurements obtained via Phase Doppler Anemometry (PDA).

This chapter aims to shed light on the internal dynamics of the spray, specifically focusing on the characterization of droplet diameters and velocities within the core region where collapse phenomena are most likely to occur. As previously discussed, jet trajectories shift under strong flash boiling conditions, often converging toward the injector axis. This behavior has been clearly observed in high-speed imaging, where the collapsing spray tends to realign along the central axis of the injector.

Building on this observation, the chapter investigates the droplet velocities and diameters measured near the injector axis in order to better understand the characteristics of flash boiling and the structure of the spray in collapsed conditions. The analysis is designed to explore how these internal spray features evolve under severe thermodynamic conditions, and how they might differ from conventional spray behavior.

To ensure a meaningful analysis, the study prioritizes measurement cases with R_P values significantly above 1, thereby minimizing the influence of collapse and providing a clearer baseline for comparison. These carefully selected cases enable a deeper examination of the spray behavior under non-collapsed and collapsed regimes.

The chapter also addresses the spatial distribution of velocities near the spray centerline, along with the methodological reasoning behind the experimental strategy. Additionally, it examines trends in droplet size distributions, offering insights into how these properties could influence engine performance, particularly in systems operating under flash boiling conditions.

7.2 Test Conditions

Initially, to investigate the velocity development within the collapse zone, a set of highly specific test conditions was selected, as summarized in the following table. These conditions were chosen to represent scenarios with subatmospheric ambient pressures, elevated ambient temperatures, and coverage across all three fuels. Special emphasis was placed on the most volatile fuels, namely hexane and ethanol, due to their higher tendency to trigger collapse phenomena under flash boiling conditions.

Table 7.1: Conditions to be tested: Rate of Injection

Parameter	**Operating Value**	**Units**	**Abbreviation**
Fuel	IsoOctane - Hexane - Ethanol*	-	$Fuel$
Injectors	C3539	-	Inj
Rail pressure	200 - 350*	bar	P_r
Injector temperature	90 - 110	°C	T_{inj}
Ambient pressure	0.2-0.5-1*	bar	P_b
Ambient Temperature	60 - 120	°C	T_b
Energizing time	800	µs	ET
Injection frequency	0.5	Hz	-

*For particular conditions

As previously detailed in chapter 3, the measurement methodology and the positioning of both the injector and the laser system were designed with the goal of capturing data directly along the injector axis. The experimental setup required precise optical alignment and injector positiong to ensure that laser beams could enter through a clear path between two adjacent spray plumes, both from a side view and a bottom view. As shown in the Figure 7.1, the

laser entry and the scattered light exit were configured to avoid interference from the spray, using regions between plumes where droplets were initially absent.

These regions, which were clear at early stages of injection, were selected based on the expectation that, due to collapse, the spray plumes would eventually converge into the centerline. This approach allowed for refracted light to reach the detector with minimal obstruction, taking advantage of the initially hollow center as the optimal optical pathway before plume convergence occurred.

It is important to note that this section only accounts to the vertical velocity component. The horizontal component was not included due to significant signal variability encountered during measurement, which led to inconsistent data quality across the mapping region. As a result, the vertical velocity was prioritized, as it provided a better representation of the spray dynamics and is the pair of lasers employed for the size determination by the PDPA equipment.

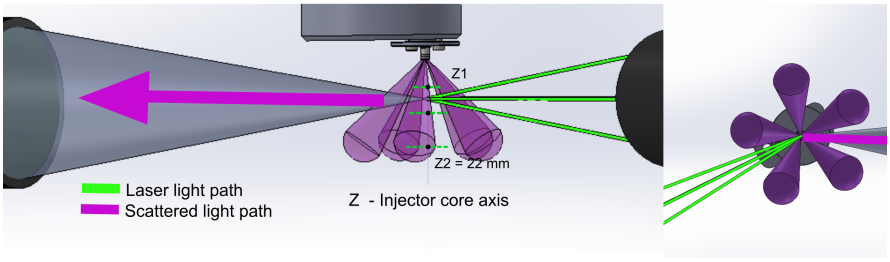


Figure 7.1: Diagram showing the passing of the lasers through the sprays for measuring at the center axis.

To visually illustrate the collapse behavior, Figure 7.2 presents the spray structures observed under key collapse conditions. Focusing on Hexane, the most volatile fuel tested, the images display a vertical variation in ambient back-pressure, keeping the ambient temperature fixed at 120 °C. As seen from bottom to top, decreasing backpressure leads to more pronounced plume collapse. At the lowest backpressure and highest fuel temperature, the spray exhibits a clear transition into a single, narrow jet, where the distinction between individual plumes becomes increasingly difficult. At 0.5 bar, the plumes begin to lose definition and merge further, forming a more diffused spray. At 0.2 bar it is indistinguishable the number of spray plumes and only one jet is perceived. This aligns with previous observations in the literature [2, 3].

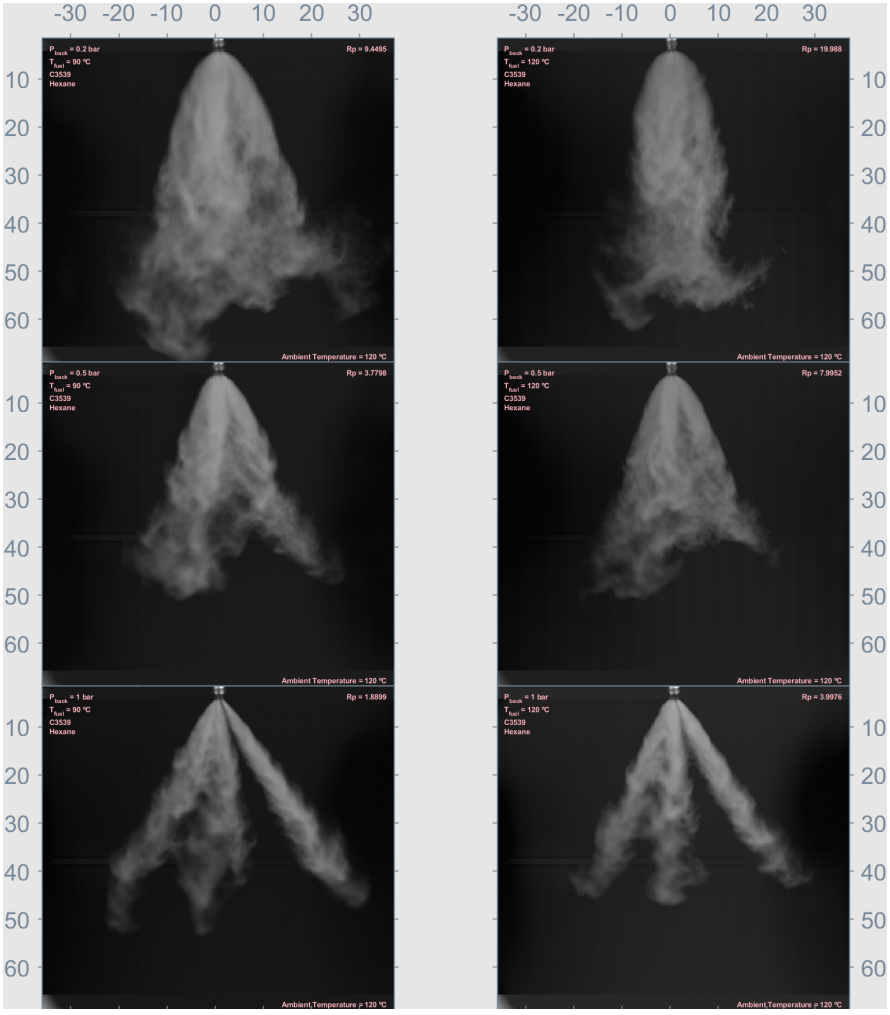


Figure 7.2: Collapse structure for the Hexane spray at various injection condition.

7.3 Spray Collapse: Velocity behaviour in the spray jets' core

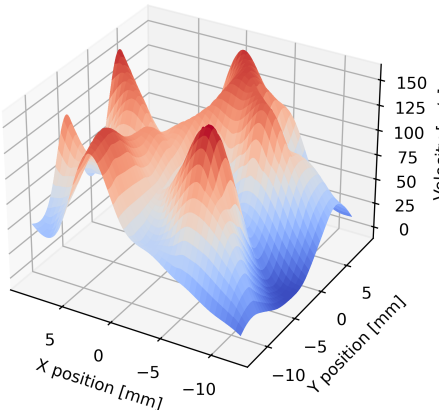
Although the collapse is clearly visible in the images, visual observation alone does not provide sufficient detail on the internal spray behavior. Therefore, aiming to characterize the droplet and velocity distribution within the collapsed spray core. The methodology described in the previous chapter for precise alignment and localization of individual jets within the spray is recalled. This positional accuracy plays a vital role for measuring this area, thanks to determining the real angular orientation of each plume, and in consequence, deciding the best orientation.

While such spatial mapping is experimentally demanding due to the large number of measurement points required, it can be focused on the two initial collapse conditions shown in the Figure 7.2. The first case represents a moderately collapsed spray forming a single coherent jet, while the second corresponds to a case of extreme collapse.

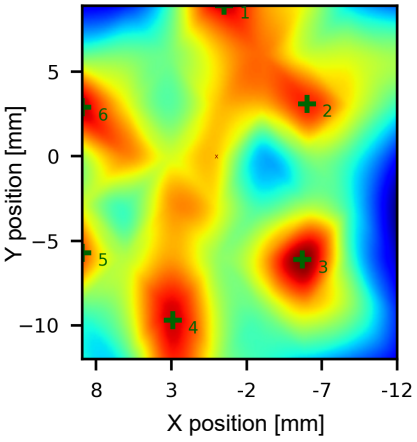
For the first case, a broader spatial map of the spray is introduced in Figure 7.3. On the left a three-dimensional velocity map highlights the presence of the main spray plumes within the injection structure. It is particularly notable that the central region exhibits elevated velocities, forming a non-uniform velocity field. A main region of high velocities seems to be formed between two of the plumes, while intermediate areas display gaps or lower-velocity zones. The image illustrates that, among the spray plumes, the two closest one, Spray 1 and 2, have notably higher velocities in the region between them. This pattern suggests a mutual attraction, consistent with previous observations in the literature [4, 5], where the degree of collapse has been correlated with the proximity of adjacent plumes or the total number of plumes within the injector nozzle. In this case, the elevated velocities observed in the inter-plume region indicate a higher level of collapse, with the jets appearing to converge not only toward each other but also toward the diametrically opposite side of the injector axis.

This interaction forms a band of high velocity and pronounced collapse along the central region, while surrounding areas remain more diffuse or, in some instances, partially void.

From the resulting distribution, it is evident that the dominant velocity patterns are still governed by the main jet structures. Meanwhile, dispersed droplets, potentially resulting from progressive plume collapse, appear to accumulate in high-velocity zones between the main plumes, indicating dynamic redistribution during the injection event.



(a) 3D view of the velocity distribution for a collapse condition.



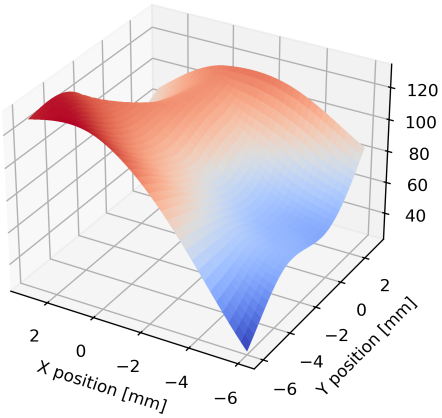
(b) Upper view of the velocity distribution for a collapse condition. The color scale is represented in the 3D map.

Figure 7.3: Collapse velocity distribution in the center of the injector. The operating condition for the C3536 injector spray is 200 bar of injection pressure, 120° C in the chamber, the nozzle temperature is 90° C, ambient pressure 0.2 bar using Hexane as fuel, for a R_P then is 9.45. The velocities were captured at 20 mm away from the nozzle tip.

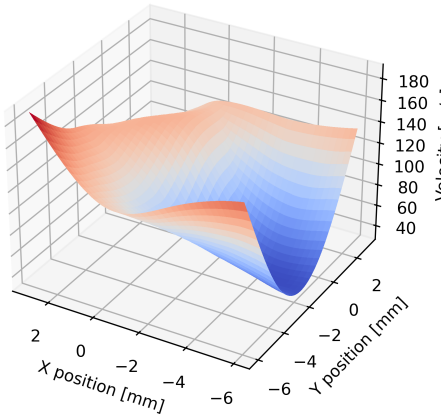
As a validation step, this same mapping procedure was repeated under non-collapsing conditions and in cases with minimal collapse. In those scenarios, no significant velocity was detected within the central region, aside from residual droplets originating from previous injections. This contrast further supports the conclusion that the measured structures in the collapse regime are indeed a direct result of the flash boiling-induced convergence and not background spray noise or measurement artifacts.

If this same mapping technique is applied to the innermost region of the spray, a more focused observation can be made compared to the broader spatial grid previously used, which captured the distribution across all spray plumes.

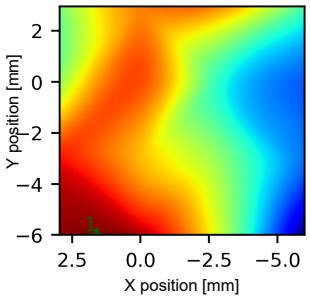
Figure 7.4 shows the measurements carried out under the most extreme collapse condition, namely, 110°C injection temperature and 0.2 bar ambient pressure, the high velocities previously observed between connected plumes in the moderate collapse case now appear more concentrated. These velocity peaks shift slightly away from the center, and the zone of collapse becomes more confined.



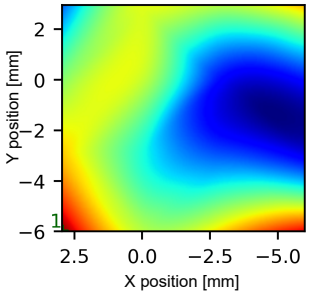
(a) 3D view for strong collapse condition at $P_{inj} = 200$ bar.



(b) 3D view for strong collapse condition at $P_{inj} = 350$ bar.



(c) Upper view of the velocity distribution. Scale is represented in the 3D map.



(d) Upper view of the velocity distribution. Scale is represented in the 3D map.

Figure 7.4: Comparison of 3D and upper views of velocity distributions for two injection pressures under strong collapse conditions: at $T_{inj} = 110° C$ and $P_{amb} = 0.2$ bar. Fuel = Hexane and thence nd $R_P = 15.81$. The injector is the 6-orifice-C3539.

Within this core region, high-velocity structures persist, but voids or interstices begin to form between them, suggesting a narrowing or focusing of the collapse. To the right of the figure, when the injection pressure is increased, the same high-velocity zones persist, but become more localized and intensified. The magnitude of the velocities is also higher at elevated injection pressure, as expected. The peaks of the velocity in the periphery of the plot, suggests measurements near the main plumes.

These measurements serve not only as standalone results for analyzing the velocity distribution, magnitude, and the spray dynamics, but also play an essential role in validating the reliability of the data acquired, and also help to provide insight into the internal momentum distribution within the collapsed spray structure.

7.4 Spray Collapse: SMD spatial distribution under extreme R_P conditions.

7.4.1 Diameter evolution in the center of the collapse zone

Considering the measurements explained before, we now apply the same methodology to analyze droplet diameters within the collapsed spray region. Figure 7.5 shows the evolution of the transient particle size profiles and the main diameter represention such as the Sauter Mean Diameter (SMD) over time at selected spatial locations.

The figure reveals that droplet sizes tend to increase toward the end of injection. Compared to standard, non-collapsed spray conditions, the variation in droplet size is significantly more pronounced which can be attributed to the complex droplet dynamics in the collapse region, where localized instabilities and varying velocities influence droplet formation and growth.

Certain regions near the center show noticeable increases in SMD due to the presence of larger droplets. In contrast, other regions exhibit more uniform droplet sizes, with SMD and D_{50} values remaining relatively stable throughout the injection event.

Figure 7.6 focuses on a more extreme collapse condition, here the high-SMD regions become even more prominent. The spatial frequency and magnitude of large-droplet zones increase, suggesting that collapse enhances coalescence phenomena. This aligns with previous findings indicating that strong plume interactions and convergence in the spray core may promote droplet agglomeration, leading to the formation of larger particles within the collapse region. It is particularly notable how the SMD values in the central collapse

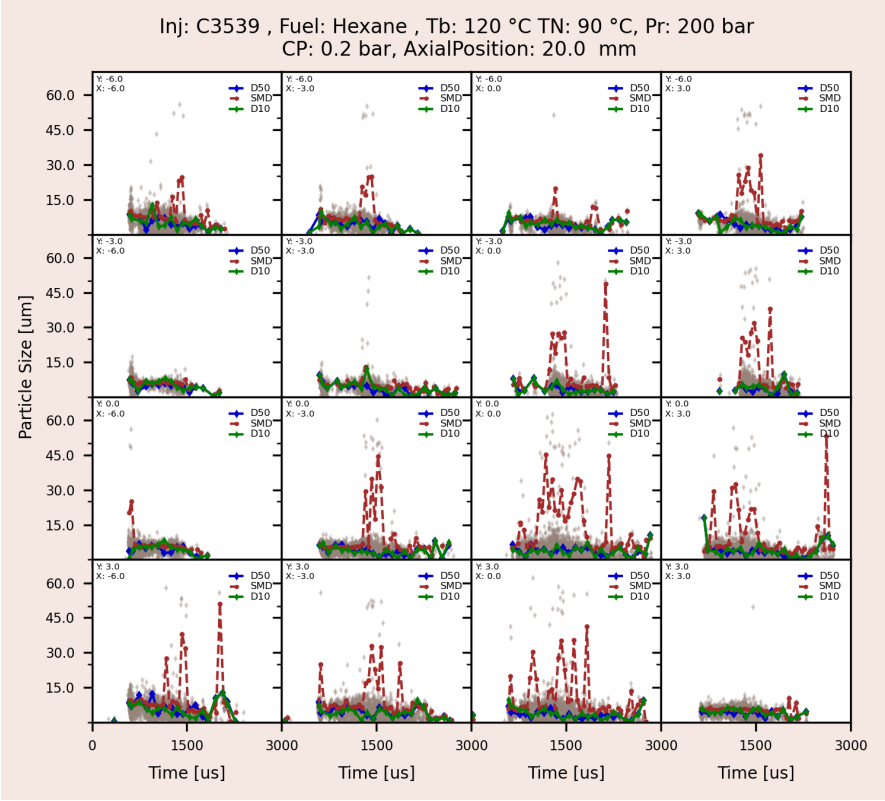


Figure 7.5: Transient diameter profiles captured in the center of the injector axis surroundings for a collapse condition. Operating conditions are depicted in the plot.

region during injection are considerably higher than those observed in any other condition analyzed in the previous chapter.

To analyze the spatial distribution of droplet sizes, lets retrieve the same three-dimensional mapping approach, replacing the vertical velocity component with the measured SMD at each point. This visualization permits to identify how droplet size varies within the collapse zone, keeping in mind the picture of the previously noted high-velocity concentrated band flanked by hollow regions.

For the SMD maps showed in Figure 7.7, the droplet sizes increase significantly in the vicinity of that band. This supports the claim that collapse not only redistributes momentum but also promotes droplet growth, through mechanisms such as coalescence or reduced atomization efficiency near the convergence axis.

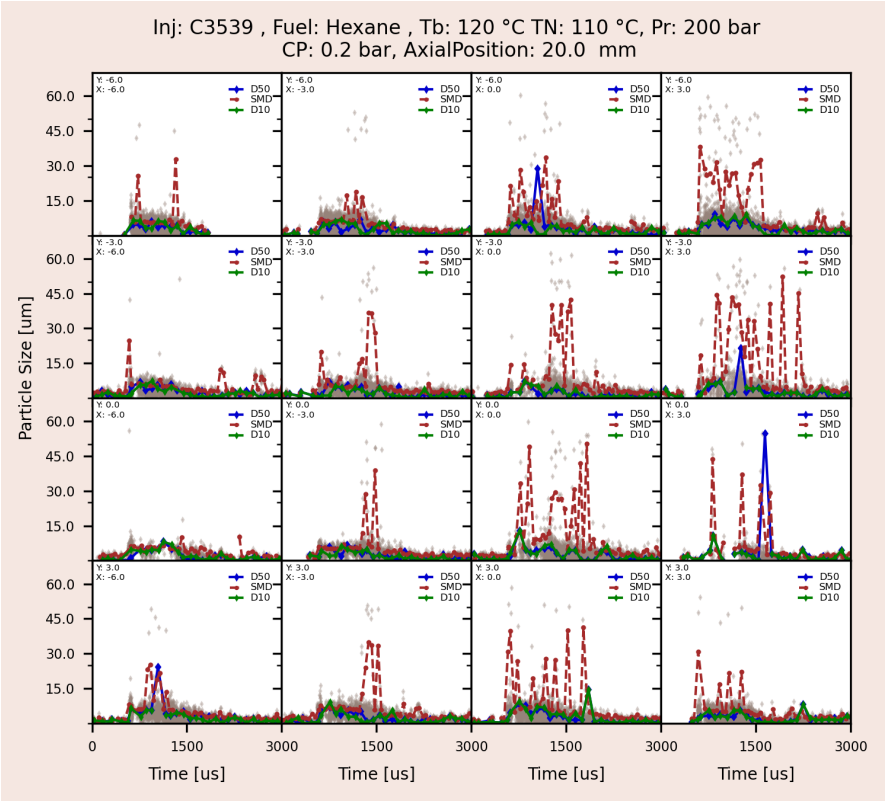
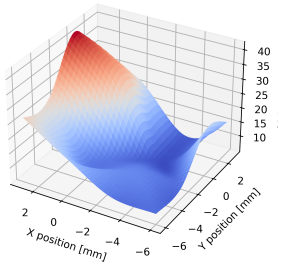


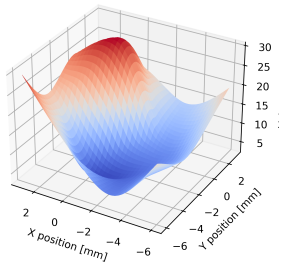
Figure 7.6: Transient diameter profiles captured in the center of the injector axis surroundings for an extreme collapse condition, usually depicted as a plume. Operating conditions are depicted in the plot.

When comparing the two injection pressures, it is also evident that while the region of large droplet accumulation remains similarly positioned, the overall magnitude of the SMD is lower at higher injection pressure. This suggests that increased injection pressure mitigates the formation of large droplets, possibly by enhancing initial atomization or suppressing plume coalescence, even under collapsing conditions.

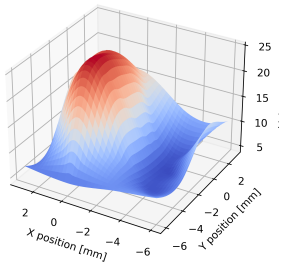
The right subplots of the figures, the SMD distribution in the same cropped area, the 90°C of injection temperature (the collapsed) condition is added for comparison. For this last column, the high-SMD region aligns more closely with the spray centerline observed in the previous velocity plots. Recalling how the collapsed band shifted with the degree of collapse or changes in R_P, the regions of elevated SMD follow that same spatial pattern. This suggests as well that increased collapse intensity correlates with the formation of larger



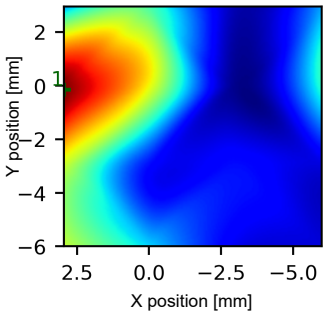
(a) 3D view of SMD for strong collapse at $T_{inj} = 110° C$ and $P_{inj} = 200$ bar.



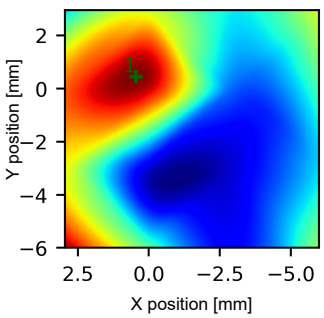
(b) 3D view of SMD for strong collapse at $T_{inj} = 110° C$ and $P_{inj} = 350$ bar.



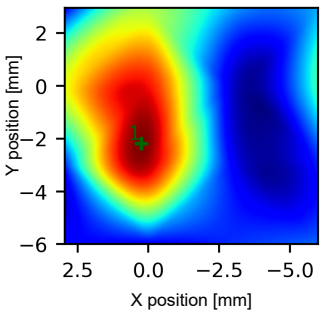
(c) Extra 3D view of the SMD distribution at $T_{inj} = 90° C$ and $P_{inj} = 200$ bar.



(d) Upper view of the SMD distribution at $R_P = 15.81$.



(e) Upper view of the SMD distribution at $R_P = 15.81$.



(f) Upper view at $T_{inj} = 90° C$ - $R_P = 9.45$ and $P_{inj} = 200$ bar.

Figure 7.7: Comparison of 3D and upper views of SMD distributions for two injection pressures under strong collapse conditions. Main conditions: $T_{inj} = 110° C$ and $P_{amb} = 0.2$ bar. Fuel = Hexane, Injector is the 6 orifice C3539. Measurements captured 20 mm from the nozzle tip.

droplets near the spray axis, and that the spatial redistribution of momentum during collapse directly impacts the droplet size field.

Importantly, the top row of the figure reveals how the overall SMD field changes with increasing collapse intensity. In less extreme conditions (collapse - final column), the high SMD values are lower in magnitude. However, under extreme collapse at low injection pressure, the highest SMD values are observed, indicating a substantial increase in droplet size solely due to collapse phenomenom. As injection pressure increases, even for the same collapse regime, the overall SMD decreases, but it still higher than the collapse condition.

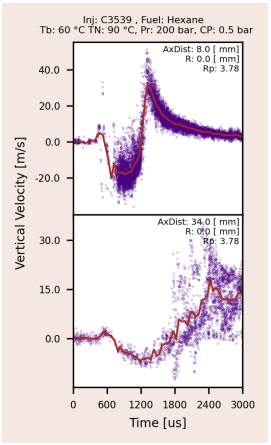
In summary, the maximum SMD is reached under the highest collapse condition combined with low injection pressure. As injection pressure increases or collapse intensity diminishes, the SMD decreases accordingly. This confirms that both the degree of collapse and the injection pressure have a compound effect on droplet size, and their interaction determines whether the spray favors coalescence or finer atomization.

7.5 Spray Collapse: A characterization at different levels of collapse

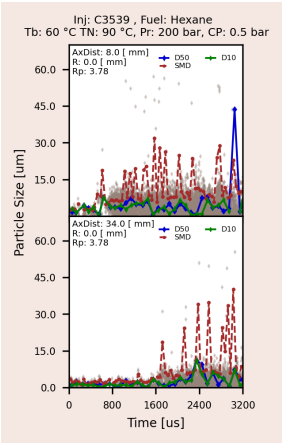
The results presented so far have focused on the distribution of droplet sizes, through the SMD descriptor, and velocity fields along the collapse zone, clearly revealing the collapse band depicted in Figure 7.3. With an established understanding of how collapse manifests under extreme conditions, this section extends the analysis to evaluate how this behavior changes across varying levels of R_P, which correspond to different degrees of flash boiling and collapse intensity.

7.5.1 On transitional collapse

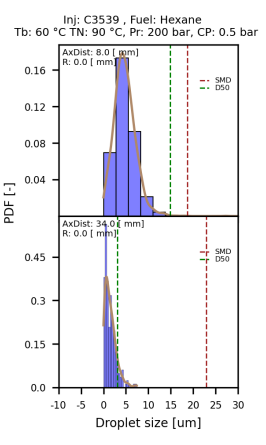
To begin with, multiple authors have proposed a collapse threshold based on R_P values around 3.5 [5–9]. A condition very close to this threshold is presented in Figure 7.8, with measurements acquired along the central line of the injector axis. The Figure is configured with subplots from left to right showing the velocity profile, the droplet size profile, and the droplet size distribution under this regime. The data correspond to two axial distances for the fuel Hexane, under an R_P of 3.78, closely matching conditions reported in previous studies that defined the onset of collapse.



(a) Transient velocity profiles at transitional collapse.



(b) Transient particle size profiles at transitional collapse.



(c) Transient PDF size distribution profiles at transitional collapse.

Figure 7.8: Characteristics of collapse under transitional flash boiling for Hexane.

One of the most notable features in this measurement is the presence of negative velocities at the spray center. These negative values were consistently observed throughout the experimental campaign, particularly under transitional collapse or early-stage collapse conditions. This behavior suggests the presence of droplets moving opposite to the main flow direction, most likely driven by vortex structures forming around the collapsing region. These negative velocities can be occasionally seen at the periphery of the mainspray in non-collapsing cases, they were much more pronounced and persistent in the central zone during collapse. Sphicas [10] also found counter-flow recirculation of the ambient gas toward the injector axis or to the region between plumes, pointing that effect as an indicator of plume interaction and collapse.

In parallel, the droplets found in this central region exhibited significantly higher SMD values compared to those in the main spray plumes. These larger droplets were typically observed toward the end of the injection event, after the primary spray phase had passed. This further reinforces the idea that vortex-induced recirculation and droplet accumulation are present in the collapse zone which might have negative effects on the combustion process [11]. The velocity profile observed in this case starts with a region of negative velocities, interpreted as vortex suction caused by intense flash boiling, and then transitions to positive velocities as the spray proceeds. This shift indicates a collapse flow pattern, where droplets initially move in reverse or recirculate, and then the main collapsing jets converge into the central axis.

These larger droplets likely originate from the primary jets, as a result of the sprays merging. As the jets come together, droplet coalescence events may occur between particles originating from different plumes. This mechanism explains the presence of larger droplets toward the end of the injection process, as the interaction between plumes intensifies and leads to localized droplet growth, retaining higher momentum and larger sizes. Meanwhile, the smaller droplets, which are drawn inward and detected earlier in the injection event, may have undergone more advanced atomization, resulting in reduced diameters.

This analysis confirms findings in the literature that associate collapsed sprays with enhanced coalescence, which promotes the formation of larger droplets. Overall, the droplet sizes recorded within the collapse structure were greater than the SMD measured under classical, non-collapsing spray conditions.

In terms of droplet size distribution, the overall behavior remains relatively consistent across the collapse region. In many cases, the distribution follows a near-normal profile, similar to that observed in non-collapsing sprays. However, in other instances, especially under strong collapse, the distribution becomes skewed or shifted to the left, indicating a higher frequency of smaller droplets. This asymmetry is also observed in the main spray plumes and is clearly reflected in the corresponding PDF plots.

7.5.2 On the vecinity of the injector centerline

A similar velocity pattern can be seen in Figure 7.9 under lower R_P or mild collapse conditions. Here the collapse is present as well near the center of the injector for the two axial positions shown in the Figure for Hexane. Although data quality at 16 mm is limited during part of the injection, which is likely due to low droplet presence or signal obstruction.

In these conditions, the velocity structure exhibits lower values near the center during the initial phase of injection, with the exception occurring in regions immediately surrounding the centerline. This suggests that, in areas where the spray has not yet fully collapsed, the influence of suction or vortex formation remains active both along the injector axis and in nearby regions. These findings, taken along the measured X-direction, reinforce the idea that collapse is not spatially uniform, with vortex behavior persisting near the core under transitional R_P conditions.

In addition, when examining the lower row of the Figure, which presents results for Hexane under a lower R_P, corresponding to a flash boiling condition

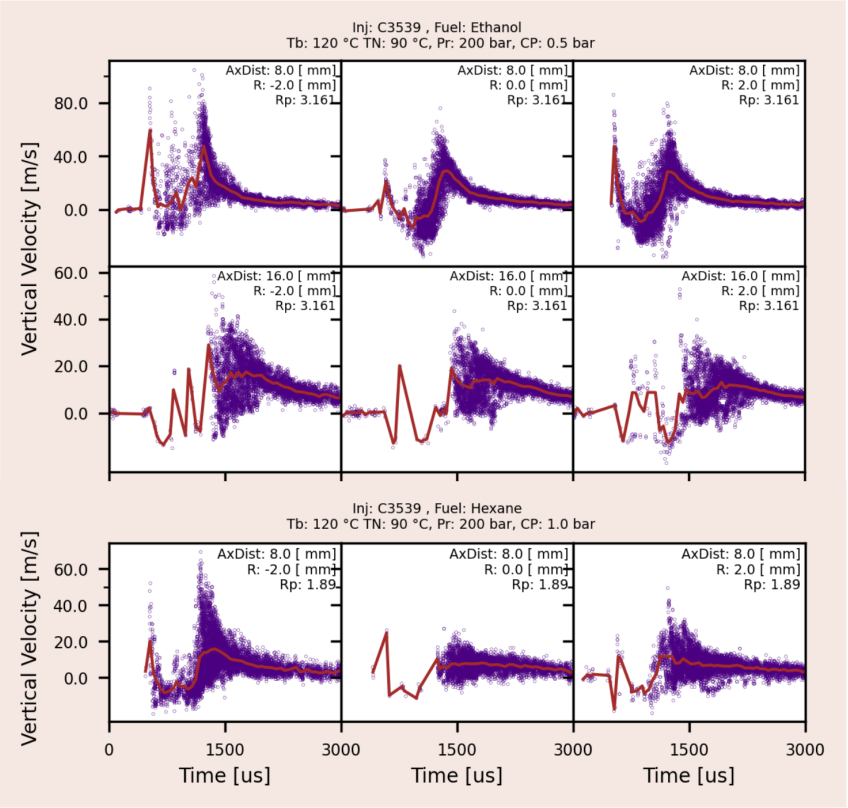


Figure 7.9: Transient velocity structure in positions near the centerline at transitional collapse condition for two fuels.

without clear evidence of collapse from previous measurements or visualizations, a distinct pattern emerges. Along the X-direction, moving radially toward the anticipated collapse band (negative radial positions), the presence of negative velocities becomes more prominent. This is particularly evident near the convergence region, where the tail of the already-redirected spray begins to appear.

These negative velocities are most noticeable at lower axial positions, such as 8 mm, and become less evident at higher positions or precisely at the injector center. The lack of detectable droplets in the center, coupled with consistent velocity readings in the surrounding regions, suggests that the collapse has not fully developed at this stage and has yet to reach the injector axis. Nonetheless, the presence of localized negative velocities and emerging directional flow changes indicate that the jets with greater collapse intensity

are beginning to influence the surrounding spray field. This supports the interpretation that vortex formation is already underway in this transitional phase, even if the full collapse has not yet occurred. Others authors have linked this backflow as indicators of collapse [4], besides, linking the plume fluctuation (mentioned in the previous chapter for the alignment of the spray) with the plume interference [12].

7.5.3 Diameter particularities in the vecinity of the centerline

As the presence of negative velocities serves as a distinctive indicator of collapse zones, another relevant marker, though less frequently observed, is the appearance of bimodal droplet size distributions. While not consistently present across all measurement cases, such bimodalities were identified in scenarios involving collapse or transitional collapse conditions.

For instance, Figure 7.10 shows a case with Ethanol in a region where the number of droplets measured was limited, and where collapse is either beginning to appear or progressing through its early stages. In this zone, two distinct droplet size groups are evident: one comprising relatively large droplets and another made up of much smaller ones. This dual population suggests a dynamic interaction between primary droplet break-up and ongoing coalescence or secondary atomization. Similar patterns were observed for the Hexane case with non clear structures being formed under this onset of collapse.

As the collapse becomes more fully developed and persistent, the droplet size distribution tends to stabilize. In these cases, the distribution shifts either toward a skewed profile with a higher frequency of smaller droplets, or towards a normal distribution, reflecting the transition from unstable transitional collapse to a more established and uniform spray structure.

7.5.4 Towards the collapse zone

If now, the velocity is measured for fixed axial distances from the nozzle, with measurements taken along a radial path from the injector center and extending toward the direction of Spray#4. This allows to spatially observe how spray dynamics evolve from the injector core outwards, and in a case of fully developed collapse, this radial path intersects the collapse band,

Figure 7.11 explores the velocities under fully collapse regime for both Ethanol and Hexane, under similar R_P values, the velocity profiles exhibit comparable shapes, with generally low positive velocities near the center and increasing slightly toward the collapse zone. In some Ethanol cases, especially

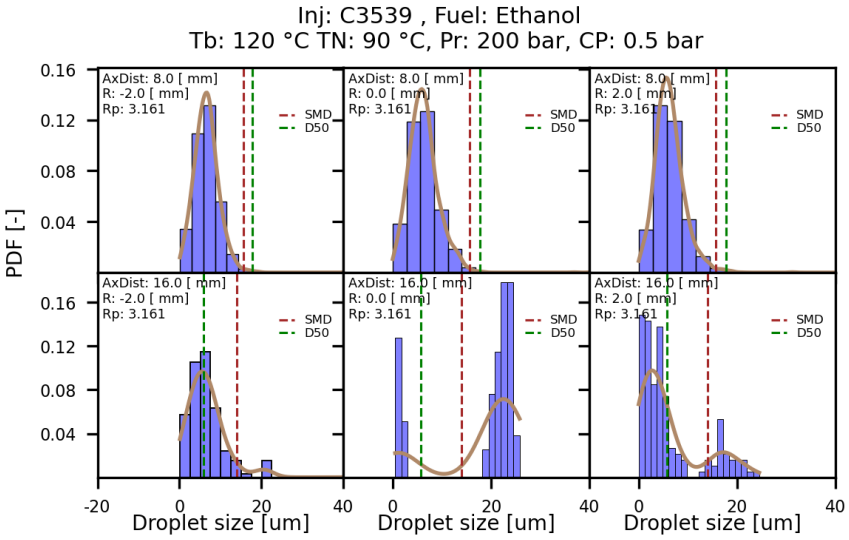


Figure 7.10: PDF droplet size distribution in positions near the centerline at transitional collapse condition.

at higher R_P, initial suction effects are observed at outer radial positions, indicating the presence of vortex structures around the collapse region, althought Ethanol has a slightly higher R_P than Hexane, it still shows small variations in velocity, while for the latter fuel, all measured velocities are positive and somewhat larger, suggesting that the collapse is more fully developed at the point of measurement.

Overall, in regions close to the injector center, both fuels show reduced velocity magnitudes, with positive values dominating across the measured range. Ethanol displays signs of flow recirculation, particularly at higher R_P, while hexane shows a more consolidated collapse, as inferred from the consistent positive velocities. This reinforce the idea that fuel properties, not just R_P, significantly influence spray collapse, something mentioned in previous studies [13].

Figure 7.12 depicts the droplet size distribution under the same conditions as the previous Figure 7.11 at the 22 mm axial cross-section, showing that Ethanol exhibits smaller droplet sizes in this case, contrary to what was observed in the fuel comparison presented in the previous chapter 5. This suggests that the degree of collapse plays a more dominant role than fuel properties alone in shaping droplet size behavior.

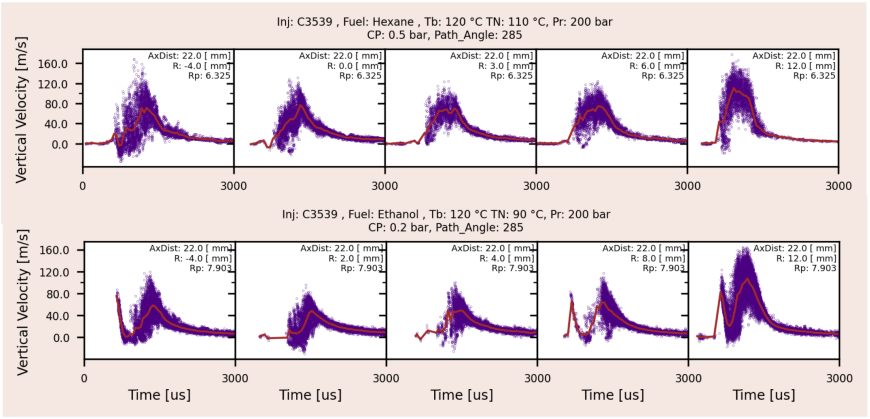


Figure 7.11: Radial evolution: Transient velocity profiles at fully collapse conditions towards the collapse band.

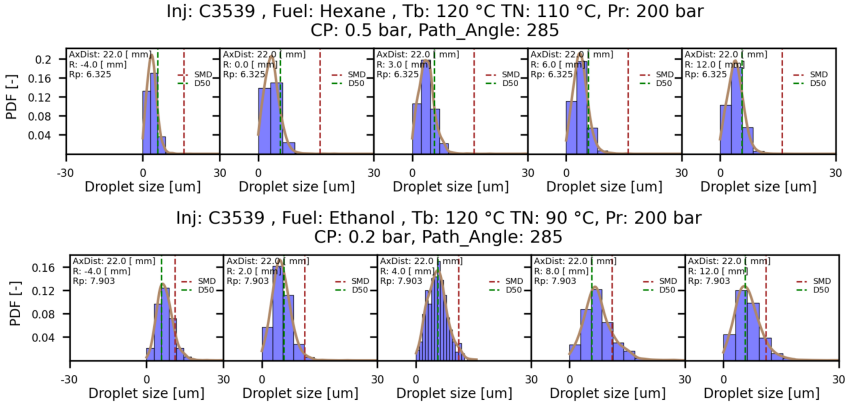


Figure 7.12: Particle size distribution shown by the PDF profiles at fully collapse conditions across positions towards the collapse band.

Additionally, the distribution profile for Ethanol changes under collapse scenarios, appearing more symmetric and approximately normal across all measured points. In contrast, Hexane continues to display higher SMD values overall, but with a distribution skewed to the left, indicating a larger population of smaller droplets.

7.5.5 Droplet characteristics in the injector centerline

Additionally, as established in the methodology, the central velocity distribution across the injector axis is also examined in Figure 7.13, where results for a highly collapsed condition, now including Iso-octane alongside Ethanol are compared.

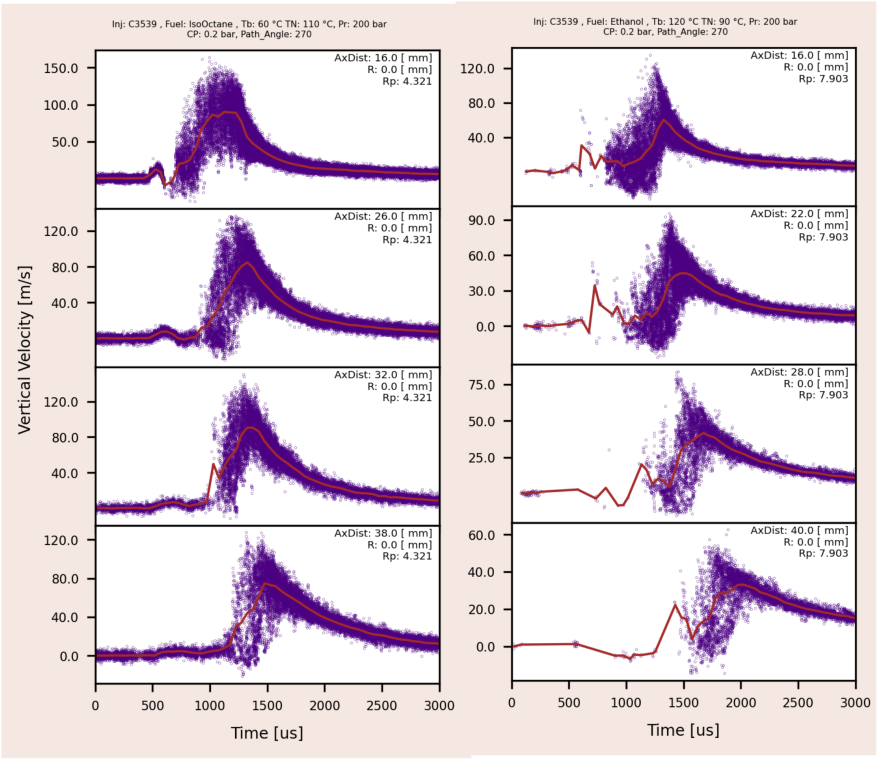


Figure 7.13: Axial evolution: Transient velocity profiles at fully collapse conditions depicting the changes in the centerline of the injector.

Both fuels clearly exhibit signs of collapse at this stage. Remarkably, for IsoOctane, analyzed here for the first time in this context, a defined collapse structure appears to have formed, with consistently positive velocities detected

at the injector center. These velocities are lower in magnitude compared to Ethanol, which operates under a higher R_P in the cases presented.

While it is difficult to determine whether the collapse band for IsoOctane is formed or has shifted to the center, the presence of a well-structured spray in the center is evident across different axial positions. As the measurement position moves further downstream from the nozzle tip, the velocity magnitude decreases, as expected from momentum decay along the axis. Only in the SOI of the IsoOctane, negative velocities are detected, only in a narrow region and with lower magnitude.

For Ethanol, the collapse structure matches previously observed transitional cases. Negative velocities are more prominent and occupy in the upper side. These velocities are strongest at the upper positions and progressively diminish further downstream. At the same time, once collapse is fully developed, the highest positive velocities appear more concentrated and dominant.

In a complementary way, Figure 7.14 is introduced for the droplet size distributions under these conditions. In general the distribution is similar to previous cases, with the IsoOctane having a left-skewed one and the Ethanol a symmetrical distribution. The farthest axial positions for Ethanol highlights in this case, showing an irregular distribution, since the droplets at this stage for a non collapse flow, has undergone multiple stages of atomization, coalescence, and possible breakup before reaching the measurement location.

7.6 Discussion and conclusions

The results presented in this chapter highlight the complex nature of spray collapse dynamics under flash boiling conditions. First by mapping sections of fully collapsed sprays anf characterizing their velocity and sizes. Further, analyzing the fuel influence in collapse and how this phenomena affects different portions of collapsed spray. The main findings are presented in Table 7.2

The detailed spatial resolution applied across axial positions proved essential in clarifying the evolution of the collapse structure. It revealed that plume convergence is not uniform throughout the injector field, but instead occurs preferentially between spray axes that are more closely aligned or energetically dominant, the closer two jets are, the more intense the collapse interaction becomes in that region, effectively pulling surrounding sprays toward the convergence zone.

A recurring observation was the axial asymmetry in vortex formation. Across several axial positions, negative velocities were more intense and frequent in the upper portion of the spray and either weaker or absent in the

Regime	Key spray characteristics	Main findings
Moderate Collapse (Single converged Jet)	Central region with high velocities, non-uniform velocity field.	A high-speed band forms near the center due to plume mutual attraction.
Transitional Collapse ($R_P \sim 3.5$)	Consistent presence of negative velocities at the spray center indicates droplets moving in the opposite direction, driven by vortex structures.	In that region, SMD is significantly higher in the center, with more occurrence of bigger droplets toward the end of injection. The velocity profile starts with vortex suction, transitioning to positive values (See transient profiles). Particle size distributions may be irregular or bimodal, as inFigure 7.10.
Extreme Collapse	Concentrated high-velocity peaks, slightly off-center, with a more confined collapse zone. Plumes become indistinguishable, forming a single narrow jet.	Regions with high SMD become more prominent, and large droplet zones appear more frequently and intensely. SMD values are significantly higher than under other conditions.
Fuel Type Influence (Hexane vs. Ethanol)	Hexane and Ethanol show greater tendency for flash boiling-induced collapse.	Ethanol exhibits recurring signs of backflow under high R_P, while Hexane at similar R_P shows more positive velocities, which suggests a more developed collapse. Fuel properties seem to affect collapse, with Ethanol showing smaller, more symmetric distribution, while Hexane has larger ones and a left-skewed profile.
Axial Asymmetry in Vortex Formation	Stronger and more frequent negative velocities in the upper part of the spray.	Suggests vortex generation initiates in the upper injector regions, with collapse propagating from top to bottom.

Table 7.2: Summary of spray regimes, main behaviors, and associated findings.

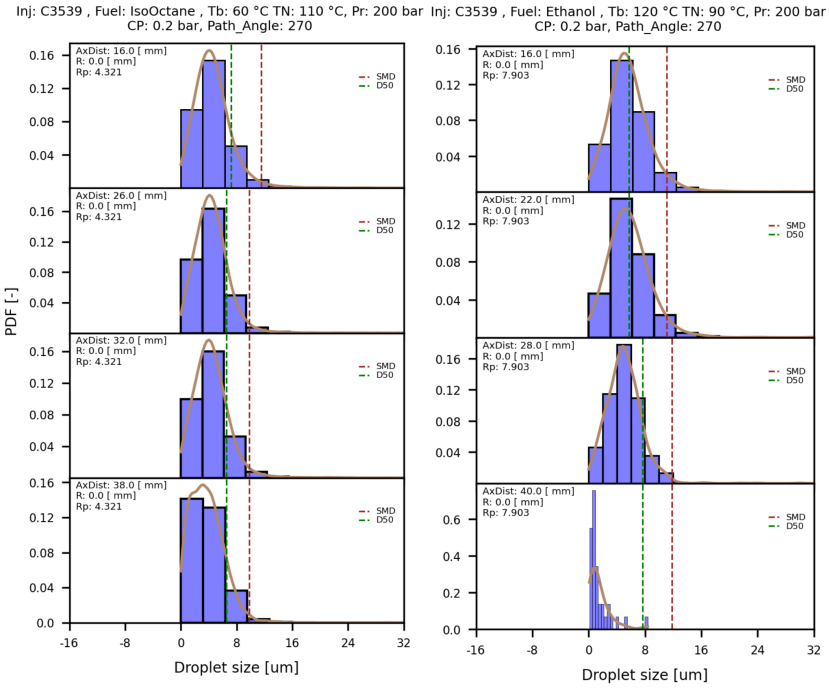


Figure 7.14: Particle size distribution shown by the PDF profiles at fully collapse conditions depicting the changes along positions in the centerline of the injector.

lower portion. This spatial distribution suggests that vortex generation is initiated in the upper regions of the injector, likely influenced by the angular conical geometry of the spray and the tighter spacing and higher velocities of jets in that area. From this point, the collapse propagates downward along the axis, reinforcing the concept of a top-to-bottom development of collapse driven by aerodynamic convergence and plume interaction.

Ethanol, displayed recurring signs of backflow, particularly under high R_P, while Hexane under similar R_P, showed more positive velocities, suggesting that collapse was already fully developed in those cases. These fuel-dependent differences in velocity structure highlight the influence of thermophysical properties on spray behavior under collapse due to flash boiling.

What is clear is that the presence of collapse zones significantly increases the droplet sizes, compared to non-collapsing conditions, even at higher injection pressures or the elevated flashing condition studied. In this context, the overall droplet size distribution often retains a left-skewed profile, which indicates an elevated presence of small droplets, which confirms that flash boiling

effects are still active. This observation aligns with findings from the previous chapter, where flash boiling by means of R_P was shown to globally reduce the Sauter Mean Diameter (SMD) across various conditions section 6.5. However, in the same analysis, certain anomalies or ourtliers were identified in the SMD trends, specially for conditions involving the Hexane. These deviations were likely caused by the onset of spray collapse at relatively low R_P values, which introduced large droplets into the distribution and distorted the average measurements. Thus, although flash boiling reduces droplet size through enhanced vaporization and breakup mechanisms, collapse acts as a counterpart by promoting droplet growth.

Droplets formed under the collapse zone are clearly influenced by the multiple phenomena taking place. Under transitional collapse conditions, complex interactions between atomization, coalescence, and droplet recirculation led to the emergence of irregular and sometimes bimodal droplet size distributions. In some Ethanol cases, distributions deviated from the more common normal or left-skewed profiles, particularly in regions further downstream, reflecting the cumulative and dynamic effects of spray collapse on droplet evolution.

Altogether, this chapter identified and characterized the conditions under which flash boiling and spray collapse occur and examined their measurable impact on droplet size, velocity, and spatial distribution. These insights contribute to a more complete understanding of advanced GDI spray behavior, and may indentify best practices to mitigate the undesired effects of collapse and improve overall combustion performance.

References

[1] Li, Y. et al. “Direct numerical simulation of atomization characteristics of ECN Spray-G injector: in-nozzle fluid flow and breakup processes”. In: *Flow, Turbulence and Combustion* 112.2 (2024), pp. 615–642.

[2] Yan, J., Gao, S., Zhao, W., Lee, T. H., and Lee, C.-F. “Experimental study of sprays with isooctane, hexane, ethanol and their binary mixtures under different flash boiling intensities”. In: *International Journal of Heat and Mass Transfer* 179 (2021), p. 121715. DOI: `https://doi.org/10.1016/j.ijheatmasstransfer.2021.121715`.

[3] Li, Y. et al. “Spray morphology transformation of propane, n-hexane and iso-octane under flash-boiling conditions”. In: *Fuel* 236.August 2018 (2019), pp. 677–685. DOI: `10.1016/j.fuel.2018.08.160`.

[4] Wu, S., Yang, S., Wooldridge, M., and Xu, M. "Experimental study of the spray collapse process of multi-hole gasoline fuel injection at flash boiling conditions". In: *Fuel* 242 (2019), pp. 109–123. DOI: https://doi.org/10.1016/j.fuel.2019.01.027.

[5] Guo, H. et al. "Comparison of spray collapses at elevated ambient pressure and flash boiling conditions using multi-hole gasoline direct injector". In: *Fuel* 199 (2017), pp. 125–134. DOI: 10.1016/j.fuel.2017.02.071.

[6] Payri, R., García-Oliver, J. M., Bracho, G., and Cao, J. "Experimental characterization of direct injection liquid ammonia sprays under non-reacting diesel-like conditions". In: *Fuel* 362 (2024), p. 130851.

[7] Du, J., Chen, H., Li, Y., Ye, L., and Li, G. "Experimental Study on Ethanol Gasoline Flash-Boiling Spray Characteristics Using Multi-hole GDI Injector". In: *Proceedings of China SAE Congress 2019: Selected Papers*. Singapore: Springer Singapore, 2021, pp. 635–645.

[8] Li, X. et al. "Insights into Microscopic Characteristics of Gasoline and Ethanol Spray from a GDI Injector Under Injection Pressure up to 50 MPa". In: *Sustainability* 16.21 (2024). DOI: 10.3390/su16219471.

[9] Chang, M., Lee, Z., Park, S., and Park, S. "Characteristics of flash boiling and its effects on spray behavior in gasoline direct injection injectors: A review". In: *Fuel* 271.December 2019 (2020), p. 117600. DOI: 10.1016/j.fuel.2020.117600.

[10] *Investigation of the Effect of Plume Number on Spray Collapse*. Vol. ASME 2019 Internal Combustion Engine Division Fall Technical Conference. Internal Combustion Engine Division Fall Technical Conference. 2019, V001T06A004. DOI: 10.1115/ICEF2019-7187.

[11] Sharma, N. and Agarwal, A. K. "Macroscopic spray characteristics of a gasohol fueled GDI injector and impact on engine combustion and particulate morphology". In: *Fuel* 295 (2021), p. 120461.

[12] Qiu, S. et al. "Dynamics and mechanisms of spray plume interference under flash boiling conditions". In: *Energy* 314 (2025), p. 134121. DOI: https://doi.org/10.1016/j.energy.2024.134121.

[13] Kale, R. and Banerjee, R. "Spray Collapse in a Multi-hole GDI Injector and Its Effect on In-Cylinder Combustion". In: *Two-Phase Flow for Automotive and Power Generation Sectors*. Ed. by K. Saha, A. Kumar Agarwal, K. Ghosh, and S. Som. Singapore: Springer Singapore, 2019, pp. 43–61. DOI: 10.1007/978-981-13-3256-2_3.

Chapter 8

Conclusions and future works

The chapter present a concise synthesis of the research process, the core discoveries obtained across the different experimental campaigns, and to place them within a broader context related to the understanding and analysis of flash boiling and spray collapse in gasoline direct injection (GDI) systems. The chapter begins with an overview of the research goals, it then revisits the primary results associated with the different test campaigns, from hydraulic characterization to spray visualization, including a wide range of fuels and operating conditions. The discussion emphasizes how these outcomes contribute to a more profound understanding of fuel spray behavior under superheated and sub-atmospheric conditions, particularly in the context of flash boiling.

Finally, this chapter outlines the potential implications of the findings, proposes future lines of investigation, and discusses how the methodologies and insights presented here could be expanded or refined to support further advancements in GDI system development.

8.1 Synthesis

Recent literature confirms that internal combustion engines remain central to current research. Their enduring relevance is supported not only by the extensive knowledge accumulated in the field, but also by its potential application to emerging technologies. Additionally, GDI combustion systems align well with transitional solutions expected to dominate the medium-term market. In this sense, market trends still favor combustion engines, as full

electrification faces ongoing challenges. Currently, GDI studies commonly focus on high-volatility fuels, especially relevant for GDI systems where clean combustion is prioritized.

Initial GDI studies at the research facility where this thesis was conducted, explored the influence of varying injection parameters on spray development and how these effects aligned with previous literature, and also adapting existing Diesel measurement techniques to GDI. The next logical step was to address more advanced and actively discussed topics in GDI spray research, such as flash boiling and spray collapse. Building on this, the present work advances the investigation by narrowing the gap between macroscopic observations and internal spray behavior. It focused primarily on the analysis of a commercially available injector capable of achieving high injection pressures in GDI systems. Specifically, the injector employed in the main experimental campaign supports injection pressures of up to 350 bar, making it suitable for evaluating spray formation under modern conditions. In addition to this primary injector, a second injector was used to enable a comparative analysis, allowing the investigation of performance variations linked to differences in nozzle geometry and configuration.

The fuels selected for this study were chosen based on their relevance to the investigation of volatility-driven spray behavior in GDI environments.

- IsoOctane: widely used in combustion simulation studies due to its similarity in octane rating to conventional gasoline. Its properties are well documented in the literature, facilitating comparisons with prior research.
- Hexane: selected for its volatility curve, which closely resembles that of commercial gasoline, making it suitable for evaluating spray characteristics under conditions that emulate real-world fuel behavior.
- Ethanol: widespread presence in literature due to being one of the most oxygenated fuels; and its contrasting volatility and density relative to other fuels make it valuable for comparative analysis with highly studied applications in GDI.

Finally, the injection conditions selected in this work are those that promote environments prone to flash boiling or spray collapse, as well as conventional cases commonly found in the literature. This approach ensures both a robust foundation for comparative analysis and the relevance of the test matrix within the broader context of GDI spray research.

8.2 Experiemental observations

The main findings resulting from each experimental campaign are presented in the following parts. These reflect the key observations and insights obtained through the different phases of testing, ranging from hydraulic characterization to optical diagnostics and droplet characteristics measurements.

8.2.1 Main hydraulic characterization findings.

- The internal geometry of the injector orifices, including diameter and conicity, was characterized using high-resolution microscopy on silicone mold replicas, a non-destructive method widely reported in the literature for assessing orifice structure.
- The rate of injection (ROI) remained stable across most surrogate fuels, with ethanol showing slightly higher values. This effect is attributed to ethanol's greater density and viscosity, which delay needle lift and injection onset. These observations are consistent with prior findings on how fuel properties influence transient injector dynamics and flow stability.
- Increases in injection pressure led to higher ROI and rate of momentum (ROM), whereas elevated nozzle temperatures extended the injection duration due to reduced fuel viscosity. Flash boiling had little effect on ROM, confirming that pressure drop is the dominant variable controlling momentum evolution under these conditions.
- The discharge coefficient (C_d) was consistently higher for the C7532 injector compared to the C3539. While C_d remained mostly stable across pressure drops, a slight decline was observed at high ΔP for the C3539, suggesting increased flow losses. ROM remained largely unaffected by fuel type, although Ethanol again introduced a delay in start of injection during cold conditions.

8.2.2 Main morphological observations.

Following the hydraulic characterization, optical visualization played its part in confirming the diverse spray structures. This was achieved through spray visualization using MIE scattering imaging, which enabled the qualitative observation of spray development under varying injection conditions.

- The morphological evaluation of the spray revealed a generally linear relationship between penetration and the density of the medium, with penetration decreasing as density increases. This trend is influenced by both temperature and ambient backpressure effects.
- An evaporative effect linked to the vessel temperature was also observed, contributing to changes in penetration behavior and overall spray structure.
- Among the tested fuels, Ethanol, the densest, exhibited the highest penetration levels. On its side, Hexane showed the most linear and stable penetration trends under a wide range of conditions.
- However, under high temperatures and low back-pressure, both Ethanol and Hexane, due to their high volatility, displayed increased irregularity in their penetration development, deviating from the expected trends.
- Despite the clear influence of R_P on overall spray dynamics, no direct correlation could be established between penetration and spray width and the flash boiling degree. This limitation is primarily attributed to the resolution of the MIE technique, which does not allow sufficiently precise differentiation of spray width across the tested conditions.

8.2.3 Main effects of operational condition on the spray microscopic variables.

The final stage of the investigation focused on measuring droplet size and spray velocity using PDA techniques. These measurements were carried out at several spatial positions across the spray.

- Empirical evidence confirms that spray collapse intensity under flash boiling conditions can be detected and characterized using PDA measurements, extending beyond the limitations of visual observation.
- Hexane, under conditions where $R_P > 3$, consistently exhibits plume collapse leading to a central redistribution of large droplets within the spray core.
- The leading parameters in defining the droplet size were the injection pressure, ambient temperature and flash boiling conditions. Althought, it was observed that an increase in injection pressure does not always improve atomization when spray collapse may be present, highlighting the complex interaction between pressure and vaporization dynamics.

- A logarithmic inverse relationship between R_P and Sauter Mean Diameter (SMD) is established, with a trend reversal at extreme R_P values, in agreement with observations in the literature.
- A comparative analysis between two injectors with different orifice counts, tested under identical thermal conditions, demonstrates how geometric configuration influences both velocity profiles and droplet size distribution remarking the effects of nozzle hole diameter on the spray momentum.

8.2.4 Characterization of a collapsed spray.

The microscopic characterization was further extended to spray collapse conditions, to study the droplet properties at the spray centerline and how these characteristics evolved with increasing degrees of collapse. This focus represents a natural progression in the research, enabling detailed insight into a phenomenon that remains relatively underexplored. By analyzing droplet behavior in the collapsed core region, the study introduces new understanding into the mechanisms of spray collapse, which is of considerable importance for advancing the predictive capability and optimization of GDI sprays.

- A robust methodology was successfully established to measure droplet velocities and sizes within the collapsed region of the spray, allowing for the identification of distinct patterns and internal flow structures.
- A well-defined collapse band was observed, strongly influenced by the proximity and velocity intensity of adjacent spray jets, and plume merge was found to be asymmetric, concentrated between energetically dominant jet pairs.
- The presence of collapse zones outweighs the expected benefits of enhancing conditions to atomization such as high injection pressure or elevated ambient temperature. Under collapse conditions, SMD mapping consistently reveals larger droplet sizes in the affected region, especially during extreme collapse events. This happened even when injection pressure was higher, showing that the collapse process takes precedence over conditions that would ordinarily promote finer atomization.
- While flash boiling generally reduced droplet sizes, the superimposed effect of collapse introduces larger droplets, resulting increased SMD values.

- Vortex structures characterized by backflow velocities were identified as key indicators and characteristics of collapse. These vortices were consistently found to initiate in the upper region of the injector, likely driven by geometrical and dynamic factors such as jet momentum and spray spacing dependent of the conical arrangement, typical of multi-hole sprays.
- The larger droplets introduced into the spray by the collapse phenomena, especially in Hexane at lower R_P, distorted the SMD trends, and in some cases, derived in bimodal distributions.

Overall, the findings deepen the understanding of spray collapse under flash boiling conditions, highlighting the interplay between atomization, fuel properties, and flow recirculation. These insights may guide strategies to improve injector design and fuel compatibility for better combustion performance. The resulting interaction between two competing phenomena, spray collapse and flash boiling, must be carefully considered when analyzing or optimizing spray behavior in GDI systems under flashing conditions.

8.3 Future works

The present study demonstrated the feasibility of accurately characterizing droplet sizes and velocities in GDI sprays unde novel operating conditions and modern hardware, particularly under flash boiling and spray collapse conditions, which are still partially understood in current literature. It provided validated measurement techniques and experimental trends that offer a robust basis for future investigation.

Building on this, several research directions can be suggested:

- Implementation of PLIF for velocity and vortex structure mapping: Planar Laser-Induced Fluorescence (PLIF) could enable detailed visualization of internal flow structures, particularly vortices associated with collapse zones. Applying PLIF under high injection pressures and volatile fuel conditions would enhance the understanding of fluid dynamics during flash boiling, complementing PDA data.
- Characterization of collapse thresholds: Although collapse was successfully identified and mapped, the point at which it becomes detrimental to atomization remains unclear. Future work should focus on identifying operational thresholds where droplet coalescence and velocity decay begin to negatively impact spray quality and combustion relevance.

- Study of spray interactions with variable jet spacing and simplified injectors: Extending the collapse analysis to injectors with varied inter-jet distances, or even single-hole nozzles, would allow the separation of spray interaction effects from geometric variables.
- Facility improvements for high-temperature and long-duration testing: Upgrading current optical chambers to reach higher ambient temperatures while preserving window clarity and scavenging efficiency would enable longer and more stable campaigns.
- Coupling with numerical modeling for validation and prediction: The experimental findings presented here could be used to validate CFD models of flash boiling and collapse, especially those that attempt to resolve transient breakup and coalescence.

Global Bibliography

(IEA), I. E. A. *World Energy Outlook 2023*. License: CC BY 4.0 (report); CC BY NC SA 4.0 (Annex A). Paris, France, 2023 (cited on page 2).

Abe, M., Ishii, E., and Ehara, H. "Atomized spray droplet size prediction from multi-hole nozzle for direct injection gasoline engines". In: *Journal of Fluid Science and Technology* 12 (2017) (cited on page 21).

El-Adawy, M., Nemitallah, M. A., and Abdelhafez, A. "Towards sustainable hydrogen and ammonia internal combustion engines: Challenges and opportunities". In: *Fuel* 364 (2024), p. 131090. DOI: https://doi.org/10.1016/j.fuel.2024.131090 (cited on page 37).

Addepalli, S. K. and Mallikarjuna, J. M. "Modelling Spray in GDI Engines: Fuel Injection Modelling". In: *Modelling Spark Ignition Combustion*. Ed. by P. A. Lakshminarayanan, A. K. Agarwal, H. Ge, and J. M. Mallikarjuna. Singapore: Springer Nature Singapore, 2024, pp. 339–389. DOI: 10.1007/978-981-97-0629-7_9 (cited on page 25).

Agarwal, A. K., Gupta, T., and Singh, A. P. "Advanced GDI combustion strategies for hybrid engines: Challenges and opportunities". In: *Renewable and Sustainable Energy Reviews* 133 (2020), p. 110264 (cited on page 39).

Agarwal, A. K., Singh, A. P., García, A., and Monsalve-Serrano, J. "Challenges and Opportunities for Application of Reactivity-Controlled Compression Ignition Combustion in Commercially Viable Transport Engines". In: *Progress in Energy and Combustion Science* 93 (2022), p. 101028. DOI: https://doi.org/10.1016/j.pecs.2022.101028 (cited on page 40).

Agrawal, Y. C. and McCullough, J. R. "Directional pedestal-free laser Doppler velocimetry without frequency biasing. Part 1". In: *Applied Optics* 20.9 (1981), pp. 1553–1556 (cited on page 78).

Aleiferis, P. G. and Van Romunde, Z. R. “An analysis of spray development with iso-octane, n-pentane, gasoline, ethanol and n-butanol from a multi-hole injector under hot fuel conditions”. In: *Fuel* 105 (2013), pp. 143–168. DOI: 10.1016/j.fuel.2012.07.044 (cited on page 37).

Aleiferis, P. and van Romunde, Z. “An analysis of spray development with iso-octane, n-pentane, gasoline, ethanol and n-butanol from a multi-hole injector under hot fuel conditions”. In: *Fuel* 105 (2013), pp. 143–168. DOI: https://doi.org/10.1016/j.fuel.2012.07.044 (cited on page 14).

Anderson, J. et al. “High octane number ethanol–gasoline blends: Quantifying the potential benefits in the United States”. In: *Fuel* 97 (2014), pp. 585–594. DOI: 10.1016/j.fuel.2012.03.017 (cited on page 58).

Avila, I. I. B. “CFD modelling and analysis of the passive pre-chamber ignition concept for future generation spark-ignition engines”. PhD thesis. Universitat Politècnica de València, 2023 (cited on page 22).

Awad, O. I. et al. “Particulate emissions from gasoline direct injection engines: A review of how current emission regulations are being met by automobile manufacturers.” In: *The Science of the total environment* 718 (2020), p. 137302 (cited on page 22).

Bar-Kohany, T., Arogeti, M., Malka, A., and Sher, E. “Advances in Liquid Atomization via Flash Boiling—A Global Overview”. In: *Energies* 16.19 (2023), p. 6763 (cited on page 33).

Bar-Kohany, T. and Levy, M. “STATE OF THE ART REVIEW OF FLASH-BOILING ATOMIZATION”. In: *Atomization and Sprays* 26 (2016), pp. 1259–1305 (cited on page 30).

Bautista Rodríguez, A. “Study of the Gasoline Direct Injection Process under Novel Operating Conditions”. PhD thesis. Universitat Politècnica de València, 2021 (cited on pages 59, 61, 69–71, 117, 129, 131, 137, 144).

Beale, J. C. and Reitz, R. D. “Modeling spray atomization with the Kelvin-Helmholtz/Rayleigh-Taylor hybrid model”. In: *Atomization and sprays* 9.6 (1999) (cited on page 25).

Beavis, N., Ibrahim, S., and Malalasekera, W. “Numerical evaluation of combustion regimes in a GDI engine”. In: *Flow, Turbulence and Combustion* 101 (2018), pp. 1035–1057 (cited on page 21).

Beleca, R., Abbod, M., Balachandran, W., and Miller, P. R. “Investigation of electrostatic properties of pharmaceutical powders using phase Doppler anemometry”. In: *IEEE Transactions on Industry Applications* 46.3 (2010), pp. 1181–1187 (cited on page 78).

Benajes, J., Payri, R., Bardi, M., and Martí-Aldaraví, P. "Experimental characterization of diesel ignition and lift-off length using a single-hole ECN injector". In: *Applied Thermal Engineering* 58.1-2 (2013), pp. 554–563. DOI: 10.1016/j.applthermaleng.2013.04.044 (cited on page 77).

Bhaskara. "Advanced combustion strategies for improving ic engine efficiency and emissions". In: *World Journal of Advanced Research and Reviews* (2023). DOI: https://doi.org/10.30574/wjarr.2023.17.2.1444 (cited on page 38).

Bornschlegel, S., Conrad, C., Eichhorn, L., and Wensing, M. "Flashboiling atomization in nozzles for GDI engines". In: 2017 (cited on pages 21, 28, 32).

Bosch, W. "The Fuel Rate Indicator: A New Measuring Instrument For Display of the Characteristics of Individual Injection". In: 1966 (cited on page 59).

Bosch Mobility. *Gasoline Direct Injection*. Accessed: March 30, 2025. 2024. URL: https://www.bosch-mobility.com/en/solutions/powertrain/gasoline/gasoline-direct-injection/ (cited on page 39).

Brenn, G. and Valkovska, D. "Modeling of vapor bubble growth and collapse in superheated liquids". In: *International Journal of Heat and Mass Transfer* 44.14 (2001), pp. 2605–2615 (cited on pages 32, 33).

Brennen, C. *Fundamentals of Multiphase Flow*. Cambridge University Press, 2005 (cited on page 33).

Burke, A., Abeles, E., and Chen, B. "The Response of the Auto Industry and Consumers to changes in the exhaust emission and fuel economy standards (1975-2003): A historical review of changes in technology, prices and sales of various classes of vehicles". In: (2004) (cited on page 12).

Buschbeck, M., Bittner, N., Halfmann, T., and Arndt, S. "Dependence of combustion dynamics in a gasoline engine upon the in-cylinder flow field, determined by high-speed PIV". In: *Experiments in fluids* 53 (2012), pp. 1701–1712 (cited on page 21).

Carburetor Blog. *How the Holley 847 Carburetor Works*. Accessed: March 23, 2025. 2023. URL: https://www.carburetor-blog.com/how-the-holley-847-carburetor-works/ (cited on page 13).

Cardosa, T. J. P. L. "Port Fuel Injection Strategies for a Lean Burn Gasoline Engine". PhD thesis. University of Brighton, 2011 (cited on page 12).

Carvallo García, C. L. "Experimental study of the behavior of gasoline direct injection GDI sprays during wall impingement under realistic engine conditions." PhD thesis. Universitat Politècnica de València, 2023 (cited on page 74).

Cavicchi, A. and Postrioti, L. "Simultaneous needle lift and injection rate measurement for GDI fuel injectors by laser Doppler vibrometry and Zeuch method". In: *Fuel* 285 (2021), p. 119021 (cited on page 106).

Cavicchi, A., Postrioti, L., Berni, F., Fontanesi, S., and Di Gioia, R. "Evaluation of hole-specific injection rate based on momentum flux measurement in GDI systems". In: *Fuel* 263.November 2019 (2020). DOI: 10.1016/j.fuel.2019.116657 (cited on pages 63, 119).

Cavicchi, A. et al. "Numerical and experimental analysis of the spray momentum flux measuring on a GDI injector". In: *Fuel* 206 (2017), pp. 614–627. DOI: 10.1016/j.fuel.2017.06.054 (cited on page 63).

Celik, M. and Ozdalyan, B. "Gasoline Direct Injection". In: 2010. DOI: 10.5772/9693 (cited on page 12).

Chai, W. S., Bao, Y., Jin, P., Tang, G., and Zhou, L. "A review on ammonia, ammonia-hydrogen and ammonia-methane fuels". In: *Renewable and Sustainable Energy Reviews* 147 (2021), p. 111254. DOI: https://doi.org/10.1016/j.rser.2021.111254 (cited on page 37).

Chala, G., Aziz, A., and Hagos, F. "Natural Gas Engine Technologies: Challenges and Energy Sustainability Issue". In: *Energies* 11 (2018), p. 2934. DOI: 10.3390/en11112934 (cited on page 22).

Chang, M., Lee, Z., Park, S., and Park, S. "Characteristics of flash boiling and its effects on spray behavior in gasoline direct injection injectors: A review". In: *Fuel* 271.December 2019 (2020), p. 117600. DOI: 10.1016/j.fuel.2020.117600 (cited on pages 35, 190).

Chang, M., Yu, Y. S., Park, S., and Park, S. "Spray dynamics and atomization characteristics of multi-hole GDI injectors under flash boiling conditions". In: *Applied Thermal Engineering* 200 (2022), p. 117626. DOI: https://doi.org/10.1016/j.applthermaleng.2021.117626 (cited on pages 17, 21).

Chigier, N., Bachalo, W. D., Reitz, R. D., Bellan, J., and Herrmann, M. "Spray control for maximizing energy efficiency and reducing emission in combustion engines". In: *Atomization and Sprays* 21.7 (2011) (cited on page 14).

Climate Change, U. N. F. C. on. *The Paris Agreement*. Accessed: 2024-06-24. 2015 (cited on page 3).

Climate Change (IPCC), I. P. on. "Framing, Context, and Methods". In: *Climate Change 2021 – The Physical Science Basis: Working Group I Contribution to the Sixth Assessment Report of the Intergovernmental Panel on Climate Change*. Cambridge University Press, 2023, pp. 147–286 (cited on page 2).

Climate Change (IPCC), I. P. on. "Technical Summary". In: *Climate Change 2021 – The Physical Science Basis: Working Group I Contribution to the Sixth Assessment Report of the Intergovernmental Panel on Climate Change*. Cambridge University Press, 2023, pp. 35–144 (cited on page 2).

Dernotte, J., Hespel, C., Foucher, F., Houillé, S., and Mounaïm-Rousselle, C. "Influence of physical fuel properties on the injection rate in a Diesel injector". In: *Fuel* 96 (2012), pp. 153–160. DOI: 10.1016/j.fuel.2011.11.073 (cited on page 109).

Dickinson, H. W. *A short history of the steam engine*. Routledge, 2022 (cited on page 1).

Dodge, L. G., Rhodes, D. J., and Reitz, R. D. "Drop-size measurement techniques for sprays: comparison of Malvern laser-diffraction and Aerometrics phase/Doppler". In: *Applied optics* 26.11 (1987), pp. 2144–2154 (cited on page 78).

Dong, R., Zhang, Z., Ye, Y., Huang, H., and Cao, C. "Review of Particle Filters for Internal Combustion Engines". In: *Processes* (2022) (cited on page 23).

Du, J., Chen, H., Li, Y., Ye, L., and Li, G. "Experimental Study on Ethanol Gasoline Flash-Boiling Spray Characteristics Using Multi-hole GDI Injector". In: *Proceedings of China SAE Congress 2019: Selected Papers*. Singapore: Springer Singapore, 2021, pp. 635–645 (cited on pages 35, 71, 190).

Du, J., Mohan, B., Sim, J., Fang, T., and Roberts, W. L. "Study of spray collapse phenomenon at flash boiling conditions using simultaneous front and side view imaging". In: *International Journal of Heat and Mass Transfer* 147 (2020), p. 118824. DOI: https://doi.org/10.1016/j.ijheatmasstransfer.2019.118824 (cited on page 71).

Du, J., Mohan, B., Sim, J., Fang, T., and Roberts, W. L. "Experimental and analytical study on liquid and vapor penetration of high-reactivity gasoline using a high-pressure gasoline multi-hole injector". In: *Applied Thermal Engineering* 163 (2019), p. 114187. DOI: https://doi.org/10.1016/j.applthermaleng.2019.114187 (cited on page 142).

Du, Z. et al. “Comparison of primary aerosol emission and secondary aerosol formation from gasoline direct injection and port fuel injection vehicles”. In: *Atmospheric Chemistry and Physics* 18.12 (2018), pp. 9011–9023 (cited on page 22).

Duan, Y., Shi, X., Kang, Y., Liao, Y., and Duan, L. *Effect of Hydrous Ethanol Combined with EGR on Performance of GDI Engine*. Tech. rep. SAE Technical Paper, 2020 (cited on page 5).

Duke, D. J. et al. “Internal and near nozzle measurements of Engine Combustion Network “Spray G” gasoline direct injectors”. In: *Experimental Thermal and Fluid Science* 88 (2017), pp. 608–621. DOI: 10.1016/j.expthermflusci.2017.07.015 (cited on pages 14, 64).

Duronio, F., De Vita, A., Allocca, L., and Anatone, M. “Gasoline direct injection engines – A review of latest technologies and trends. Part 1: Spray breakup process”. In: *Fuel* 265.November 2019 (2020), p. 116948. DOI: 10.1016/j.fuel.2019.116948 (cited on pages 25, 26).

Duronio, F., De Vita, A., Montanaro, A., and Allocca, L. “Experimental investigation and numerical cfd assessment of a thermodynamic breakup model for superheated sprays with injection pressure up to 700 bar”. In: *Fluids* 8.5 (2023), p. 155 (cited on page 137).

Durst, F. and Zaré, M. “Laser Doppler measurements in two-phase flows”. In: *The accuracy of flow measurements by laser Doppler methods* (1976), pp. 403–429 (cited on page 80).

Duy, N. H. X. and Lim, O. “An investigation of the effect of chamber temperature on macroscopic spray characteristic under GCI engine conditions”. In: *Fuel* 346 (2023), p. 128239. DOI: https://doi.org/10.1016/j.fuel.2023.128239 (cited on page 142).

Engine Combustion Network. *https://ecn.sandia.gov/diesel-spray-combustion/*. Online. 2010 (cited on page 99).

Engine Combustion Network. *Spray G Parametric Variation*. https://ecn.sandia.gov/gasoline-spray-combustion/target-condition/spray-g-parametric-variation/. Online; accessed 29 April 2020. 2020 (cited on pages 55, 58, 109).

European Automobile Manufacturers Association (ACEA). *Press release: Car registrations February 2024*. European Automobile Manufacturers Association. 2024. URL: https://www.acea.auto/files/Press_release_car_registrations_February_2024.pdf (cited on page 5).

Fanick, R. E., Kroll, S., Swarts, A., and Quarderer, S. "Effects of Dual Port Injection and Direct-Injection Technology on Combustion Emissions from Light-Duty Gasoline Vehicles". In: *SAE Technical Paper Series* (2019). DOI: https://doi.org/10.4271/2019-01-0999 (cited on page 38).

Fayyazbakhsh, A. et al. "Engine emissions with air pollutants and greenhouse gases and their control technologies". In: *Journal of Cleaner Production* 376 (2022), p. 134260. DOI: https://doi.org/10.1016/j.jclepro.2022.134260 (cited on page 22).

Geschwindner, C. et al. "Analysis of the interaction of Spray G and in-cylinder flow in two optical engines for late gasoline direct injection". In: *International Journal of Engine Research* 21.1 (2020), pp. 169–184. DOI: https://doi.org/10.1177/1468087419881535 (cited on page 72).

Gimeno, J. "Desarrollo y aplicación de la medida de flujo de cantidad de movimiento de un chorro Diesel". PhD thesis. E.T.S. Ingenieros Industriales, Universidad Politécnica de Valencia, 2008. DOI: 10.4995/Thesis/10251/8306 (cited on pages 62–66, 68, 119).

Gong, C., Yu, J., and Liu, F. "Combined impact of excess air ratio and injection strategy on performances of a spark-ignition port- plus direct-injection dual-injection gasoline engine at half load". In: *Fuel* 340 (2023), p. 127605. DOI: https://doi.org/10.1016/j.fuel.2023.127605 (cited on page 38).

Gong, H. et al. "End-of-injection fuel dribbling dynamics of multi-hole GDI injector". In: *Fuel* 317 (2022), p. 123406 (cited on page 15).

Grimaldi, C. N., Millo, F., et al. "Internal combustion engine (ICE) fundamentals". In: *Handbook of clean energy systems*. Vol. 2. John Wiley & Sons Limited, 2015, pp. 907–938 (cited on pages 22, 24).

Guo, H., Wang, B., Li, Y., Xu, H., and Wu, Z. "Characterizing external flashing jet from single-hole GDI injector". In: *International Journal of Heat and Mass Transfer* 121 (2018), pp. 924–932. DOI: https://doi.org/10.1016/j.ijheatmasstransfer.2018.01.042 (cited on page 32).

Guo, H. et al. "Comparison of spray collapses at elevated ambient pressure and flash boiling conditions using multi-hole gasoline direct injector". In: *Fuel* 199 (2017), pp. 125–134. DOI: 10.1016/j.fuel.2017.02.071 (cited on pages 141, 183, 190).

Al-Hakim, K., Wigley, G., and Stapley, A. "Phase Doppler Anemometry Studies of Spray Freezing". In: *Chemical Engineering Research and Design* 84.12 (2006), pp. 1142–1151. DOI: https://doi.org/10.1205/cherd06014 (cited on page 78).

Hamzah, A. et al. “A comparison of diffuse back-illumination (DBI) and Mie-scattering technique for measuring the liquid length of severely flashing spray”. In: *20th Australasian Fluid Mechanics Conference (AFMC)*. 2016 (cited on page 72).

He, H. et al. “An Experimental Study on the Flash Boiling Characteristics of Liquid Ammonia Spray in a Constant Volume Chamber under High Injection Pressure”. In: *Processes* 12.6 (2024). DOI: 10.3390/pr12061076 (cited on page 37).

Hecht, E. *Optics*. Pearson Education, Incorporated, 2017 (cited on page 78).

Helldorff, H. von and Micklow, G. J. “Primary and Secondary Spray Breakup Modelling for Internal Combustion Engine Applications”. In: 2019 (cited on page 28).

Hu, C. et al. “Spray dynamics characteristics in gasoline direct injection injectors at varied orifice inlet angles”. In: *Physics of Fluids* 37.1 (2025) (cited on page 14).

Hung, D. L. et al. *A high speed flow visualization study of fuel spray pattern effect on mixture formation in a low pressure direct injection gasoline engine*. Tech. rep. SAE Technical Paper, 2007 (cited on page 14).

Injector RX. *Fuel Injector Diagram | Injector RX*. Accessed: March 23, 2025. 2023. URL: https://www.injectorrx.com/fuel-injector-cleaning-and-flow-testing-service/fuel-injectors/fuel-injector-diagram/ (cited on page 17).

Jiang, C. et al. “Impact of gasoline direct injection fuel injector hole geometry on spray characteristics under flash boiling and ambient conditions”. In: *Fuel* 241 (2019), pp. 71–82. DOI: https://doi.org/10.1016/j.fuel.2018.11.143 (cited on page 14).

Jiang, Y. et al. “Impacts of cold starts and hybrid electric vehicles on on-road vehicle emissions”. In: *Transportation Research Part D: Transport and Environment* 126 (2024), p. 104011. DOI: https://doi.org/10.1016/j.trd.2023.104011 (cited on page 39).

Jin, Y. et al. “Comparison of diesel spray with small injection amount between single-hole and multi-hole injectors: results under same rail pressure and similar injection rate”. In: *International Communications in Heat and Mass Transfer* 118 (2020), p. 104862 (cited on page 18).

Joshi, A. and Johnson, T. V. “Gasoline particulate filters—A review”. In: *Emission Control Science and Technology* 4.4 (2018), pp. 219–239 (cited on page 23).

Kale, R. and Banerjee, R. "Spray Collapse in a Multi-hole GDI Injector and Its Effect on In-Cylinder Combustion". In: *Two-Phase Flow for Automotive and Power Generation Sectors*. Ed. by K. Saha, A. Kumar Agarwal, K. Ghosh, and S. Som. Singapore: Springer Singapore, 2019, pp. 43–61. DOI: 10.1007/978-981-13-3256-2_3 (cited on pages 26, 76, 195).

Kale, R. and Banerjee, R. "Experimental investigation on GDI spray behavior of isooctane and alcohols at elevated pressure and temperature conditions". In: *Fuel* 236 (2019), pp. 1–12. DOI: https://doi.org/10.1016/j.fuel.2018.08.153 (cited on pages 71, 168).

Kalwar, A. and Agarwal, A. "Overview, Advancements and Challenges in Gasoline Direct Injection Engine Technology". In: 2020, pp. 111–147. DOI: 10.1007/978-981-15-0368-9_6 (cited on page 38).

Kapusta, Ł. J. "Understanding the collapse of flash-boiling sprays formed by multi-hole injectors operating at low injection pressures". In: *Energy* 247 (2022), p. 123388. DOI: https://doi.org/10.1016/j.energy.2022.123388 (cited on pages 30, 31).

Karimi, M., Wang, X., Hamilton, J., Negnevitsky, M., and Lyden, S. "Status, challenges and opportunities of dual fuel hybrid approaches-a review". In: *International Journal of Hydrogen Energy* 46.70 (2021), pp. 34924–34957. DOI: https://doi.org/10.1016/j.ijhydene.2021.08.008 (cited on page 40).

Khandekar, S., Jaiswal, A. K., and Sahu, G. "Chapter Four - Spray cooling: From droplet dynamics to system level perspectives". In: ed. by J. P. Abraham, J. M. Gorman, and W. J. Minkowycz. Vol. 54. Advances in Heat Transfer. Elsevier, 2022, pp. 135–177. DOI: https://doi.org/10.1016/bs.aiht.2022.07.002 (cited on page 28).

Kim, Y., Il Kim, W., Min, B., Seo, J., and Lee, K. "Experimental investigation of combustion characteristics of ethanol–gasoline blended fuel in a T-GDI engine". In: *Applied Thermal Engineering* 208 (2022), p. 118168. DOI: https://doi.org/10.1016/j.applthermaleng.2022.118168 (cited on page 37).

Kraus, F., Martins Oliveira, A. A., Bueno Bontorin, A. C., Rouge dos Santos, A., and Cancino, L. R. "i-pentane and i-pentene as gasoline surrogates for the transport industry: a numerical analysis on ignition delay times using detailed chemical kinetics". In: *Brazilian Congress of Thermal Sciences and Engineering*. 2020. DOI: 10.26678/abcm.encit2020.cit20-0512 (cited on page 58).

Lacey, J. et al. “Effects of refinery stream gasoline property variation on the auto-ignition quality of a fuel and homogeneous charge compression ignition combustion”. In: *International Journal of Engine Research* 18.3 (2017), pp. 226–239 (cited on page 58).

Le Quéré, C. et al. “Global carbon budget 2017”. In: *Earth System Science Data* 10.1 (2018), pp. 405–448 (cited on page 2).

Lee, S. and Park, S. “Experimental study on spray break-up and atomization processes from GDI injector using high injection pressure up to 30 MPa”. In: *International Journal of Heat and Fluid Flow* 45 (2014), pp. 14–22 (cited on page 13).

Lee, S. and Park, S. “Spray atomization characteristics of a GDI injector equipped with a group-hole nozzle”. In: *Fuel* 137 (2014), pp. 50–59 (cited on page 26).

Lee, Z., Kim, D., and Park, S. “Effects of spray behavior and wall impingement on particulate matter emissions in a direct injection spark ignition engine equipped with a high pressure injection system”. In: *Energy Conversion and Management* 213.February (2020), p. 112865. DOI: 10.1016/j.enconman.2020.112865 (cited on page 30).

Lee, Z., Kim, T., Park, S., and Park, S. “Review on spray, combustion, and emission characteristics of recent developed direct-injection spark ignition (DISI) engine system with multi-hole type injector”. In: *Fuel* 259 (2020), p. 116209. DOI: 10.1016/j.fuel.2019.116209 (cited on page 13).

Lee, Z., Kim, T., Park, S., and Park, S. “Review on spray, combustion, and emission characteristics of recent developed direct-injection spark ignition (DISI) engine system with multi-hole type injector”. In: *Fuel* 259 (2020), p. 116209. DOI: https://doi.org/10.1016/j.fuel.2019.116209 (cited on page 56).

Lefebvre, A. H. “Atomization and Sprays”. In: 1988 (cited on page 28).

Lehnert, B., Conrad, C., and Wensing, M. *GDI Sprays with up to 200 MPa fuel pressure and comparison of diesel-like and gasoline-like injector designs*. Tech. rep. SAE Technical Paper, 2020 (cited on page 56).

Lemmon, E. W., Bell, I., Huber, M., and McLinden, M. O. “Thermophysical Properties of Fluid Systems”. In: *NIST Standard Reference Database Number 69*. Ed. by P. J. Linstrom and W. G. Mallard. Gaithersburg MD, 20899, USA.: National Institute of Standards and Technology, 1998. DOI: https://doi.org/10.18434/T4D303 (cited on pages 58, 59, 109, 129).

Lemmon, E. W., McLinden, M. O., and Friend, D. G. "Thermophysical Properties of Fluid Systems". In: *NIST Chemistry WebBook, NIST Standard Reference Database Number 69*. Ed. by P. J. Linstrom and W. G. Mallard. 2011 (cited on page 63).

Leng, P. et al. "Cavitation instability in real-size GDI nozzle using X-ray phase-contrast imaging". In: *International Journal of Heat and Mass Transfer* 235 (2024), p. 126137 (cited on page 15).

Lesnik, L., Kegl, B., Bombek, G., Hočevar, M., and Biluš, I. "The influence of in-nozzle cavitation on flow characteristics and spray break-up". In: *Fuel* 222 (2018), pp. 550–560. DOI: https://doi.org/10.1016/j.fuel.2018.02.144 (cited on page 32).

Li, X. et al. "Insights into Microscopic Characteristics of Gasoline and Ethanol Spray from a GDI Injector Under Injection Pressure up to 50 MPa". In: *Sustainability* 16.21 (2024). DOI: 10.3390/su16219471 (cited on pages 35, 190).

Li, X., Li, T., and Xu, M. "Effect of ambient temperature on flash-boiling spray characteristics for a multi-hole gasoline injector". In: *Experiments in Fluids* 60 (2019), pp. 1–12 (cited on page 30).

Li, X., Sun, Z., Yang, S., Wang, H., and Nour, M. "Flash boiling combustion of isomeric butanol and gasoline surrogate blends using constant volume spray chamber and GDI optical engine". In: *Fuel* 286.P1 (2021), p. 119328. DOI: 10.1016/j.fuel.2020.119328 (cited on page 6).

Li, X. et al. "Investigations on the impact of phase change on single plume flash boiling radial expansion and drop-sizing characteristics". In: *Applied Thermal Engineering* 202 (2022), p. 117911. DOI: https://doi.org/10.1016/j.applthermaleng.2021.117911 (cited on page 137).

Li, X. et al. "A review on the recent advances of flash boiling atomization and combustion applications". In: *Progress in Energy and Combustion Science* 100 (2024), p. 101119. DOI: https://doi.org/10.1016/j.pecs.2023.101119 (cited on page 32).

Li, Y. et al. "An exploration on collapse mechanism of multi-jet flash-boiling sprays". In: *Applied Thermal Engineering* 134.May 2017 (2018), pp. 20–28. DOI: 10.1016/j.applthermaleng.2018.01.102 (cited on pages 32, 141).

Li, Y. et al. "Spray morphology transformation of propane, n-hexane and iso-octane under flash-boiling conditions". In: *Fuel* 236.August 2018 (2019), pp. 677–685. DOI: 10.1016/j.fuel.2018.08.160 (cited on page 181).

Li, Y. et al. “Direct numerical simulation of atomization characteristics of ECN Spray-G injector: in-nozzle fluid flow and breakup processes”. In: *Flow, Turbulence and Combustion* 112.2 (2024), pp. 615–642 (cited on page 179).

Liu, W., Lu, Y., Kang, Y., Yan, J., and Lee, C.-F. “Macroscopic characteristics of flash-boiling spray focused on plume interaction”. In: *International Journal of Heat and Mass Transfer* 170 (2021), p. 120999. DOI: https://doi.org/10.1016/j.ijheatmasstransfer.2021.120999 (cited on page 76).

Liu, Y. et al. “Spray development and droplet characteristics of high temperature single-hole gasoline spray”. In: *Fuel* 191 (2017), pp. 97–105. DOI: 10.1016/j.fuel.2016.11.068 (cited on pages 21, 166).

Lubrizol Corporation. *How It Works – PFI vs GDI Engines*. Accessed: March 20, 2025. 2023 (cited on page 13).

Luo, K., Changxiao, S., Min, C., and Fan, J. “Level set method for atomization and evaporation simulations”. In: *Progress in Energy and Combustion Science* 73 (2019), pp. 65–94. DOI: 10.1016/j.pecs.2019.03.001 (cited on page 27).

Ma, L.-P. et al. “Kinetic study of three-way catalyst of automotive exhaust gas: Modeling and application”. In: *Chemical Engineering Journal* 155.1-2 (2009), pp. 241–247 (cited on page 23).

Macian, V., Payri, R., Margot, X., and Salvador, F. J. “A CFD analysis of the influence of diesel nozzle geometry on the inception of cavitation”. In: *Atomization and Sprays* 13 (2003), pp. 579–604 (cited on page 100).

Martinez, S., Irimescu, A., Merola, S., Lacava, P., and Curto-Riso, P. “Flame Front Propagation in an Optical GDI Engine under Stoichiometric and Lean Burn Conditions”. In: *Energies* 10 (2017), p. 1337. DOI: 10.3390/EN10091337 (cited on page 12).

Martinez, S., Irimescu, A., Merola, S. S., Lacava, P., and Curto-Riso, P. “Flame Front Propagation in an Optical GDI Engine under Stoichiometric and Lean Burn Conditions”. In: *Energies* 10.9 (2017). DOI: 10.3390/en10091337 (cited on page 21).

Martínez, M., Martí-Aldaraví, P., Salvador, F. J., and Martínez-Miracle, E. C. “In-and near-nozzle and external flow characterization in Gasoline Direct injection (GDi) engines–A review of latest technologies and trends. Part 2: Computational background”. In: *International Journal of Engine Research* (2024), p. 14680874241309959 (cited on page 26).

Martínez, M., Martí-Aldaraví, P., Salvador, F. J., and Martínez-Miracle, E. C. "In- and near-nozzle and external flow characterization in Gasoline Direct injection (GDi) engines – A review of latest technologies and trends. Part 2: Computational background". In: *International Journal of Engine Research* 0.0 (0000), p. 14680874241309959. DOI: 10.1177/14680874241309959 (cited on page 15).

Martins, J. and Brito, F. P. "Alternative Fuels for Internal Combustion Engines". In: *Energies* 13.16 (2020). DOI: 10.3390/en13164086 (cited on page 4).

MathWorks. *image Function - MATLAB Documentation*. MathWorks. Accessed 2024. URL: https://es.mathworks.com/help/matlab/ref/image.html (cited on page 74).

Medina, M., Bautista, A., Wooldridge, M., and Payri, R. "The effects of injector geometry and operating conditions on spray mass, momentum and development using high-pressure gasoline". In: *Fuel* 294.December 2020 (2021), p. 120468. DOI: 10.1016/j.fuel.2021.120468 (cited on pages 13, 108).

Mishra, Y. N. et al. "3D mapping of droplet Sauter mean diameter in sprays." In: *Applied optics* 58 14 (2019), pp. 3775–3783 (cited on page 28).

Mojtabi, M., Chadwick, N., Wigley, G., and Helie, J. "The effect of flash boiling on break up and atomization in GDI sprays". In: *Proceedings of the 22nd European Conference on Liquid Atomization and Spray Systems. ILASS Europe. Como Lake, Italy*. 2008, pp. 08–10 (cited on page 31).

Montanaro, A., Allocca, L., Meccariello, G., and De Vita, A. "Very high-pressure sprays of gasoline from a GDI multi-hole injector". In: *Proceedings of the 29th Conference on Liquid Atomization and Spray Systems*. 2019 (cited on page 18).

Moon, S., Li, T., Sato, K., and Yokohata, H. "Governing parameters and dynamics of turbulent spray atomization from modern GDI injectors". In: *Energy* 127 (2017), pp. 89–100 (cited on pages 25, 26).

Moon, S. et al. "Ultrafast X-ray study of multi-hole GDI injector sprays: Effects of nozzle hole length and number on initial spray formation". In: *Experimental Thermal and Fluid Science* 68 (2015), pp. 68–81 (cited on pages 14, 16, 160).

Muhammed, H., Balaji, K., Tamilarasan, N., Sakthivel, R., et al. "A Review on Alternative Fuels: Spray Characteristics, Engine Performance and Emissions Effect". In: *Sustainable Futures* (2025), p. 100456 (cited on page 15).

Muriungi, B., Wang, L., and Shahbazi, A. “Comparison of Bimetallic Fe-Cu and Fe-Ca Oxygen Carriers for Biomass Gasification”. In: *Energies* 13.8 (2020). DOI: 10.3390/en13082019 (cited on page 4).

Nayak, G. et al. “An Experimental Investigation into the GDI Spray Characteristics of Ethanol and Lemon Peel Oil”. In: *Conference on Fluid Mechanics and Fluid Power*. Springer. 2022, pp. 67–79 (cited on page 144).

Nour, M. et al. “Effect of flash boiling injection on combustion and PN emissions of DISI optical engine fueled with butanol isomers/TPRF blends”. In: *Proceedings of the Combustion Institute* 38.4 (2021), pp. 5923–5931. DOI: 10.1016/j.proci.2020.10.006 (cited on page 6).

Oh, H., Hwang, J., White, L., Pickett, L. M., and Han, D. “Spray collapse characteristics of practical GDI spray for lateral-mounted GDI engines”. In: *International Journal of Heat and Mass Transfer* 190 (2022), p. 122743. DOI: https://doi.org/10.1016/j.ijheatmasstransfer.2022.122743 (cited on pages 31, 147).

Otsu, N. “A Threshold Selection Method from Gray-Level Histograms”. In: *IEEE Transactions on Systems, Man, and Cybernetics* 9.1 (1979), pp. 62–66. DOI: 10.1109/TSMC.1979.4310076 (cited on page 76).

Oza, R. D. and Sinnamon, J. F. “An experimental and analytical study of flash-boiling fuel injection”. In: *SAE Technical Papers* (1983). DOI: 10.4271/830590 (cited on page 32).

Park, J. and Park, S. “Spray Development Process Utilizing a Multi-Hole GDI Injector with Different Spray Hole Lengths and Step Hole Diameters”. In: *International Journal of Automotive Technology* 23.3 (2022), pp. 641–649 (cited on page 18).

Park, S. W. and Sik Lee, C. “Investigation of atomization and evaporation characteristics of high-pressure injection diesel spray using Kelvin—Helmholz instability/droplet deformation and break-up competition model”. In: *Proceedings of the Institution of Mechanical Engineers, Part D: Journal of Automobile Engineering* 218.7 (2004), pp. 767–777 (cited on page 25).

Payri, R., Bracho, G., Soriano, J. A., Fernández-Yáñez, P., and Armas, O. “Nozzle rate of injection estimation from hole to hole momentum flux data with different fossil and renewable fuels”. In: *Fuel* 279.May (2020), p. 118404. DOI: 10.1016/j.fuel.2020.118404 (cited on pages 64, 66).

Payri, R., Salvador, F., Gimeno, J., and Bracho, G. "A NEW METHODOLOGY FOR CORRECTING THE SIGNAL CUMULATIVE PHENOMENON ON INJECTION RATE MEASUREMENTS". In: *Experimental Techniques* 32.1 (2008), pp. 46–49. DOI: 10.1111/j.1747-1567.2007.00188.x (cited on page 61).

Payri, R., Bracho, G., Marti-Aldaravi, P., and Viera, A. "Near field visualization of diesel spray for different nozzle inclination angles in non-vaporizing conditions". In: *Atomization and Sprays* 27.3 (2017), pp. 251–267. DOI: 10.1615/AtomizSpr.2017017949 (cited on page 76).

Payri, R., Garcia, A., Domenech, V., Durrett, R. P., and Plazas, A. H. "An experimental study of gasoline effects on injection rate, momentum flux and spray characteristics using a common rail diesel injection system". In: *Fuel* 97 (2012), pp. 390–399. DOI: 10.1016/j.fuel.2011.11.065 (cited on page 109).

Payri, R., García-Oliver, J. M., Bracho, G., and Cao, J. "Experimental characterization of direct injection liquid ammonia sprays under non-reacting diesel-like conditions". In: *Fuel* 362 (2024), p. 130851 (cited on pages 37, 59, 129, 190).

Payri, R., García-Oliver, J. M., Mendoza, V., and Viera, A. "Analysis of the Influence of Diesel Spray Injection on the Ignition and Soot Formation in Multiple Injection Strategy". In: *Energies* 13.13 (2020). DOI: 10.3390/en13133505 (cited on page 74).

Payri, R., Gimeno, J., Martí-Aldaraví, P., and Vaquerizo, D. "Momentum Flux Measurements on an ECN GDi Injector". In: *SAE Technical Paper 2015-01-1893*. 2015, p. 11. DOI: 10.4271/2015-01-1893 (cited on pages 64, 66, 67, 107, 115, 116).

Payri, R., Gimeno, J., Martı-Aldaravi, P., and Viera, A. "Measurements of the mass allocation for multiple injection strategies using the rate of injection and momentum flux signals". In: *International Journal of Engine Research* (2020). DOI: 10.1177/1468087419894854 (cited on pages 59, 61, 66, 119).

Payri, R., Martí-Aldaraví, P., Alvarez, V. M., and Bautista, A. "Evaluation of GDI spray structures under flash boiling and strong collapse conditions with diverse fuels". In: *Applied Thermal Engineering* 234 (2023), p. 121195 (cited on pages 72, 137, 147).

Payri, R., Salvador, F. J., Bracho, G., and Viera, A. "Differences between single and double-pass schlieren imaging on diesel vapor spray characteristics". In: *Applied Thermal Engineering* 125 (2017), pp. 220–231. DOI: 10.1016/j.applthermaleng.2017.06.140 (cited on pages 76, 77).

Pérez-Ones, O., Díaz-Rodríguez, J., Zumalacárregui, L., and Gozá-León, O. "Evaluación de propiedades físicas de mezclas etanol-agua (II)". In: *Revista Facultad de Ingeniería Universidad de Antioquia* 52 (2010), pp. 62–74 (cited on pages 58, 108, 109).

Piehl, J. A., Zyada, A., Bravo, L., and Samimi-Abianeh, O. "Review of Oxidation of Gasoline Surrogates and Its Components". In: *Journal of Combustion* 2018 (2018). DOI: 10.1155/2018/8406754 (cited on page 58).

Pilch, M. and Erdman, C. "Use of breakup time data and velocity history data to predict the maximum size of stable fragments for acceleration-induced breakup of a liquid drop". In: *International Journal of Multiphase Flow* 13.6 (1987), pp. 741–757. DOI: https://doi.org/10.1016/0301-9322(87)90063-2 (cited on page 26).

Postrioti, L., Bosi, M., Mariani, A., and Ungaro, C. *Momentum flux spatial distribution and pda analysis of a gdi spray.* Tech. rep. SAE Technical Paper, 2012 (cited on page 21).

Privitera, S., Manetto, G., Pascuzzi, S., Pessina, D., and Cerruto, E. "Drop Size Measurement Techniques for Agricultural Sprays:A State-of-The-Art Review". In: *Agronomy* 13.3 (2023). DOI: 10.3390/agronomy13030678 (cited on page 78).

Qiu, S. et al. "Dynamics and mechanisms of spray plume interference under flash boiling conditions". In: *Energy* 314 (2025), p. 134121. DOI: https://doi.org/10.1016/j.energy.2024.134121 (cited on page 194).

Rachakonda, S. K., Paydarfar, A., and Schmidt, D. P. "Prediction of spray collapse in multi-hole gasoline direct-injection fuel injectors". In: *International Journal of Engine Research* 20.1 (2019), pp. 18–33. DOI: 10.1177/1468087418819527 (cited on page 141).

Ramirez, A. et al. "Quantitative X-ray measurements of high-pressure fuel sprays from a production heavy duty diesel injector". In: *Experiments in fluids* 47 (2009), pp. 119–134 (cited on page 25).

Rashed, R. "Geometrical optics". In: *Encyclopedia of the history of Arabic science*. Routledge, 2019, pp. 618–646 (cited on page 130).

Raza, M., Chen, L., Leach, F., and Ding, S. "A Review of Particulate Number (PN) Emissions from Gasoline Direct Injection (GDI) Engines and Their Control Techniques". In: *Energies* 11.6 (2018). DOI: 10.3390/en11061417 (cited on page 30).

Reckers, W., Befrui, B., and Corbinelli, G. "Investigation of high pressure GDi conical spray atomization for spray-guided combustion systems". In: *AVL 8th International Symposium on Combustion Diagnostics*. 2008 (cited on page 25).

Reitz, R. D. and Diwakar, R. "Structure of high-pressure fuel sprays". In: *SAE transactions* (1987), pp. 492–509 (cited on pages 25, 26).

Robert Bosch GmbH. *Gasoline Direct Injection: Bosch Aftermarket Services*. Accessed: March 23, 2025. 2021 (cited on page 20).

Saliba, G. et al. "Comparison of gasoline direct-injection (GDI) and port fuel injection (PFI) vehicle emissions: emission certification standards, cold-start, secondary organic aerosol formation potential, and potential climate impacts". In: *Environmental science & technology* 51.11 (2017), pp. 6542–6552 (cited on page 12).

Salvador, F. J., Gimeno, J., Carreres, M., and Crialesi-Esposito, M. "Fuel temperature influence on the performance of a last generation common-rail diesel ballistic injector. Part I: Experimental mass flow rate measurements and discussion". In: *Energy Conversion and Management* 114 (2016), pp. 364–375. DOI: 10.1016/j.enconman.2016.02.042 (cited on pages 62, 108, 109).

Sellnau, M. et al. "Aftertreatment System for Light-Duty Gasoline Compression Ignition (LD-GCI) for Ultra-Low Criteria Emissions". In: *Internal Combustion Engine Division Fall Technical Conference*. Vol. 88520. American Society of Mechanical Engineers. 2024, V001T05A008 (cited on page 23).

Sforzo, B., Tekawade, A., Matusik, K. E., Kastengren, A. L., and Powell, C. F. "3D Measurements of the Geometry, Internal Flow and Emerging Fuel Jet from the ECN Spray C Injector". In: *ILASS Europe 29th Conference on Liquid Atomization and Spray Systems*. 2019 (cited on page 102).

Sforzo, B. A. et al. "X-ray characterization of real fuel sprays for gasoline direct injection". In: *Journal of Energy Resources Technology* 144.2 (2022), p. 022303 (cited on pages 13, 15, 102).

Shahangian, N. et al. "Spray Orientation Assessment and Correction Method for GDI Momentum Flux Measurements". In: *"17th Conference. The Working Process of the Internal Combustion Engine"*. 2019, pp. 231–241 (cited on pages 69, 115).

Sharma, N. and Agarwal, A. K. "Macroscopic spray characteristics of a gasohol fueled GDI injector and impact on engine combustion and particulate morphology". In: *Fuel* 295 (2021), p. 120461 (cited on pages 137, 191).

Shuai, S., Ma, X., Li, Y., Qi, Y., and Xu, H. “Recent progress in automotive gasoline direct injection engine technology”. In: *Automotive Innovation* 1 (2018), pp. 95–113 (cited on page 39).

Singh, E. et al. “Particulate Matter Emissions in Gasoline Direct-Injection Spark-Ignition Engines: Sources, Fuel Dependency, and Quantities”. In: *Fuel* 338 (2023), p. 127198. DOI: https://doi.org/10.1016/j.fuel.2022.127198 (cited on page 5).

Skiba, S. and Melbert, J. “Dosing performance of piezo injectors and sensorless closed-loop controlled solenoid injectors for gasoline direct injection”. In: *SAE International Journal of Engines* 5.2 (2012), pp. 330–335 (cited on page 13).

Skogsberg, M., Dahlander, P., Lindgren, R., and Denbratt, I. *Effects of injector parameters on mixture formation for multi-hole nozzles in a spray-guided gasoline DI engine*. Tech. rep. SAE Technical Paper, 2005 (cited on page 14).

Soleimani, A. et al. “Progress in hydrogen fuel cell vehicles and up-and-coming technologies for eco-friendly transportation: an international assessment”. In: *Multiscale and Multidisciplinary Modeling, Experiments and Design* (2024), pp. 1–20 (cited on page 4).

Investigation of the Effect of Plume Number on Spray Collapse. Vol. ASME 2019 Internal Combustion Engine Division Fall Technical Conference. Internal Combustion Engine Division Fall Technical Conference. 2019, V001T06A004. DOI: 10.1115/ICEF2019-7187 (cited on page 191).

Takagi, Y. “A new era in spark-ignition engines featuring high-pressure direct injection”. In: *Symposium (international) on combustion*. Vol. 27. 2. Elsevier. 1998, pp. 2055–2068 (cited on page 13).

Tekawade, A. et al. “Time-resolved 3D imaging of two-phase fluid flow inside a steel fuel injector using synchrotron X-ray tomography”. In: *Scientific Reports* 10 (2020). DOI: 10.1038/s41598-020-65701-x (cited on page 102).

Tripathy, S., Sahoo, S., and Srivastava, D. “Gasoline Direct Injection—Challenges”. In: (2017), pp. 367–379. DOI: 10.1007/978-981-10-3785-6_16 (cited on page 12).

Tropea, C. “Optical particle characterization in flows”. In: *Annual Review of Fluid Mechanics* 43 (2011), pp. 399–426 (cited on page 78).

Uberall, A., Otte, R., Eilts, P., and Krahl, J. “A literature research about particle emissions from engines with direct gasoline injection and the potential to reduce these emissions”. In: *Fuel* 147 (2015), pp. 203–207. DOI: https://doi.org/10.1016/j.fuel.2015.01.012 (cited on page 22).

Valderrama, G. and Sebastián, J. "Macroscopic and microscopic characterization of non-reacting diesel sprays at low and very high injection pressures". In: 2018 (cited on pages 25, 26, 28, 133, 170).

Vaquerizo, D. "Study on Advanced Spray-Guided Gasoline Direct Injection Systems". PhD thesis. Universitat Politècnica de València, 2017 (cited on pages 63, 64, 69).

Viera, A. "Effect of multiple injection strategies on the diesel spray formation and combustion using optical diagnostics". PhD thesis. Universitat Politècnica de València, 2019 (cited on pages 60–62, 64, 74).

Vlad, T. S. "Phase doppler measurement in diesel dense sprays: optimisation of measurements and study of the orifice geometry influence over the spray at microscopic level". PhD thesis. Universitat Politècnica de València, 2007 (cited on page 91).

Wang, B. et al. "Investigation of deposit effect on multi-hole injector spray characteristics and air/fuel mixing process". In: *Fuel* 191 (2017), pp. 10–24 (cited on pages 19, 166).

Wang, B., Pamminger, M., Vojtech, R., and Wallner, T. "Impact of injection strategies on combustion characteristics, efficiency and emissions of gasoline compression ignition operation in a heavy-duty multi-cylinder engine". In: *International Journal of Engine Research* 21.8 (2020), pp. 1426–1440 (cited on page 12).

Wang, D., Ji, C., Wang, S., Yang, J., and Wang, Z. "Numerical study of the premixed ammonia-hydrogen combustion under engine-relevant conditions". In: *International Journal of Hydrogen Energy* 46.2 (2021), pp. 2667–2683. DOI: https://doi.org/10.1016/j.ijhydene.2020.10.045 (cited on page 37).

Wang, H. et al. "Promotion of particle agglomeration by different vortex generator angles based on PIV-PDPA experiment". In: *Chemical Engineering Journal* 486 (2024), p. 150308. DOI: https://doi.org/10.1016/j.cej.2024.150308 (cited on page 78).

Wissink, M. L. et al. "Measurement of needle and armature dynamics in a gasoline direct injector by high-speed neutron imaging". In: *International Journal of Engine Research* 25.2 (2024), pp. 347–357 (cited on page 15).

Wooldridge, M. S., Singh, R., Gutierrez, L. G., and Clancy, S. "Survey of strategies to reduce cold-start particulate, CO, NOx, and hydrocarbon emissions from direct-injection spark-ignition engines". In: *International Journal of Engine Research* 24.2 (2023), pp. 456–480. DOI: 10.1177/14680874211068576 (cited on page 22).

Wu, S., Gandhi, A., Li, H., and Meinhart, M. "Experimental and numerical study of the effects of nozzle taper angle on spray characteristics of GDI multi-hole injectors at cold condition". In: *Fuel* 275 (2020), p. 117888. DOI: https://doi.org/10.1016/j.fuel.2020.117888 (cited on page 26).

Wu, S., Yang, S., Wooldridge, M., and Xu, M. "Experimental study of the spray collapse process of multi-hole gasoline fuel injection at flash boiling conditions". In: *Fuel* 242 (2019), pp. 109–123. DOI: https://doi.org/10.1016/j.fuel.2019.01.027 (cited on pages 141, 183, 194).

Xu, Q., Pan, H., Gao, Y., Li, X., and Xu, M. "Investigation of two-hole flash-boiling plume-to-plume interaction and its impact on spray collapse". In: *International Journal of Heat and Mass Transfer* 138 (2019), pp. 608–619. DOI: https://doi.org/10.1016/j.ijheatmasstransfer.2019.04.111 (cited on page 30).

Xuefeng, Z. and Xiu-min, Y. "Reserch on lean burning characteristics experiment based on GDI engine". In: *2011 International Conference on Materials for Renewable Energy & Environment*. Vol. 2. IEEE. 2011, pp. 1258–1262 (cited on page 13).

Yamaguchi, A., Koopmans, L., Helmantel, A., Dillner, J., and Dahlander, P. "Spray behaviors and gasoline direct injection engine performance using ultrahigh injection pressures up to 1500 bar". In: *SAE International Journal of Engines* 15.2 (2022), pp. 167–184 (cited on pages 13, 15).

Yan, J., Gao, S., Zhao, W., Lee, T. H., and Lee, C.-F. "Experimental study of sprays with isooctane, hexane, ethanol and their binary mixtures under different flash boiling intensities". In: *International Journal of Heat and Mass Transfer* 179 (2021), p. 121715. DOI: https://doi.org/10.1016/j.ijheatmasstransfer.2021.121715 (cited on pages 76, 144, 181).

Yang, J. et al. "Gasoline particulate filters as an effective tool to reduce particulate and polycyclic aromatic hydrocarbon emissions from gasoline direct injection (GDI) vehicles: a case study with two GDI vehicles". In: *Environmental Science & Technology* 52.5 (2018), pp. 3275–3284 (cited on page 23).

Yang, W., Zhang, Z., Li, J., and Xue, Y. "Experimental investigation of nucleation rate and flash boiling spray behavior under low-pressure conditions". In: *Fuel* 267 (2020), p. 117262. DOI: 10.1016/j.fuel.2020.117262 (cited on pages 32–34).

Ye, Z. "GDI engine exhaust aftertreatment system analysis and oxygen sensor based identification, modeling and control of lean NOx trap". In: *Internal Combustion Engine Division Spring Technical Conference*. Vol. 36789. 2003, pp. 713–719 (cited on page 23).

Zhang, W. et al. "Effect of gasoline aromatic compositions coupled with single and double injection strategy on GDI engine combustion and emissions". In: *Fuel* 278 (2020), p. 118308. DOI: https://doi.org/10.1016/j.fuel.2020.118308 (cited on pages 37, 38).

Zhao, F., Lai, M.-C., and Harrington, D. L. "Automotive spark-ignited direct-injection gasoline engines". In: *Progress in energy and combustion science* 25.5 (1999), pp. 437–562 (cited on pages 12, 13).

Zhao, H. "1 - Overview of gasoline direct injection engines". In: *Advanced Direct Injection Combustion Engine Technologies and Development*. Ed. by H. Zhao. Vol. 1. Woodhead Publishing, 2010, pp. 1–19. DOI: https://doi.org/10.1533/9781845697327.1 (cited on page 12).

Zhao, W., Yan, J., Gao, S., Lee, T. H., and Li, X. "Effects of fuel properties and aerodynamic breakup on spray under flash boiling conditions". In: *Applied Thermal Engineering* 200 (2022), p. 117646. DOI: https://doi.org/10.1016/j.applthermaleng.2021.117646 (cited on page 18).

Zhao, X. and Xiong, W. "Notice of RetractionCombustion characteristics of test and research on electronic control fuel injection system of cars GDI engine". In: *2011 Second International Conference on Mechanic Automation and Control Engineering* (2011), pp. 123–126 (cited on page 13).

Zhou, L., Zhang, X., Zhong, L., and Yu, J. "Effects of Flame Propagation Velocity and Turbulence Intensity on End-Gas Auto-Ignition in a Spark Ignition Gasoline Engine". In: *Energies* 13.19 (2020). DOI: 10.3390/en13195039 (cited on page 21).

Appendices

Appendix A

Appendix

This section includes the full test matrix measured in the different campaigns including the R_P calculated.

A.1 Conditions measured for Rate of Momentum.

For Rate of Momentum (ROM) measurements, @Ambient Temperature in the vessel, the conditions are shown below:

Table A.1: Full ROM test matrix with R_P values for each operating condition.

#	Injector	Fuel	T_n [°C]	P_r [bar]	CP [bar]	R_P
0	C3539	Ethanol	25	200	0.2	0.335
1	C3539	Ethanol	25	200	0.5	0.134
2	C3539	Ethanol	25	200	1	0.067
3	C3539	Ethanol	25	200	6	0.011
4	C3539	Ethanol	25	200	15	0.004
5	C3539	Ethanol	25	200	21.5	0.003

Continued on next page

#	Injector	Fuel	T_n [°C]	P_r [bar]	CP [bar]	R_P
6	C3539	Ethanol	25	350	0.2	0.335
7	C3539	Ethanol	25	350	0.5	0.134
8	C3539	Ethanol	25	350	1	0.067
9	C3539	Ethanol	25	350	6	0.011
10	C3539	Ethanol	25	350	15	0.004
11	C3539	Ethanol	25	350	21.5	0.003
12	C3539	Ethanol	90	200	0.2	7.903
13	C3539	Ethanol	90	200	0.5	3.161
14	C3539	Ethanol	90	200	1	1.581
15	C3539	Ethanol	90	200	6	0.263
16	C3539	Ethanol	90	200	15	0.105
17	C3539	Ethanol	90	200	21.5	0.074
18	C3539	Ethanol	90	350	0.2	7.903
19	C3539	Ethanol	90	350	0.5	3.161
20	C3539	Ethanol	90	350	1	1.581
21	C3539	Ethanol	90	350	6	0.263
22	C3539	Ethanol	90	350	15	0.105
23	C3539	Ethanol	90	350	21.5	0.074
24	C3539	Hexane	25	200	0.2	0.809
25	C3539	Hexane	25	200	0.5	0.324
26	C3539	Hexane	25	200	1	0.162
27	C3539	Hexane	25	200	6	0.027
28	C3539	Hexane	25	200	15	0.011
29	C3539	Hexane	25	200	21.5	0.008
30	C3539	Hexane	25	350	0.2	0.809
31	C3539	Hexane	25	350	0.5	0.324
32	C3539	Hexane	25	350	1	0.162
33	C3539	Hexane	25	350	6	0.027
34	C3539	Hexane	25	350	15	0.011
35	C3539	Hexane	25	350	21.5	0.008
36	C3539	Hexane	90	200	0.2	9.45
37	C3539	Hexane	90	200	0.5	3.78

Continued on next page

#	Injector	Fuel	T_n [°C]	P_r [bar]	CP [bar]	R_P
38	C3539	Hexane	90	200	1	1.89
39	C3539	Hexane	90	200	6	0.315
40	C3539	Hexane	90	200	15	0.126
41	C3539	Hexane	90	200	21.5	0.088
42	C3539	Hexane	90	350	0.2	9.45
43	C3539	Hexane	90	350	0.5	3.78
44	C3539	Hexane	90	350	1	1.89
45	C3539	Hexane	90	350	6	0.315
46	C3539	Hexane	90	350	15	0.126
47	C3539	Hexane	90	350	21.5	0.088
48	C3539	IsoOctane	25	200	0.2	0.07
49	C3539	IsoOctane	25	200	0.5	0.028
50	C3539	IsoOctane	25	200	1	0.014
51	C3539	IsoOctane	25	200	6	0.002
52	C3539	IsoOctane	25	200	15	0.001
53	C3539	IsoOctane	25	200	21.5	0.001
54	C3539	IsoOctane	25	350	0.2	0.07
55	C3539	IsoOctane	25	350	0.5	0.028
56	C3539	IsoOctane	25	350	1	0.014
57	C3539	IsoOctane	25	350	6	0.002
58	C3539	IsoOctane	25	350	15	0.001
59	C3539	IsoOctane	25	350	21.5	0.001
60	C3539	IsoOctane	90	200	0.2	1.671
61	C3539	IsoOctane	90	200	0.5	0.668
62	C3539	IsoOctane	90	200	1	0.334
63	C3539	IsoOctane	90	200	6	0.056
64	C3539	IsoOctane	90	200	15	0.022
65	C3539	IsoOctane	90	200	21.5	0.016
66	C3539	IsoOctane	90	350	0.2	1.671
67	C3539	IsoOctane	90	350	0.5	0.668
68	C3539	IsoOctane	90	350	1	0.334
69	C3539	IsoOctane	90	350	6	0.056

Continued on next page

#	Injector	Fuel	T_n [°C]	P_r [bar]	CP [bar]	R_P
70	C3539	IsoOctane	90	350	15	0.022
71	C3539	IsoOctane	90	350	21.5	0.016

A.2 PDA test matrix for all conditions measured

For the visualization and PDA measurement campaigns, the test matrix was expanded by including additional ambient temperatures and modifying some of the ambient pressure conditions compared to the ROM measurements. Although not included in the Table A.2, in this case, the matrix also incorporates multiple measurement positions along the spray axis, including different axial distances from the nozzle tip and several radial offsets.

Table A.2: Full visualization and PDA test matrix with R_P values for each operating condition

#	Inj	Fuel	Tb (°C)	Tn (°C)	Pr (bar)	Cp (bar)	Rp	Notes
1	C3539	Ethanol	25	25	200	1	0.6	
2	C3539	Ethanol	25	25	200	6	0.01	
3	C3539	Ethanol	25	90	200	0.2	7.903	
4	C3539	Ethanol	25	90	200	0.5	3.161	
5	C3539	Ethanol	25	90	200	1	1.581	
6	C3539	Ethanol	25	90	200	6	0.263	
7	C3539	Ethanol	25	90	200	12	0.132	
8	C3539	Ethanol	25	90	350	6	0.263	
9	C3539	Ethanol	25	90	350	12	0.132	
10	C3539	Ethanol	60	25	200	6	0.011	
11	C3539	Ethanol	60	25	350	6	0.011	
12	C3539	Ethanol	60	90	100	6	0.263	
13	C3539	Ethanol	60	90	200	1	1.581	
14	C3539	Ethanol	60	90	200	6	0.263	
15	C3539	Ethanol	60	90	200	12	0.132	

Continued on next page

#	Inj	Fuel	Tb (°C)	Tn (°C)	Pr (bar)	Cp (bar)	Rp	Notes
16	C3539	Ethanol	60	110	200	1	1.581	
17	C3539	Ethanol	60	110	200	6	0.263	
18	C3539	Ethanol	60	110	200	12	0.132	
19	C3539	IsoOctane	120	25	200	6	0.011	
20	C3539	Hexane	120	25	200	6	0.027	
21	C3539	IsoOctane	120	90	200	0.5	0.056	
22	C3539	IsoOctane	120	90	200	0.5	0.13	
23	C3539	Ethanol	120	90	200	12	0.132	
24	C3539	Ethanol	120	90	350	0.5	3.161	
25	C3539	Ethanol	120	90	350	6	0.263	
26	C3539	IsoOctane	120	110	200	6	0.144	
27	C3539	Hexane	120	90	200	12	0.157	
28	C3539	Ethanol	120	90	200	6	0.263	
29	C3539	Ethanol	120	90	200	12	0.132	
30	C3539	Hexane	120	110	200	12	0.224	
31	C3539	Hexane	25	25	200	1	0.162	
32	C3539	Hexane	25	90	200	0.5	3.78	
33	C3539	Hexane	25	90	200	1	1.89	
34	C3539	Hexane	25	90	200	6	0.315	
35	C3539	Hexane	25	90	350	0.5	3.78	
36	C3539	Hexane	25	90	350	6	0.315	
37	C3539	Hexane	60	25	200	0.2	0.809	
38	C3539	Hexane	60	25	200	1	0.162	
39	C3539	Hexane	60	25	200	6	0.027	
40	C3539	Hexane	60	25	350	6	0.027	
41	C3539	Hexane	60	90	100	6	0.315	
42	C3539	Hexane	60	90	200	0.5	3.78	
43	C3539	Hexane	60	90	200	1	1.89	
44	C3539	Hexane	60	90	200	6	0.315	
45	C3539	Hexane	60	90	200	12	0.157	
46	C3539	Hexane	60	90	300	6	0.315	
47	C3539	Hexane	60	90	350	0.5	3.78	

Continued on next page

#	Inj	Fuel	Tb (°C)	Tn (°C)	Pr (bar)	Cp (bar)	Rp	Notes
48	C3539	Hexane	60	110	200	0.5	3.78	
49	C3539	Hexane	60	110	200	6	0.315	
50	C3539	Hexane	120	25	200	6	0.027	
51	C3539	Hexane	120	25	200	12	0.0135	
52	C3539	Hexane	120	25	350	0.5	0.324	
53	C3539	Hexane	120	25	350	1	0.162	
54	C3539	Hexane	120	25	350	6	0.027	
55	C3539	IsoOctane	120	110	200	0.2	0.325	
56	C3539	Ethanol	120	110	200	6	0.498	
57	C3539	Hexane	120	110	200	6	0.157	
58	C3539	IsoOctane	120	90	200	0.5	0.668	
59	C3539	Ethanol	120	90	200	1	1.581	
60	C3539	Hexane	120	90	350	0.2	9.449	
61	C3539	Hexane	120	90	350	0.5	3.78	
62	C3539	Hexane	120	90	350	1	1.89	
63	C3539	IsoOctane	120	90	200	0.2	1.671	
64	C3539	IsoOctane	120	110	200	0.5	1.728	
65	C3539	Hexane	120	110	200	1	1.89	
66	C3539	Ethanol	120	110	200	1	6.29	
67	C3539	Hexane	120	110	350	0.5	3.325	
68	C3539	Hexane	120	110	350	1	3.162	
69	C3539	Hexane	120	110	350	6	0.527	
70	C3539	Hexane	120	110	350	12	0.264	
71	C3539	Hexane	200	90	200	0.5	3.78	
72	C3539	Hexane	200	90	200	1	1.89	
73	C3539	Hexane	200	90	200	6	0.315	
74	C3539	Hexane	200	90	350	6	0.315	
75	C3539	IsoOctane	25	25	200	1	0.056	
76	C3539	IsoOctane	25	90	200	0.2	1.671	
77	C3539	IsoOctane	25	90	200	0.5	0.668	
78	C3539	IsoOctane	25	90	200	6	0.056	
79	C3539	IsoOctane	25	90	200	12	0.028	

Continued on next page

#	Inj	Fuel	Tb (°C)	Tn (°C)	Pr (bar)	Cp (bar)	Rp	Notes
80	C3539	IsoOctane	25	90	350	0.5	0.668	
81	C3539	IsoOctane	25	90	350	6	0.056	
82	C3539	IsoOctane	25	90	350	12	0.028	
83	C3539	IsoOctane	60	25	200	0.5	0.325	
84	C3539	IsoOctane	60	25	200	6	0.011	
85	C3539	IsoOctane	60	25	200	12	0.0055	
86	C3539	IsoOctane	60	25	200	1	0.065	
87	C3539	IsoOctane	60	25	200	6	0.011	
88	C3539	IsoOctane	60	90	200	0.2	1.671	
89	C3539	IsoOctane	60	90	200	0.5	0.668	
90	C3539	IsoOctane	60	90	200	1	0.334	
91	C3539	IsoOctane	60	90	200	6	0.056	
92	C3539	IsoOctane	60	90	200	12	0.028	
93	C3539	IsoOctane	60	110	200	0.2	4.321	
94	C3539	IsoOctane	60	110	200	0.5	1.728	
95	C3539	IsoOctane	60	110	200	6	0.144	
96	C3539	IsoOctane	60	110	200	12	0.072	
97	C3539	Ethanol	120	90	200	0.5	3.161	
98	C3539	Hexane	120	110	200	1	3.162	
99	C3539	Hexane	120	90	200	0.5	3.78	
100	C3539	IsoOctane	120	25	350	0.5	0.668	
101	C3539	IsoOctane	120	25	350	6	0.011	
102	C3539	IsoOctane	120	110	200	0.2	4.321	
103	C3539	Ethanol	120	110	200	0.5	5.38	
104	C3539	Hexane	120	110	200	0.5	6.325	
105	C3539	Ethanol	120	90	200	0.2	14.95	
106	C3539	Hexane	120	90	200	0.2	9.449	
107	C3539	Ethanol	120	110	200	0.2	14.95	
108	C3539	IsoOctane	200	90	200	0.5	0.668	
109	C3539	IsoOctane	200	90	200	6	0.056	
110	C3539	IsoOctane	200	90	350	0.5	0.668	
111	C3539	IsoOctane	200	90	350	6	0.056	

Continued on next page

#	Inj	Fuel	Tb (°C)	Tn (°C)	Pr (bar)	Cp (bar)	Rp	Notes
112	C3539	IsoOctane	200	110	200	0.2	4.321	
113	C7532	Ethanol	25	25	100	1	0.067	
114	C7532	Ethanol	25	25	200	6	0.263	
115	C7532	Ethanol	25	90	200	6	0.011	
116	C7532	Ethanol	60	25	100	6	0.263	
117	C7532	Ethanol	60	90	100	6	0.263	
118	C7532	Ethanol	60	90	200	0.2	7.903	
119	C7532	Ethanol	60	90	200	1	1.581	
120	C7532	Ethanol	60	90	200	6	0.263	
121	C7532	Ethanol	60	90	200	12	0.132	
122	C7532	Ethanol	60	90	350	6	0.263	
123	C7532	Ethanol	60	110	200	0.2	14.95	
124	C7532	Ethanol	60	110	200	0.5	5.38	
125	C7532	IsoOctane	25	90	200	0.5	0.668	
126	C7532	IsoOctane	25	90	200	6	0.056	
127	C7532	IsoOctane	60	25	100	6	0.011	
128	C7532	IsoOctane	60	90	100	6	0.056	
129	C7532	IsoOctane	60	90	200	0.2	1.671	
130	C7532	IsoOctane	60	90	200	0.5	0.668	
131	C7532	IsoOctane	60	90	200	1	0.334	
132	C7532	IsoOctane	60	90	200	6	0.056	
133	C7532	IsoOctane	60	90	200	12	0.028	
134	C7532	IsoOctane	60	90	350	0.5	0.668	
135	C7532	IsoOctane	60	90	350	6	0.056	
136	C7532	IsoOctane	60	110	200	0.2	4.321	
137	C7532	IsoOctane	60	110	200	0.5	1.728	
138	C7532	IsoOctane	60	110	200	0.5	1.728	